Momentum and Mass Transport by Coherent Structures in a Shallow Vegetated Shear Flow

by

Brian L. White

Submitted to the Department of Civil and Environmental Engineering
in partial fulfillment of the requirements for the degree of

Doctor of Philosophy in the field of Environmental Fluid Mechanics

at the

MASSACHUSETTS INSTITUTE OF TECHNOLOGY

February 2006

Author ....
Department of Civil and Environmental Engineering
January 24, 2006

Certified by ....
Heidi M. Nepf
Professor of Civil and Environmental Engineering
Thesis Supervisor

Accepted by ....
Andrew J. Whittle
Chairman, Departmental Committee for Graduate Students

Momentum and Mass Transport by Coherent Structures in a Shallow Vegetated Shear Flow

by

Brian L. White

Submitted to the Department of Civil and Environmental Engineering
on January 24, 2006, in partial fulfillment of the
requirements for the degree of
Doctor of Philosophy in the field of Environmental Fluid Mechanics

Abstract

In many aquatic systems, from tidal creeks with fringing mangroves to rivers and associated floodplains, there exists an interface between dense vegetation and a high conveyance channel. A shear flow develops across this interface and its dynamics influences the exchange of mass and momentum between the vegetation and the channel. This thesis describes an experimental study in a shallow laboratory channel with 1/3 of its width filled with circular cylinders, a model for emergent vegetation. The experiments reveal the formation of a shear layer with nearly periodic vortex structures. The vortices are documented with respect to their physical characteristics and their effect on mass and momentum exchange.

Distributions of mean velocity and turbulent Reynolds stress show a two layer structure in the shear flow. An inner layer exists near the interface, with a width that establishes the penetration of momentum into the vegetation; an outer boundary layer exists in the main channel, where the vortices reside, with a width independent of the vegetation. In each layer the mean velocity distributions are self-similar.

Results of a linear stability analysis suggest that channels with differential drag are conducive to the growth of Kelvin-Helmoltz shear instabilities. Indeed vortices are observed for all experimental conditions, and their passage frequency matches the most unstable frequency from linear theory. A typical vortex structure is educed by conditional sampling, and reveals strong crossflows consisting of sweeps from the main channel and ejections from the vegetation, leading to high Reynolds stress at the interface. The sweeps also maintain the coherent structures by increasing the shear at the interface and enhancing energy production.

Finally, a model is developed for exchange between the vegetation and the channel in terms of the vortex size and passage frequency. The semi-empirical model describes both mass transfer coefficients and interfacial friction coefficients in data from a range of vegetated flows, and suggests that a constant proportion of the vortex volume is exchanged over each cycle. The exchange coefficient is used to quantify the flushing timescale of a vegetated layer, and is applied to the problem of overbank transport of suspended sediment between a river and its floodplain.

Thesis Supervisor: Heidi M. Nepf
Title: Professor of Civil and Environmental Engineering

Acknowledgments

The completion of this thesis is the accomplishment of a few people who have generously shared with me their their time, knowledge, creativity, and encouragement. First among them is my advisor, Heidi Nepf, who has spent endless hours, often at one sitting, discussing particularly tricky problems with me, and lending a true experimentalist's creativity to work in the laboratory. Her commitment to education and her ability to bring out the best in students with widely varying personalities and research approaches is truly an inspiration that I hope to have at least partially absorbed.

I would like to thank members of my thesis committee, Eric Adams and Chiang Mei for their time and for their many helpful comments. I am grateful to fellow Parsons Environmental Fluid Mechanics students Marco Ghisalberti, Yukie Tanino, Anne Lightbody, Enda Murphy, Molly Palmer, Paul Fricker, Hrund Andradottir, Aaron Chow, and Peter Israelson for enlightening discussions, particularly when it was about their work, which provided both respite from and fresh perspectives on my own.

I am endlessly grateful to my parents, who as educators taught me to value knowledge and truth, or at least the pursuit thereof, and to my sister for her unique cultural and artistic perspective. Finally, and most paramount, I am boundlessly grateful to Kristin Blank. Although her contributions and support are innumerable, I must rectify a prior oversight and at long last acknowledge her work on nearly all illustrated figures contained in my M.S. Thesis (a copy is available in the library if one wishes to peruse the very fine artwork).

Lastly, a quote from the great Werner Herzog which applies equally well to science as to cinema:

Very often, [film] footage develops its own dynamic, its own life, that is totally unexpected, and moves away from your original intentions. And you have to acknowledge, yes, there is a child growing and developing and moving in a direction that isn't expected–accept it as it is and let it develop its own life.

Contents

Chapter 1

Introduction

1.1 Motivation

Many aquatic systems, such as tidal creeks with fringing mangroves, rivers and associated floodplains, and salt marshes and tidal channels, exhibit an interface between dense vegetation and a high conveyance channel. The differential in hydrodynamic drag between the vegetated plain and the main channel results in a shear flow often characterized by the formation of coherent turbulent structures, which influence the exchange of mass and momentum between the two zones. This material exchange is important for the hydrologic, morphodynamic, and ecological processes in these systems. The faster flowing channels carry much of the sediment and nutrient load, but within the vegetation lies a great deal of ecological diversity and physical capacity for sediment retention. The following examples illustrate the range of processes affected by this exchange process. The accretion of a salt marsh, and thus its ability to keep pace with rising sea level is in part dictated by sediment supply from the main channel (Stumpf, 1983). Heavy metals and other contaminants are preferentially associated with fine grain sediments and their transport to a river floodplain depends on overbank exchange with the main channel (Macklin, 1996). The exchange of freshwater between a tidal creek and fringing mangrove is necessary to prevent hypersaline conditions adverse to the health of the mangroves (Wolanski *et al.*, 2001). Finally, external nutrient supply is necessary to maintain rates of primary production in coastal macrophyte stands (Buzzelli *et al.*, 1999).

While a variety of factors will influence exchange in natural systems, including tidal flows and severe storm-driven flows, a description of the basic hydrodynamics of the shear layer at the interface is important for a system-level understanding. To this end, experiments have been carried out in a laboratory channel partially filled with model emergent vegetation, in the form of circular cylinders. The dynamics of exchange between the vegetated region and the main channel is studied by detailed measurements of velocity and turbulent stress. The most striking feature of the shear flow are the periodic coherent vortices that form at the vegetation interface. These structures result in large momentum fluxes, which are due to strong lateral motions consisting of sweeps toward the vegetation and ejections away from the vegetation. Figure 1-1*a* shows a typical velocity time series with the periodic vortex signal and the high-stress-producing sweeps and ejections. Figure 1-1*b* shows an ejection visualized by reflective tracer sprinkled on the water surface. Throughout the thesis, the coherent structures are a consistent theme, and the physical measurements are often interpreted in light of their structure. Ultimately, the thesis documents the physical characteristics of the structures, explains their dynamic cycle of generation and maintenance, and quantifies their impact on the flux of both momentum and mass across the vegetation-main channel interface.

1.2 Outline

The outline of the thesis is as follows. In chapter 2, the mean velocity and turbulent Reynolds stress are discussed. The mean distributions reveal a two layer structure to the shear flow. An inner layer, near the interface, limits the penetration of momentum into the vegetation, with a decreasing length scale for higher stem density. In the main channel, there is an outer boundary layer, with a width independent of the vegetation characteristics, but which correlates with the water depth, indicative of influence by bed friction. In each of these two distinct layers the mean velocity distributions are self-similar. The inner layer distributions collapse to a hyperbolic tangent profile

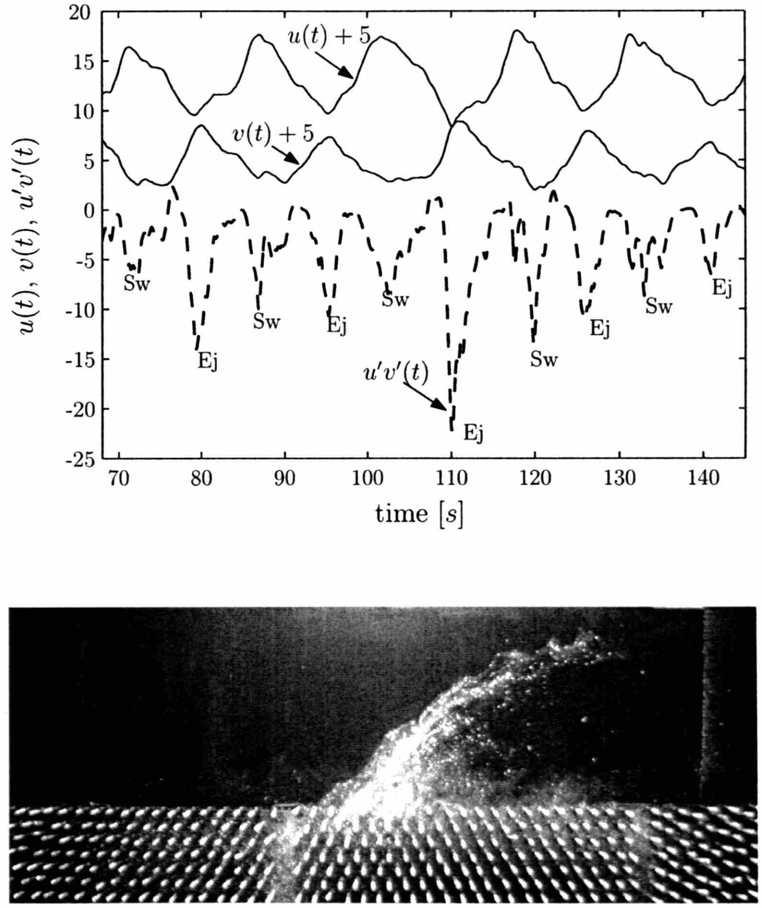

Figure 1-1: Sweeps and Ejections from Coherent Structures. (*a*) shows a time series of streamwise velocity, u, transverse velocity, v, and instantaneous Reynolds stress, $u'v'$, measured near the interface. The time series is marked by nearly periodic fluctuations corresponding to traveling vortices. Sweeps and Ejections are noted. (*b*) shows a visualization of an ejection event, a strong outflow from the vegetation (flow is from left to right).

characteristic of a mixing layer, while the outer flow collapses very nearly to a Blasius boundary layer profile. There exists a logarithmic region in the outer layer, and, analogous to the special case of "d-type" boundary layers, the roughness length scale, k_o, for the outer flow is independent of the vegetation density.

In chapter 3, a hydrodynamic stability analysis is described for channels with differential hydrodynamic drag. It is shown that for uniform drag, typical of open channels with bed friction, instabilities are damped, but differential drag, typical of the experimental channel, is more conducive to instability. Moreover, the frequency predicted by linear theory for the most unstable disturbance closely matches the frequency of the vortices from experiments.

In chapter 4, the structure of the coherent vortices is described. Though initiated by the inflection point in the inner layer, their size scales with the outer boundary layer width. The characteristic vortex was educed using a method of conditional sampling which gives a composite picture of the streamlines and vorticity. From these observations, the spatial distribution of stress-producing events, and the turbulent kinetic energy budget associated with the structures is described. Conclusions are then drawn about the mechanisms of vortex generation, maintenance, and spatial development. Results suggest that sweeps are the most important mechanism or maintaining the vortices.

In chapter 5, a model is developed for momentum and material exchange between the vegetation and the channel in terms of the vortex size and passage frequency. The model relies on a parameter, α, which describes the proportion of the vortex volume that is exchanged over each period of its passage. Data for scalar and momentum fluxes in canopy flows and momentum fluxes in the present experiments suggest α is a constant for a wide range of vegetated flows. Good agreement is shown between the model for interfacial flux and the friction coefficient from different data sets. The timescale for flushing from the vegetated layer is then predicted by solving a simplified form of the advection-diffusion equation with the interfacial mass transfer as a boundary condition. Finally, this method is applied to the problem of overbank transport of suspended sediment between a river and its floodplain, which demonstrates patterns of deposition for different channel flow conditions.

Chapter 2

Experimental Results: Mean Velocity and Shear Stress

2.1 Introduction: Flow in a Partially Vegetated Channel

2.1.1 Problem Description

The problem of interest is that of flow in an open channel that is partially filled with emergent vegetation. The vegetation is assumed to consist of individual shoots with a cylindrical morphology. We thus model the vegetation as an array of circular cylinders. The rigid cylinder array is ideal for modeling the flow-vegetation interaction because it is both simple and provides a reasonable morphological approximation of the stem region of emergent vegetation like reeds and rushes, which exhibit very limited bending when exposed to currents (Leonard & Luther, 1995). The simple geometry also places the problem in the context of a large class of well-studied boundary-flow interaction problems, such as rough-wall boundary layers that form in grooved channels (Ghaddar *et al.*, 1986; Djenidi *et al.*, 1999), channels with cylindrical span-wise roughness (Schatz *et al.*, 1995), and terrestrial canopies (Finnigan, 2000), as well as the problem of open flows adjacent to a porous medium (Beavers & Joseph, 1967;

Jimenez *et al.*, 2001; James & Davis, 2001).

A schematic of the problem is shown in figure 2-1. The cylinder array is described by the following properties: the mean cylinder diameter, d, the solid volume fraction of the array, ϕ, and the average center-to-center distance between cylinders, s. In addition, if the areal number density of cylinders is n $[cylinders\ area^{-1}]$, the average solid frontal area per unit volume in the plane perpendicular to the flow is $a = nd$.

The schematic depicts the staggered, equilateral arrangement of rods used in the present experiments (also considered by James & Davis, 2001). For this geometry, the solid fraction is related to the spacing and diameter by $\phi = \frac{\sqrt{3}\pi}{6}\frac{d^2}{s^2}$. Other geometries commonly studied are square arrays (James & Davis, 2001; Prinos *et al.*, 2003), for which $\phi = \frac{\pi}{4}\frac{d^2}{s^2}$, and random arrays (White & Nepf, 2003), for which the spacing scale is less clear, but in analogy to square arrays, a characteristic mean value, $s = \sqrt{\frac{\pi}{4\phi}}d$ can be defined. Also shown is the velocity distribution across the vegetation interface. The velocity approaches a constant value of U_1 inside the vegetation, when a spatial average is taken over the flow heterogeneity around the individual stems, and approaches a constant U_2 in the channel. The velocity in each zone results from the balance between the driving pressure gradient and the frictional resistance, applied by the individual obstructions in the vegetation, and bed drag in the channel. Also shown is the the slip velocity, U_s, defined in the schematic as the difference between the velocity at the interface and U_1. The interface is taken as the center-line of the outermost row of cylinders, and is defined as $y = 0$. Some researchers have defined U_s at this centerline (Larson & Higdon, 1986), while others have defined it at the line tangent to the outermost edge (James & Davis, 2001; Beavers & Joseph, 1967). This disparity in the definition of U_s illustrates the complexity of the problem and the lack of consensus around what the important metric is. Ideally, U_s should measure the degree of penetration of channel momentum into the array. It is shown in this chapter that this is best accomplished by defining U_s at the inflection point of the velocity profile, which is very close to, but not necessarily equal to $y = 0$. The penetration of momentum from the main channel, and hence the slip velocity, is controlled in general by the resistance of the medium. Differences in array geometry

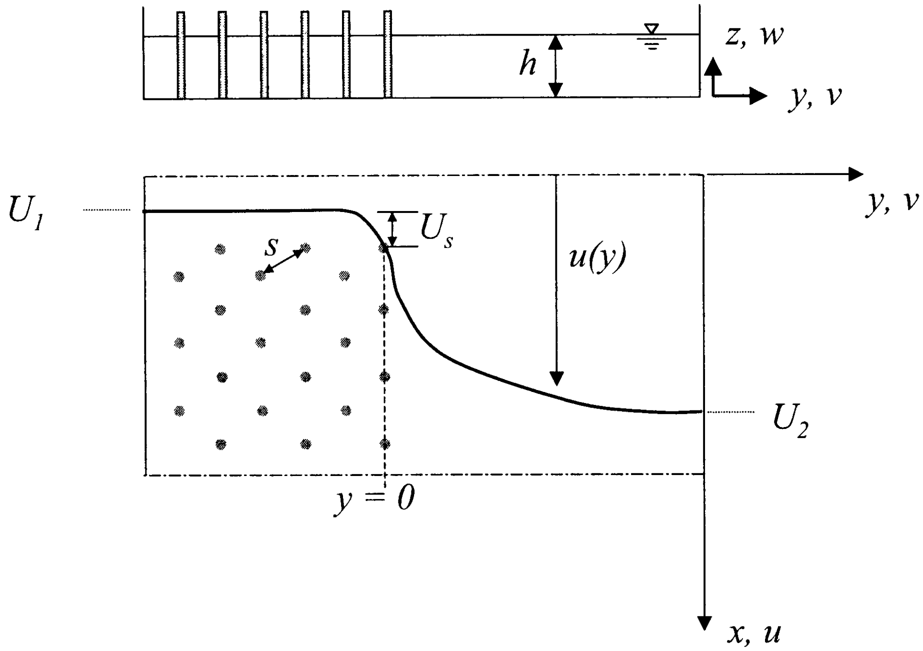

Figure 2-1: A schematic of the partially vegetated channel. The velocity distribution is $u(y)$ (down the page), the cylinder spacing is s, the slip velocity is U_s, and the velocity difference across the layer is $\Delta U = U_2 - U_1$. The horizontal, transverse, and vertical coordinates and velocity components are, respectively, x, u; y, v; z, w.

are expected to influence the degree of penetration and the slip velocity by altering the local resistance near the interface. Previous studies of low Reynolds number flow at the edge of fibrous media suggest that array geometry is important, particulary at the interface, and that the outer row of cylinders contributes disproportionately more than inner rows to limiting the penetration depth (James & Davis, 2001). Significant differences in the slip velocity were found by Sahraoui & Kaviany (1992) depending on whether or not the cylinders in the outermost row are aligned. Just as in low Reynolds number flows, the degree of penetration and the slip velocity are expected to depend both on the bulk properties of the medium, ϕ and s, and properties of the individual obstructions, like d and the specifics of the arrangement.

For this study we varied only the bulk continuum properties of the medium, ϕ, and thereby s, but kept the staggered equilateral array pattern and the cylinder diameter identical for all experiments. This was done both due to the inherent experimental difficulty in studying a large set of geometries, as well as to isolate the dependence of experimental variables on bulk properties. Thus, while absolute magnitudes of experimental variables are restricted to this array geometry, general trends showing their variation with ϕ and s should extend to a wide range of configurations. Natural vegetation is likely to have a heterogeneous local distribution, rather than the regular distribution studied here. However, the dependence of the flow characteristics on ϕ is expected to have the same general trends in a heterogeneous distribution as in the regular distribution. Moreover, the dominant length scales of the shear flow, both in natural vegetated channels and in the laboratory experiments, scale with the shear layer width, which is much larger than the spacing of the stems, s, and hence much larger than the details of the cylinder distribution.

2.1.2 Results from Low Reynolds Number Shear Flows Adjacent to Porous Media

In classic work by Beavers & Joseph (1967), experiments were done to determine the velocity slip at the interface between a clear channel and a variety of porous media at low Reynolds number. The goal was to ascertain both the degree of flow penetration, and shear-induced flux in the media, as well as the appropriate boundary conditions for the open channel. They modeled the flow within the medium according to Darcy's law, with

$$U = -\frac{k}{\mu} P_x \tag{2.1}$$

where k is the permeability of the medium, P_x is the applied pressure gradient, and μ is the fluid viscosity, and U is the Darcy velocity. They found that the slip velocity was related to the permeability and the shear at the interface as

$$\left.\frac{\partial U}{\partial y}\right|_{y=0} = \frac{\beta}{\sqrt{k}} U_s. \tag{2.2}$$

The resulting coefficient β was found to vary substantially for media of different type and geometry, suggesting that the bulk continuum properties, expressed through the permeability, do not sufficiently describe the interfacial flow. This result may be anticipated by closer inspection of (2.2). This equation predicts that the length scale for penetration, as expressed through the interfacial shear, is proportional to *sqrtk*, which is of the order of the pore scale in the medium, e.g., the spacing scale, s, in a cylinder array. The permeability, however, is a bulk property of the medium, and as such is well-defined only in a spatially-averaged sense, over a length scale $L \gg \sqrt{k}$. Thus the permeability alone cannot be expected to describe the flow over scales smaller than this averaging scale, such as the thin region of sharp flow variation at the interface for dense media. Hence the large variation in observations of β, implying a strong dependence on geometry at the interface.

Although β is highly dependent on geometry across the broad spectrum of porous media types and configurations, recent results on interfacial flow in cylinder arrays suggest a weaker dependence on cylinder geometry. In a theoretical description of flow in two different array types, square and staggered equilateral, James & Davis (2001) found a weak dependence of β on the solid volume fraction, but little difference between the two array types. Experimental work by Tachie *et al.* (2003) supported the theory, finding weak reduction in β with volume fraction, but little difference between square-, circular-, and triangular-shaped rods. Thus, while not universal across different types of media, the low Reynolds number Beavers & Joseph scaling relationship for the slip velocity in terms of the array permeability appears to be sound for similar array configurations.

2.1.3 Results from High Reynolds Number Canopy Flow

While work in porous media reveals some general relationships between interfacial flow and the properties of the solid medium, the results have been predominantly restricted to low Reynolds number flows in the Darcy limit. Hence the instabilities and coherent turbulent structures that arise in higher-Reynolds number flows, and significantly affect momentum transport between the array and the open region have been neglected. However a significant body of literature covering rough-wall boundary layers and flow over terrestrial and aquatic canopies, explores these topics.

An extensive review of the turbulent characteristics of canopy shear layers is given in Finnigan (2000). The review is focused on terrestrial canopies, found above forests

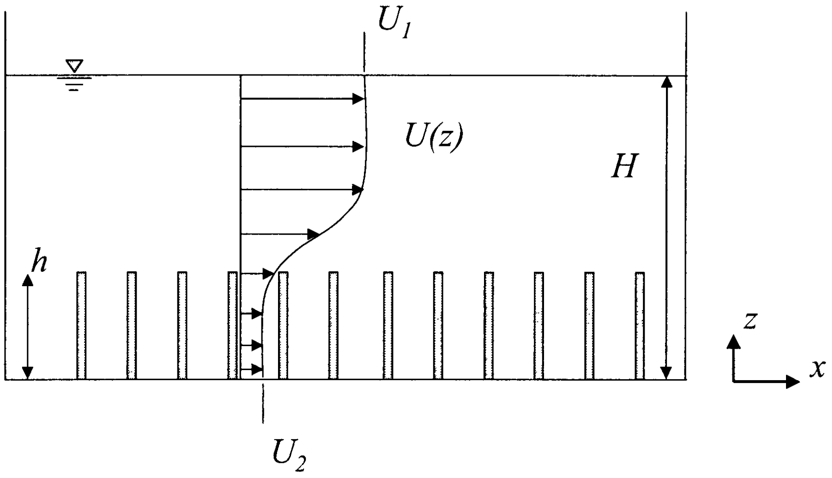

Figure 2-2: A schematic of a submerged aquatic canopy flow. The velocity distribution, $U(z)$ varies with vertical distance above the bed, and the velocity difference is $\Delta U = U_2 - U_1$. The canopy height is h, and the water depth is H. Terrestrial canopies are not bounded by a free surface and transition to the atmospheric boundary layer with increasing height.

or grasses, which transition to the atmospheric boundary layer far above the canopy. The concepts have also been applied to aquatic canopies, which are bounded by a free surface (Ghisalberti & Nepf, 2002; Nepf & Vivoni, 2000). A schematic of an aquatic canopy flow is shown in figure 2-2. Note the similarity to the shallow vegetated flow (figure 2-1), with only a change of orientation from the vertical to horizontal plane. As discussed in the review by Finnigan, an understanding of canopy flows has emerged that compares them to plane mixing layers. Strong shear across the top of the canopy gives rise to Kelvin-Helmholtz instabilities which form regular coherent vortices. These coherent structures control exchange of momentum and scalars across the canopy edge, with most of the turbulent transport linked to sweeps, which bring high momentum fluid from the faster flowing free stream down into the canopy (see Ghisalberti & Nepf, 2002, figure 9). The characteristic length scale of the structures is related to the maximum shear, which occurs at or near the top of the canopy, $z = h$,

$$L_s = \left. \frac{U}{\frac{\partial U}{\partial z}} \right|_{z=h}, \tag{2.3}$$

where U denotes the time-averaged velocity, i.e., averaged over turbulent fluctuations.

The mean (time-averaged) velocity across the canopy shear layer, as in plane mixing layers, is often well-approximated by a antisymmetric hyperbolic tangent or error function profile, similar to that shown in figure 2-2 (Raupach *et al.*, 1996), so that $L_s \approx \frac{1}{2}\omega$, where $\omega = \Delta U / \left.\frac{\partial u}{\partial z}\right|_{max}$ is the vorticity thickness. The inflection point characteristic to these profiles, gives rise to a Kelvin-Helmholtz instability, in accordance with Rayleigh's inviscid instability theorem. The slip velocity appears in (2.3), through $(U|_{z=h})$, making its form analogous to (2.2).

Unlike the Beavers and Joseph condition (2.2), the dependence of L_s on canopy characteristics is not suggested by (2.3). As the penetration is linked to the resistance, and thus momentum absorption, of the canopy, a resistance equation is needed. The consensus in the canopy literature (see, e.g., Finnigan, 2000) is that when the flow is averaged over the details of the leaf and stem heterogeneity, the mean drag force created by the canopy opposing the flow can be written as a quadratic drag law,

$$F_D = -\frac{1}{2} C_D a \{U_i\} |\{U_i\}| \tag{2.4}$$

with the density a (canopy solid area projected to the flow per volume) as defined earlier, and C_D the effective drag coefficient. The velocity, $\{U_i\}$, is volume-averaged over the fluid-filled space. From here forward the brackets will be dropped for simplicity and to coincide with the terminology used in figure 2-2. Note that 2.4 is analogous to the Darcy resistance, $\mu U/k$, but has a quadratic, rather than linear, dependence on U, due to the high Reynolds number flow.

Using the canopy drag and an integral momentum balance over the top of the canopy, Poggi *et al.* (2003) give an estimate for L_s in terms of the Reynolds shear stress at the top of the canopy, $u_*^2 = \langle u'w' \rangle_{z=h}$,

$$L_s = \frac{2}{C_D a} \left(\frac{u_*^2}{U(h)^2} \right). \tag{2.5}$$

A different formulation was employed by Ghisalberti & Nepf (2004) based on energy arguments that the production of coherent structure kinetic energy by mean shear should balance dissipation by canopy drag. A universal constant was obtained that related the characteristic length scale for canopy penetration, L_p, to the canopy drag,

$$L_{z_1} = \frac{1}{\Omega C_D a} \frac{(\Delta U)^2}{(U(h)^2 - U_1^2)}, \tag{2.6}$$

where L_{z_1} is the distance between the top of the canopy and the point at which $U = U_1$ (in the terminology of Ghisalberti & Nepf (2004), $L_{z_1} = h - z_1$) and $\Omega = 8.7 \pm 0.5$.

Finally, for canopy flows in the limit where $U_1 \ll U_2$, White, Ghisalberti & Nepf (2004) also used energy arguments to show that the characteristic shear layer width and the penetration length scale are both proportional to the inverse of canopy drag,

$$L_s = \frac{\alpha}{C_D a} \tag{2.7a}$$

$$L_p = \frac{\beta}{C_D a}, \tag{2.7b}$$

where $L_s = \Delta U / \left.\frac{\partial u}{\partial z}\right|_{z=0}$ and L_p is the distance from the canopy edge to the point at which the Reynolds stress decays to $0.1u_*$. These scaling relationships were supported by a wide range of compiled canopy flow data, which consistently showed $\alpha \approx 0.25$ and $\beta \approx 0.1$.

Equations (2.5), (2.6), and (2.7) all have in common the fact that the dependence of the characteristic penetration scale is inversely related to the canopy resistance, making these formulations analogous to the Beavers and Joseph condition (2.2). All of these interfacial conditions relate the shear, and its length scale, at the edge of the solid medium, to the bulk continuum resistance of the medium through a single length scale, $\sqrt{k}$ for porous media in the Darcy limit, and $(C_D a)^{-1}$ for turbulent canopy flow.

2.2 Flows on Vegetated Floodplains

Several workers have studied the flow in composite channels with a vegetated floodplain, primarily in laboratory settings. Vionnet *et al.* (2004) proposed an eddy viscosity model to describe the momentum exchange between the main channel and the floodplain, and used results from a laboratory model to calibrate it. Helmiö (2004) also used a one-dimensional model, with a calibrated Darcy-Weisbach friction factor at the vegetation interface, to describe the flow conveyance of two lowland rivers. Each of these studies used a simplified one-dimensional model to estimate resistance, without describing the lateral distribution of velocity, or the turbulence structure.

Pasche & Rouvé (1985) developed a more advanced model which divides the channel into three zones: the main channel, the vegetated plain, and a communication zone between them. A Darcy-Weisbach-like friction law is proposed and calibrated by laboratory measurements in a composite channel with emergent cylinders. An *ad hoc* cubic velocity distribution is used in the main channel, which, along with the friction factor, describes the experimental velocity profile well. Ikeda *et al.* (1991) use an eddy viscosity model to predict the lateral distribution of velocity, and further apply the model to sediment transport into the vegetation.

While these latter two studies attempt to capture lateral variability and communication between the main channel and floodplain, they do not capture the effect of the shear layer vortices that are know to form at the interface. These have been recognized in laboratory studies by Tamai *et al.* (1986); Nezu & Onitsuka (2000). The measurements of Tamai *et al.* demonstrated the coherent vortices were driven by a Kelvin-Helmholtz instability similar to that found in a free shear layer. Nezu & Onitsuka measured the spatial distribution of turbulent shear stresses and turbulent production and also noted secondary circulations that were initiated by the unstable inflection point at the vegetation interface. Finally, Large Eddy Simulation (LES) models by Nadaoka & Yagi (1998); Xiaohui & Li (2002) have attempted to simulate the unsteady flow at the vegetation interface that is driven by the shear instability. However, due to computational limitations, the LES models treat the vegetation only as a distributed drag body force. Nonetheless, the simulations appear to reproduce the large vortices seen in the laboratory experiments. To date, none of the studies in channels with vegetated floodplains has established the dynamics of the cycle that forms and maintains the vortices, the effect of the large vortices on the communication between the main channel and the vegetation, or their effect on the spatial distribution of velocity and turbulent stress. The present study attempts to fill these gaps.

2.3 Shallow Vegetated Shear Layers

In the following section, we describe experiments undertaken on shallow shear flows, at moderate to high Reynolds number, in a partially vegetated laboratory channel. Objectives are the description of the distributions and scales of velocity and shear stress, penetration of momentum into the vegetated layer, and interfacial slip velocity. The results demonstrate that unlike previous results from canopy flows and interfacial porous layers, the shear layer in a shallow vegetated shear layer (SVSL) is not characterized by a single length scale related to the properties of porous medium. Rather, results will be presented which show two distinct regions and thus two distinct length scales exist in these flows: a thin, inner region near the interface, which establishes the penetration length scale, and which depends on the properties of the solid medium, and a larger outer region which depends on the characteristics of the open channel. It will be shown that for a wide range of Reynolds number and cylinder volume fraction there is good collapse of the velocity distributions in each of the two layers, indicative of similarity. Results also show that the slip velocity is a function of the ratio of the two scales.

Before proceeding, it is useful to describe the balance of momentum for a shallow vegetated flow. The reader may make reference to 2-2 for a definition of coordinate system. The equations of motion for flow in the vegetated channel can be simplified because it is shallow, $h \ll B$, where h is the mean depth and B the characteristic horizontal length scale. In addition, there exists a scale separation between the large scale coherent structures, which are intrinsic to vegetated shear flows, and the smaller length and shorter time scales of the turbulence generated by friction at the bed and by wake turbulence behind vegetation. As a result, the equations can be averaged over depth and time-averaged over an intermediate time scale that is short compared with the fluctuations due to the coherent structures, but long compared with small-scale turbulence. Moreover, within the vegetated layer, a spatial averaged is taken over the characteristic scale of the heterogeneity. In the experimental array this scale is the mean cylinder spacing. Spatial- and depth-average quantities are expressed with an overbar. The short time average is denoted with a tilde. The result of the averaging are the shallow water equations, which govern the two-dimensional flow in the horizontal plane.

longitudinal momentum:

$$\frac{\partial h\overline{u}}{\partial t}+\frac{\partial h\overline{u}\,\overline{u}}{\partial x}+\frac{\partial h\overline{u}\,\overline{v}}{\partial y}=-gh\frac{\partial\left(h+z_b\right)}{\partial x}+\frac{1}{\rho}\left[\frac{\partial h\overline{\tau}_{xx}}{\partial x}+\frac{\partial h\overline{\tau}_{xy}}{\partial y}\right]-hF_{Dx} \tag{2.8a}$$

transverse momentum:

$$\frac{\partial h\overline{v}}{\partial t}+\frac{\partial h\overline{u}\,\overline{v}}{\partial x}+\frac{\partial h\overline{v}\,\overline{v}}{\partial y}=-gh\frac{\partial\left(h+z_b\right)}{\partial y}+\frac{1}{\rho}\left[\frac{\partial h\overline{\tau}_{yx}}{\partial x}+\frac{\partial h\overline{\tau}_{yy}}{\partial y}\right]-hF_{Dy} \tag{2.8b}$$

continuity:

$$\frac{\partial h}{\partial t}+\frac{\partial h\overline{u}}{\partial x}+\frac{\partial h\overline{v}}{\partial y}=0. \tag{2.8c}$$

where $\overline{u}$ and $\overline{v}$ are the mean pore velocities within the vegetation. The shear stress terms are given by

$$\overline{\tau}_{xy}=\mu\frac{\partial\overline{u}}{\partial y}-\rho\overline{\widetilde{u'v'}}-\rho\overline{(\widetilde{u}-\overline{u})\left(\widetilde{v}-\overline{v}\right)} \tag{2.9a}$$

$$\overline{\tau}_{yx}=\mu\frac{\partial\overline{v}}{\partial x}-\rho\overline{\widetilde{u'v'}}-\rho\overline{(\widetilde{u}-\overline{u})\left(\widetilde{v}-\overline{v}\right)} \tag{2.9b}$$

$$\overline{\tau}_{xx}=\mu\frac{\partial\overline{u}}{\partial x}-\rho\overline{\widetilde{u'v'}}-\rho\overline{(\widetilde{u}-\overline{u})\left(\widetilde{u}-\overline{u}\right)} \tag{2.9c}$$

$$\widetilde{\tau}_{yy}=\mu\frac{\partial\overline{v}}{\partial y}-\rho\overline{\widetilde{v'v'}}-\rho\overline{(\widetilde{v}-\overline{v})\left(\widetilde{v}-\overline{v}\right)}. \tag{2.9d}$$

Each stress term consists of contributions from, respectively, viscous stress, $\mu\partial x_j\overline{u_i}$, turbulent Reynolds stress, $\overline{\widetilde{u_i'v_j'}}$, where the primes represent turbulent deviations from the time average, and spatial correlations in the temporally-averaged velocity components, $\overline{(\widetilde{u}_i - \overline{u}_i)(\widetilde{u}_j - \overline{u}_j)}$. These latter contributions typically come about from secondary circulations (Shiono & Knight, 1991). The pressure forcing term is dictated by the surface slope, and contains the local bed elevation, z_b. The body force, F_{Di}, in (2.8) results from the spatial averaging and is the net effect of drag from the vegetation and from bottom friction. This can be taken to be a piecewise function from within the vegetation into the open channel, by using the expression for vegetative drag (2.4) to write

$$F_{Dx} = \begin{cases} \frac{1}{2}\left(C_D a + c_f/h\right)\ \overline{u}\sqrt{\overline{u}^2 + \overline{v}^2}, & y < 0 \\ \frac{1}{2}(c_f/h)\ \overline{U}\sqrt{\overline{u}^2 + \overline{v}^2}, & y > 0 \end{cases} \tag{2.10a}$$

$$F_{Dy} = \begin{cases} \frac{1}{2}\left(C_D a + c_f/h\right)\ \overline{v}\sqrt{\overline{u}^2 + \overline{v}^2}, & y < 0 \\ \frac{1}{2}(c_f/h)\ \overline{v}\sqrt{\overline{u}^2 + \overline{v}^2}, & y > 0, \end{cases} \tag{2.10b}$$

where c_f is the bed friction coefficient due to the bed stress. The vegetative drag applies only within the vegetated portion of the channel, $y < 0$, bottom friction supplying the only resistance in the open region. It will be shown in the following sections that the length scale associated with the flow near the vegetation interface depends on the vegetative resistance, while the outer length scale depends primarily on the balance between shear stress and bottom friction in the open channel.

When the flow is fully-developed, and it is desired to describe the mean flow on time scales much longer than the coherent structure fluctuations, a long time-average applied to (2.8)–(2.10) yields

$$0 = gS - \frac{\partial}{\partial y}\left[\overline{\langle u'v' \rangle} + \overline{(U - \overline{U})(V - \overline{V})\rangle}\right] - \overline{\langle F_{Dx} \rangle}. \tag{2.11}$$

where $S = -dh/dx$ is the free surface slope, the angle brackets represent the long-time average, the overbar represents the depth-and-spatial average, and $U \equiv \langle U \rangle$ is the long time-averaged velocity (but not depth-averaged). Equation (2.11) is used in section 2.5.11 in describing a method for predicting the lateral velocity distribution in natural vegetated channels.

Finally, a note about nomenclature. In the remainder of this chapter, unless otherwise defined, capitalization, e.g., U, is meant to denote experimental quantities that are long-time averaged, but measured at mid-depth, and thus assumed to approximately represent a depth average, $U \approx \overline{U}$. Instantaneous time measurements, e.g., $u(t)$, are denoted in lower case, while temporal deviations are denoted with a prime, e.g., $u'(t)$. In addition, angle brackets will represent a long-time average, i.e., over all temporal fluctuations.

2.4 Experimental Methods

Experiments were carried out in a 1.2 m wide, 13 m long laboratory flume partially filled with a model layer of vegetation. A schematic of the laboratory setup is shown in 2-3. The vegetated layer was approximately 40 cm wide (1/3 of the flume width) and consisted of an array of wooden circular cylinders, 6 mm in diameter held by 0.25 inch perforated PVC base boards (Ametco Manufacturing Corporation). The dowels swelled when submerged, increasing the diameter to 6.5 ± 0.2 mm and holding the dowels rigidly in the base boards. By filling different percentages of the base holes, solid volume fractions of $\phi = 0.02$, $\phi = 0.045$, $\phi = 0.10$ were studied. Experimental configurations and results are summarized in table 2.1.

The initial section of the array, 1.2 m, was separated from the main channel by a splitter plate. This allowed the flow to develop separately within the array and the main channel, minimizing transverse motions due to flow adjustment at the array onset (see Bousmar *et al.*, 2005). The flow depth, h, was varied between 5.5 cm and 15 cm, with most experiments carried out for depth to width ratios of $h/B \ll 0.1$ in order to preserve shallow flow conditions. A recirculating pump provided flows of between approximately $2 - 50$ Ls^{-1}.

Simultaneous two-component velocity measurements were taken in the horizontal plane with a Laser Doppler Velocimetry (LDV) system in backscatter mode (Dantec Dynamics). The LDV system was mounted on a positioning system driven by a

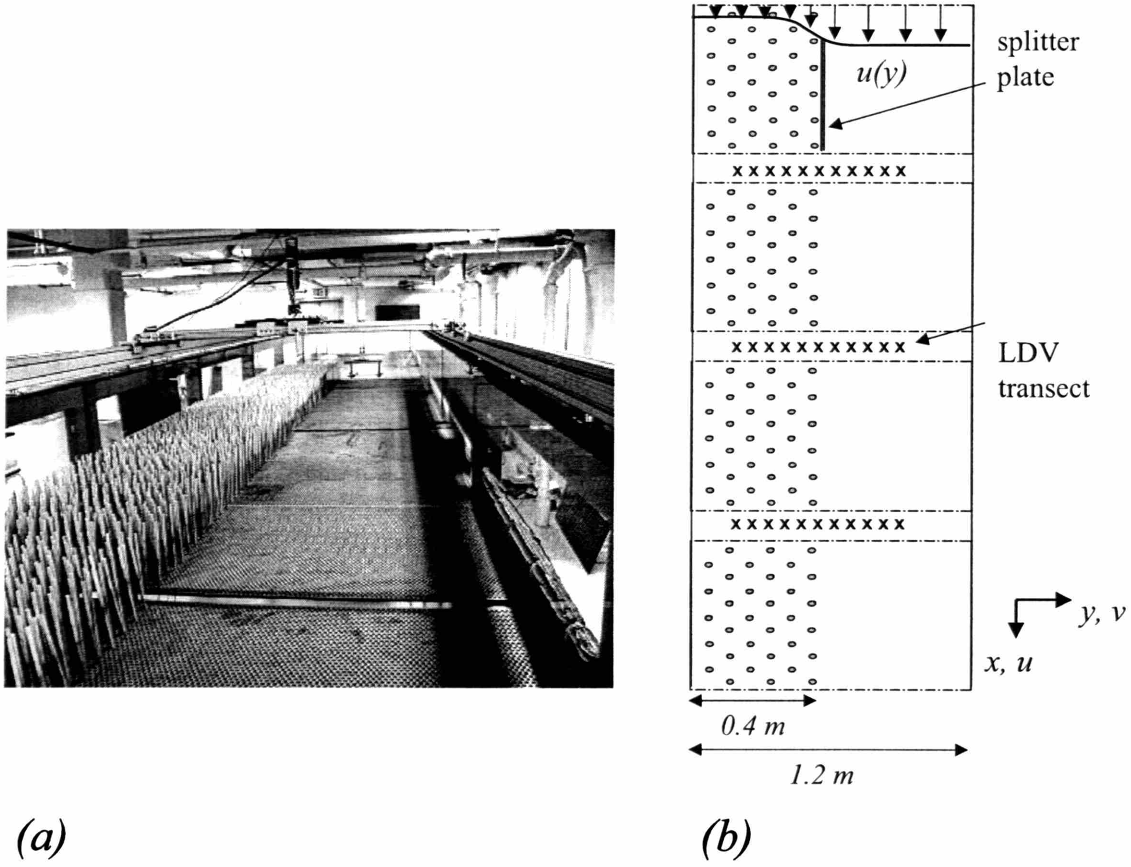

Figure 2-3: A schematic of the laboratory setup. Photograph of the flume channel with model vegetation (a) and illustration of the model array with splitter plate and representative longitudinal spacing of the LDV transects (b).

stepper motor, with accuracy better than 0.1 mm. Lateral velocity transects were made at mid-depth, and at various longitudinal positions downstream of the splitter plate. Each transect spanned approximately $y = -20$ to $y = 60$ cm, and consisted of approximately 70 separate lateral positions, spaced between 0.5 and 3 cm, with greater spatial resolution in regions of higher lateral shear. Note that $y = 0$ is taken to be the array interface, defined as the centerline of the first row of cylinders. The outermost 20 cm of the 120 cm width flume were not sampled as this was outside the shear layer, and the velocity was approximately constant. Each individual LDV position record was sampled sufficiently long to reach convergence of the mean velocity, Reynolds stress, and velocity triple correlations. This required between 4 and 10 minutes depending upon the flow conditions. To ensure a clear optical path for the LDV beams, 1/2" wide, cast acrylic spacers were placed between adjacent PVC base boards. The open space introduced into the array by the spacers never exceeded s, the cylinder spacing.

2.5 Experimental Results

2.5.1 General Features of the Flow

Before detailing the experimental results, it is useful to give a general introduction to the structure of the shear layer. Characteristic LDV transects are shown in figure 2-4. Velocity profiles are shown in 2-4*a*, measured at different longitudinal positions downstream of the splitter plate. The region from $y = -15$ to $y = 35$ cm is shown here. The flume is wider, extending from $-40\ cm < y < 80\ cm$, but the section shown includes the entire region of shear, outside of which the velocity approaches constant values of $U \approx U_2$ in the open region for $y > 35$ cm, and $U \approx U_1$ in the array for $y < -15$. After the fast and slow streams merge following the splitter plate, the velocity undergoes adjustment and eventually reaches an equilibrium distribution (shown in the $x = 3.86\ m$ profile). The adjustment is characterized by an initial growth in the shear layer width, measured by the momentum thickness, θ, which eventually reaches a constant (figure 2-4*b*).

The most striking feature of the shear layer is the regular periodic nature of the velocity time series (figure 2-4*c*). This is a signature of the regular coherent structures formed by the shear layer instability, which forms a traveling vortex street. At the position shown in 2-4*c* ($y = 2$ cm), just outside the array, the u and v components of the velocity are in-phase, producing periodic large peaks in the correlation, $u'v'$. These peaks are, referred to as sweeps ($u > 0$, $v < 0$) and ejections ($u < 0$, $v > 0$) and make the dominant contributions to the time-averaged Reynolds stress, $\langle u'v' \rangle$. The shear layer growth and equilibrium, and the regular coherent structures are common to all experimental configurations studied. The various metrics used to characterize the shear layer will be interpreted in light of the regular coherent structures. That is, they will be viewed as a leading order structure of the flow, rather than as a random turbulent signature.

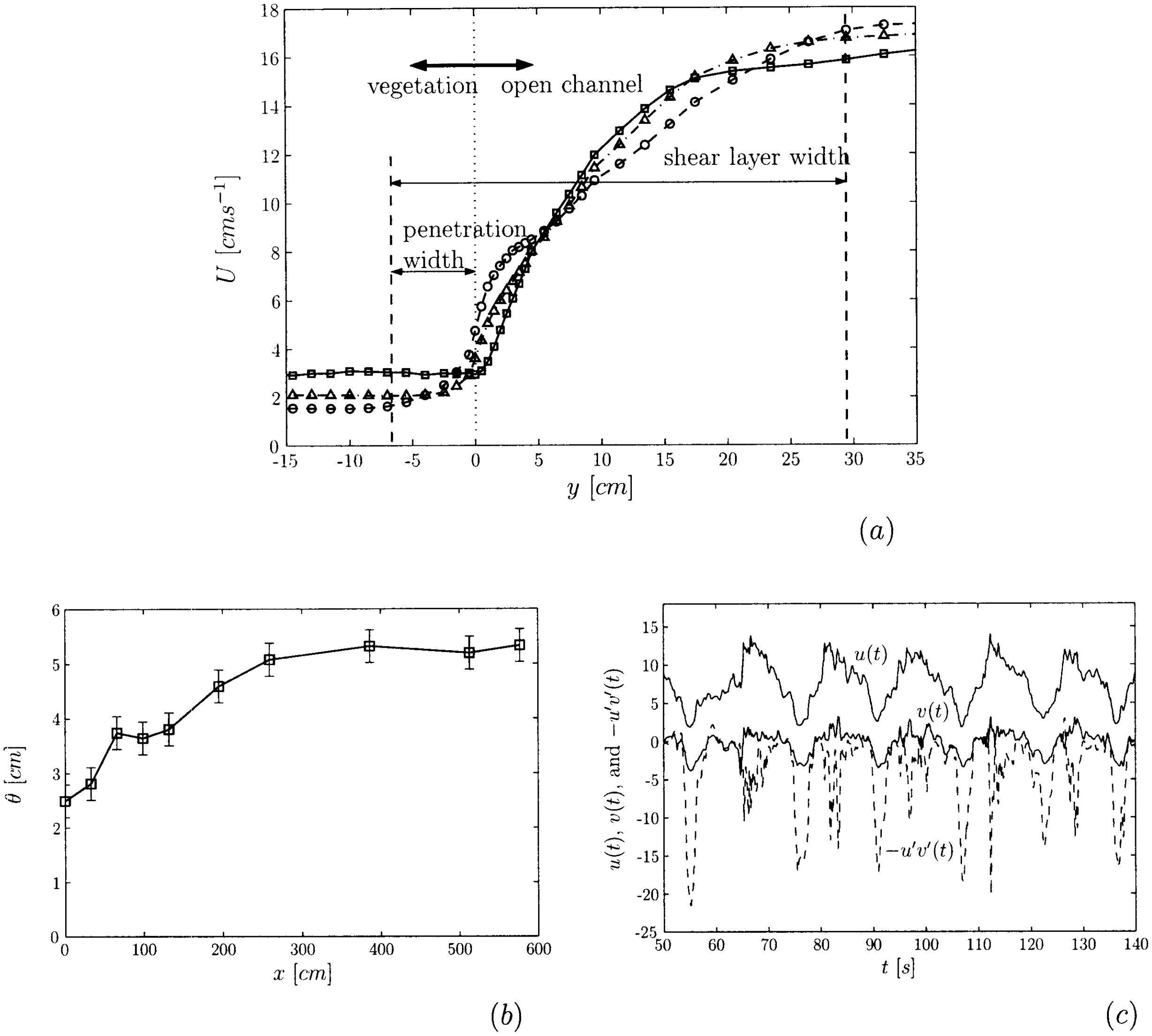

Figure 2-4: Characteristic measurements of shear layer behavior in the laboratory experiments. (a) shows three streamwise velocity profiles at various stages of development, $x = 0.33$ m (□–), $x = 1.32$ m (△ – ·), and $x = 3.86$ m (○ – –), measured from the splitter plate. Recall that the total flume width varies from $-40\,cm < y < 80\,cm$, but the shear is approximately zero outside the limits shown in the plot. (b) shows the longitudinal growth of the momentum thickness, θ, a measure of the shear layer width. A constant width is reached asymptotically, as the equilibrium velocity profile is approached (see the $x = 3.86$ m profile in (a)). (c) shows a time series of streamwise velocity u, transverse velocity v, and the cross correlation, $u'v'$, measured at $y = 2$ cm, $x = 3.86$ m. The time series is marked by strongly periodic fluctuations corresponding to traveling Kelvin-Helmholtz vortices.

2.5.2 Mean Velocity and Shear Stress Distributions

First, time-averaged streamwise velocity, $U(y)$, and Reynolds stress, $-\langle u'v' \rangle$, distributions across the shear layer for various cylinder volume fractions are shown in figure 2-5. Each transect is the ensemble mean of at least five individual transects at different $x-$ coordinates within the fully-developed region. The average removes fluctuations due to the heterogeneity within the array. Characteristic velocity profiles are shown in figure 2-5a-c. These are measured at three different array densities, ϕ, but under similar open channel conditions, with a Reynolds number based on the free stream velocity and the water depth of $Re_h = U_2 h/\nu \approx 10^4$. The profiles appear similar in the open region for each value of ϕ, but exhibit varying velocities, U_1, within the cylinder array, $y < 0$. In all profiles a point of inflection exists within 1 to 2 cm of the edge, corresponding very nearly to the point of maximum Reynolds stress (2-5d-f). From the Reynolds stress maximum an effective interfacial shear stress, τ_i and friction velocity, u_* can be defined,

$$\tau_i = u_*^2 = -\langle u'v' \rangle_{max}. \tag{2.12}$$

The correspondence of the points of maximum shear and maximum Reynolds stress make the interface a point of high turbulent energy production, $P_t = \langle u'v' \rangle \frac{\partial u}{\partial y}$. The high production rate is linked to the strong presence of coherent structures, and the strong correlation between $u'(t)$ and $v'(t)$ during inflows (sweeps) and outflows (ejections) across the sharp interface (see figure 2-4*c*).

In the open region, the velocity distributions are broad, whereas within the array they decay sharply, with little penetration. Because the array provides a frictional resistance at the interface, the the open region is analogous to a boundary layer adjacent to a wall, in this case a porous one. Following this analogy, the structure of the vegetation influences the boundary conditions, namely the shear stress and slip velocity at the edge, through the dynamics in a thin layer near the interface. Results presented hereafter bear out this two layer structure.

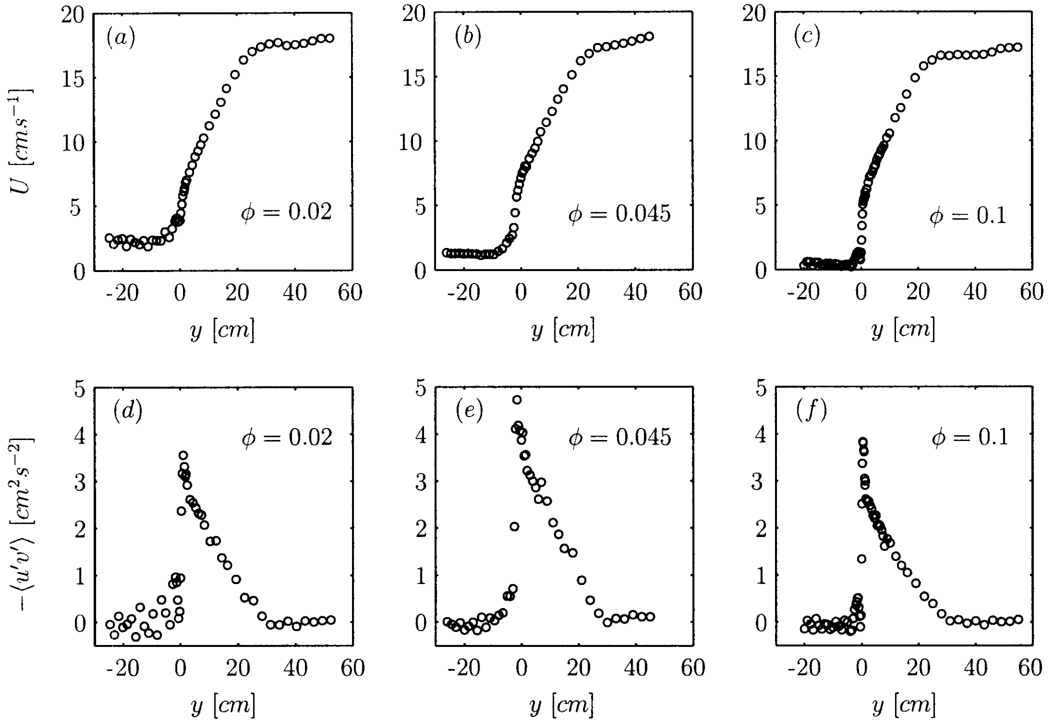

Figure 2-5: Transverse distributions of mean streamwise velocity, U, and Reynolds stress, $-\langle u'v' \rangle$ for various cylinder volume fractions. Distributions represent the mean of approximately five profiles taken at different $x-$ positions in the equilibrium region. Reynolds number based on depth for each case is $Re_h = 1 \times 10^4$.

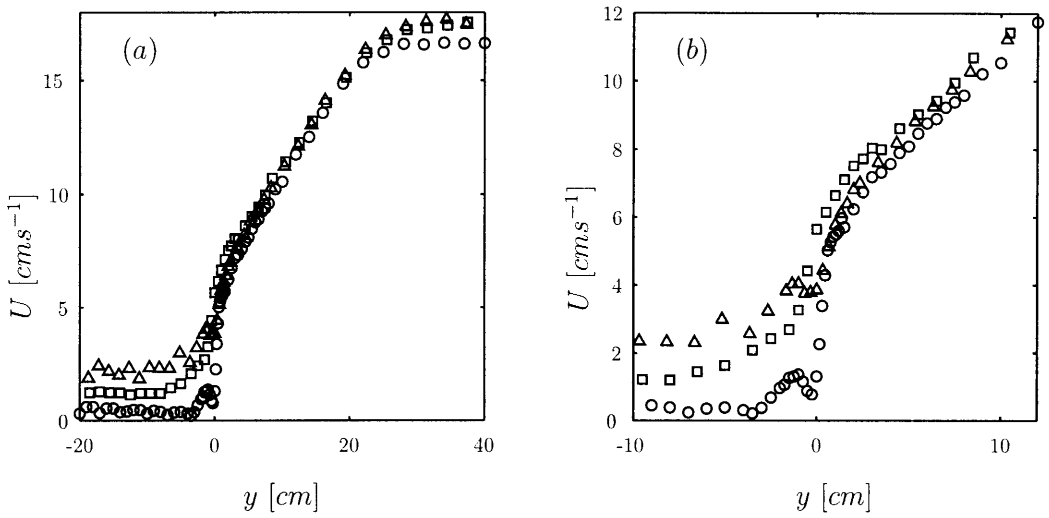

Figure 2-6: Velocity profiles for various volume fractions (*a*) (see figure 2-5 for details), with close-up view of the interface near $y = 0$ (*b*). Cases shown are $\phi = 0.02$ ($\triangle$), $\phi = 0.045$ ($\square$), and $\phi = 0.1$ ($\circ$).

2.5.3 Inner-Layer Scaling

The velocity profiles for $Re_h = U_2 h/\nu \approx 10^4$ and for three different values of the cylinder volume fraction, ϕ, are shown in figure 2-6 with an expanded view of the interfacial region. The velocity in the open channel region is nearly identical across the three solid fractions (2-6*a*), resembling a boundary layer profile. In 2-6*b*, the velocity profiles all exhibit an inflection point within approximately 1 cm of the interface, $y = 0$. However, the shear at the point of inflection varies, with the highest array density ($\phi = 0.10$) case exhibiting the steepest gradient, and less penetration into the array. All profiles asymptotically approach an array-average velocity, U_1, which decreases with increasing ϕ. The high density ($\phi = 0.1$) case exhibits a spatial fluctuation near the interface due to the wake behind the first row of cylinders. The spatial fluctuations in the flow on the scale of the cylinders is most pronounced at high array densities (see, e.g., White & Nepf, 2003). Near the interface, the velocity resembles a free shear layer in each profile, but transitions to the boundary layer shape in the open channel region, suggesting that the flow possesses two distinct length scales.

In the inner, interfacial region the velocity was treated as distinct from the outer channel region. For each velocity transect, nonlinear regression was used to determine the best profile of the form

$$u_I = U_1 + U_s\left(1 + \tanh\left(\frac{y - y_o}{\delta_I}\right)\right), \tag{2.13}$$

where $y = y_o$ is the inflection point of the hyperbolic tangent profile, and the 'I' subscript denotes the inner layer. The slip velocity is defined at the inflection point, $U_s = U(y_o) - U_1$, as in figure 2-1, and δ_I is the width of the inner layer. The offset y_o, is a virtual origin for the outer flow, identical to the "error in origin" in boundary layers above surface roughness (Antonia & Krogstad, 2001; Bandyopadhyay, 1987). For all experimental profiles $y_o \approx 0$, i.e., the inflection point effectively coincides with the interface. It appears that this is a universal behavior, which has been noted as well by Nezu & Onitsuka (2000), and is due to the fact that the sharpest transition in the flow must lie at the vegetation edge, where the step change in hydraulic resistance occurs. Having measured U_1 from the LDV transect, it is then possible to find U_s, δ_I, and y_o from the experimental velocity profiles using nonlinear regression. The Matlab function NLINFIT was used for all regression analysis. In addition, for comparison, the velocity profiles near the interface were spatially-averaged to remove fluctuations within the cylinder array. This was done with a moving average filter, with a window length of approximately s, the mean cylinder spacing.

The velocity distributions in the inner layer from two representative cases ($Re = 1 \times 10^4$; ($\phi = 0.02$) and ($\phi = 0.045$)) are shown along with the hyperbolic tangent profile in figure 2-7*a*. The fit is reasonable in the inner region, but diverges as the outer region is approached, consistent with the notion of two regions controlled by two distinct length scales.

To assess whether there existed a self-similar velocity distribution, the data from all transects across the full range of Re and ϕ were normalized with the hyperbolic tangent scaling,

$$u_I^* = \frac{1}{2}\frac{u(\eta_I) - U_1}{U_s}, \quad \eta_I = \frac{y - y_o}{\delta_I}, \tag{2.14}$$

where the star denotes non-dimensionalization. Figure 2-8*a* shows the normalized

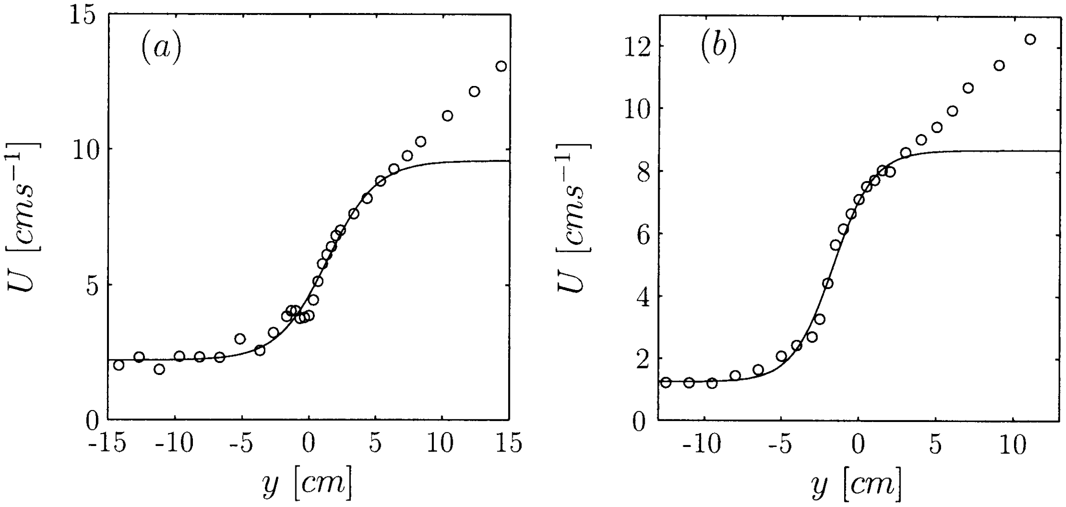

Figure 2-7: Inner layer velocity profiles for $Re_h = 1 \times 10^4$, $\phi = 0.02$ (case I) and $\phi = 0.045$ (case IV). For each case, raw LDV data is shown in open circles, and the hyperbolic tangent profile which best fits the inner layer is shown as a solid line.

inner layer velocity profiles from all experimental cases (see table 2.1), while 2-8*b* shows the spatially-averaged data. The spatially-averaged data for each experimental case, averaged using the moving average filter described above, are normalized with the same length and velocity scales as the raw data for that particular case, δ_I and U_s. The collapse of the velocity profiles within the inner region is quite good for the raw data and even better for the spatial average. Despite fluctuations within the array in the unfiltered data, owing to heterogeneity of the porous medium, the collapse of the data suggests a self-similar inner-layer form. Within the vegetation and across the interface, the data all lie along an anti-symmetric curve that closely resembles the hyperbolic tangent profile of a plane mixing layer. This inner layer velocity profile is in accord with observations from canopy shear layers which show a plane mixing layer velocity structure at the canopy edge (Finnigan, 2000; Ghisalberti & Nepf, 2002). This mixing layer structure, with the inflection point at $\eta_I = 0$ is responsible for the instability that leads to the formation of coherent structures.

At a distance of approximately $\eta_I = 1.5$, i.e., outside the interface, the data from different experimental cases begin to diverge. This demonstrates that self-similarity does not exist throughout the flow, and that the shear layer possesses at minimum two different length and/or velocity scales. The next section demonstrates that there

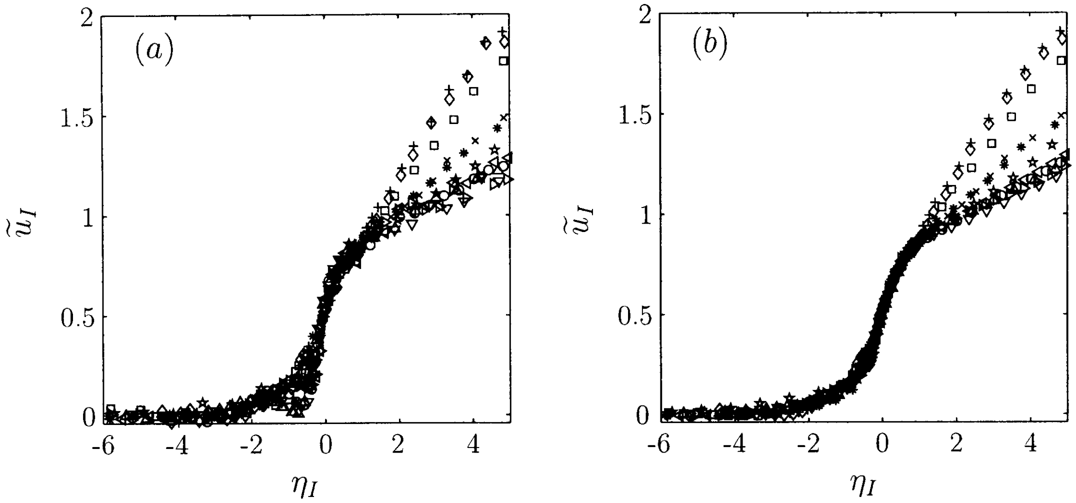

Figure 2-8: Normalized inner layer velocity distributions for the range of experimental conditions: raw data (*a*), and spatially-averaged to remove cylinder-scale fluctuations (*b*). Experimental cases corresponding to data are (from table 2.1): □ (I), ◊ (II), + (III), × (IV), ∗ (V), ⋆ (VI), ∘ (VII), △ (VIII), ▽ (IX), ◁ (X), ▷ (XI).

are indeed two velocity and length scales that universally describe the flow: one pair for the inner layer and one pair for the outer region.

Finally, because the outer flow resembles a boundary layer, it is useful to compare the width of the inner layer to the viscous sublayer for a wall-bounded flow. In commonly used "wall units", the width of the inner layer is, $\delta_I^+ = \delta_I u_* / \nu$. The Reynolds shear stress at the interface, u_*^2, is used to calculate δ_I^+ and the results are shown in table 2.1. It can be seen that the values of δ_I^+ are exceedingly large, demonstrating that the inner layer is between one to three orders of magnitude larger than the viscous sublayer for all cases studied. Thus for these moderate Reynolds-numbers, the width of the inner layer should be relatively independent of viscous effects.

2.5.4 Drag Within the Vegetation

The array resistance both controls the velocity within the array, U_1, and balances the velocity shear at the interface, influencing the momentum penetration length. The mean array resistance, F_D, the product of the cylinder number density and the mean drag per unit length along each cylinder, balances the mean pressure gradient due to

Table 2.1: Details of experimental parameters and results for all cases.

	I	II	III	IV	V	VI	VII	VIII	IX	X	XI
o	0.020	0.020	0.020	0.045	0.045	0.045	0.10	0.10	0.10	0.10	0.10
$C_D a\ cm^{-1}$	0.092	0.092	0.092	0.285	0.242	0.255	2.43	2.74	2.04	1.77	2.43
$s\ cm$	4.38	4.38	4.38	2.92	2.92	2.92	1.96	1.96	1.96	1.96	1.96
Re_θ	8.15E+03	1.24E+04	1.35E+04	7.56E+03	1.57E+03	6.04E+03	6.88E+03	2.35E+03	3.62E+03	1.18E+04	1.10E+04
Re_h	2.04E+04	3.00E+04	1.04E+04	1.84E+03	6.73E+03	1.00E+04	2.91E+03	5.57E+03	2.10E+04	2.78E+04	1.09E+04
$U_1\ (cms^{-1})$	2.21	1.74	1.89	1.25	0.25	0.84	0.43	0.15	0.25	0.89	0.41
$U_2\ (cms^{-1})$	17.68	21.69	23.97	17.37	3.82	12.32	16.82	5.85	9.05	29.59	22.02
$u_*\ (cms^{-1})$	1.81	2.27	2.67	2.06	0.35	1.48	1.93	0.44	0.84	3.44	2.51
$u_b^*\ (cms^{-1})$	0.94	1.41	1.72	0.95	0.21	0.66	0.92	0.32	0.39	0.50	1.68
$U_s\ (cms^{-1})$	3.68	5.12	5.59	3.72	0.80	2.52	3.41	1.03	1.79	6.11	4.51
y_o	1.34	1.91	1.41	-0.65	-0.24	-0.71	0.48	0.81	0.51	0.35	0.81
$\delta_I\ (cm)$	3.71	6.03	6.20	2.61	2.19	1.89	1.24	0.89	1.06	1.34	1.35
δ_I^+	625	1250	1515	500	69	256	217	36	83	417	313
$\delta_O\ (cm)$	15.95	19.07	19.86	16.69	16.90	18.20	16.50	15.53	15.20	17.84	21.54
$U_m\ (cms^{-1})$	7.41	10.20	12.02	7.87	1.62	5.57	6.71	2.11	3.64	12.03	9.00
$y_m\ (cm)$	4.12	5.12	4.64	1.54	1.71	1.15	2.21	2.09	2.01	2.24	2.84
ϵ	0.34	0.27	0.31	0.72	0.45	1.09	1.32	0.73	0.96	1.29	1.47
f_t	0.027	0.026	0.029	0.033	0.019	0.033	0.028	0.012	0.018	0.029	0.027
$\theta\ (cm)$	5.07	6.30	6.22	4.79	4.52	5.39	4.50	4.43	4.39	4.40	5.49
symbol	□	◇	+	×	∗	⋆	○	△	▽	◁	▷

the surface slope,

$$\frac{a}{d}F_D = -(1-\phi)\rho g\frac{dh}{dx}, \tag{2.15}$$

where the factor $(1-\phi)$ is the array porosity. The drag force can be written in terms of a mean drag coefficient so that the total resistance is

$$\frac{1}{2}C_D a U_1^2 = -(1-\phi)g\frac{dh}{dx}. \tag{2.16}$$

It is important to note that in this equation, and throughout this work, U_1 is defined as the mean velocity averaged over the fluid-filled space, often denoted the interstitial velocity.

Experiments were undertaken to measure the mean drag coefficient for various cylinder volume fractions and Reynolds numbers. These measurements pose experimental problems as they require the accurate measurement of the exceedingly small surface slopes. Surface displacement gauges, with an accuracy of ±0.05 mm were used to measure the difference in the surface height across the approximately 7 m long array test section. However, despite the fine resolution of the displacement gauges, it was not possible to accurately measure the drag when either the volume fraction or the Reynolds number were small.

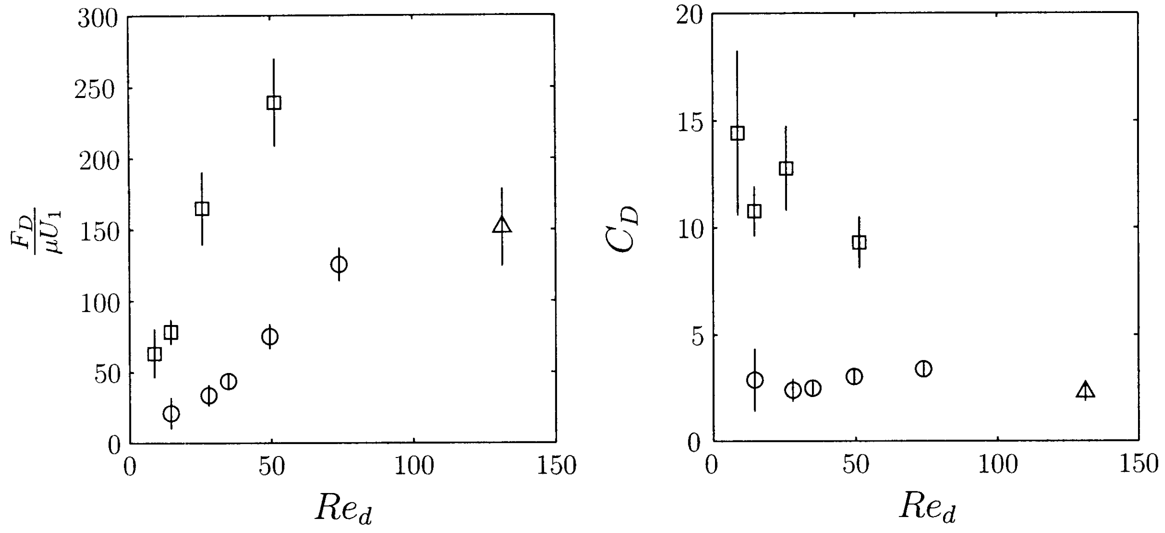

Figure 2-9: Bulk resistance within the array. (*a*) shows the experimental results for the increase in the normalized mean drag, $F_D/\mu U_1$ with the cylinder Reynolds number, $Re_d = U_1 d/\nu$, comparable with plots in Koch & Ladd (1997). (*b*) shows the mean drag coefficient, C_D with stem Reynolds number. Symbols represent $\phi = 0.02$ (△), $\phi = 0.045$ (∘), and $\phi = 0.10$ (□).

The results for the total drag are shown in figure 2-9. In 2-9*a* the mean drag is normalized as, $F_D/\mu U_1$ and plotted with the stem Reynolds number, $Re_d = U_1 d/\nu$. This normalization illustrates the viscous contribution to the drag, the value for $Re_d = 0$, which is too small to be accurately measured directly, but can be inferred from the intercept value of $F_D/\mu U_1$ at $Re_d = 0$ in 2-9*a*. This plot can be compared to those presented in Koch & Ladd (1997), who found numerically the drag in square, staggered, and random cylinder arrays for a range of solid volume fractions. For the two largest volume fractions, $\phi = 0.045$ and 0.1, the mean drag increases in proportion to Re_d, consistent with results from Koch & Ladd for staggered and random arrays. If the slope of $F_D/\mu U_1$ vs. Re_d is constant, C_D will approach a constant asymptotically as Re_d increases, and as form drag begins to dominate the viscous ($Re_d = 0$) contribution. From 2-9*b*, for $\phi = 0.045$ the C_D is approximately constant with Re_d, but for $\phi = 0.1$, C_D decreases slightly with Re_d, suggesting lingering viscous drag. In general, the higher the array density, the greater the viscous drag contribution, due to the larger proportion of solid surfaces, and decrease in the fluid space between them.

While the mean array drag establishes the mean array velocity, U_1, its influence on the dynamics near the interface are less clear. The expressions presented in section 2.1.3 (equations (2.5), (2.6), and (2.7)) relate the penetration length to the mean canopy resistance. This may not always be appropriate, as the mean resistance is well-defined only in an averaged sense over a spacial scale of many cylinders. If the penetration length is comparable to the scale of the spatial fluctuations in the array, it may be disproportionately influenced by flow effects around individual cylinders near the edge. This is discussed in the next section.

2.5.5 Dependence of δ_I on Vegetation Characteristics

The self-similarity within the inner region, and divergence in the open region suggests that δ_I is a function of the vegetation characteristics alone. From the discussion in sections 2.1.2 and 2.1.3 it is expected that δ_I will depend on the length scale characterizing the bulk canopy resistance, which is related to the cylinder spacing, s. For the present experiments in cylinder arrays at medium to high Reynolds number, the drag within the array is $F_D = -1/2 C_D a U^2$, following the canopy literature, and also Koch & Ladd (1997), who verified the quadratic drag law for moderate to high Reynolds number in random cylinder arrays. From this drag law, the length scale associated with the resistance is $(C_D a)^{-1}$. It is simple to see how this penetration length scale arises by noting that the inner layer is the region of maximum shear, and thus, in the thin transition layer, the dominant momentum balance is between the lateral shear stress and array drag. Balancing these two terms in the inner layer gives

$$\frac{\partial \tau}{\partial y} = F_D \tag{2.17}$$

and taking $\tau = u_*^2$, the value at the interface, and the penetration length scale as δ_I, the inner layer thickness scales as

$$\delta_I \sim \frac{u_*^2}{C_D a U(y_o)^2}. \tag{2.18}$$

where $U(y_o) = U_1 + U_s$ is the velocity evaluated at the interface. Note the similarity between (2.18) and the prediction from Poggi *et al.* (2003) (2.5), as both derive from a momentum balance in the region of maximum shear.

Figure 2-10 shows the dependence of δ_I on $C_D a$ for all experimental conditions. The dependence suggests two distinct regions of behavior. For lower values of $C_D a$ (sparser array configuration), there is a decrease in δ_I with increasing $C_D a$. For these data, there is good agreement with the expected behavior, $\delta_I \propto (C_D a)^{-1}$. The experimental result is

$$\delta_I = 0.5(C_D a)^{-1} \tag{2.19}$$

However, for the highest cylinder volume fraction ($\phi = 0.10$), δ_I appears to approach a constant value, $\delta_I \approx 1.8d$. For this highest packing density, the cylinder spacing is of the order of the diameter, $s \approx 3d$. Moreover, for $\phi = 0.1$, the penetration length predicted by the $(C_D a)^{-1}$ scaling would be less than the cylinder diameter, d. A physical argument can be made that the inner layer cannot be less than d because, at minimum, the transition of the velocity must occur over the first row of cylinders. This suggests a dual scaling for the inner layer width of the form

$$\delta_I \sim max\left(\frac{1}{C_D a}, d\right). \tag{2.20}$$

Thus, when the array is sufficiently sparse that there is scale separation between the cylinder spacing and the diameter, δ_I should be set by the length scale associated with the bulk array resistance, $(C_D a)^{-1}$. As the array becomes denser, and $(C_D a)^{-1}$ approaches d, δ_I becomes limited by the cylinder diameter. Thus from figure 2-10, δ_I approaches a constant, $\approx 1.8d$.

The dual scaling for δ_I is expected to be a general property of all flows adjacent to a porous medium for the following reason. The resistance of the medium, whether given by Darcy's law for low Reynolds number, or the quadratic drag law for high Reynolds number, relies on a spatial average over the characteristic scale of heterogeneity, which is $O(s)$, the spacing between elements in the medium. When the scale for flow transition, i.e., δ_I, is much smaller than s, the effective medium scaling will cease to

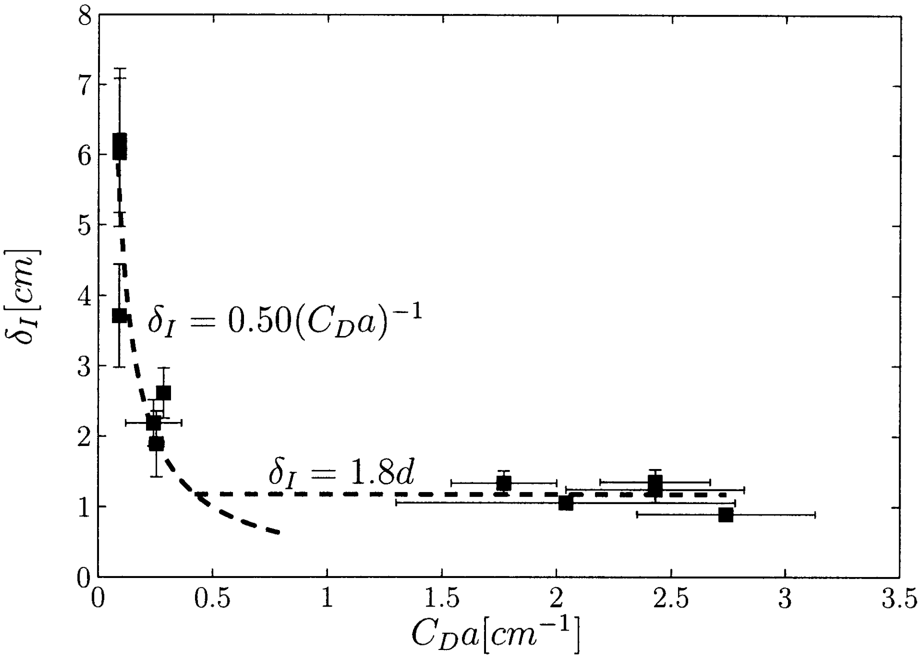

Figure 2-10: Inner layer width, δ_I vs. bulk resistance length scale, C_Da. Also shown are best-fit line to the sparse array behavior, $\delta_I = \alpha(C_Da)^{-1}$, where $\alpha = 0.50 \pm 0.12$ and the asymptotic value in the dense array limit, $\delta_I = 1.18 \pm 0.17\ cm = 1.81d \pm 0.26d$. Error bars show uncertainty in both C_Da, predominantly due to uncertainty in measured C_D, and in δ_I.

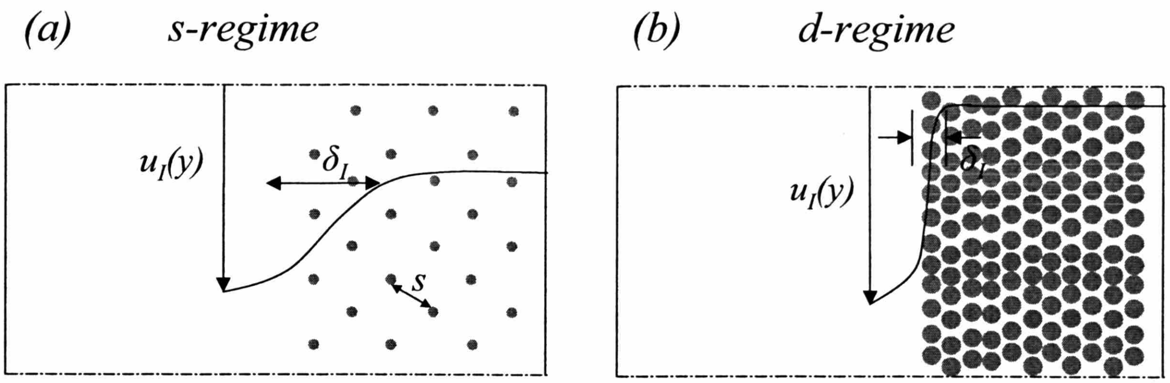

Figure 2-11: A schematic of the dual dependence of the inner layer width, δ_I on the array characteristics. In the s-regime (a), $s \gg d$, and δ_I is set by the length scale associated with the bulk array resistance. In the d-regime (b), s and d are comparable, and δ_I is controlled by local geometry at the interface, and scales with the diameter d.

hold and the transition will be set by the small-scale array geometry, in this case the width of the outermost row of cylinders. The transition is approached when s becomes comparable to d. Thus, one may define two regimes, the s-regime, in which the the penetration width is controlled by the properties of the bulk medium, particularly interstitial spacing, and the d-regime, in which it is controlled by the geometry at the edge, particularly the element size, d. A graphical depiction of the two regimes is shown in figure 2-11.

2.5.6 Outer-Layer Scaling

Outer Layer Width

The flow in the open region, $y > 0$, termed the "outer layer", closely resembles a wall-bounded flow (see figure 2-6). Because there appears to be a clear separation of scales between the inner layer and this outer flow, a characterization of the velocity in the outer region is sought in terms of a length scale, δ_O. The length scale for this outer layer flow is suggested by analogy with flat plate boundary layers. In such flows, the velocity profile in the wall-normal direction is expressed as

$$\frac{u}{U_o} = f(\eta), \quad \eta = y/\delta, \tag{2.21}$$

where U_o and δ are characteristic scales for the free stream velocity and boundary layer width. The famous Blasius solution gives the velocity profile, $f(\eta)$, but is a complicated series solution (Kundu & Cohen, 2004). A simpler quadratic or cubic shape function is often assumed when obtaining solutions for boundary layer quantities using the Von Kármán-Pohlhausen integral method (Schlichting, 1979). To determine the width of the outer layer, a nonlinear regression fit was performed on the open channel region of each measured velocity profile to find the best fit to the quadratic profile

$$f(\eta) = \eta_O - \frac{\eta_O^2}{4}. \tag{2.22}$$

This profile was chosen because it satisfies the appropriate boundary conditions

$$f(0) = 0, \quad f(1) = 1, \quad f'(1) = 0. \tag{2.23}$$

However, because of the slip condition at the interface, the function, $f(\eta_O)$ must be defined relative to some, as yet undetermined, origin, y_m, and velocity, U_m, as

$$f(\eta_O) = \frac{U - U_m}{U_2 - U_m} \tag{2.24a}$$

where

$$\eta_O = \frac{y - y_m}{\delta_O} \tag{2.24b}$$

and $U_m = U(y_m)$. To ensure continuity of the velocity profile, the inner layer and the outer layer must match in a transition region outside the interface. This matching point defines y_m,

$$u_I(y_m) = u_O(y_m) \tag{2.25a}$$

and

$$\frac{du_I(y_m)}{dy} = \frac{du_O(y_m)}{dy}, \tag{2.25b}$$

where $u_I(y)$ is the velocity in the inner layer and $u_O(y)$ is the velocity in the outer layer. Note that the continuity of the velocity gradient in condition (2.25b), which is required, does not presuppose continuity of the shear stress at the interface. To illustrate, the Beavers and Joseph condition at the edge of a laminar porous medium (2.2) maintains stress continuity, but, e.g., Goyeau *et al.* (2003) proposed a stress jump condition at the edge of a porous medium. This can occur if the effective viscosity within the medium is different from that in the main channel. From (2.13) and (2.24)

$$u_I = U_1 + U_s \left(1 + \tanh\left(\frac{y - y_o}{\delta_I}\right)\right) \tag{2.26a}$$

and

$$u_O = U_m + (U_2 - U_m)\left[\frac{y - y_m}{\delta_O} - \frac{1}{4}\left(\frac{y - y_m}{\delta_O}\right)^2\right]. \tag{2.26b}$$

An iterative process is used to determine U_m, y_m, and δ_O from the experimental data, and is demonstrated graphically in figure 2-12. First an initial guess is made for the matching point and velocity, $U_m(y_m) = U_1 + 2U_s$, the upper limit of the hyperbolic tangent profile (2.26a). Then, δ_O is determined by nonlinear regression in the outer region, according to (2.26b). Given δ_O, the the slope at the matching point, y_m is determined from (2.26b) as

$$m_o = \frac{U_2 - U_m}{\delta_O}. \tag{2.27}$$

This outer layer slope matches the slope of the inner layer profile (2.26a) at y_m to give

$$y_m = \delta_I \tanh^{-1}\sqrt{1 - \frac{m_o \delta_I}{U_s}} + y_o. \tag{2.28}$$

In theory, the quadratic fit should then be performed on the data with y_m as the outer layer origin and the process repeated. In practice, this was unnecessary, and the first iteration was sufficient to determine m_o and thus y_m. The velocity at the matching point is then determined from (2.26a) as

$$U_m = u_I(y_m) = U_1 + U_s\left(1 + \tanh\left(\frac{y_m - y_o}{\delta_I}\right)\right). \tag{2.29}$$

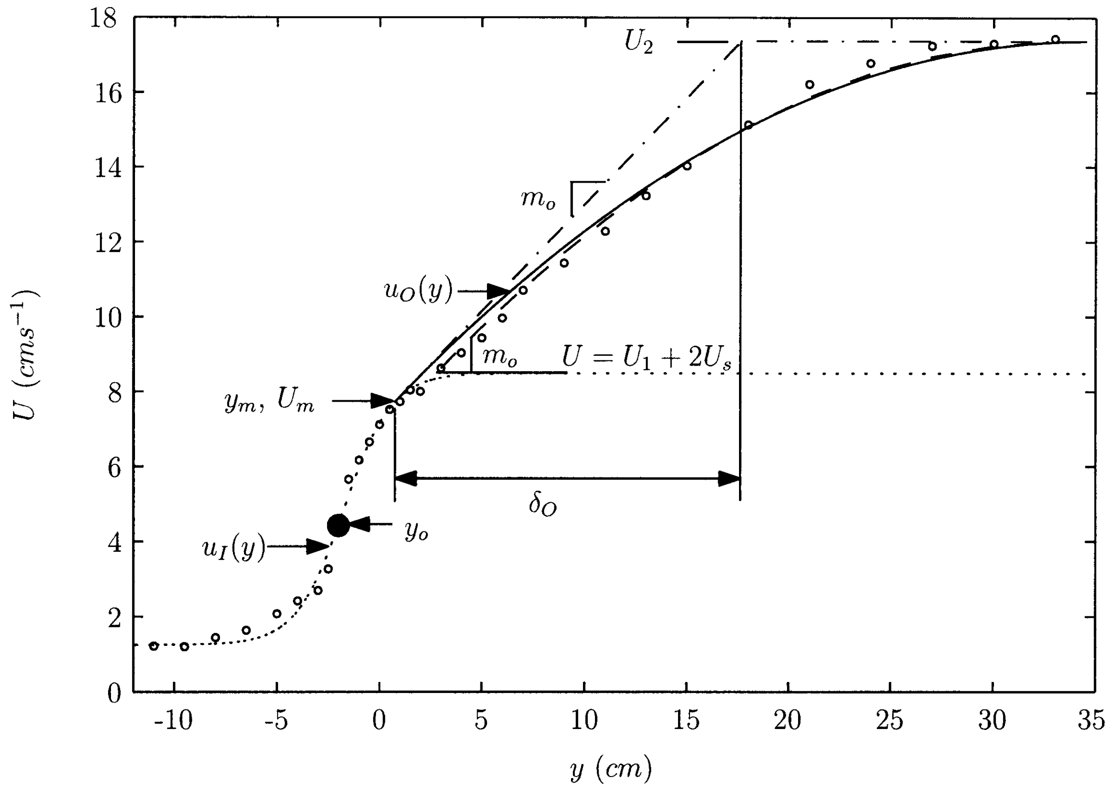

Figure 2-12: Graphical depiction of method to determine δ_O from experimental velocity profile. Starting at the nearest point to $U = U_1 + 2U_s$, quadratic regression is used to fit the outer layer data to (2.26b). This gives the outer layer width, δ_O, and initial slope, m_o, and the regression line (– –). The slope m_o is matched to the inner layer profile, $u_I(y)$ (dotted line) to yield y_m and U_m. The outer layer profile, $u_O(y)$ (—) is then determined. The line (— · —) illustrates the initial slope m_o and the definition of the outer layer width, $\delta_O = (U_2 - U_m)/m_o$

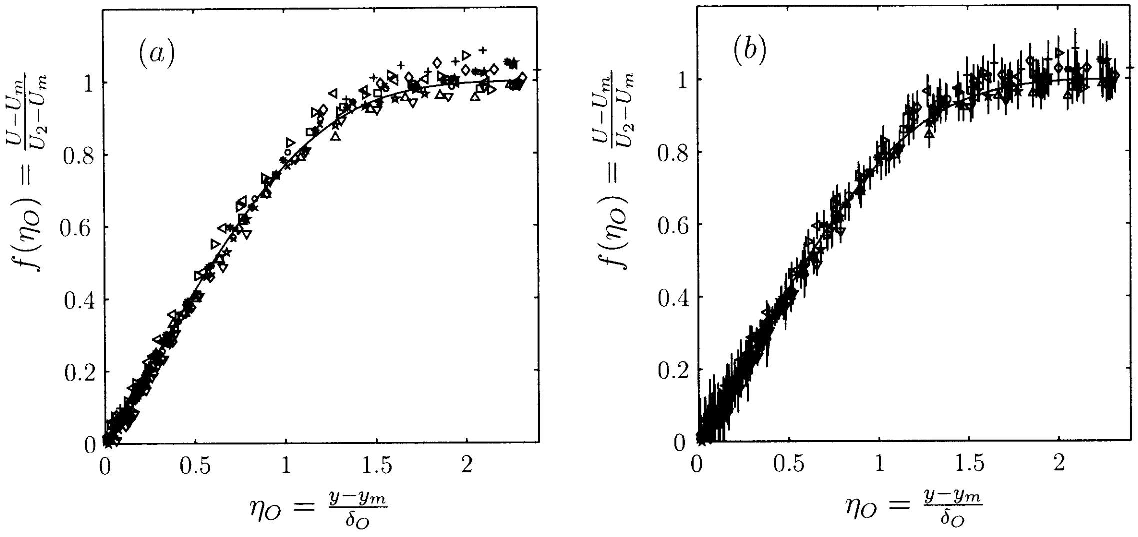

Figure 2-13: Rescaled outer layer velocity profiles with (*a*) and without (*b*) error bars. Symbols are as in Table 2.1. Blasius boundary layer solution shown for reference (solid line).

Self-Similarity of Outer Layer Profiles

Given δ_O, U_m and y_m for each experimental case, the outer layer profiles can be rescaled according to (2.24) and plotted together. The results are shown in figure 2-13. There is good collapse of the data from all experimental profiles along a line resembling the Blasius boundary layer solution, which is shown for reference (Schlichting, 1979). The collapse is particularly good in the initial, approximately linear region. Small deviations are observed as $f(\eta) = (u - U_m)/(U_2 - U_m) \rightarrow 1$. This is mainly due to uncertainty in the free stream velocity U_2, which approaches, but fluctuates around a constant value for most experimental profiles. The collapse of the profiles suggests self-similar outer-layer behavior, and as a result, independence from the inner layer flow. Outer layer similarity is characteristic of laminar boundary layers described by the Blasius profile, but whether it is characteristic of rough-wall turbulent boundary layers is still a subject of active debate (Krogstad *et al.*, 1992; Akinlade *et al.*, 2004; Jimenez, 2004). Krogstad *et al.* (1992) found that the effects of surface roughness extend outside the inner wall-layer and into the outer region, challenging the hypothesis of outer and inner-layer independence originally proposed by Townsend (1976). Recently, Akinlade *et al.* (2004) demonstrated that outer layer velocity profiles over different roughness surfaces could be made self-similar by scaling with a mixed outer-inner velocity scale, which also suggests a link between the outer and inner layers. However, it has also been proposed that certain types of wall roughness exist for which the outer layer flow is independent of the roughness height, k_s, and scales only with the outer layer thickness. These are termed "d-type" (for the outer scale, d) roughness, in contrast to "k-type" roughness for which the outer flow depends on the roughness characteristics (Jimenez, 2004). In the review by Jimenez (2004), it is suggested that the independence of the outer layer scaling may occur because, rather than acting individually, multiple roughness elements eject vorticity simultaneously, and that this process is driven by large-scale sweeps controlled by the outer flow. If the ejection frequency depends on outer layer scales, the flow will be independent of inner layer details. Ghaddar *et al.* (1986) has found such behavior in grooved walls, wherein the grooves eject fluid by an instability that originates at the grooves but occurs at a frequency dictated by the channel length scale. The shear instability and coherent structures in the present shallow vegetated flow, which originates at the velocity inflection point, but has a frequency that scales with the outer flow, are remarkably similar to Ghaddar *et al.*'s observations. The details of the instability are discussed in detail in chapter 4, but it is interesting to note that these dynamics seem be a mark of the outer layer similarity.

The outer layer independence from the array details, and hence the inner layer, is demonstrated definitively in figure 2-14, which plots δ_O versus $C_D ad$, a measure of the array density. There is no significant correlation, as $r = -0.13$, with a P-value of 0.70. However, there is a strong correlation of δ_O with the water depth, h, 99% confidence. This is consistent with the open channel drag, presented in section 2.3, which has the form $F_D = (c_f/2h)U^2$. The characteristic length scale for the resistance is thus h/c_f. To see that this length scale should establish δ_O, we assume that the outer boundary layer width is established by a balance between lateral shear stress and bed drag. This simple scaling argument, analogous to the balance (2.17) at the array interface, gives

$$\frac{\partial \langle u'v' \rangle}{\partial y} \approx -\frac{1}{2}\frac{c_f}{h}U^2. \qquad (2.30)$$

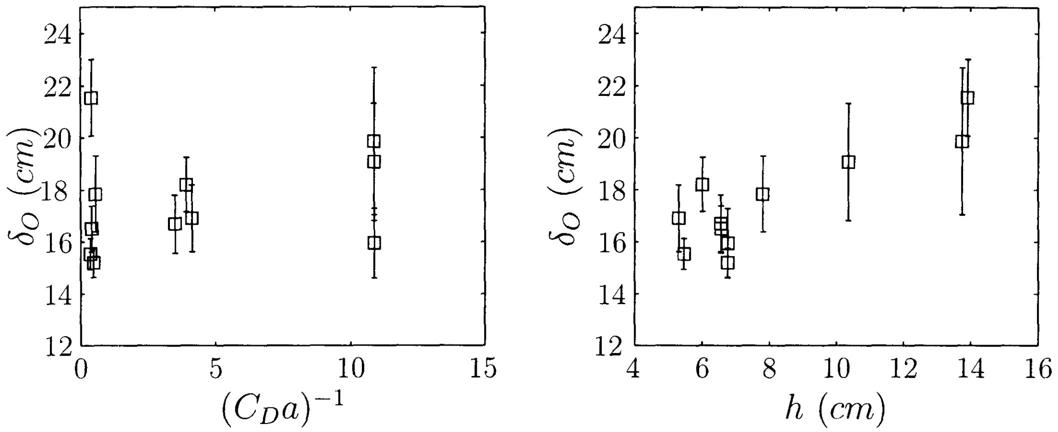

Figure 2-14: Outer layer width, δ_O, for all experimental profiles plotted with array resistance length scale $(C_d a)^{-1}$ (*a*) and the water depth, h (*b*). There is no significant correlation between δ_O and array resistance (P-value 0.5), but a significant correlation exists with h (P-value 0.0005).

Taking u_*^2 as the scale for $\langle u'v' \rangle$, δ_O as the length scale over which the lateral shear stress decays (see figure 2-5d-f for visual reference), and U_2 as the velocity scale, it follows from (2.30) that

$$\delta_O \sim \frac{h}{c_f} \frac{U_2^2}{u_*^2}, \tag{2.31}$$

which explains the observed dependence of the outer layer width on h.

2.5.7 Slip Velocity

The slip velocity, U_s, like the width, δ_I, is a property of the inner layer velocity profile, given by (2.26a). However, unlike δ_I, which appears to be a property of the cylinder array properties alone, U_s is a mixed property of the inner and outer layer flow. It also acts as a boundary condition for the outer layer flow. This can be seen by differentiating (2.13) to obtain the relation

$$\left. \frac{\partial U}{\partial y} \right|_{y=y_o} = \frac{1}{\delta_I} U_s. \tag{2.32}$$

Equation (2.32), analogous to the Beavers & Joseph condition (2.2), relates the slip velocity to the shear at the interface through a single length scale that is a function of the array characteristics, δ_I. A boundary condition for the outer layer flow can be constructed by rearranging 2.32,

$$\left.\frac{\partial U}{\partial y}\right|_{y=y_o} - \frac{1}{\delta_I}\left(U|_{y=y_o} - U_1\right) = 0. \tag{2.33}$$

Although 2.32 relates U_s to $\partial U(y_o)/\partial y$ through properties of the inner layer alone, both are indeterminate, and the equations cannot be closed, without considering the outer layer. Physically, this must be the case, as the total shear across the shear layer depends both on the flow in the channel and in the vegetation. The slip velocity, and through it the interfacial shear, may be determined from outer layer variables by considering the flow in the transition layer, where the inner and outer layers match. By continuity of the inner and outer layer velocities and derivatives at the matching point (2.25), we find that

$$U_s = \frac{\delta_I}{\delta_O}\frac{U_2 - U_1}{(1-\alpha^2) + (1+\alpha)\frac{\delta_I}{\delta_O}} \tag{2.34a}$$

where

$$\alpha = \tanh\left(\frac{y_m - y_o}{\delta_I}\right) \tag{2.34b}$$

defines the matching point. Physical intuition would suggest that α must be related to the relative steepness of the inner and outer layer profiles, suggesting $\alpha = f(\delta_I/\delta_O)$. For each experimental profile, α is measured by matching the inner and outer profiles as described in section 2.5.6. Figure 2-15 shows α and $\tanh^{-1}\alpha = (y_m - y_o)/\delta_I$ plotted against δ_I/δ_O. From figure 2-15*a*, the normalized matching point, $(y_m - y_o)/\delta_I$, increases as the inner layer width decreases. This implies that for denser arrays the matching point is pushed further from the center of the inner layer profile. This occurs because as the inner layer becomes thinner relative to the outer layer, the point at which the slopes match is pushed to the fringes of the hyperbolic tangent profile. The data in 2-15*a* show good agreement with the exponential fit $y = 1.89\exp\left(-4.03\frac{\delta_I}{\delta_O}\right)$, which implies

$$\alpha = \tanh\left[1.89\exp\left(-4.03\frac{\delta_I}{\delta_O}\right)\right]. \tag{2.35}$$

Measured values of α are shown along with this empirical fit in 2-15*b*. The empirical fit is extended beyond the data to demonstrate the limits $\alpha \to 0$ and $\alpha \to 1$. As $\delta_I/\delta_O \to 0$, i.e., a solid wall, $\alpha \to 1$, which it cannot exceed because of the tanh form (2.34b). The matching point thus approaches the flat part of the tanh curve (see figure 2-12). In the sparse array limit, $\delta_I/\delta_O \to 1$, $\alpha \to 0$, i.e., the matching point approaches the inflection point, and the overall shear-layer profile becomes symmetric, with the two distinct scales having merged into a single shear layer width. This is the free shear layer limit. The dependence of $(y_m - y_o)/\delta_I$ on array density is shown in figure 2-16 for reference. For sparse arrays, $(y_m - y_o)/\delta_I$ increases with increasing density, corresponding to a decrease in the inner layer width relative to the outer layer. However the data asymptote to $(y_m - y_o)/\delta_I \approx 1.4$ at higher density, as the inner layer width becomes constant in the d-regime (see section 2.5.5). This asymptotic value of $(y_m - y_o)/\delta_I$ is not universal, as it depends on the inner layer width in the d-regime, which, as discussed in 2.5.5, is sensitive to the geometry of the cylinders near the array edge.

The empirical fit for $\alpha(\delta_I/\delta_O)$ can be combined with the theoretical expression (2.34) to yield a semi-empirical prediction for the slip velocity,

$$U_s = \frac{\delta_I}{\delta_O} \frac{U_2 - U_1}{(1 - \alpha(\delta_I/\delta_O)^2) + (1 + \alpha(\delta_I/\delta_O))\frac{\delta_I}{\delta_O}}. \tag{2.36}$$

Experimental values for the slip velocity are shown in figure 2-17 along with the semi-empirical prediction. Across the range of array densities in the present experiments, $U_s/(U_2 - U_1)$ increases weakly with δ_I/δ_O and are well-predicted by the theory. The data from the submerged canopy experiments of Ghisalberti (2005) are also shown for comparison. These data lie only slightly above the prediction and shown the same weakly increasing trend with δ_I/δ_O. For more dense arrays than those for which data are available (small δ_I/δ_O), the theoretical prediction shows a precipitous decline, while a slow approach to $U_s/(U_2 - U_1) = 0.5$ is predicted in the sparse array limit ($\delta_I/\delta_O \to 1$). Outside the range of data, the theory predicts the limits $U_s/(U_2 - U_1) \to 0$ as $\delta_I/\delta_O \to 0$ and $U_s/(U_2 - U_1) \to 0.5$ as $\delta_I/\delta_O \to 1$, which

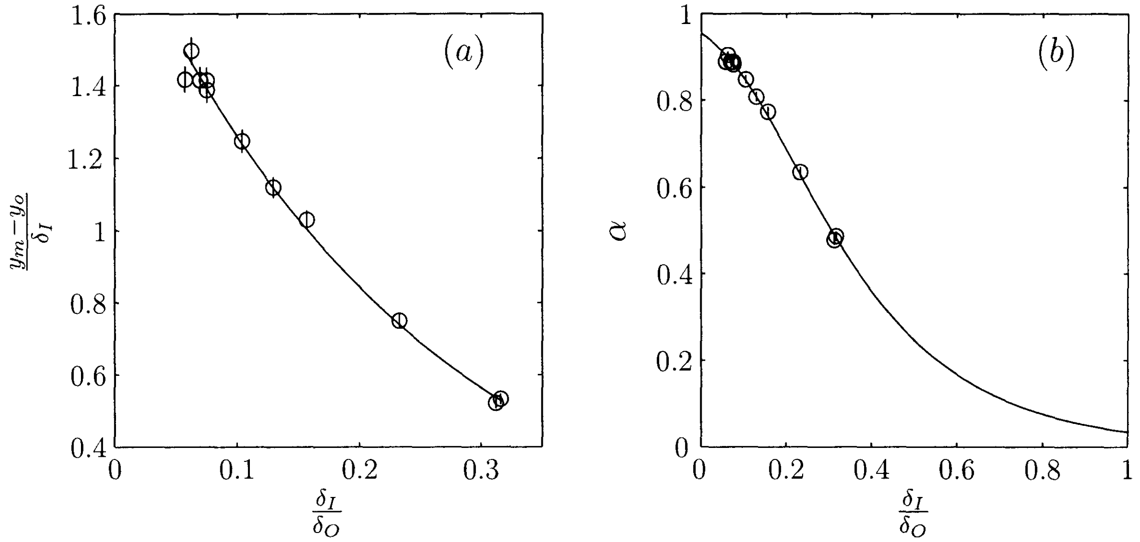

Figure 2-15: Dependence of the normalized matching point on δ_I/δ_O for all experiments. (a) shows $\tanh^{-1}\alpha = \frac{y_m - y_o}{\delta_I}$ along with the best exponential fit, $y = c_1 \exp\left(-c_2\frac{\delta_I}{\delta_O}\right)$, where $c_1 = 1.89 \pm 0.03$, $c_2 = 4.03 \pm 0.08$. (b) shows α along with the best fit, $\tanh\left[c_1 \exp\left(-c_2\frac{\delta_I}{\delta_O}\right)\right]$.

follow simply from the form of (2.34). In the dense array limit, $\delta_I/\delta_O \to 0$, the flow approaches that of a solid wall boundary layer, with no penetration, and zero slip velocity. In the sparse array limit, the flow approaches that of a classical plane mixing layer, with significant penetration and an antisymmetric velocity profile. In this case U_s is the center-line velocity, equal to the arithmetic mean of the slow and fast streams. The structure predicted by (2.36) is consistent with these two limits.

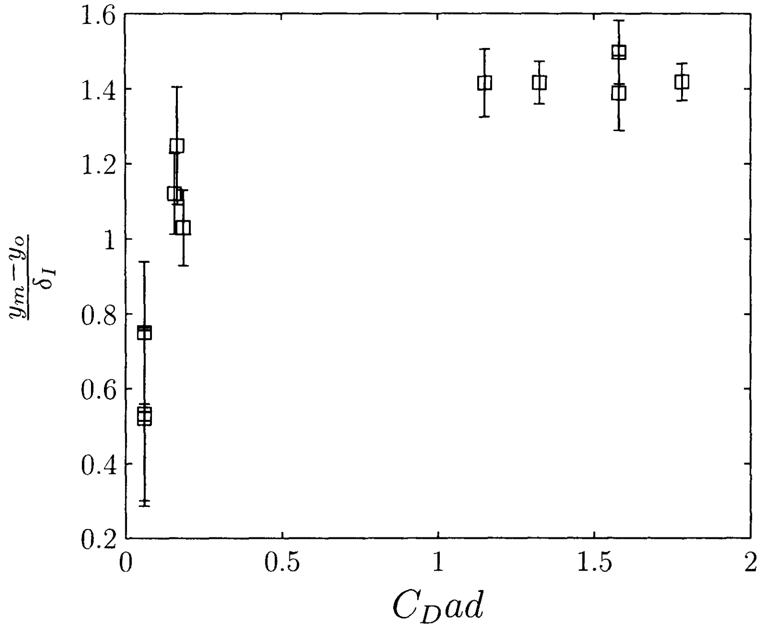

Figure 2-16: Dependence of the normalized matching point, $\tanh^{-1} \alpha = (y_m - y_o)/\delta_I$, on $C_D ad$.

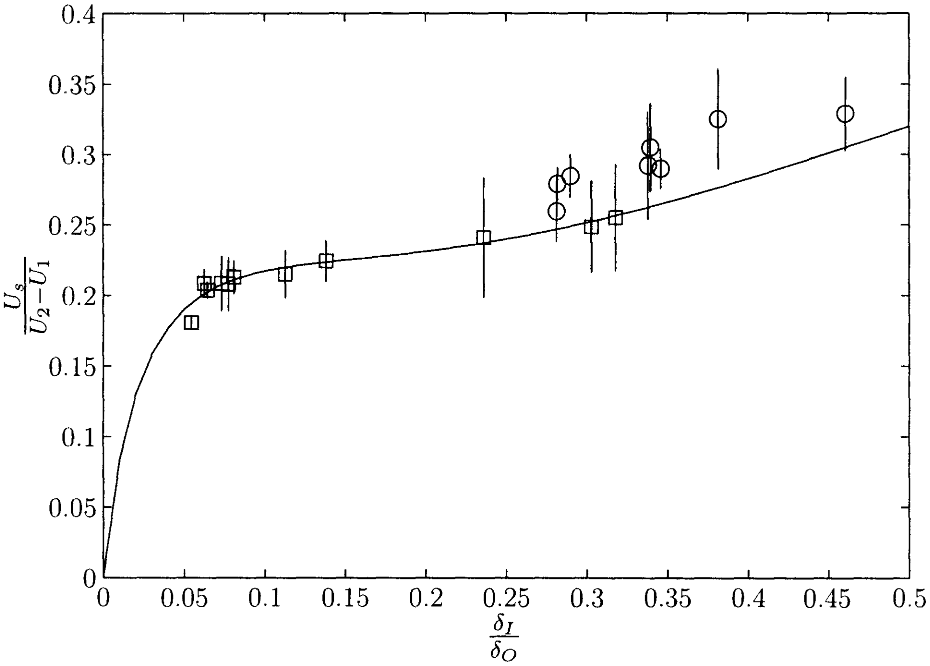

Figure 2-17: Normalized slip velocity, $U_s/(U_2 - U_1)$ plotted with the semi-empirical expression (2.36). Results from all experimental velocity profiles in the present experiments shown in squares; results from Ghisalberti (2005) shown in circles.

2.5.8 Virtual Origin

The offset between the point of inflection in the velocity profile and the edge of the array, y_o, as defined in (2.13), may be viewed as a virtual origin for the outer layer flow, analogous to the zero plane displacement, z_m, in a logarithmic boundary layer profile, $u = u_* log((z - z_m)/z_o)$ (Nepf & Vivoni, 2000). It is also the origin of the inflectional instability which leads to coherent structure formation. For each experimental velocity profile, the value of y_o was obtained from the hyperbolic tangent fit to the inner layer. These values are plotted in 2-18 as a function of array density, measured by $C_D a d$. All values are within 2 cm of $y = 0$, with a mean of 0.66 cm, approximately equal to one diameter. However, there is no trend with density, as the correlation is well below 50% significance. There is considerable scatter, likely due to uncertainty in experimentally locating the true edge of the array as well as fluctuations of the array edge over the length of the array. Together, these account for uncertainty of approximately 1 cm, larger than the mean value of y_o. Because y_o is very close to the true edge of the array, and is very small compared with the outer layer width, δ_O ($y_o/\delta_O < 0.07$ for all experimental cases), the approximation $y_o \approx 0$ is a good one for the outer layer boundary condition (2.33). That is, the outer layer flow sees the origin, and the source of instability, as occurring at the array interface.

2.5.9 Reynolds Stress and Interfacial Friction Laws

Reynolds Stress and Interfacial Shear

The transverse distributions of Reynolds stress, $\langle u'v' \rangle$ for all experimental profiles are shown in figure 2-19. There is a distinct maximum that coincides very nearly with the edge of the array, and defines the interfacial shear stress, as in (2.12). To within measurement resolution, the maximum always occurs at the point of inflection, y_o. The Reynolds stress profiles shown in 2-19 are normalized by u_*^2, which is estimated for each data set by smoothing the Reynolds stress profiles with a moving average filter and taking the maximum. The smoothing eliminated a bias toward strong fluctuations. As a result, in the normalized (unfiltered) Reynolds stress profiles in

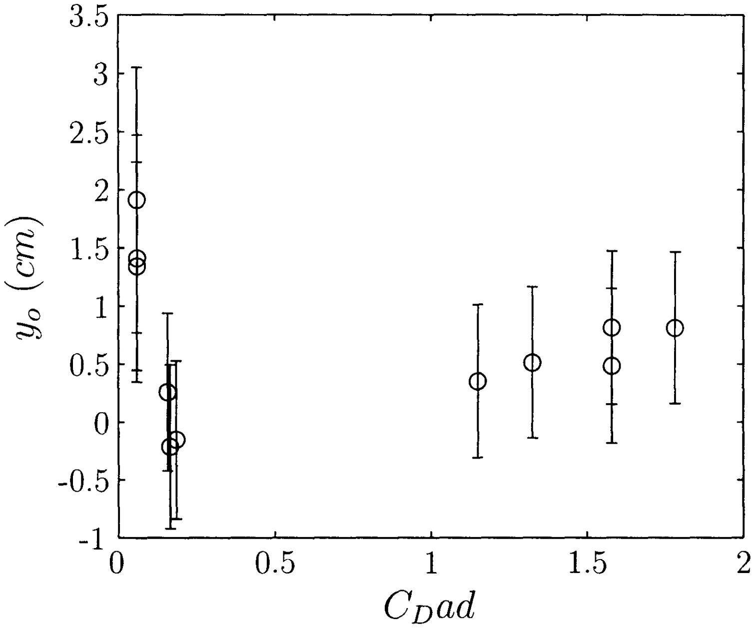

Figure 2-18: Virtual origin, y_o, for all experimental profiles plotted with C_dad, a measure of array density.

figure 2-19, the peak often slightly exceeds unity.

In figure 2-19*a*, the normalized Reynolds stress is plotted versus the outer layer coordinate. While the Reynolds stress profiles do not uniformly collapse onto a single curve, it is clear that δ_O is the appropriate length scale to describe the transverse dependence. All profiles decay to nearly zero around $y/\delta_O \approx 2$, suggesting that this is the transverse extent of the shear layer. In the following chapter, it is shown that the primary component of the Reynolds stress is the momentum exchange created by the transverse motions of the coherent shear layer vortices. This dependence of $\langle u'v' \rangle$ implies that that the transverse extent of the vortices is also set by δ_O.

In figure 2-19*b*, the Reynolds stress is plotted in inner layer coordinates. From its peak value at the edge, there is a is a very steep decline in Reynolds stress moving into the array. The length scale over which the decay occurs is $O(\delta_I)$. It is clear from this scaling that the length scale for the penetration of main channel momentum into the array is set by the inner layer thickness. Moving into the main channel the Reynolds stress profiles begin to diverge. By $\eta_I \approx 2$, there is significant spread, demonstrating that inner layer scaling does not hold in the open region.

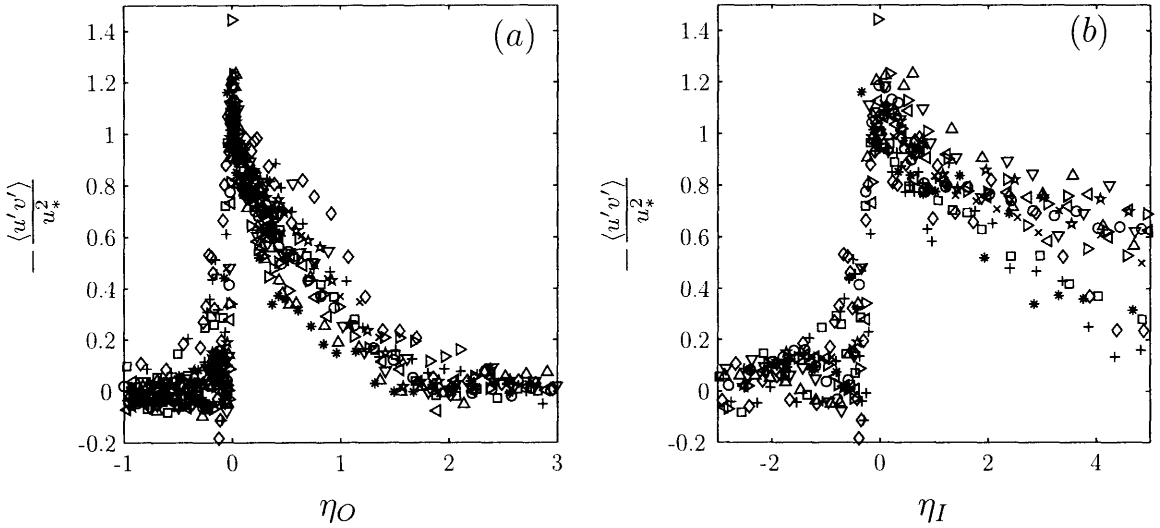

Figure 2-19: Distributions of normalized Reynolds stress, $-\frac{\langle u'v' \rangle}{u_*^2}$ for all experiments in outer layer (*a*) and inner layer (*b*) coordinates.

Interfacial Friction Coefficient

The effective absorption of channel momentum by the vegetated layer can be described by defining an interfacial friction coefficient, f_i,

$$f_i = \frac{u_*^2}{\frac{1}{2}\Delta U^2}. \tag{2.37}$$

Figure 2-20 shows f_i computed for all profiles, as a function of the outer layer Reynolds number, $Re_{\delta_O} = \Delta U \delta_O / \nu$. Also shown are the friction coefficient for turbulent solid walls, from Pope (2000, p. 278). For the turbulent wall, the Reynolds number is $Re_\delta = U_2 \delta / \nu$, with δ the channel width. The shallow vegetated layer exerts much greater drag on the channel momentum, by an order magnitude, than would a solid wall. This observation is important for flow conveyance in compound channels, as it demonstrates the large increase in drag created by floodplain vegetation as compared with a solid bank. There is a slight increase in f_i with increasing Reynolds number, but a constant value, $f_i \approx 0.03$, is reached for high Re. For comparison, the LES simulations of Nadaoka & Yagi (1998) for a shallow vegetated channel flow show an interfacial friction coefficient of approximately 0.02 for comparable vegetation density and Reynolds number.

The increase of f_i with Re_{δ_O} is in contrast to the decline in c_f with Re for solid walls. This difference is due to the fundamentally different nature of drag production in the two cases. For the turbulent wall, drag is created by the turbulent energy cascade near the wall and maintained by viscous dissipation, which becomes less important as the Reynolds number increases. In contrast, in the partially vegetated channel, drag is created by the exchange of low momentum fluid from the vegetated layer with high momentum fluid from the channel by large scale coherent sweeps and ejections. These coherent motions are less efficient at low Reynolds number, where viscosity is still appreciable, but become more efficient at higher Reynolds number, such that the interfacial shear stress appears to be proportional to the velocity difference,

$$u_*^2 = \frac{f_i}{2}\Delta U^2. \tag{2.38}$$

Also, from figure 2-20, f_i is not strongly dependent on array density. In chapter 5 it is demonstrated that there is a weak dependence of f_i on density over a wider range of vegetated flows. However, the dependence on density is weak, and the present experiments are taken from too narrow a range of array density (on the high packing density side) for the trend to be apparent.

Logarithmic Scaling

In rough boundary layers a logarithmic region is typically observed of the form

$$\frac{U}{u_*} = \frac{1}{\kappa}\log\left(\frac{y}{k_o}\right) \tag{2.39}$$

where $\kappa \approx 0.41$ is the von Kármán constant and k_o is known as the roughness length (Jimenez, 2004). Further insight into the absorption of channel momentum at the vegetated interface can be gained by plotting the experimental velocity distributions from the open region on a semi-logarithmic scale, to examine whether there exists a logarithmic region near the interface. The results are shown in figure 2-21. The velocity in the open region is normalized by the interfacial friction velocity, u_*, and plotted against distance from the edge in the rescaled coordinates $(y - y_o)/k_o$. Note

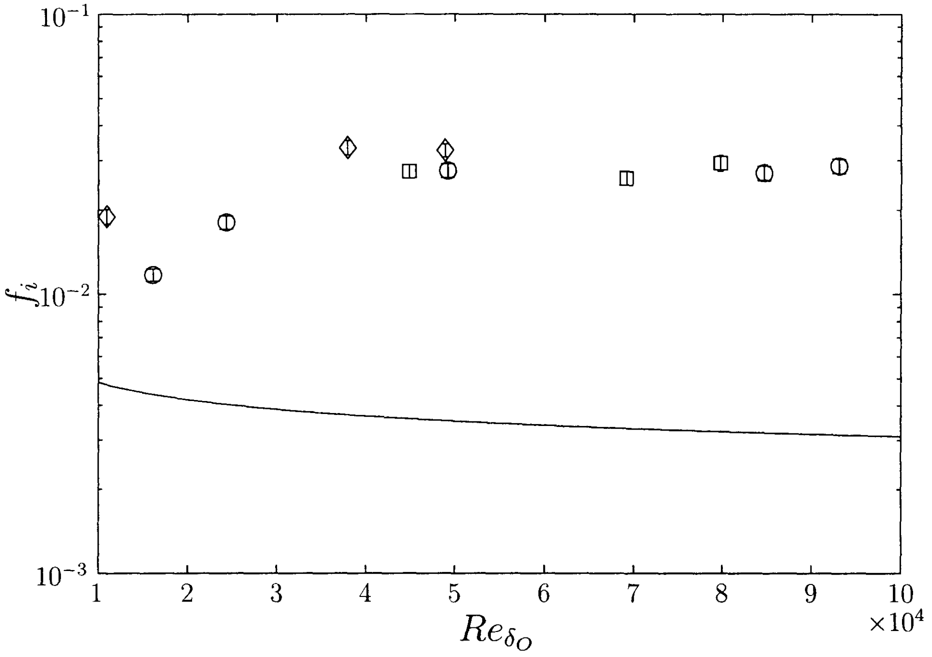

Figure 2-20: Interfacial friction coefficient, $f_i = u_*^2/(\frac{1}{2}\Delta U^2)$ vs the channel Reynolds number, $Re_{\delta_O} = 2\delta_O \Delta U/\nu$ for all experimental profiles: $\phi = 0.02$ (□), $\phi = 0.045$ (◇), and $\phi = 0.1$ (○). Also shown is the theoretical prediction for the friction coefficient, $c_f = u_*^2/(\frac{1}{2}U_o^2)$ for a turbulent solid wall given by Pope (2000, p.278).

that y_o, the inflection point, and point of maximum shear stress, is used as the origin here. In a smooth wall boundary layer, the choice of the origin is straightforward, but in rough walls the origin is typically taken as roughness height plus some offset to be optimally determined by fitting (Jimenez, 2004). Here the choice of y_o is made because it is the location of the boundary shear stress for the outer flow. The results shown in figure 2-21 support this choice. There is a region in the outer layer where all of the profiles collapse to the semi-logarithmic scaling of the form $u/u_* = 1/b \log((y - y_o)/k_o)$. However, $b \approx 0.318$, different from the usual Von Kármán constant, $\kappa \approx 0.41$. The discrepancy is likely due to the effect of bed friction in the open region, which limits the region of logarithmic scaling. From figure 2-21, the profiles diverge from the log scaling and asymptote to $u = U_2$, apparently when bed friction begins to dominate shear stress in the momentum balance. In the inner region, which extends between $y = 0$ and approximately $(y - y_o)/k_o = 5$, the profiles do not collapse, verifying the separate inner layer scaling discussed in section 2.5.3.

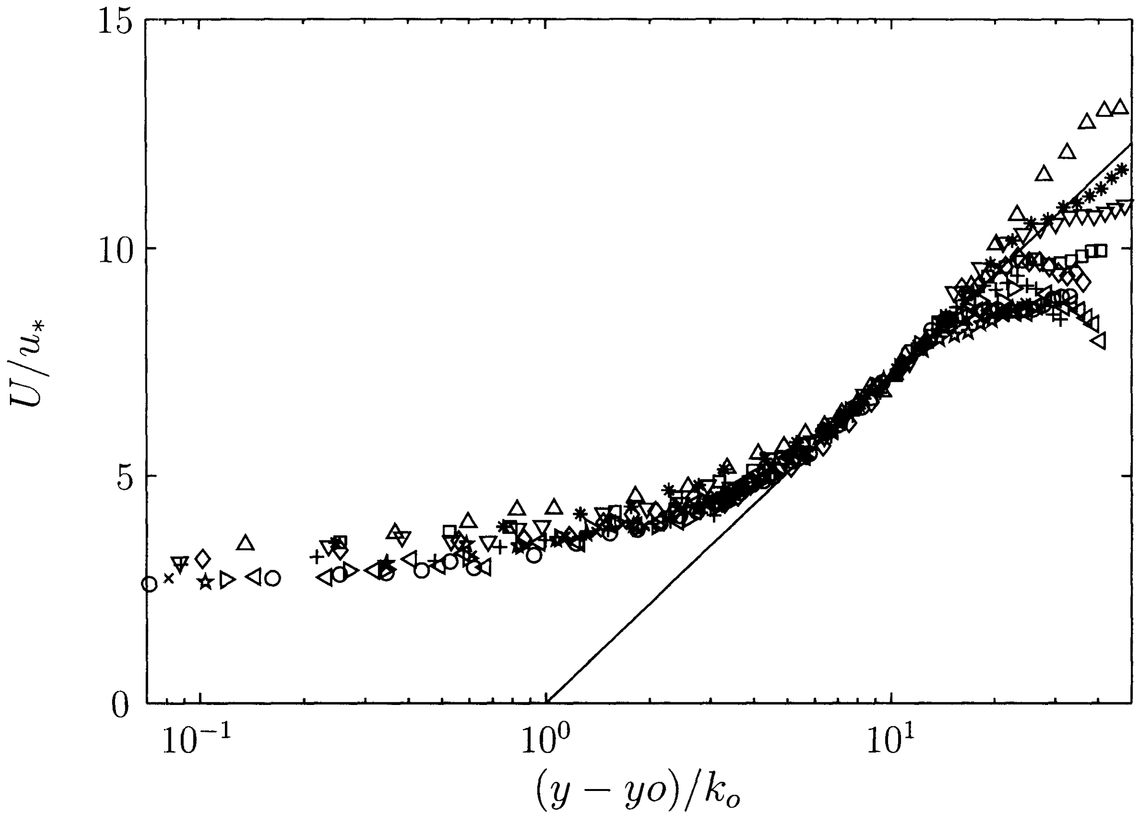

Figure 2-21: Mean velocity distributions in the open region for all cases plotted on a semi-log scale. The velocity is normalized by the shear velocity, u_*, and plotted against $(y - y_o)/k_o$, where k_o is the roughness length. The solid line is the logarithmic profile of the form $u/u_* = \frac{1}{b}\log((y - y_o)/k_o)$, where $b = 0.318 \pm 0.025$.

While the self-similar form of the outer layer velocity has already been established in section 2.5.6, the U/u_* logarithmic dependence is important because it demonstrates that there is a region of the outer flow that is controlled exclusively by the interfacial shear stress. This is a transition region between the inner layer, where the velocity is highly influenced by the vegetation, and the region outside the shear layer where the flow is entirely controlled by bed friction.

The results for the behavior of the roughness length scale, k_o, are shown in figure 2.5.9. It appears that the roughness is of the unusual "d-type", in contrast to the more common "k-type" roughness (Jimenez, 2004). There is no significant correlation between k_o and the array density, measured by $(C_D a)^{-1}$, a proxy for the length scale associated with the array. However, a significant correlation (99% confidence) exists between k_o and the outer layer width, δ_O. This demonstrates, in accordance with

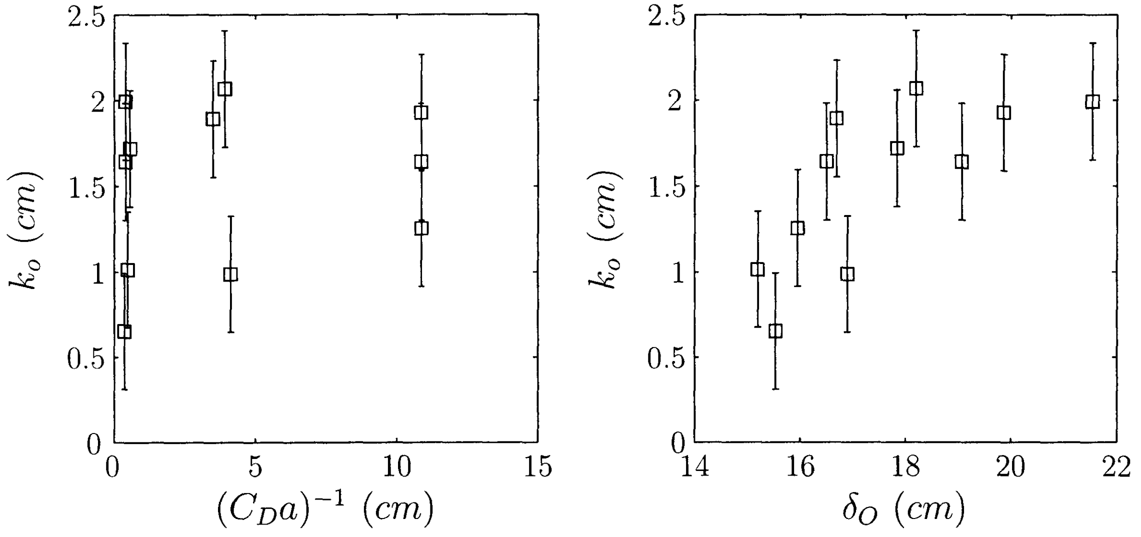

Figure 2-22: Dependence of the roughness length on $(C_Da)^{-1}$ (a) and δ_O (b). In (a), there is no significant correlation between k_o and the array length resistance length scale $(C_Da)^{-1}$ (P-value is 0.62). In (b), the correlation between k_o and the outer layer width, δ_O, is significant (99% confidence). This is the mark of "d-type" roughness.

the discussion in section 2.5.6 that the outer layer flow is independent of the inner layer details and hence the geometry and density of the array. Similarly, in boundary layers with "d-type" roughness, the outer flow is independent of the roughness element size, and k_o scales with the boundary layer width. These "d-type" boundary layers are uncommon and not yet understood. Jimenez (2004) suggests that the outer layer scaling may arise from a channel-scale instability whose scale is independent of the roughness. Indeed, this well-describes the shear flow studied here, as coherent structures whose frequency scales with δ_O dominate the momentum transport. Their dynamics will be discussed at length in the next chapter. Finally, note that the independence of k_o of the array density is consistent with the same independence of the friction coefficient, from figure 2-20.

2.5.10 Eddy Viscosity and Mixing Length

Insight into the structure of turbulence and coherent vortices across the shear layer can be gained from profiles of the effective eddy viscosity,

$$\nu_t = -\langle u'v' \rangle / \frac{\partial U}{\partial y}, \tag{2.40}$$

and mixing length,

$$L_m = -\langle u'v' \rangle / \left(\frac{\partial U}{\partial y} \right)^2 . \tag{2.41}$$

The eddy viscosity quantifies the strength of lateral momentum transfer across the shear layer, while the mixing length quantifies the length scale associated with the transfer.

To obtain profiles of ν_t and L_m, $\langle u'v' \rangle$ and $u(y)$ were both smoothed with a moving-average filter. Estimates of $\partial U/\partial y$ were then obtained by the central difference method. The results for all experimental profiles are shown in figures 2-23 and 2-24. The eddy viscosity is normalized by $u_*^2 \delta_O/(U_2 - U_m)$ and the mixing length by $u_* \delta_O/(U_2 - U_m)$. These scales are required by the similarity of the outer layer velocity, whose gradient scales as $(U_2 - U_m)/\delta_O$, and the Reynolds stress profiles which scale as u_*^2. Indeed, both ν_t and L_m approach ≈ 1 in the central region of the shear layer, suggesting that the scaling is appropriate. It is common is free shear flows to assume the scaling $\nu_t \sim \Delta U \delta_O$ (see, e.g., Schlichting, 1979), but it was found to be inappropriate for these data.

The eddy viscosity is small within the array ($y < 0$), with a sharp decline from the array edge. This demonstrates the inability of momentum to penetrate the layer of obstructions. The peak lies just outside the interface at $y/\delta_O \approx 0.2$, beyond the point of maximum shear ($y \approx y_o$). This suggests the most efficient transverse momentum transfer occurs further to the open side than the point of peak energy production. This maximum efficiency likely corresponds to the region where coherent structures are most intense. There is a decline beyond this region, with momentum exchange less efficient as the edge of the shear layer is reached and the coherent vortices weaken. Values beyond $\eta_O \approx 1.3$ are omitted as they show significant fluctuations, a numerical error due to division by very small values of $\partial U/\partial y$.

The mixing length declines sharply moving into the array from the edge. At the array edge, the length scale for turbulent motion sharply transitions from that of the coherent shear layer structures, to that of the cylinder wakes. The individual obstructions dissipate and redirect large-scale vorticity into the wake-scale vorticity through the interaction with the solid obstructions. This process has been observed in a canopy flow by Poggi *et al.* (2003), and Nepf (1999) gives the scaling for the dissipation of large-scale energy by the obstructions.

Beyond the array edge, the mixing length approaches a constant value of $L_m \approx 1$. There is a slight local maximum near the point of maximum ν_t, but L_m remains approximately constant across the mixing layer, until small values of $\partial U/\partial y$ begin to give spurious results (not shown in plot).

The mixing length has also been normalized by the outer layer width and plotted in outer layer coordinates in figure 2-25. As expected, the scaling L_m/δ_O does not collapse the data as well, but is a simpler formulation to apply in practice than $Lm(U_2 - U_m)/u_*\delta_O$ when U_m may not be available.

While physically tenuous in principle (Tennekes & Lumley, 1972), constant eddy viscosity and mixing length models are often used for engineering purposes and for modeling natural flows. The constant eddy viscosity model is based on the flux-gradient approximation, which is physically incorrect for shear flows because the large scale structures are of the order of the shear layer width (Broadwell & Breidenthal, 1982). Figure 2-23 demonstrates the inaccuracy of a constant ν_t- model. However, based on the experimental results presented here, a constant mixing length model with $L_m \approx \delta_O u_*/(U_2 - U_m)$ could be used to reasonably model the flow in the open region. In fact, Ghisalberti & Nepf (2004) used a mixing length model to successfully model the shear layer above a submerged aquatic canopy.

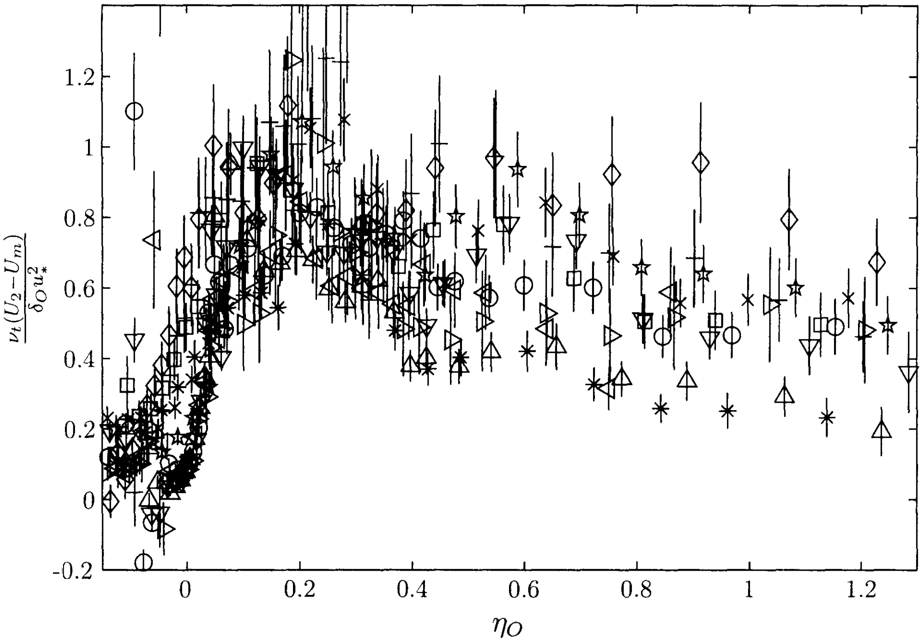

Figure 2-23: Profiles of normalized eddy viscosity for all experimental profiles plotted in outer layer coordinates. The uncertainty is due primarily to division by the local velocity gradient, prone to strong fluctuations.

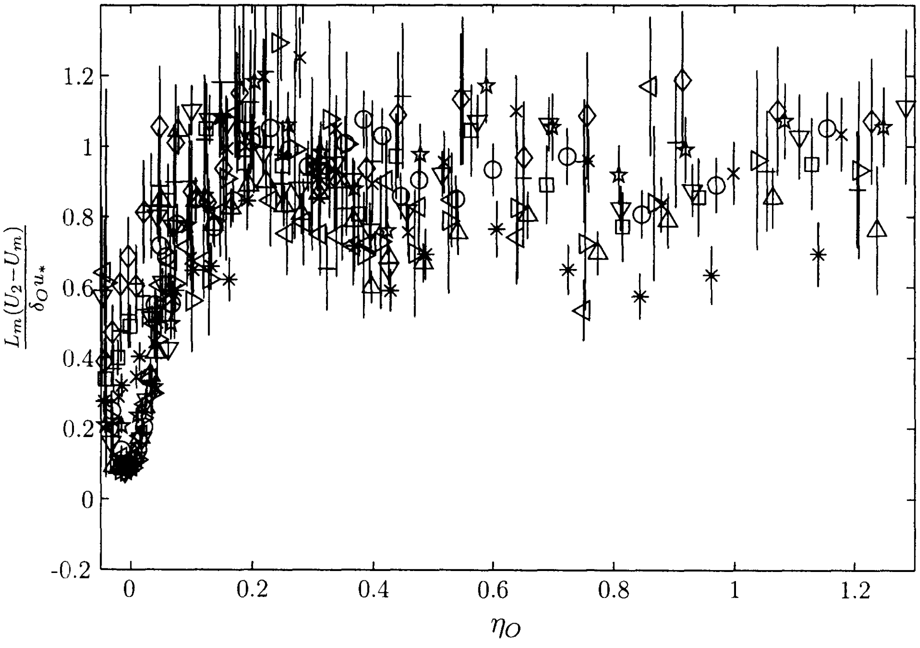

Figure 2-24: Profiles of normalized mixing length for all experimental profiles plotted in outer layer coordinates. As with ν_t, significant uncertainty is due to division by the local velocity gradient.

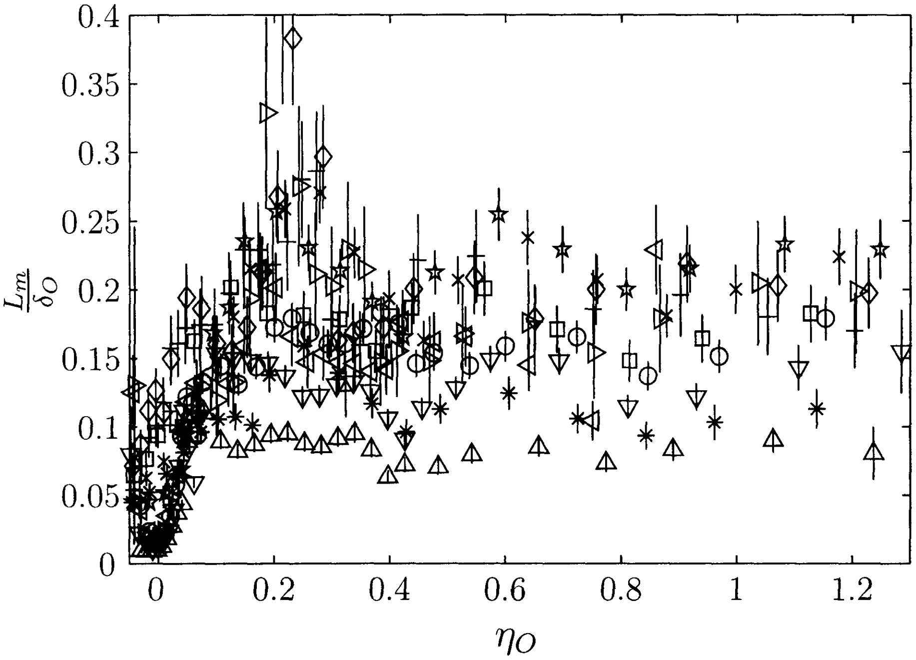

Figure 2-25: Profiles of mixing length normalized with the outer layer width, L_m/δ_O, for all experimental profiles.

2.5.11 Conclusions and Extension to Natural Systems

Results have been presented for mean velocity and turbulent stresses in a channel partially filled with an array of cylinders to model vegetation. The flow is shown to consist of two distinct regions, an inner region near the array interface, and an outer region in the open channel, with self-similar velocity distributions in each. In the inner layer, the experimental velocity distributions all collapse to a hyperbolic tangent profile with a width, and array penetration scale, that is dependent upon array characteristics alone. In a sparse array limit, the *s*-regime, the penetration depends on the effective resistance of the array, set by the cylinder spacing; in the dense array limit, the *d*-regime, the cylinder diameter becomes the dominant length scale, limiting the penetration to the outermost row of cylinders. In the outer layer, the velocity profiles collapse to a distribution resembling the Blasius boundary layer solution. The outer layer width, δ_O, is found to be independent of the vegetation density, and thus of the inner layer. However δ_O is highly correlated with the water depth, h, suggesting that it is established, by a balance between shear stress and bed friction in the open channel. Moreover, there is a region of the outer flow that exhibits logarithmic scaling of the form $U/u_* = \log((y - y_o)/k_o)$, with k_o, the characteristic roughness height, independent of array density, but correlated with the outer layer width, δ_O. This makes the outer layer flow analogous to the uncommon "d-type" boundary layers, for which the effective roughness scales with the boundary layer width. Finally, The drag exerted on the main channel by the interfacial shear stress is found to be substantially greater than that for a solid wall and is found to approach a constant, independent of volume fraction, for high Reynolds number.

The results of this chapter can be extended to efforts to model the mean flow in shallow vegetated channels, e.g., for the purposes of predicting sediment transport or flood conveyance in river-floodplain systems. Given the characteristics of the vegetated region, expressed through $C_D a$, the water depth, h, and the bed friction coefficient, c_f, the velocity distribution across the shear layer may be modeled. First, the momentum equations presented in section 2.3 may be simplified for steady, fully-developed flow, i.e., $\partial/\partial x = 0$ and $\partial/\partial t = 0$ for all quantities. To calculate the free stream velocity, U_2, note that at some point in the open region, outside the shear layer, the shear stress vanishes and U_2 is given by a balance between pressure forcing and bed drag,

$$0 = gS - \frac{1}{2}\frac{c_f}{h}U_2^2, \tag{2.42}$$

where S is the (constant) free surface gradient, $-\partial\left(h + z_b\right)/\partial x$. Similarly, sufficiently far into the vegetated layer, the shear stress vanishes, and the constant velocity, U_1, is determined by a balance between pressure forcing and vegetative drag,

$$0 = gS - \frac{1}{2}C_D a U_1^2. \tag{2.43}$$

Next, the inner layer width, δ_I can be calculated from the results of section 2.5.5 as

$$\delta_I = max\left(c_1(C_D a)^{-1},\ c_2 d\right) \tag{2.44}$$

where the empirical results $c_1 = 0.5$, $c_2 = 1.8$ were obtained from the present experiments.

Having obtained U_1, U_2, and δ_I, what remains is to calculate the outer layer velocity scale, δ_O, necessary to link the inner layer and outer layer velocity profiles. This can be done by an iterative method detailed below. The method of Ghisalberti & Nepf (2004), which was used to calculate the fully-developed velocity profile above a submerged canopy, can be adapted to the present case of shallow channels with bottom friction. Ghisalberti & Nepf found that in the shear layer above a canopy, the mixing length, L_m, is approximately constant. Similarly, in the present experiments, L_m was approximately constant for each profile throughout the outer layer (see their figure 6 and our figure 2-24 for comparison). Thus, a constant mixing length model is reasonable for the transverse Reynolds shear stress term (2.9a),

$$\overline{\tau}_{xy} \approx -\rho\overline{\langle u'v' \rangle} = L_m^2 \left(\frac{\partial \overline{U}}{\partial y} \right)^2 . \tag{2.45}$$

Note that the viscous stress has been neglected on the grounds that the Reynolds number is large, certainly true for field conditions. In addition, the secondary stress term, $\overline{\left(U - \overline{U}\right)\left(V - \overline{V}\right)}$ has also been neglected. Shiono & Knight (1991), among others, have shown that this term is significant, particularly for two stage channels with depth variation across the floodplain interface. In the present experiments, no depth variation existed, although there still existed a secondary circulation near the interface (see section 5.8 in chapter 5). Nonetheless, it was shown in that section that the circulation contributes little stress in the laboratory flume. Thus the stress from secondary circulations is neglected here, but see Shiono & Knight (1991) for a complete discussion for typical magnitudes in depth-varying channels.

Using the constant mixing length model, the momentum balance in the open channel is

$$0 = gS + L_m^2 \frac{\partial}{\partial y} \left(\frac{\partial \overline{U}}{\partial y} \right)^2 - \frac{1}{2} \frac{c_f}{h} \overline{U}^2 . \tag{2.46}$$

In section 2.5.10, the mixing length was found experimentally to be

$$L_m \approx \frac{\delta_O u_*}{U_2 - U_m} . \tag{2.47}$$

The matching velocity, U_m is a function of δ_I/δ_O and the interfacial shear velocity, u_* is a function only of U_1 and U_2 (see section 5.4 in chapter 5). The boundary conditions for $\overline{U}(y)$ come from the matching conditions with the inner layer,

$$\overline{U}(y) = U_m, \quad y = y_m \tag{2.48a}$$

and

$$\tfrac{\partial \overline{U}}{\partial y} = \tfrac{U_s - U_1}{\delta_I}(1 - \alpha^2), \quad y = y_m \tag{2.48b}$$

where

$$y_m = \delta_I \tanh^{-1} \alpha, \tag{2.48c}$$

$$U_m = U_1 + U_s(1 + \alpha), \tag{2.48d}$$

and

$$\alpha = \tanh(1.89 \exp(-4.03\delta_I/\delta_O)) \tag{2.48e}$$

derive from the matching relationships in sections 2.5.6 and 2.5.7 and the empirical fit for α. In addition, the slip velocity, $U_s = f(\delta_I/\delta_O)$ can be evaluated from (2.36). Thus it can be seen that the system (2.46-2.48) can be written in terms of only two unknowns, $\overline{U}(y)$ and δ_O. Following Ghisalberti & Nepf (2004), an iterative method is needed to determine δ_O and thus the outer layer velocity profile, $\overline{U}(y)$. Starting with an initial guess, $(\delta_O)_i$, (2.8) is solved for $\overline{U}(y)$. The actual boundary layer width of the solution, $\overline{U}(y)$ is then evaluated. If this width, $(\delta_O)_a$, does not match the initial guess, $(\delta_I)_i$, then the process is repeated with $(\delta_O)_a$ as the guess. When the process converges, both δ_O and $\overline{U}(y)$ are determined. Since δ_O is related to the open channel bed friction, a reasonable first guess, following the arguments in section 2.5.6, would be

$$(\delta_O)_i = \frac{h}{c_f}\frac{u_*^2}{U_2^2}. \tag{2.49}$$

Once δ_O is obtained from the iterative method, $U_s = f(\delta_I/\delta_O)$ can be evaluated from (2.36), yielding the inner layer velocity profile,

$$u_I = U_1 + U_s\left(1 + \tanh\left(\frac{y}{\delta_I}\right)\right), \tag{2.50}$$

where y_o, the inflection point, is taken as the vegetated layer edge, consistent with experimental results. Combining the inner layer and outer layer velocity distributions the solution for $\overline{U}(y)$ may then be used for studies of floodplain erosion and deposition, material transport, and channel conveyance.

Chapter 3

Hydrodynamic Stability Analysis

3.1 Introduction

In chapter 2, the scaling of the mean velocity distribution in the experimental vegetated channel was discussed, and the effects of coherent turbulent structures was suggested. In chapter 4 experimental measurements of the coherent structures are discussed in terms of their frequency, length scale, and effects on momentum transport. In this short chapter, the focus is on the initiation of the coherent structures, which is studied using linear hydrodynamic stability analysis (see, e.g., Drazin & Reid, 1981).

It is known that the coherent structures are related to the Kelvin-Helmholtz instability initiated by the inflectional velocity profile of the shear layer. The structures are observed experimentally to consist of a traveling periodic vortex street, as described in chapter 4. Based on these observations, a linear stability analysis is carried out, by viewing the structures as having originated from some initial wave-like disturbance superimposed on the shear flow. The theory assumes that a spectrum of wave, or disturbance, frequencies exists in the initial flow due to background turbulence. Of these, the coherent structures result from the wave or spectrum of waves that is most amplified by the shear flow. The disturbance begins with an infinitesimally small amplitude, but becomes amplified by the background shear flow and eventually grows to the finite scale observed in the laboratory. When first initiated, the small amplitude disturbance is viewed as a small perturbation on the shear flow, and thus the equations of motion may be linearized, and hydrodynamic stability theory used. However, as the amplitude of the disturbance grows, it interacts in a nonlinear way both with itself and with the background shear flow, transporting momentum and energy (for a good discussion, see Stuart, 1958). In the shallow vegetated layer this results in the attainment of a finite amplitude equilibrium with a constant frequency, the experimental observations of which are discussed in chapter 4. The growth and equilibration is a nonlinear process, and cannot be described by linear theory. Given these constraints, hydrodynamic stability theory will be used in this chapter to predict the frequencies which are most prone to amplification and their corresponding *initial* rates of growth in the downstream direction.

3.2 Linear Stability and the Modified Orr-Sommerfeld Equation

The stability problem begins with the equations of motion for a two-dimensional shallow flow with vegetation and bottom friction, given in section 2.3. Additionally, the turbulent Reynolds stresses are parameterized with a constant eddy viscosity,

$$-\rho\langle u_i' u_j'\rangle = \nu_t \frac{\partial \overline{u}_i}{\partial x_j}. \tag{3.1}$$

Although experimental data, as shown in section 2.5.10, are better described by a constant mixing length model, the constant eddy viscosity formulation is adopted for computational simplicity. This is has precedent in previous work on shallow channels (Chu *et al.*, 1991; Shiono & Knight, 1991). In addition, a rigid lid approximation is made which assumes the variation in water depth, h, contributes only to a pressure gradient, and does not support support free surface waves. The result momentum equations are a form of the Saint-Vénant equations,

$$\frac{\partial \overline{u}}{\partial t} + \frac{\partial \overline{u}^2}{\partial x} + \frac{\partial \overline{u}\,\overline{v}}{\partial y} = -\frac{1}{\rho}\frac{\partial \overline{p}}{\partial x} + \nu_t\left(\frac{\partial^2 \overline{u}}{\partial x^2} + \frac{\partial^2 \overline{u}}{\partial y^2}\right) - F_{Dx} \tag{3.2a}$$

$$\frac{\partial \overline{v}}{\partial t} + \frac{\partial \overline{u}\,\overline{v}}{\partial x} + \frac{\partial \overline{u}^2}{\partial y} = -\frac{1}{\rho}\frac{\partial \overline{p}}{\partial y} + \nu_t \left(\frac{\partial^2 \overline{v}}{\partial x^2} + \frac{\partial^2 \overline{v}}{\partial y^2} \right) - F_{Dy} \tag{3.2b}$$

$$\frac{\partial \overline{u}}{\partial x} + \frac{\partial \overline{v}}{\partial y} = 0, \tag{3.2c}$$

where p is the dynamic pressure, and the drag terms are

$$F_{Dx} = \begin{cases} \frac{1}{2}\left(C_D a + c_f/h\right) \overline{u}\sqrt{\overline{u}^2 + \overline{v}^2}, & y < 0 \\ \frac{1}{2}(c_f/h)\overline{u}\sqrt{\overline{u}^2 + \overline{v}^2}, & y > 0, \end{cases} \tag{3.3a}$$

$$F_{Dy} = \begin{cases} \frac{1}{2}\left(C_D a + c_f/h\right) \overline{v}\sqrt{\overline{u}^2 + \overline{v}^2}, & y < 0 \\ \frac{1}{2}(c_f/h)\overline{v}\sqrt{\overline{u}^2 + \overline{v}^2}, & y > 0. \end{cases} \tag{3.3b}$$

To review, the overbar represents a quantity that has been depth-averaged, spatially-averaged over the heterogeneity within the vegetation, and time-averaged over the time scale of the small-scale turbulence. The small scale turbulence can be defined as that due to the bed, with length scales up to h, and that due to the wake turbulence by the vegetation, with scales of order of the plant diameter (d) or spacing (s). Equations (3.2-3.3) thus represent the equations for the evolution of the mean flow plus the coherent structures.

The evolution of the small amplitude disturbance leading to coherent structures is described by writing all quantities as the sum of their mean values (long-time averaged) plus the disturbance,

$$\begin{aligned} \overline{u} &= U(y) + u'(x, y, t) \\ \overline{v} &= V(y) + v'(x, y, t) \\ \overline{p} &= P(y) + p'(x, y, t). \end{aligned} \tag{3.4}$$

Substituting these quantities into (3.2-3.3), linearizing to remove terms that are quadratic in the small-amplitude disturbance, and subtracting the mean yields the disturbance evolution equations,

$$\frac{\partial u'}{\partial t} + U\frac{\partial u'}{\partial x} + v'\frac{\partial U}{\partial y} = -\frac{1}{\rho}\frac{\partial p'}{\partial x} + \nu_t \left(\frac{\partial^2 u'}{\partial x^2} + \frac{\partial^2 u'}{\partial y^2} \right) - 2 f_D U u' \tag{3.5a}$$

$$\frac{\partial v'}{\partial t} + U\frac{\partial v'}{\partial x} = -\frac{1}{\rho}\frac{\partial p'}{\partial y} + \nu_t\left(\frac{\partial^2 v'}{\partial x^2} + \frac{\partial^2 v'}{\partial y^2}\right) - f_D U v' \tag{3.5b}$$

$$\frac{\partial u'}{\partial x} + \frac{\partial v'}{\partial y} = 0, \tag{3.5c}$$

with

$$f_D = \begin{cases} \frac{1}{2}\left(C_D a + c_f/h\right), & y < 0 \\ \frac{1}{2}c_f/h, & y > 0. \end{cases} \tag{3.6}$$

It is assumed that the basic shear flow, $U(y)$ is parallel, and that the large scale motion balances the mean pressure gradient, dP/dx. Following classic hydrodynamic stability theory (see,e.g., Drazin & Reid, 1981), the velocity and pressure disturbances are assumed sinusoidal,

$$\begin{aligned} u &= \phi_u(y)e^{i(kx-\omega t)} \\ v &= \phi_v(y)e^{i(kx-\omega t)} \\ p &= \phi_p(y)e^{i(kx-\omega t)}. \end{aligned} \tag{3.7}$$

Further, the following non-dimensionalizations are made,

$$U = U_o u^*, \quad c = U_o c^*, \quad \phi = U_o \phi^*, \quad y = by^*, \quad k = k^*/b \tag{3.8}$$

where U_o and b are velocity and length scales to be determined. The star subscripts are subsequently dropped, and 3.7 and 3.8 are substituted into the disturbance equation (3.5-3.6). Manipulation to remove ϕ_u and ϕ_p yields the modified Orr-Sommerfeld equation for for shallow water,

$$\begin{aligned} &(c-u)\phi_{yy} + \left(u_{yy} + k^2(u-c)\right)\phi \\ &\quad = \frac{S\mathcal{D}(y)u}{ik}\left(\phi_{yy} + \frac{u_y\phi_y}{u} - \frac{k^2\phi}{2}\right) + \frac{1}{ikRe}\left(2k^2\phi_{yy} - \phi_{yyyy} - k^4\phi\right) \end{aligned} \tag{3.9}$$

where now $\phi \equiv \phi_v$ and $c = \omega/k$ is the wave speed, and the "y" subscripts denote differentiation with respect to y. In addition the Reynolds number and the dimensionless drag have been introduced,

$$Re = \frac{U_o b}{\nu_t} \tag{3.10a}$$

$$S\mathcal{D}(y) = 2f_D b \tag{3.10b}$$

where, the drag has been written as the product of a dimensionless number, S, and a spatially-varying function $\mathcal{D}$, for reasons to be discussed. The modified Orr-Sommerfeld equation (3.9) and the assumptions leading to it have been previously derived and used in numerous studies of hydrodynamic stability of jets, wakes, and shear flows in shallow layers (Chu *et al.*, 1991; Chen & Jirka, 1997, 1998; Socolofsky & Jirka, 2004). However, in previous applications, a single value of c_f/h has been used throughout the shear flow and thus a constant friction number, $S_f = c_f b/h$ is defined to characterize the effect of the bed (Socolofsky & Jirka, 2004). For the shallow vegetated layer, the discontinuous drag condition (3.10b) was added in order to model the dominance of vegetative drag within the vegetated layer and bed friction outside. As such, the number S from (3.10b) must be defined in a way that characterizes the effects of both bottom friction and vegetative drag. This will be addressed shortly.

Equation (3.9) is a eigenvalue problem for the wavenumber k and frequency ω. The eigenfunction, ϕ satisfies the boundary conditions,

$$\phi \to 0, \quad y \to \pm\infty, \tag{3.11}$$

and has solutions only for particular relationships between k and ω, that is, if a dispersion relation,

$$F(\omega, k, S, Re) = 0 \tag{3.12}$$

is satisfied. For the the vegetated shear layer problem, the disturbance frequency, ω will be specified for given Re and S and the eigenvalue problem will be solved to find the complex wave number, $k = k_r + ik_i$. From equations (3.7), it can be seen that if the imaginary part, k_i, is negative, then the disturbance, with will grow exponentially with downstream distance, in proportion to $e^{k_i x}$. This is the mark of an unstable frequency. Solving the eigenvalue problem for k_i, the downstream growth rate, is known as the spatial instability problem (see, e.g., Monkewitz & Huerre, 1982). In contrast, the growth in time of a given wavenumber, k, can be determined from the complex frequency, ω, i.e., if ω_i is positive, the disturbance grows in time like $e^{\omega_i t}$. This is termed the temporal instability problem. The spatial problem is more relevant to the experimental vegetated shear layer in which the instability develops downstream of a splitter plate.

3.3 Kinetic Energy Analysis

Before proceeding with the solution to the eigenvalue problem, a simplified analysis can be carried out to predict the effect of friction on the growth of the instability. Using the method of Chu *et al.* (1991), an energy balance for the small perturbation can be derived from the linearized equations (3.5), by multiplying (3.5a) by u' and (3.5b) by v' and summing to obtain

$$\frac{\partial k}{\partial t} + U\frac{\partial k}{\partial x} = -\underbrace{\left\langle u'\frac{\partial p'}{\partial x} + v'\frac{\partial p'}{\partial y}\right\rangle}_{I} - \underbrace{\langle u'v'\rangle\frac{\partial U}{\partial y}}_{II} - \underbrace{f_D U\left(2\langle u'^2\rangle + \langle v'^2\rangle\right)}_{III}. \qquad (3.13)$$

where $k = 1/2\langle u'^2 + v'^2\rangle$ is the kinetic energy associated of the two-dimensional disturbance. Term I is the rate of work done by the fluctuating pressure, term II is the rate of energy production by the mean shear in combination with the Reynolds stress, and term III is the dissipation of disturbance energy due to vegetative drag and bottom friction. Due to the negative sign, it can be seen that the drag term will tend to reduce the growth of disturbance energy, i.e., will have a stabilizing effect on the shear flow.

In the laboratory experiments described in this thesis, as well as in the canopy flow studied by Ghisalberti & Nepf (2004), the coherent structures that form in the shear layer eventually reach an equilibrium after which they no longer grow. The energy equation for the disturbance (3.13) suggests that if the dissipation term (III) balances the shear production term (II), then the disturbance can reach an equilibrium. If these terms are in balance, the following relationship should hold

$$S_f = \frac{2\langle u'^2\rangle + \langle v'^2\rangle}{\langle u'v'\rangle}\left(f_D\frac{U}{U_y}\right) \approx 1. \qquad (3.14)$$

This is identical to the flux bed-friction number, S_f, introduced by Chu *et al.* (1991), save for the spatial dependence of f_D caused by the drag discontinuity. In White, Ghisalberti & Nepf (2004), an equilibrium condition for canopy flows was derived by applying the condition (3.14) at the vegetation interface. At the interface, but still within the vegetation, it was assumed that $C_D a \gg c_f/h$ (Typical field conditions are $C_D = 0(1)$, $a = 0.01$–$1\ cm^{-1}$, $c_f = O(0.01)$, and $h = 10$–$100\ cm$). It was thus suggested that the growth of the instability would become suppressed when the vegetation stability number, S_v, attains a critical value

$$S_v \equiv \frac{C_D a U}{(U_y)_{\max}} \approx \frac{2\langle u'v'\rangle}{2\langle u'^2\rangle + \langle v'^2\rangle} \tag{3.15}$$

where $(U_y)_{max}$ represents the maximum shear, assumed to occur at the interface. Experimental results from shear flows (see, e.g., Townsend, 1976) have shown that typically,

$$\frac{2\langle u'v'\rangle}{\langle u'^2\rangle + \langle v'^2\rangle} \approx 0.3 \tag{3.16}$$

and this is confirmed by measurements near the interface of the experimental channel (see figure 4-17*c* of chapter 4). Assuming $\langle u'^2\rangle \approx \langle v'^2\rangle$ gives an equilibrium condition at the interface

$$S_v = \frac{C_D a U}{(U_y)_{\max}} \approx 0.2. \tag{3.17}$$

As the initial instability grows downstream of the splitter plate, the shear layer width also grows, decreasing U_y and hence reducing the production relative to the drag dissipation. The theory assumes that when the shear layer width is such that the critical value, $S_v \approx 0.2$, is attained, the instability will cease to grow. For comparison, experimental values of S_v can be obtained From the inner layer scaling in chapter 2, yielding

$$S_v \approx \frac{C_D a U_s}{U_s/\delta_I} \approx 0.5 \tag{3.18}$$

where $U \approx U_s$ is assumed as the velocity scale at the interface and the experimental result $\delta_I = 0.5(C_D a)^{-1}$ is used. The comparison between the prediction ($S_v = 0.2$) and experiments are not quantitatively identical, but are of the same order of magnitude.

Thus the condition (3.17) appears to reasonably predict the inner layer equilibrium. However, the shortcoming of (3.17) is that, by assuming the velocity shear possesses only one length scale, it does not predict the separate outer layer equilibrium. In chapter 4 it is shown that the coherent structures reside predominantly in the outer layer and that the instability is influenced by both the inner and outer layers. The results from the solution of the Orr-Sommerfeld equation, presented below, will demonstrate that regardless of the value of $C_D a$, and hence the magnitude of the inner layer shear, the instability will always grow if there is no bed friction in the outer region.

3.4 Solution of the Eigenvalue Stability Problem

The modified Orr-Sommerfeld eigenvalue problem (3.9) was solved with a pseudo-spectral collocation method using Chebyshev polynomials. This method is employed in a the MATLAB program suite SWESC-M (Shallow Water Eigenvalue Stability Calculator - Matlab) developed by Scott A. Socolofsky. Details of the method are given in Socolofsky & Jirka (2004). As a baseline, the temporal amplification of a hyperbolic tangent free shear layer, without friction, was computed and compared to the well-known solution given in Betchov & Criminale (1967). The comparison was very good, lending credibility to the numerical method.

By solving the eigenvalue problem, the stability of parallel shear velocity profiles of a hyperbolic tangent form is tested for various vegetative drag conditions. Specifically, mean velocity profiles of the form

$$U(y) = U_o(1 + R\tanh(y/b + \epsilon)) \tag{3.19}$$

were studied, where U_o is the centerline velocity, ϵ is a small offset allowing the inflection point of the velocity profile to be displaced into or out of the vegetation, and R is the velocity difference between the streams far outside the shear layer,

$$R = \frac{U_2 - U_1}{U_2 + U_1} \tag{3.20}$$

Note that for this velocity profile, the momentum thickness is $\theta = b/2$. The dimensionless drag, from (3.10b), is given by

$$S\mathcal{D}(y) = \begin{cases} (C_D a + c_f/h)\, b, & y < 0 \\ c_f b/h, & y > 0. \end{cases} \tag{3.21}$$

To avoid discontinuities, this discontinuous drag profile was smoothed numerically using a very thin hyperbolic tangent profile, with a width, $\lambda << 1$,

$$S\mathcal{D}(y) \approx \overline{D}(1 - \gamma \tanh(y/\lambda b)) \tag{3.22}$$

where

$$\overline{D} = \frac{b}{2}(C_D a + 2c_f/h) \tag{3.23a}$$

is the mean drag, and

$$\gamma = \frac{C_D a b}{2\overline{D}} \tag{3.23b}$$

is a measure of the drag differential. Note that (3.22) and (3.21) are equivalent for $\lambda \to 0$. In the numerical method, $\lambda = 0.02$. Finally, (3.22) suggests the appropriate definition of the stability parameter, S, to be

$$S \equiv \overline{D} = \frac{b}{2}(C_D a + 2c_f/h). \tag{3.24}$$

The velocity profiles and corresponding drag distributions studied are shown in figure 3-1. The effect of varying the offsets, ϵ, relative to the vegetation interface is shown. As discussed in chapter 2, the experimental profiles do not match a hyperbolic tangent profile exactly, instead exhibiting two separate length scales. However, the hyperbolic tangent is expected to reasonably capture the effect of drag on inhibiting stability. As the mean velocity is displaced toward the free stream in the experimental profiles (see, e.g., figure 2-4 of chapter 2), they are best approximated by the hyperbolic tangent profiles with negative values of ϵ (3-1 *b* and *c*).

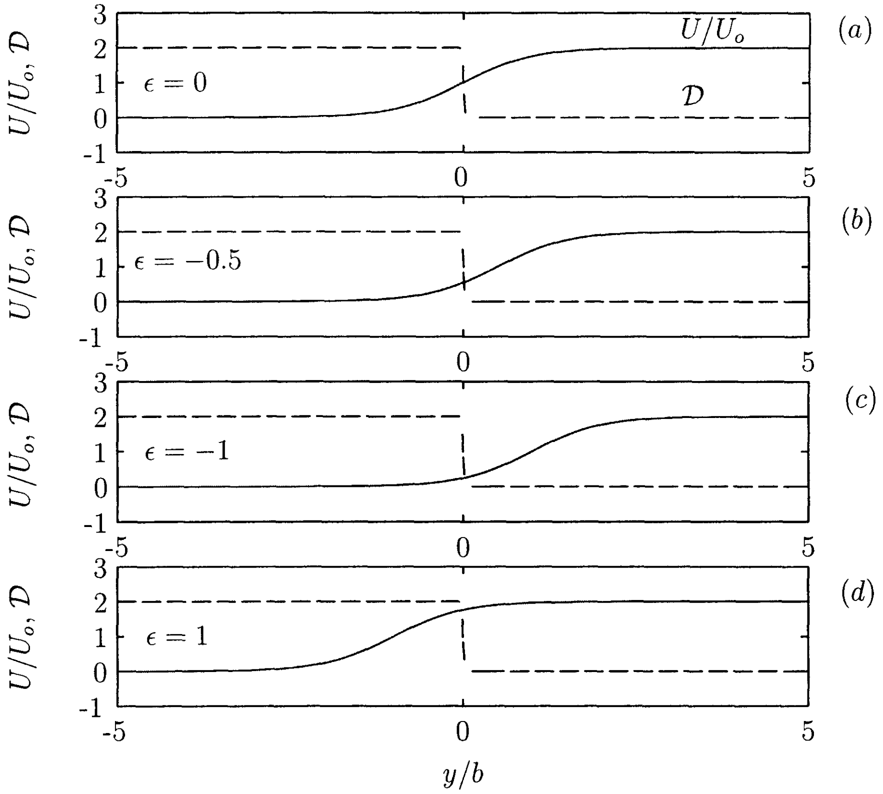

Figure 3-1: Hyperbolic tangent velocity and Drag profiles used in the stability analysis. In (a) – (d), the velocity, U/U_o, is shown for with various offsets, ϵ, relative to the vegetation interface.

3.5 Results of Stability Analysis

The first case studied was the spatial growth rate for a velocity ratio $R = 1$ and uniform friction (the $\gamma = 0$ condition). This represents an initial shear flow in either a layer with uniform vegetation, or the unvegetated channel with uniform bed friction. The growth rate for increasing values of the friction number, S are shown in figure 3-2. The $S = 0$ (free shear layer) case is comparable to the results of Monkewitz & Huerre (1982). The most unstable frequency occurs at $\omega\theta/2\pi U_o \approx 0.032$, the natural frequency for a free shear layer. As the drag is increased, by increasing S, the growth rate decreases for all frequencies. The reduction is nearly uniform across frequency space, suggesting friction does not preferentially affect any particular range. When $S \approx 0.25$, even the most unstable frequency becomes stabilized ($k_i \approx 0$), and for higher values of S all modes are damped.

When the drag is allowed to vary spatially ($\gamma = 1$), the case of partial vegetation, the results are quite different. The growth rates are shown for various values of the friction number S, and center offset, ϵ, in figures 3-3–3-7. For $\epsilon = 0$, i.e., the inflection point coinciding with the vegetation edge, the effect of drag is to reduce the growth rate (figure 3-3). However, high frequency modes are preferentially damped, with the most unstable mode shifting to a lower frequency with increasing values of S. In addition, the damping is much less pronounced than in the uniform friction case, as there are still frequencies with significant growth rates for $S = 1$, at which all modes are damped in the case of uniform drag. In fact, over the entire frequency range studied, $-k_i$ never becomes negative (stable), but asymptotically approaches zero for large S. This is illustrated in figure 3-4, which shows the decrease in growth rate of the most unstable mode, $\omega\theta/2\pi U_o = 0.032$, for both the uniform and nonuniform drag cases. The difference is significant, as k_i declines almost linearly with S in the uniform drag case (see figure 3-2), crossing zero to become significantly stable for $S \gtrsim 0.25$. The nonuniform drag case ($\epsilon = 0$, $\gamma = 1$), declines almost linearly for small S, but then asymptotically approaches zero for large S, never crossing $k_i = 0$ to become stable. This is consistent with experimental results in shallow channels with uniform drag, which suggest coherent structures can be completely damped and ultimately annihilated by bottom friction. However, it suggests that in flows with drag discontinuity, such as canopy flows, there will always be modes that are at least neutrally stable, implying that coherent structures existing in the flow will not be strongly damped.

Figure 3-3 shows the results when the hyperbolic tangent profile is shifted into the free stream a distance equal to the momentum thickness, $\epsilon = -0.5$. The disturbance growth is even less inhibited by drag in this case, as the entire frequency range is still unstable at $S = 5$. This is not surprising, as the source of the instability, the inflection point, is now in the open region, unaffected by vegetative drag. Moreover, the preferential damping of the $\epsilon = 0$ case is not observed, as the most unstable frequency remains approximately constant ($\omega\theta/2\pi U_o \approx 0.032$) as S is increased. The $\epsilon = -1$ case, shown in figure 3-6 is even less affected by drag. For this case, only the outer edge of the shear layer lies within the vegetation (see figure 3-1), and thus very little reduction in the growth rate is seen as S is increased. Finally, figure 3-7 shows the disturbance growth rate when the velocity profile is shifted into the vegetative region. For this case, high frequencies, ($\omega\theta/2\pi U - O \gtrsim 0.04$) are damped linearly with increasing S, as in the uniform drag case. This is expected since the inflection point is now well within the vegetated layer, and thus the higher frequency (shorter wavelength) disturbances exist solely within the drag-dominated region. However, lower frequency waves are asymptotically damped, remaining unstable as $\omega \rightarrow 0$. The $\epsilon = 1$ case does not resemble the experimental profiles, for which the shear layer centroid (point of mean velocity) lies outside the vegetation, and thus is simply shown for completeness.

There are two significant results from the linear stability analysis. The first is the determination of the most unstable wavelength, $\omega\theta/2\pi U_o \approx 0.32$. This frequency remains approximately constant with increasing vegetative drag if the shear layer is slightly displaced into the free stream, as in the experimental velocity profiles. This frequency corresponds to the dominant frequency of the coherent structures measured experimentally, as described in chapter 4. The second result is the flows

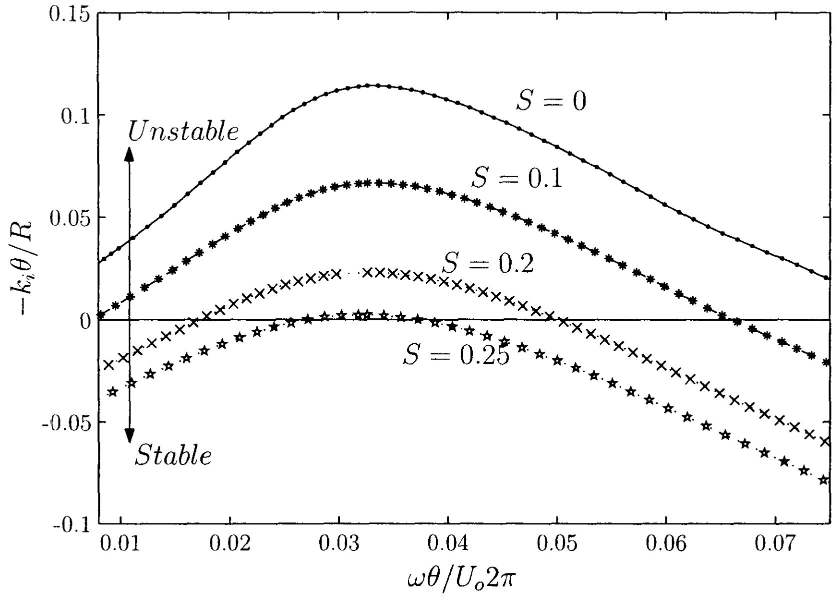

Figure 3-2: Spatial growth rate for uniform drag and various values of the friction number. Growth rate, k_i normalized by the momentum thickness, θ, and plotted versus the frequency, ω, normalized by θ and U_o.

with uniform drag become uniformly stabilized (dissipated) for large S, but flows with a drag discontinuity do not. This suggests that drag from partial vegetative coverage alone is insufficient to completely damp coherent structures, and thus conditions in vegetated flows with a drag discontinuity should be more conducive to the persistence of coherent structures than flows with uniform bed friction. This is confirmed in the present experimental study, in which the friction number based on array drag ranged from $S \approx 0.3$ to $S \approx 30$, but coherent structures were observed without fail and always persisted. In contrast, studies in shallow mixing layers with uniform bed drag find that coherent structures rapidly dissipate when their horizontal length scales (and thus, S) reach a critical scale (van Prooijen & Uijttewaal, 2002), consistent with the uniform drag prediction from the linear stability theory shown here.

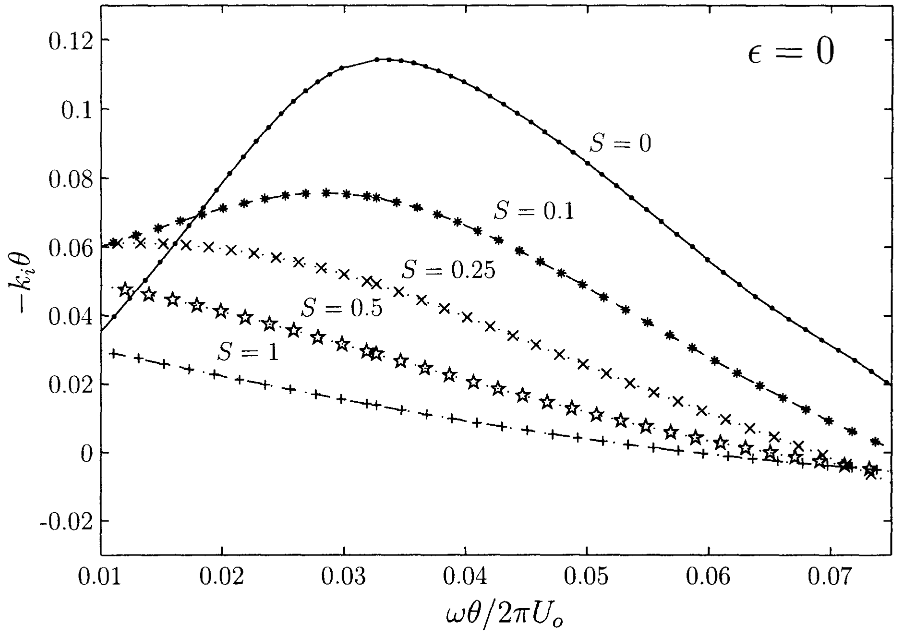

Figure 3-3: Spatial growth rate, k_i as a function of frequency for various values of the friction number, S for $\epsilon = 0$.

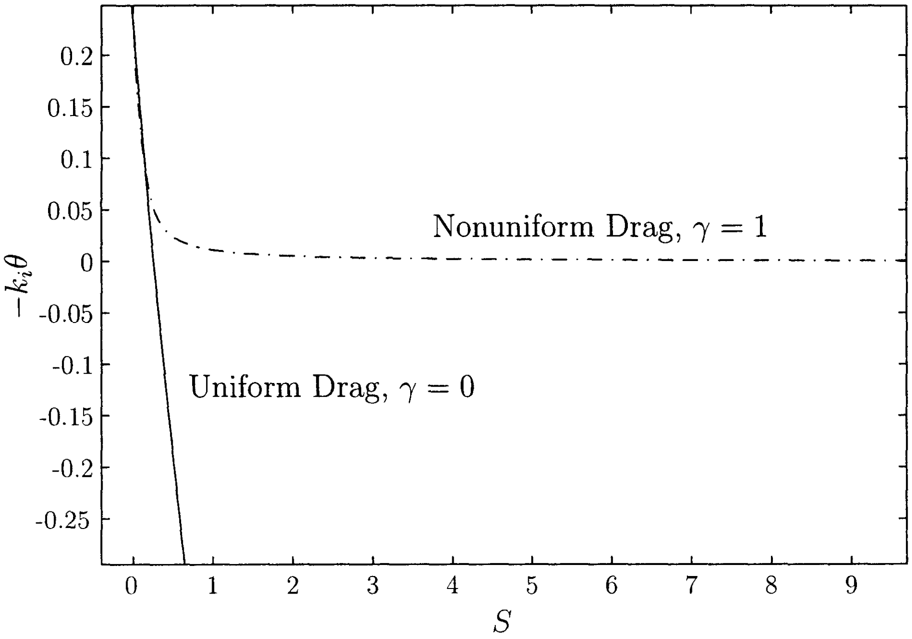

Figure 3-4: Spatial growth rate of the most unstable mode as a function of friction number, S, for uniform ($\gamma = 0$) and nonuniform ($\gamma = 1$) drag.

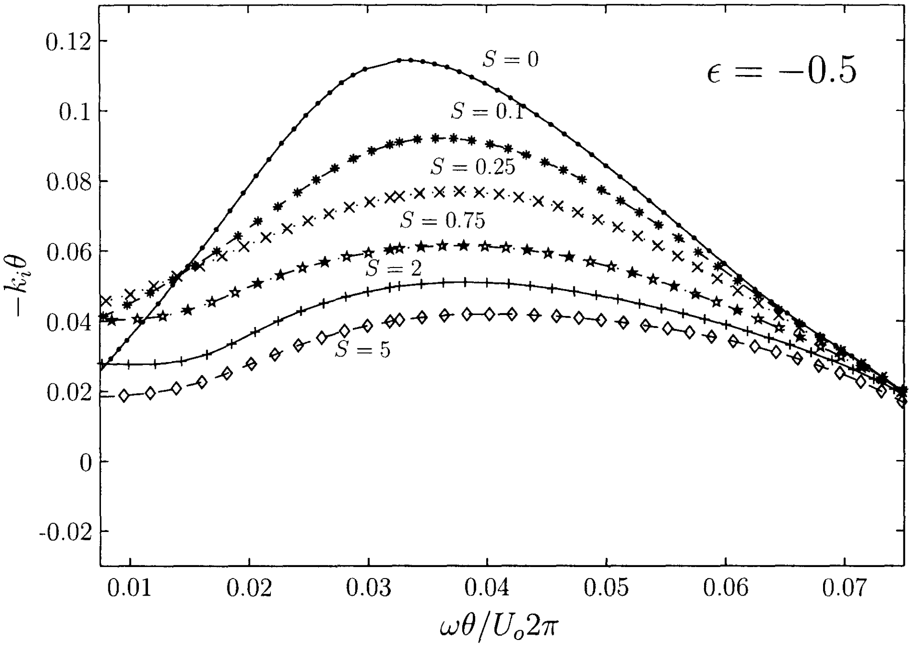

Figure 3-5: Spatial growth rate, k_i as a function of frequency for various values of the friction number, S for $\epsilon = -0.5$, an offset of θ away from the vegetation edge.

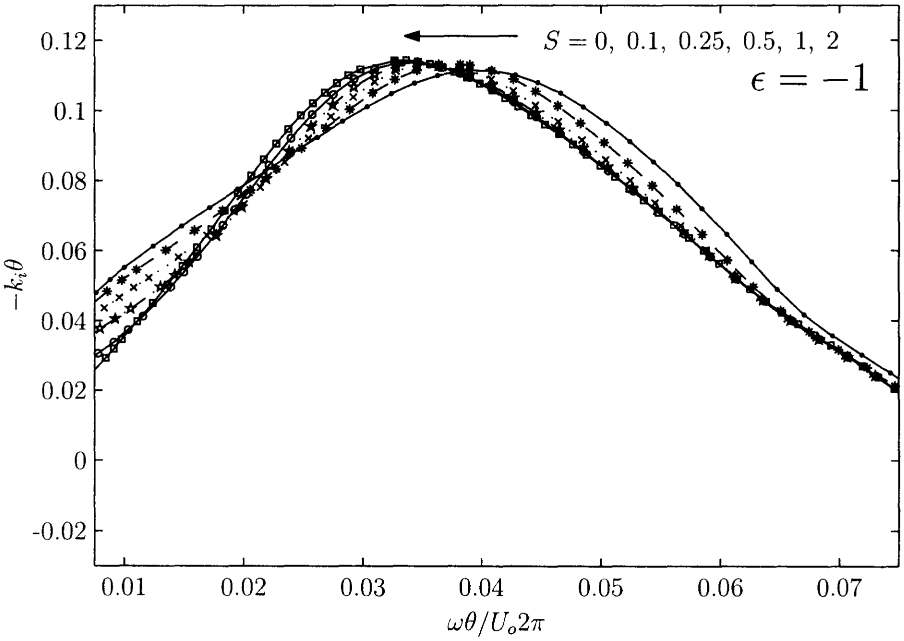

Figure 3-6: Spatial growth rate, k_i as a function of frequency for various values of the friction number, S for $\epsilon = -1$, an offset of 2θ away from the vegetation edge.

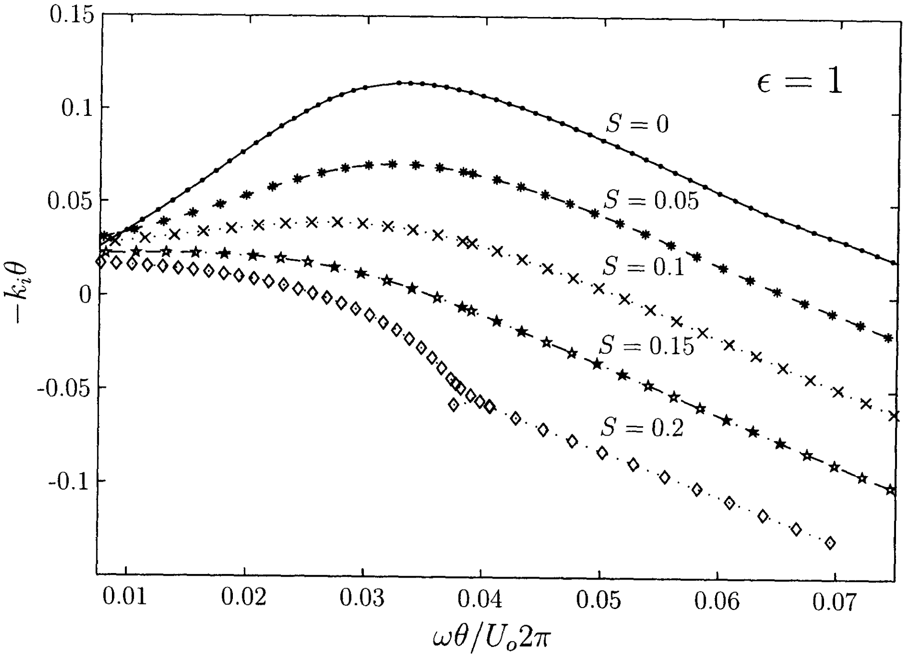

Figure 3-7: Spatial growth rate, k_i as a function of frequency for various values of the friction number, S for $\epsilon = 1$, an offset of 2θ into the vegetation.

Chapter 4

Experimental Results: Instability and Coherent Structures

4.1 Introduction

In shear layers possessing an inflection point, linear stability theory predicts the onset and growth of the Kelvin-Helmoltz instability (Drazin & Reid, 1981). The instability begins as a linear wave and quickly grows to a nonlinear state, characterized by a row of coherent turbulent structures with a length scale comparable to the shear layer width (Brown & Roshko, 1974). Linear stability theory successfully predicts the natural frequency of the passing structures,

$$f_n\theta/\overline{U} = 0.032, \tag{4.1}$$

where $\overline{U} = 1/2(U_1 + U_2)$ (see figure 2-1 of chapter 2) and

$$\theta = \int_{-\infty}^{\infty} \left[\frac{1}{4} - \left(\frac{U - \overline{U}}{\Delta U} \right)^2 \right] dy \tag{4.2}$$

is the momentum thickness, a measure of shear layer width (Ho & Huerre, 1984). The coherent structures are responsible for shear layer growth, by the process of vortex merging, whereby two or more adjacent traveling vortices enjoin, engulfing irrotational fluid in the process (Winant & Browand, 1974). The pairing is a result of a subharmonic instability, which has also been demonstrated by linear theory (Ho & Huerre, 1984; Pierrehumbert & Widnall, 1982).

In reality, shear flows are often affected by the presence of solid boundaries, which constrain growth. In shallow mixing layers, present in river-floodplain systems, composite channels, and shallow coastal regions, large, nearly two-dimensional coherent structures, with a length scale much greater than the depth, are often observed (Chu & Babarutsi, 1988; Tamai *et al.*, 1986). However, in contrast to free shear layers, the friction imparted by the shallow bed acts to diminish the shear-layer growth rate, and can inhibit the growth of the coherent structures (Uijttewaal & Booij, 2000; Chu *et al.*, 1991).

Coherent structures are also formed in the shear layer at the top of a submerged canopy (Raupach *et al.*, 1996; Ghisalberti & Nepf, 2002). Ghisalberti & Nepf found experimentally that the natural frequency of the shear layer above an aquatic canopy was very close to the value for free shear layers from linear stability theory, $f_n\theta/\overline{U} = 0.032$. In contrast to the continual growth of a free shear layer, however, the canopy flow reaches an equilibrium, with $\theta \rightarrow \theta_{eq}$, a constant, and locks into the corresponding f_n. However, although linear theory predicts the dimensionless frequency, $f_n\theta/\overline{U} = 0.032$, it explicitly predicts neither f_n nor θ. In fact θ is determined predominantly by the balance between drag and Reynolds stress across the shear layer (see, e.g., Ghisalberti & Nepf, 2002), a nonlinear process.

Partially-vegetated channels occupy the median on the spectrum between canopy shear layers and shallow mixing layers. The latter are formed downstream of a splitter plate in a uniform, shallow bed and have been studied extensively (van Prooijen & Uijttewaal, 2002; Chu & Babarutsi, 1988; Uijttewaal & Tukker, 1998; Uijttewaal & Booij, 2000). In these flows, the shear layer vortices are restricted in the vertical but grow in horizontal dimension, becoming effectively two-dimensional. However, bottom friction constrains the growth of the shear layer downstream of the splitter plate, limiting the size of the vortices (Uijttewaal & Booij, 2000). This is due first to a direct damping of the vortex instability, which has been shown by van Prooijen

& Uijttewaal (2002) using linear stability theory, and secondly, to a reduction in the velocity difference,

$$R = \frac{U_2 - U_1}{U_1 + U_2}, \tag{4.3}$$

between the fast and slow streams, which is eventually erased as the slow stream accelerates and the fast stream decelerates due to bed friction. Like bed friction in shallow layers, the drag from the vegetation in a partially vegetated channel limits the growth of the vortices into the vegetated layer. However, in contrast to shallow mixing layers, the shear is maintained by the drag discontinuity between the vegetation and the main channel and the velocity difference, R, reaches a constant. For this reason, as in submerged and terrestrial canopy flows, the shear layer reaches an equilibrium.

4.2 Periodic Fluctuations and Instability

4.2.1 Periodic Fluctuations

Laboratory experiments carried out in the partially vegetated channel described in section 2.4 reveal that coherent structures play a dominant role in the shear layer dynamics. The presence of the structures is indicated by coherent, nearly periodic fluctuations in velocity and surface displacement records, the signature of a traveling wave train of vortices. Figure 4-1 shows representative time series of the streamwise velocity, $u(t)$, the transverse velocity, $v(t)$, and the free surface variation relative to the temporal mean, $h(t)$, for a point just outside the vegetation interface, $y = 3\ cm$. From here forward the instantaneous velocity components will be written $u(y,t) = U(y,t) + u'(y,t)$, with $U(y,t)$ the temporally-averaged velocity and $u'(y,t)$ the temporal fluctuation (similarly, $v = V + v'$). The temporally-averaged turbulent quantities will be denoted with angle brackets, for example the Reynolds stress, $\langle u'v' \rangle$. Each of the time series exhibits nearly periodic fluctuations of considerable amplitude. The fluctuations in the streamwise velocity are of the same order as the mean flow, with a local turbulence intensity $\langle u'^2 \rangle^{\frac{1}{2}}/U = 0.5$ and regular oscillations between $0.1U_2$ and $0.7U_2$. Also, a significant periodic oscillation of the free surface accompanies the

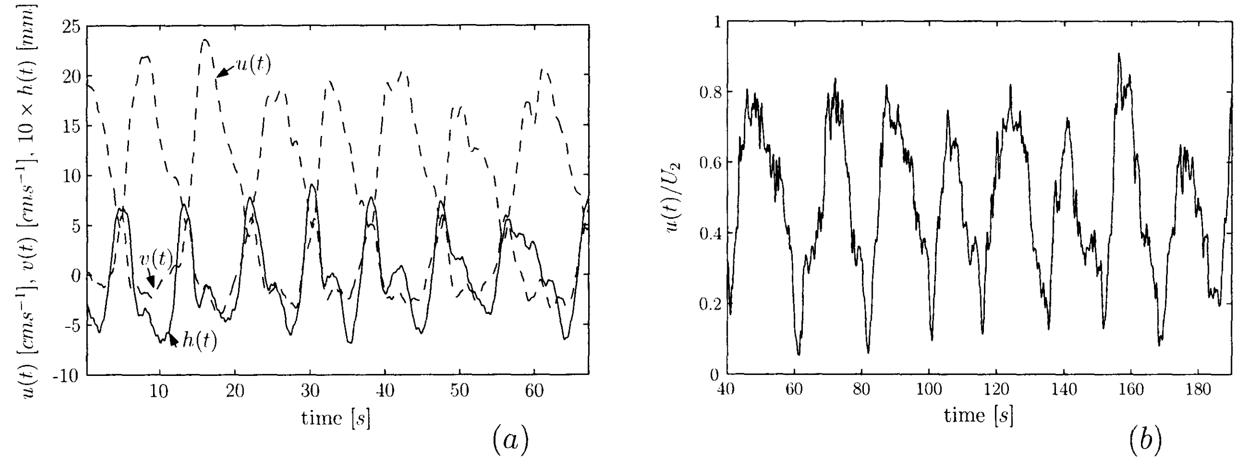

Figure 4-1: Temporal oscillations of the velocity and free surface. Time series of the longitudinal ($u(t)$) and transverse ($v(t)$) velocity components and the surface displacement ($h(t)$) for case X. Simultaneous time series shown in (a); streamwise velocity normalized by free stream velocity shown in (b) (case VII).

passage of the vortex structures, with $\langle h'^2 \rangle \approx 0.5\ mm$ due to a free surface depression at the vortex center. For reference, the mean water depth is $\overline{h} = 6.6\ cm$.

4.2.2 Development of Instability

Frequency spectra reveal that the regular oscillations are a result of the fundamental shear layer instability. Velocity transects have been made across the shear layer at various longitudinal positions (see figure 2-3). For each transect, the power spectral density of the transverse fluctuations at a position, $y \approx 3\ cm$, just outside the array interface, has been computed. The downstream development is shown in figure 4-2. For comparison, the development of the shear layer width is shown in figure 4-3. Profiles of longitudinal development were carried out for three experimental conditions, $(a - c)$, with all cases exhibiting qualitatively similar behavior. At $x = 0$, immediately following the splitter plate, the frequency spectrum is broad-banded.

As the flow develops downstream, a finite number of frequencies begin to take shape, typically with bimodal structure (see, e.g., (b), $x = 33\ cm$; (c), $x = 64\ cm$), but sometimes exhibiting three or more modes ((b), $x = 95\ cm$; (c), $x = 189\ cm$). Eventually, nearly all energy is transferred to a single dominant frequency, which becomes progressively more peaked, while the higher modes decay. The flow reaches

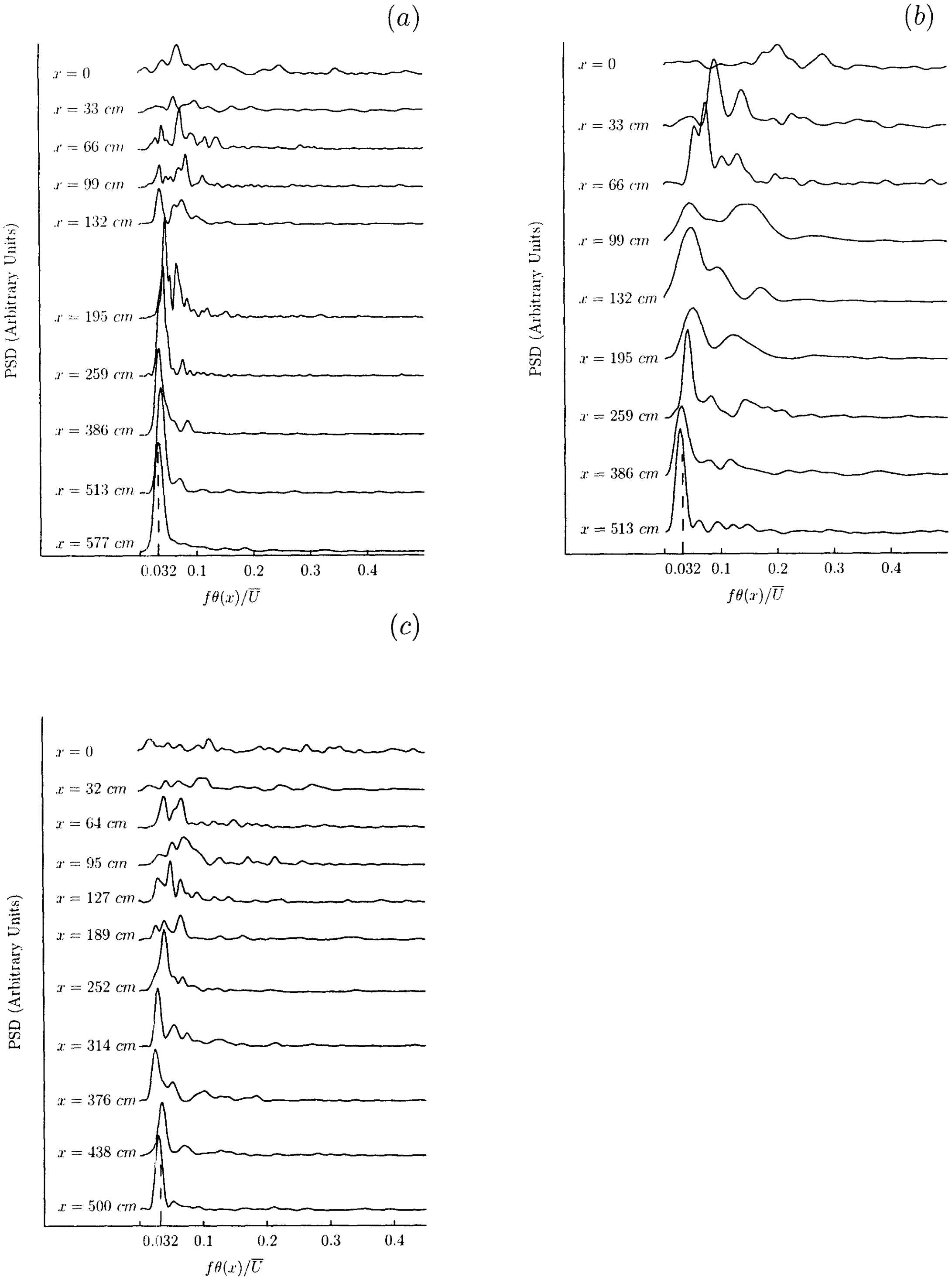

Figure 4-2: Development of the instability downstream of the splitter plate. The Power spectral density for $v'(t)$ is plotted for different $x-$ positions for cases IV (a) case V (b) and case VII (c). Abscissae for the PSD plots is the normalized frequency, $f\theta(x)/\overline{U}$. The natural frequency for a free shear layer, $f_n\theta/\overline{U} = 0.032$ is shown by the dotted line. The Magnitude of the PSD curves is not shown, but each is scaled to be energy-preserving, i.e., $\int_0^\infty P_{vv} df = \overline{v'^2}$.

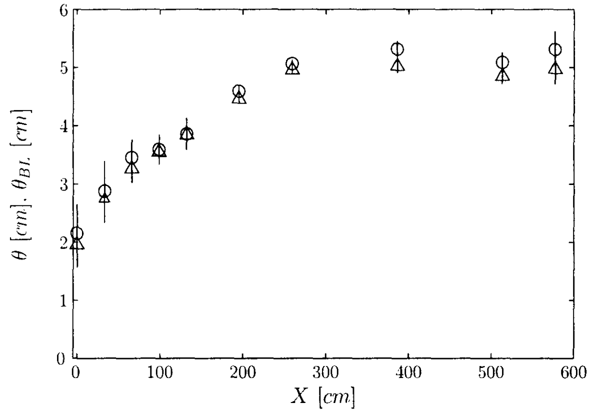

Figure 4-3: Development of the shear layer momentum thickness, θ and the outer layer momentum thickness, θ_{BL} for case IV.

an equilibrium with the saturation of this frequency, after which there is no further growth of lower modes. For each case, this equilibrium frequency, f_{eq}, is nearly equal to the natural harmonic for a free shear layer (4.1), $f_{eq}\theta_{eq}/\overline{U} = 0.032$, where θ_{eq} is the equilibrium momentum thickness. This is consistent with the flow equilibrium and frequency lock-in observed by Ghisalberti & Nepf in a submerged canopy shear layer.

The transfer of energy from higher to lower frequency is consistent with the subharmonic instability in a free mixing layer. In these flows the mode which is initially most unstable eventually saturates and begins transferring energy to its subharmonic (Pierrehumbert & Widnall, 1982; Ho & Huerre, 1984). Physically, this subharmonic instability manifests itself as a process of merging between adjacent vortices, which is the primary mechanism behind mixing layer growth (Winant & Browand, 1974). A similar mechanism appears to be occurring here. A portion of the high frequency energy present in the spectra at $x = 0$ and $x = 33$ cm, immediately downstream of the splitter plate, is due to entrance conditions and upstream turbulence, not a result of shear layer development. However, further downstream (see, e.g., (a)) most of this energy is no longer present, and two dominant frequencies have emerged, the natural frequency, f_n, and a second higher mode at approximately $2f_n$. The higher mode progressively loses energy to the natural frequency downstream and at equilibrium is nearly completely erased. This subharmonic transfer suggests vortex merging may play a role in shear layer growth here, as in free mixing layers.

The total power spectra, P_t, at equilibrium is shown in figure 4-4 for each of the experimental cases. These spectra are calculated by averaging the spectral density for each velocity component over the shear layer width

$$P_t = \frac{1}{\delta_O}\int_0^{\delta_O}(P_{uu} + P_{vv})dy, \tag{4.4}$$

where δ_O is the outer layer width. Thus they express the total energy density across the shear layer. That is, for the mean kinetic energy associated with temporal fluctuations, averaged over the shear layer width, given by

$$Q = \frac{1}{\delta_O}\int_0^{\delta_O}\frac{1}{2}(\langle u'(t,y)^2\rangle + \langle v'(t,y)^2\rangle)dy, \tag{4.5}$$

it follows that

$$\int_0^{+\infty} P_t df = Q. \tag{4.6}$$

The frequency peaks for each case line up very well with the most unstable frequency, $f_n\theta/\overline{U}$, predicted by linear theory. The mean value across all experimental cases is $\overline{f}_d = 0.032 \pm 0.003$. Consider that the linear theory result was obtained under inviscid assumptions for an idealized hyperbolic tangent velocity profile (Ho & Huerre, 1984). Its ability to predict the fundamental frequency for a shear flow formed in a partially-obstructed channel with a highly asymmetric velocity profile is a remarkable success for linear theory. This agreement suggests that the natural frequency of a shear layer is shape-independent, predictable from only the integral measure of the width and the mean velocity. This is a significant and powerful result indeed.

It can be demonstrated that the fundamental frequency scales predominantly with the outer layer width, associated with the main channel. To demonstrate, consider the outer layer to be analogous to a boundary layer originating at the inner layer origin, y_o. It is possible to rewrite the momentum thickness, θ, for the entire shear layer (4.2) in a form that more closely resembles the momentum thickness for a boundary layer,

$$\theta = \int_{-\infty}^{\infty}\frac{U - U_1}{\Delta U}\left(1 - \frac{U - U_1}{\Delta U}\right)dy. \tag{4.7}$$

The contribution to the momentum thickness from the outer (boundary layer) region is

$$\theta_{BL} = \int_{y_o}^{\infty} \frac{U - U_1}{\Delta U}\left(1 - \frac{U - U_1}{\Delta U}\right) dy, \tag{4.8}$$

and the inner layer contribution is

$$\theta_{IL} = \int_{-\infty}^{y_o} \frac{U - U_1}{\Delta U}\left(1 - \frac{U - U_1}{\Delta U}\right) dy. \tag{4.9}$$

The total is their sum,

$$\theta = \theta_{BL} + \theta_{IL}. \tag{4.10}$$

In figure 4-5, the ratio θ_{BL}/θ is plotted for all experimental cases. The outer layer accounts for the majority of the shear layer width across all cases (also see figure 4-3). The contribution of the inner layer, as expected, increases with δ_I/δ_O, but even for the largest ratio (sparsest cylinder fraction), $\theta_{BL} \approx 0.8\theta$. This is a significant result because the fundamental frequency, f_n, scales with θ, and thus the frequency of instability is set predominantly by the outer layer scale. Interestingly, the instability originates at the inflection point within the inner layer, but it appears that the inner layer width wields little influence over the frequency once the instability is established.

Channel-scale oscillations have also been observed by Ghaddar *et al.* (1986) in a grooved-wall channel and Schatz *et al.* (1995) in rod-roughened Poisseuille flow. Both found self-sustained oscillations leading to a two-dimensional flow which resembled Tollmien-Schlichting waves. Ghaddar *et al.* discovered that the grooved-wall oscillation was formed by a Kelvin-Helmoltz instability at the velocity inflection point in a thin layer near groove, but had a wavelength set by the Tollmien-Schlichting boundary layer instability mode corresponding to the channel scale. Both the partially obstructed channel considered here and boundary layers with an inflection point near roughness elements have in common the existence of two length scales: a thin layer with an inflection point, where the instability is initiated, and a larger channel scale which sets the frequency of the oscillation. In contrast, traditional free shear layers possess only a single length scale characterizing the width, which grows downstream

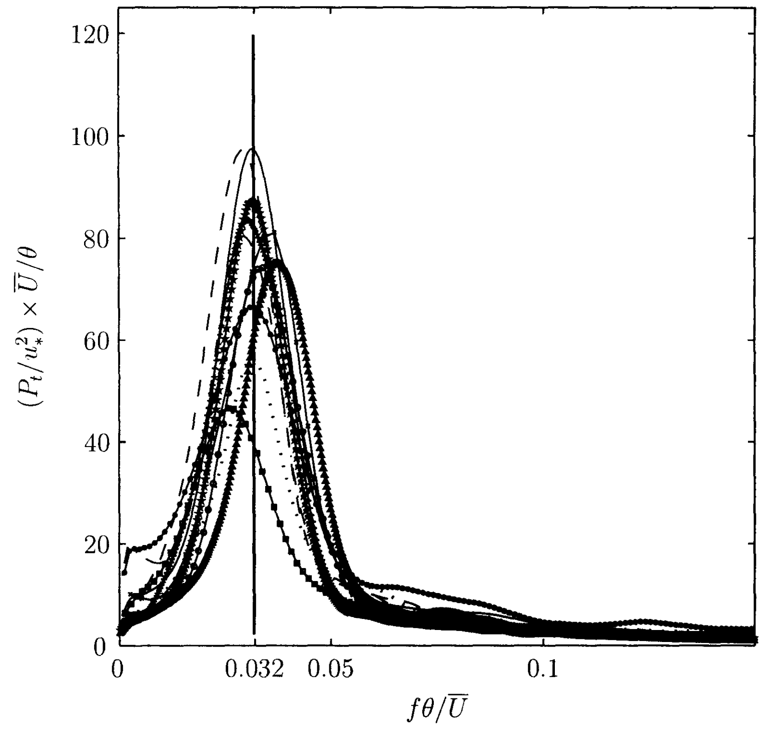

Figure 4-4: Power spectral density (PSD) plots for each experimental case at equilibrium. The PSD scale is such that the integral gives the total kinetic energy across the layer normalized by u_*^2 (see text). The most unstable free shear layer frequency from linear theory, $f\theta/\overline{U} = 0.032$ is shown by the vertical line. The mean frequency peak from all cases is $f\theta/\overline{U} = 0.032 \pm 0.003$, in nearly perfect agreement with linear theory.

in a self-similar manner. Thus they continually evolve rather than locking into a fixed frequency.

4.2.3 Vortex/Pressure Wave Characteristics of the Instability

The coherent oscillations suggest the initial instability evolves into coherent flow structures in the form of a traveling wave. Here evidence is given that the wave train has a dual form consisting of both a concentrated vortex and a far-field pressure wave response. Velocity and free surface fluctuations are shown in figure 4-6 for three positions across the shear layer, $y = 10$ *cm* (*a*) and $y = 3$ *cm* (*b*), both in the free stream, and $y = -10$ *cm* (*c*), within the array (see (*d*) for channel position). In addition, the lateral variation of the phase shift, ϕ, in radians, of the $v(t)$ and $h(t)$

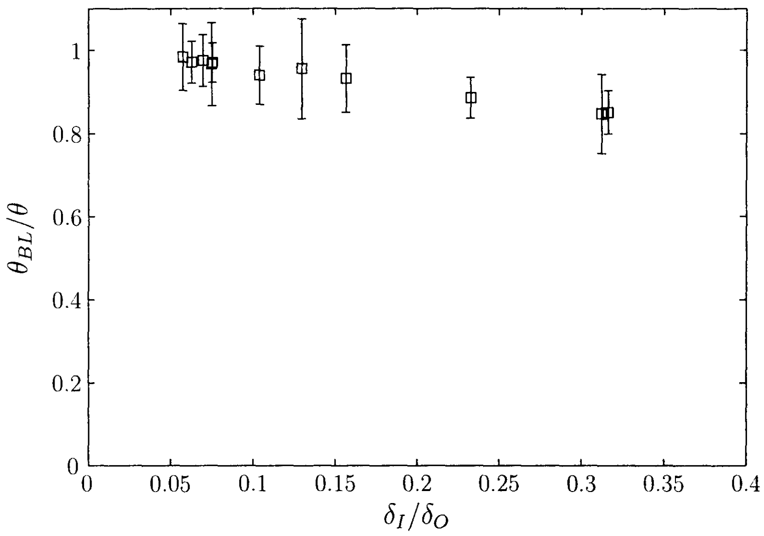

Figure 4-5: Ratio of the outer layer thickness to the total shear layer thickness, θ_{BL}/θ plotted as a function of the ratio of the inner layer to outer layer thickness, δ_I/δ_O for all experimental cases.

signals relative to the reference $u(t)$ signal is shown in (e). The phase shift is computed from the cross-correlation sequences, $\overline{u'(t)v'(t+\tau)}$ and $\overline{u'(t)h'(t+\tau)}$, with the phase shift defined as τ corresponding to the cross-correlation maximum, $\phi = 2\pi\tau_{max}f_d$.

At $y = 10$ cm $4-6a$, well into the free stream, the oscillations are pronounced, and $v(t)$ and $h(t)$ are nearly in phase. However, both are nearly antiphase with respect to the streamwise velocity, $u(t)$. In fact, from $4-6e$, $v(t)$ is approximately $3\pi/4$ out of phase with $u(t)$. This is characteristic of a vorticity wave, as discussed in Betchov & Criminale (1967). This is expected, as $y = 10$ cm is near the core of the coherent vortices, to be shown in section 4.4.

In $4-6b$, at $y = 3$ cm, closer to the interface, the same phase relations hold, but the oscillations are significantly greater in magnitude and more coherent in phase. The $u(t)$ and $v(t)$ signals are strongly anti-correlated ($\phi \approx 3\pi/4$). It will be demonstrated that these anti-correlated fluctuations correspond to strong momentum transport events by the coherent structures. In general, the vortex is marked by the region in which $u'(t)$ and $v'(t)$ are strongly anti-correlated. Thus the point at which the phase shift, ϕ, is reduced to $\pi/2$ is a measure of the vortex penetration into the array. From $4-6e$ this occurs near $y \approx -3$ cm for this case, but in general this penetration is approximately equal to the inner layer width, δ_I.

Beyond the penetration distance, the oscillations within the array are significantly different in form $4 - 6c$. First, the strength of the oscillations is considerably less than near the interface. In addition, $h(t)$ and $v(t)$ are no longer correlated, but are approximately $\pi/2$ out of phase, while the $u(t)$ and $v(t)$ signals are now close to $\pi/2$ out of phase. These relative phase relationships are consistent with a pressure wave Betchov & Criminale (1967) or, e.g., a free surface gravity wave. Because the velocity components are out of phase they transport no net momentum. The structure of the oscillations inside and outside the array thus suggests that the coherent structures possess a central core that acts as a traveling vortex wave, and a more diffuse region, with lower fluctuation strength, within the array that acts as a traveling pressure wave. The oscillatory flow is observed as far into the array as measurements would allow, and presumably extends to the channel wall. However, in natural flows, the drag from vegetation will tend to damp wave energy (see, e.g., Massel *et al.*, 1999) and there will be some attenuation length for the wave motion. The pressure wave response also occurs in the free stream beyond the vortex core (see figure 4-7*c* and *d* for extent) and is observable in frequency spectra as far toward the outer wall as measurements were made. In both the array and the free stream, the pressure wave response is due to the streamline curvature around the vortex core, which induces pressure oscillations in the far field as the wave train passes. This streamline structure is measured experimentally and will be shown in section 4.4.

More information about the characteristics of the fluctuations across experimental scenarios may be gained from the root mean square velocity fluctuations, $\langle u'^2 \rangle^{1/2}$ and $\langle v'^2 \rangle^{1/2}$. These are shown in figure 4-7 for array volume fractions in the range $\phi = 0.02$ to $\phi = 0.10$. From 4-7(a), the mean velocity varies within the array, decreasing with increasing ϕ. Outside the array, the distributions are nearly self-similar when scaled with the free channel velocity, U_2, a sign of the inner layer and outer layer separation. The relative local turbulence intensity, defined as the ratio between the fluctuation strength and the local velocity, $I = \langle u'^2 \rangle^{1/2}/U$ is shown in 4-7(b). In regions with large I, temporal fluctuations are large relative to the local mean velocity. Thus where $I > 0$, only within the array and only for the highest density cases, there is flow reversal during a significant portion of the oscillation period. From 4-7(*b*), the distributions of $I(y)$ collapse in the open region, but are highly dependent upon volume fraction within the array, $y < 0$. For the lowest density cases, $\phi = 0.02$ and $\phi = 0.045$, I never exceeds unity, suggesting very little, if any, flow reversal in the array. This is confirmed by many $u(t)$ time series observed within the canopy. However, for $\phi = 0.1$, the highest density, I is in the range between $1 - 2$ throughout the array, suggesting significant flow reversal. This is borne out by flow visualizations as well as by time series (see, e.g. figure 4-6(*c*)).

The increase in I with increased packing density is due primarily to the decrease in the mean velocity, $U(y)$, within the array, seen in (*a*). From (*b*) and (*c*), there also appears to be a slight reduction in u_{rms} and v_{rms} within the array. However, for all cases, the fluctuations are still significantly nonzero as far into the array as measurements were made (generally within 10 *cm* of the wall), illustrating the far-reaching effects of the pressure-induced oscillations, and demonstrating that U decreases faster than u_{rms} with increasing ϕ. Outside the array, there is a less marked change with ϕ in the strength of the fluctuations, the distributions of both $\langle u'^2 \rangle^{1/2}$ and $\langle v'^2 \rangle^{1/2}$ being comparable throughout the outer region. In particular, the $\langle v'^2 \rangle^{1/2}$ distributions collapse throughout much of the outer region. They also exhibit a distinct peak at the array interface, the magnitude of which is constant across the range of ϕ. The large value of $\langle v'^2 \rangle^{1/2}$ at the interface coincides with the region of maximum velocity shear, $\partial U / \partial y$, suggesting that the interface is a region of very strong Reynolds shear stress production.

4.2.4 Phase-Dependence of the Oscillatory Motion

While the power spectra give information about the dominant frequencies of the velocity fluctuations, they do not contain information about their relative phases. To measure the phase variations across the shear layer, an Acoustic Doppler Velocimeter (ADV) (SonTek, Inc.) was held fixed at a point near the array interface, $y = 0$ and simultaneous LDV measurements were taken at various points across the shear layer. The two point cross-correlation was then used to infer the velocity phase

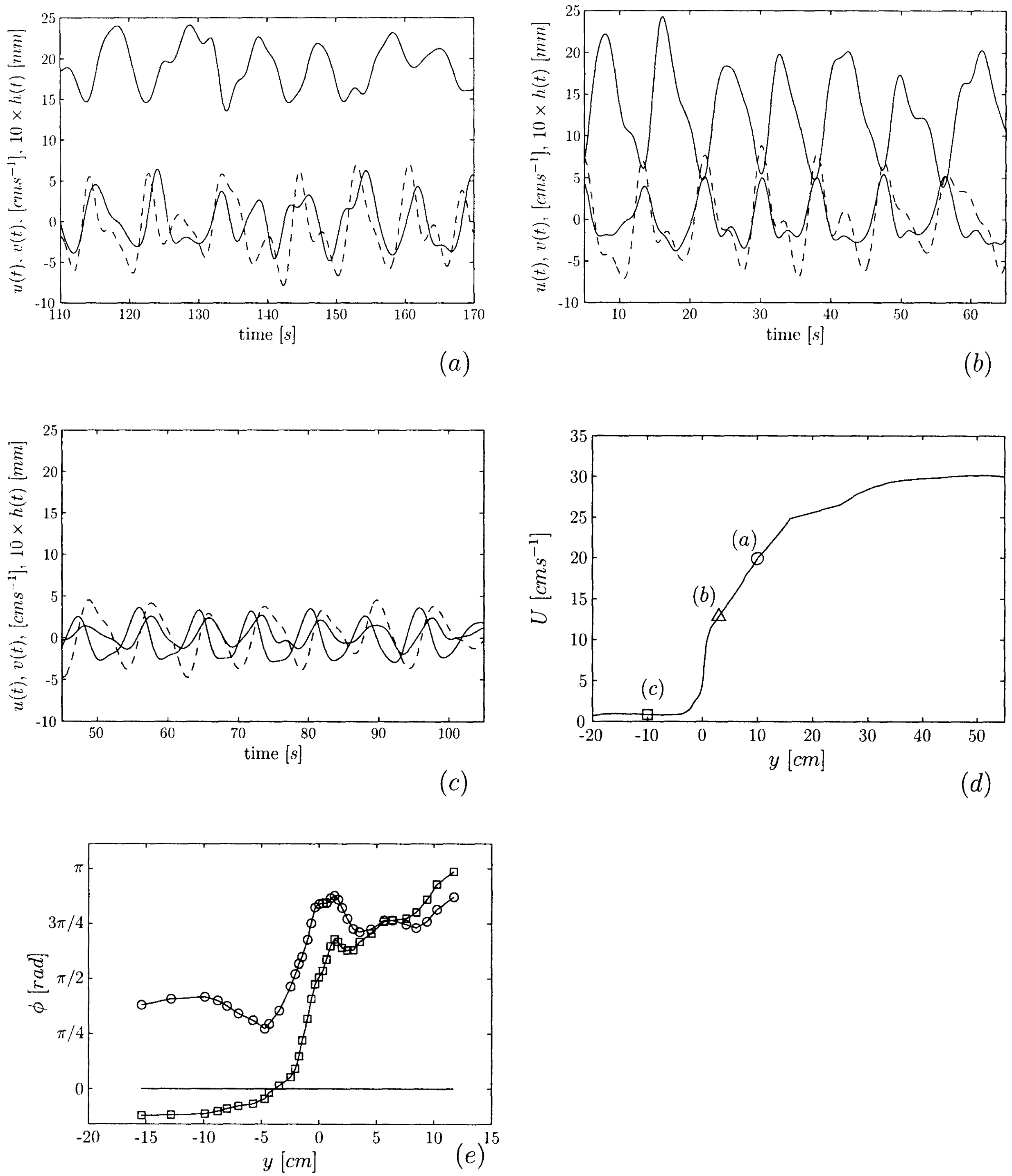

Figure 4-6: Time series of velocity and free surface fluctuations measured at various positions across the shear layer. $u(t)$, $v(t)$ (solid lines), and $h(t)$ (broken line) are shown for $y = 10$ cm (a), $y = 3$ cm (b), $y = -10$ cm (c) for case X; for reference these points are marked in (d) relative to the mean velocity distribution, $U(y)$: $y = -10$ cm (□), $y = 3$ cm (△) and $y = 10$ cm (○). In (e), phase shifts, ϕ, of $v(t)$ (○) and $h(t)$ (□), in radians, relative to the phase of $u(t)$ (solid line at $\phi = 0$).

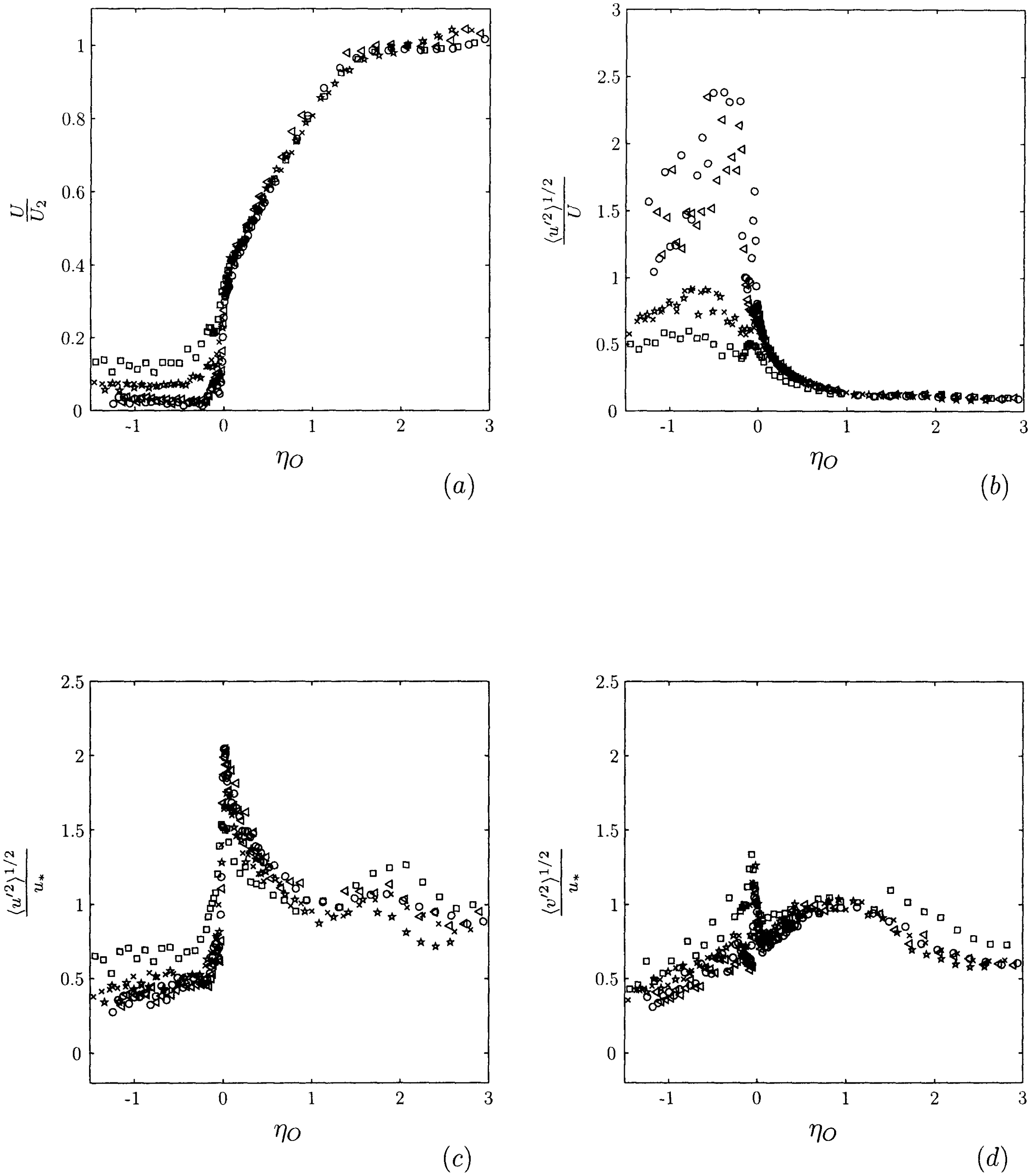

Figure 4-7: Transverse distributions of turbulent fluctuation strength with volume fraction, ϕ. Normalized velocity, U/U_2, shown in (*a*) for reference, local turbulence intensity, $\langle u'^2\rangle^{1/2}/U$ in (*b*), and normalized root mean square fluctuations, $\langle u'^2\rangle^{1/2}/u_*$ in (*c*) and $\langle v'^2\rangle^{1/2}/u_*$ in (*d*). Data ranges from sparse to dense packing densities: $\phi = 0.02$ (□), $\phi = 0.045$ ($\times$, $\star$) and $\phi = 0.1$ ($\circ$, $\triangleleft$). Symbols are as in Table 2.1.

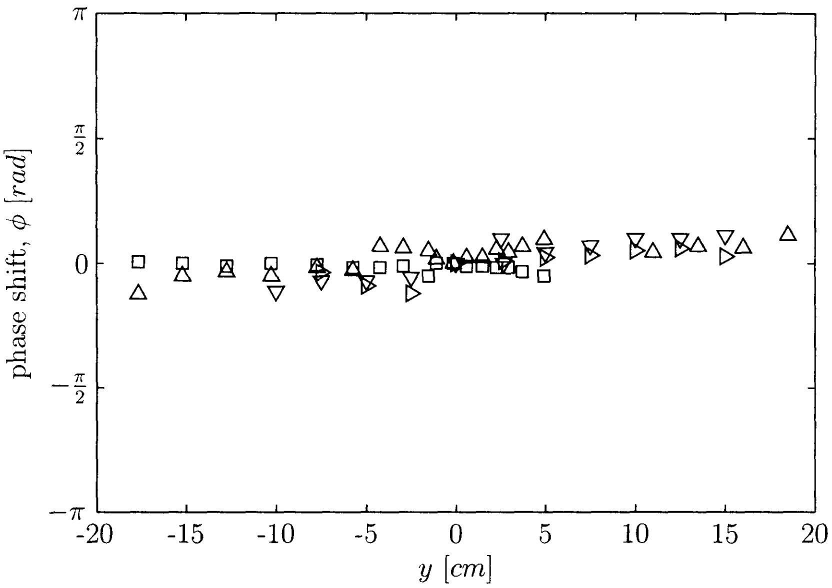

Figure 4-8: Relative phase shift, ϕ of $v(t)$ and $h(t)$ The phase shift across the layer is measured relative to a reference probe at $y = 0$. Case I ($\triangle$), case IV ($\triangledown$), and case V ($\triangleright$); and $h(t)$: case I ($\square$). Shift is measured in *radians* relative to the vortex cycle. Uncertainty is the sampling interval of the ADV, and is smaller than the data markers.

difference between the reference position and the other points. In one additional experiment, simultaneous measurements of surface displacement were made between the fixed reference position, and a set of positions across the shear layer. The cross-correlation of these measurements yielded the phase variation of the wave-like free surface oscillation.

Figure 4-8 shows the phase results for $v(t)$ for several experimental cases, and $h(t)$ for one particular case. The phase difference is measured in radians, relative to the mean period of the dominant oscillation found from spectral analysis, $T_d = 1/f_d$. The transverse velocity component is nearly in-phase across the entire shear layer for all cases. As described in the next section, taking advantage of the zero-phase-lag of $v(t)$ allows the vortex structure to be educed from individual velocity records by conditional sampling.

4.3 Coherent Structure Eduction

While the spectral distribution shows the characteristic time scales of the coherent structures, and the phase information gives some indication of their spatial extent, it is desirable to have quantitative details of the spatial velocity field. To accomplish this, and overcome the lack of spatial detail available from the single-point LDV measurements, techniques of coherent structure eduction were used. Eduction refers to the process of identifying coherent structures embedded in a turbulent time series measured at one or more discrete points in an experimental shear flow. Conditional sampling techniques are used to identify structures in the time series, with instantaneous flow properties such as vorticity (requires multi-point sampling) (Hussain & Hayakawa, 1987; Bisset *et al.*, 1990) or lateral velocity fluctuations (Bisset *et al.*, 1990) used as triggers for sampling. An extensive review and evaluation of structure eduction techniques is given in (Bonnet *et al.*, 1998).

The regularity of the nearly-periodic coherent structures in the present experiments made coherent structure identification a much simpler task than in many turbulent shear flows. The conditional sampling was done using the transverse velocity, $v(t)$, as the trigger, with a single structure identified as lying between two successive zero-crossings of the $v'(t)$ signal. In order to eliminate high frequency fluctuations, $v(t)$ was first band-pass filtered using a notch filter (Press *et al.*, 1992) centered around f_d. The results of the filtering and the identified zero-crossings are shown for a sample time series in figure 4-9. Between $10 < N < 20$ structures were identified for each individual position record, higher numbers corresponding to faster flows with a higher frequency of structure passage. In general, $N = 10$ was found to be sufficient number of samples to converge to the conditional average within a logistically reasonable sampling duration. The conditionally-averaged velocity at each position was obtained by an ensemble average over the N structures, following Hussain (1983):

$$\overline{\vec{u}}(t) = \sum_{i=1}^{N} \vec{u_i} \left(\frac{T_i}{T_d} t + t_{zi} \right) \tag{4.11}$$

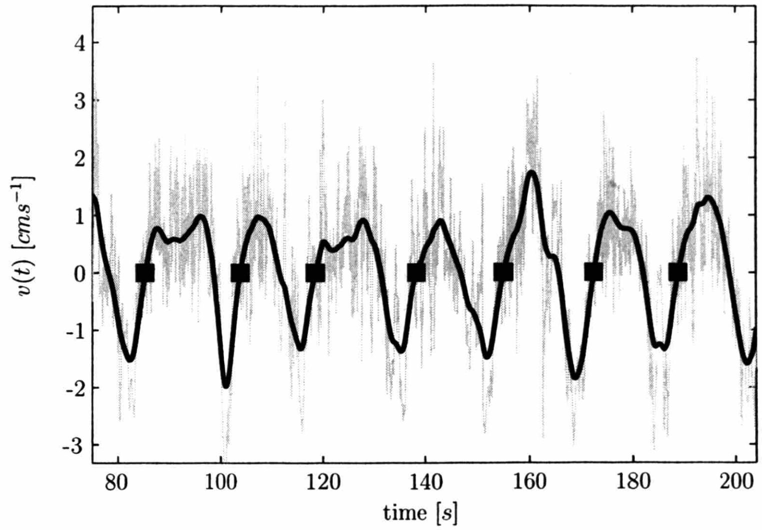

Figure 4-9: Representative time series of the transverse velocity, $v(t)$ with zero-crossings. Raw time series (gray), band-pass filtered (black), with zero crossings (■) used as the trigger for conditional sampling.

where $\vec{u}(y,t)$ is the instantaneous two-component velocity vector, t_{zi} is the absolute time at which the i^{th} zero crossing occurs, t is the time relative to the mean coherent structure period, $t \in [0, T_d]$, and the factor T_i/T_d stretches the i^{th} structure such that it has the same period as the mean. That is, the structures are phase-aligned, stretched onto the $[0, T_d]$ grid, and then averaged. This removes small scale fluctuations and phase jitter, but retains the large-scale structure. Note that the unfiltered velocity is used in the ensemble average, the filtered velocity being used only to identify zero-crossings.

The structure eduction and conditional averaging procedure is carried out for each position in each lateral transect. Then, in light of the zero-phase-lag of $v(t)$, the zero-crossings of $\overline{v}(t)$ for all transverse position-records are aligned. Note that this is the same as writing (4.11) as

$$\overline{\vec{u}}(y, t + \phi(y)) = \lim_{N\to\infty} \sum_{i=1}^{N} \vec{u_i}\left(y, t\frac{T_i}{T_d} + t_{zi}(y)\right) \tag{4.12}$$

with $\phi(y) = 0$. The result yields $\overline{u}(y,t)$ and $\overline{v}(y,t)$, the conditionally averaged spatially-dependent velocity components over a single period of the coherent struc-

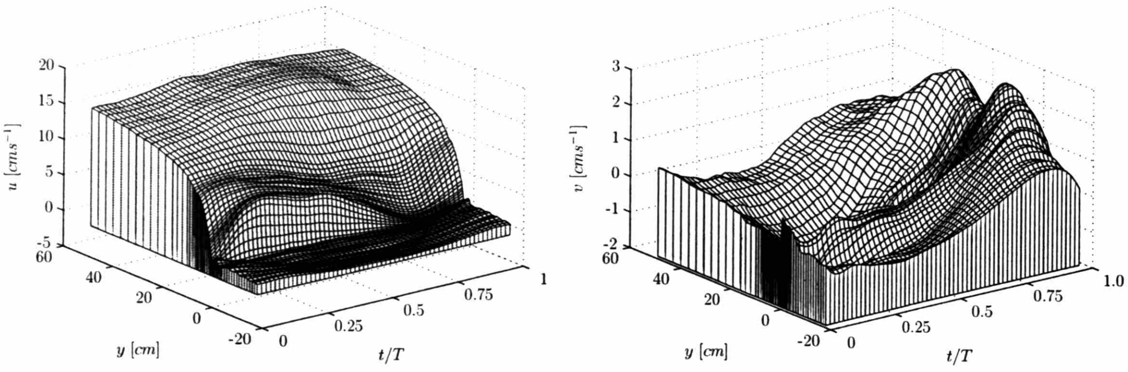

(*a*) (*b*)

Figure 4-10: Conditionally-averaged velocity components, $u(y,t)$ (a) and $v(y,t)$ (b) over one temporal period, T, of the dominant coherent structure. Averages are obtained by an ensemble average over N structure samples at each position, and aligned in the transverse direction by virtue of the zero-phase-lag result.

ture. These are shown in figure 4-10 for a representative case. The same conditional averaging scheme is used for turbulence quantities, such as the Reynolds stress. To gain yet more information about spatial velocity structure from figure 4-10, it is possible to make an approximation to convert the time coordinate to the streamwise ($x-$coordinate). This can be done using the Taylor hypothesis, often called the "frozen turbulence" hypothesis, which states that time record of flow at a fixed point can be regarded as due to the convection of a spatial pattern passing the point at a fixed velocity. Using the hypothesis, the coherent structure, with a passage speed of U_v, can be converted to a spatial frame of reference moving with the structure by the following transformation,

$$\tilde{x} = U_v(T_d - t), \quad t \in [0, T_d] \qquad (4.13a)$$

$$\tilde{u}(x_v, y) = \overline{u}(x_p, y, t) - U_v \qquad (4.13b)$$

where x_p is the streamwise coordinate of the fixed measurement point and $\tilde{x}$ and $\tilde{u}$ are the transformed spatial coordinate, and streamwise velocity.

Zaman & Hussain (1981) tested the accuracy of the Taylor hypothesis for coherent structure eduction from fixed point measurements in a shear flow. They determined that the spatial features of the coherent structure, such as vorticity and turbulence intensity, are accurately reproduced with the Taylor hypothesis provided (i) a single convective velocity equal to the structure passage speed is used for the transformation everywhere across the shear flow and (ii) structures are not undergoing rapid evolution or interaction between neighbors. The first condition has been strictly adhered to in all data analysis. The second condition holds when the flow has reached equilibrium and the dominant frequency, f_d, has locked in and is no longer evolving (see figure 4-4).

The structure passage speed was measured for a range of experimental conditions using simultaneous two-point surface displacement gauge measurements. Two gauges were separated by a fixed distance, D, in the streamwise direction, and time series were measured at each point, $h_1(t)$ and $h_2(t)$. The time necessary for the structure to travel between the probes is the time lag, τ, corresponding to the maximum of the cross-correlation sequence $max(\overline{h_1(t)h_2(t+\tau)})$. The structure passage speed is then

$$U_v = \frac{D}{\tau}. \tag{4.14}$$

In the next section, the structure of the velocity field in the frame of reference of the passing structures is discussed. From the structure, conclusions will be drawn about the dynamic role of the coherent vortices and their contributions to the overall energy and momentum balances in the shear layer.

4.4 Conditionally-Averaged Vortex Structure

The conditionally-averaged structure for a representative experimental condition (case I) is shown in figure 4-11. The structure is shown in a reference frame moving with the vortex passage speed, U_v, and the time axis has been converted to longitudinal coordinates using the Taylor hypothesis. Based on the observation that the vortex passage frequency scales with the outer layer width (section 4.2.2), the spatial coordinates are normalized by δ_O. The conditional average yields the structure over only a single cycle, and therefore, does not reveal the way two successive vortices are connected in a wave train. However, the continuity is demonstrated in the figure by repeating the structure over slightly longer than one period, demonstrating the head (the front) of the trailing vortex and the tail of the preceding vortex.

The structure shown in figure 4-11 is representative of those obtained across all experimental cases. Because of the transformation to the traveling vortex frame, the flow in the array, $y < 0$, and the flow in the open region are in opposite directions. Moreover, there exists a region of circular vortex motion, primarily in the open flow region ($y > 0$) with a width of approximately $2\delta_O$. The vortex is elongated in the streamwise direction, with a wavelength of approximately $10\delta_O$.

Figure 4-11(*b*) shows the sectional streamlines, the lines that are tangent to the velocity vectors at every point. These are not streamlines in the strict sense, as the divergence in the horizontal plane, being a two-dimensional slice of a three-dimensional flow, is not everywhere zero. However, the flow is predominantly two dimensional, with the water depth, $h \approx 5\ cm$, much less than the flume width, $B \approx 120\ cm$. The sectional streamlines delineate critical points in the flow, or points where the velocity, in the chosen reference frame, is zero. The topology around a critical point is determined by the eigenvalues of the local velocity gradient tensor, and reveals flow trajectories within the given frame of reference (see Perry & Chong, 1987).

The sectional streamlines in (*b*) demonstrate the existence of a vortex center and two saddle points, characteristic of the Kelvin cats eyes vortex train observed in free shear flows (Drazin & Reid, 1981). Interestingly, the topology around the vortex is that of an unstable focus, with trajectories spiralling outwards from the vortex center, in contrast to the more common stable focus (inward spiral). This is due to the presence of secondary circulations associated with shallowness, which will be discussed in section 5.8. Because of the viscous boundary layer, the vortex rotation is slower near the bed and pressure gradient draws fluid toward the center and up through the core. In the upper depths, the rotation rate is slightly faster, and the pressure gradient drives flow outward. This phenomenon has observed in other shallow flows, e.g., in the shallow wake study of (Fu & Rockwell, 2005). The sectional streamlines

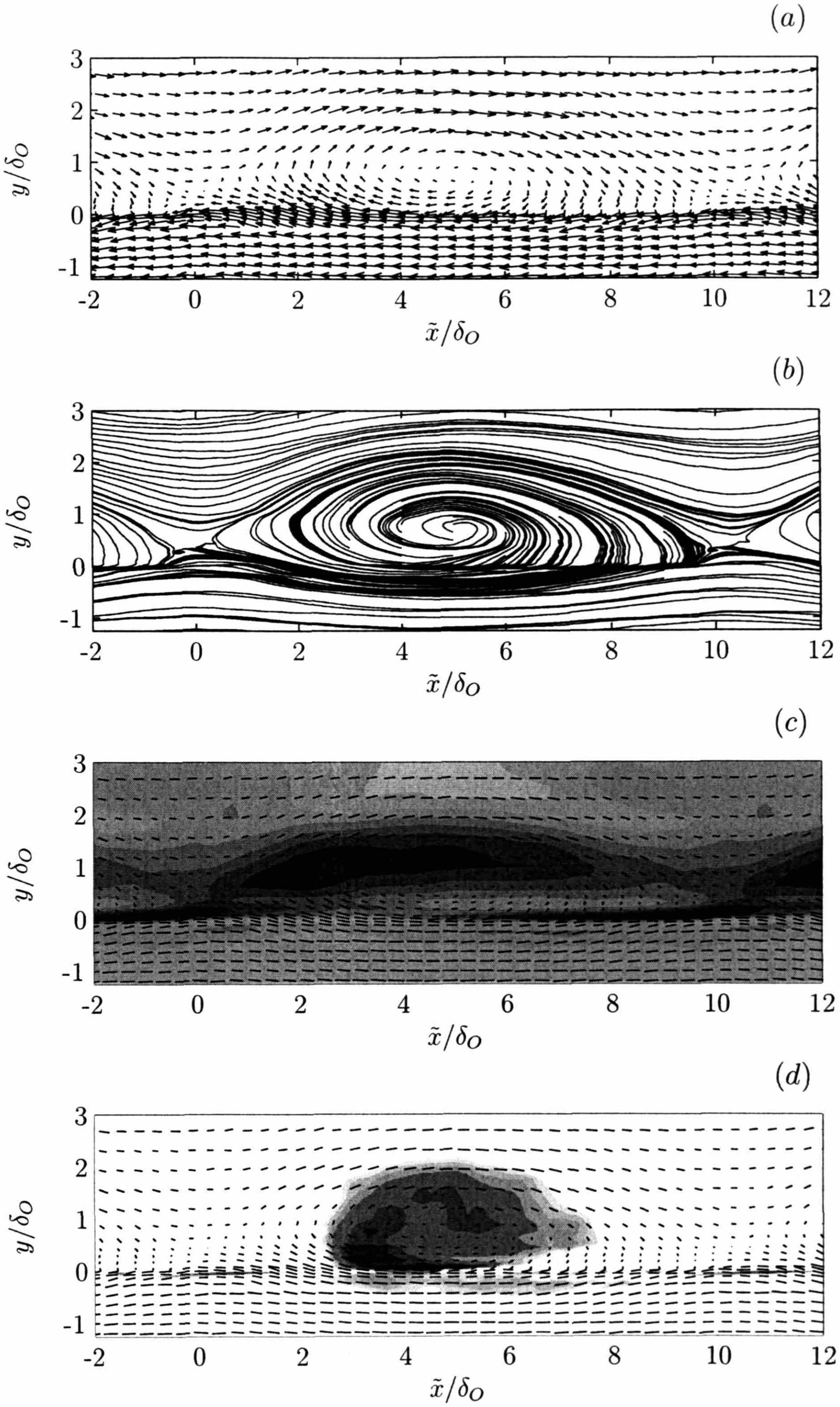

Figure 4-11: Structure of the conditionally-averaged flow for case I, in a frame moving with the passage speed. Velocity vectors (a) and sectional streamlines (b) are shown for slightly more than one period of the vortex structure. The head and tail of the structure are repeated to demonstrate overlap. In (c), the vorticity field, normalized by the inner layer shear, U_s/δ_I. Grayscale range is from 0 (white) to approximately 1 (dark). In (d), the swirl, λ_i, normalized by U_s/δ_I. Grayscale range is from 0 to approximately 0.3.

also demonstrate that while the core of the vortex resides almost entirely within the open region, there are oscillating streamlines much further into the array, and in the free steam outside the core. This illustrates the far field pressure wave discussed in section 4.2.3.

Figure 4-11(c) shows the distribution of conditionally-averaged vorticity,

$$\omega = \frac{\partial \overline{v}}{\partial x} - \frac{\partial \overline{u}}{\partial y} \tag{4.15}$$

which gives insight into the dynamics of the coherent structures. The vorticity is normalized by the maximum shear in the mean velocity profile, U_s/δ_I. The region of peak vorticity lies in the inner layer near the interface, $y = 0$, in the front of the vortex, between $x/\delta_O \approx 7$ and $x/\delta_O \approx 11$. The shear in this layer is enhanced by sweeps of high momentum, open region fluid carried by the vortex toward the interface. In contrast, at the tail of the vortex, between $x/\delta_O \approx 0$ and $x/\delta_O \approx 4$ there are strong ejections of low-momentum fluid originating in the array. The maximum cross-flow of the ejection occurs just ahead of the saddle. From 4-11(c) the ejections demarcate a region of strong vorticity that takes the form of a tongue ejected into the open region from the array interface, between $x/\delta_O \approx 1$ and $x/\delta_O \approx 6$. A tongue of nearly irrotational fluid, from $x/\delta_O \approx 4$ and $x/\delta_O \approx 9$, exists between the high-vorticity fluid and the array interface.

The existence of low-vorticity fluid within the vortex core region can be explained as follows. The high vorticity fluid originating in the inner layer and ejected into the free stream has a high degree of rotation. The rotation allows high momentum fluid from the free stream to be entrained into the vortex, resulting in a sweep toward the array. The high momentum fluid possesses lower vorticity because it originates in a region of the flow with lower shear ($\partial U/\partial y$). The disparity between the high-vorticity ejection (tail) region of the vortex and the low-vorticity sweep (front) is thus primarily due to the asymmetry in the streamwise velocity gradient between the inner layer (high shear) and outer layer (low shear). This disparity is not present, for example, in free shear layers for which the velocity profile is antisymmetric and the shear possesses only one length scale. The asymmetry also suggests a feedback mechanism which contributes to the maintenance of the vortices. By bringing high momentum fluid toward the array interface, the sweeps reinforce the high shear in the inner layer. This enhances the vorticity of the fluid ejected into the free stream, engendering a greater degree of rotation to the vortex. The result is more efficient entrainment of free stream fluid, and a more energetic sweep, thus maintaining the cycle.

Although the vorticity distribution illustrates vortex dynamics, it is not effective for demarcating the boundaries of the vortex core. This is because vorticity exists not only in the core, but in all regions of strong shear. While there is still some debate as to the precise definition of a vortex, Kline & Robinson (1989) give the following definition: "A vortex exists when instantaneous streamlines mapped onto a plane normal to the core exhibit a roughly circular or spiral pattern, when viewed in a reference frame moving with the center of the vortex core." Perhaps the best quantitative tool for identifying such regions uses the critical point concepts of Perry & Chong (1987) to define regions of "swirl". At any point in a two-dimensional flow, the deformation, or velocity gradient, tensor is

$$\mathbf{D} = \begin{bmatrix} \frac{\partial u}{\partial x} & \frac{\partial u}{\partial y} \\ \frac{\partial v}{\partial x} & \frac{\partial v}{\partial y} \end{bmatrix} . \tag{4.16}$$

If the determinant of this 2×2 matrix is negative, $\mathbf{D}$ will have two complex conjugate eigenvalues, $\lambda_r \pm i\lambda_i$. In this case, the trajectories defined by $\mathbf{D}$ will exhibit a spiral motion, around a central focus, with the λ_i representing the strength of the swirl (Adrian *et al.*, 2000). Note that λ_i has the same units as vorticity, $[time^{-1}]$.

The distribution of swirl is shown in Figure 4-11(d), along with the velocity vectors. The central core of the vortex is delineated by the swirl distribution. The region of positive λ_i extends up to $2\delta_O$ into the outer region, and coincides with the region in which the velocity vectors in 4-11(a) appear circular. The maximum of λ_i occurs in the ejection region, with lower values in the sweep region. This suggests that the most intense rotation is associated with the low-momentum ejections. This is consistent with the preceding discussion of the vorticity dynamics. However, because it does not reflect regions of strong shear outside the central core, λ_i is a more effective metric than vorticity for making comparisons of vortex size and relative strength across different experimental cases. This will be done in the following section.

4.4.1 Comparison of Velocity Structure across Experimental Configurations

Sectional Streamlines

In figures (4-12)-(4-13) the structure of the conditionally-averaged vortex field is compared across different experimental cases. Cases I ($Re = 5.1 \times 10^4$, $\phi = 0.02$), VII ($Re = 5.1 \times 10^4$, $\phi = 0.10$), and V ($Re = 1.2 \times 10^4$, $\phi = 0.045$) are chosen for comparison as they are representative of the span of the parameter range in both Reynolds number and cylinder volume fraction. Figure 4-12 shows the sectional streamlines over one wavelength of the coherent motion in a frame moving with the vortex passage speed. The wavelength, L_v, is seen to be comparable across all three cases, with an approximate value $\mathrm{L}_v/\delta_O \approx 10$. In each case, the vortices exist almost entirely in the open region, extending between 1 to 2 δ_O into the free stream. The consistency across experimental conditions, suggests the scaling of the wavelength and width with δ_O is sound.

Vortex Dimensions

The size of the vortex central region can be obtained from the swirl eigenvalue, λ_i, shown in figure 4-13$(a-c)$. The $\lambda_i > 0$ contours are shown in grayscale, denoting the vortex core for each experimental case. For cases I $(4-13a)$ and VII $(4-13b)$, which represent identical Re and main channel conditions, but, respectively, sparse ($\phi = 0.02$) and dense ($\phi = 0.1$) arrays, $\lambda_i > 0$ is similar in magnitude and extent of the distribution. However, the lower Re case (V) exhibits a more disorganized core and more elliptical structure. Results from section 2.5.9 showed that the interfacial friction coefficient, a measure of the momentum transport effectiveness of the coherent

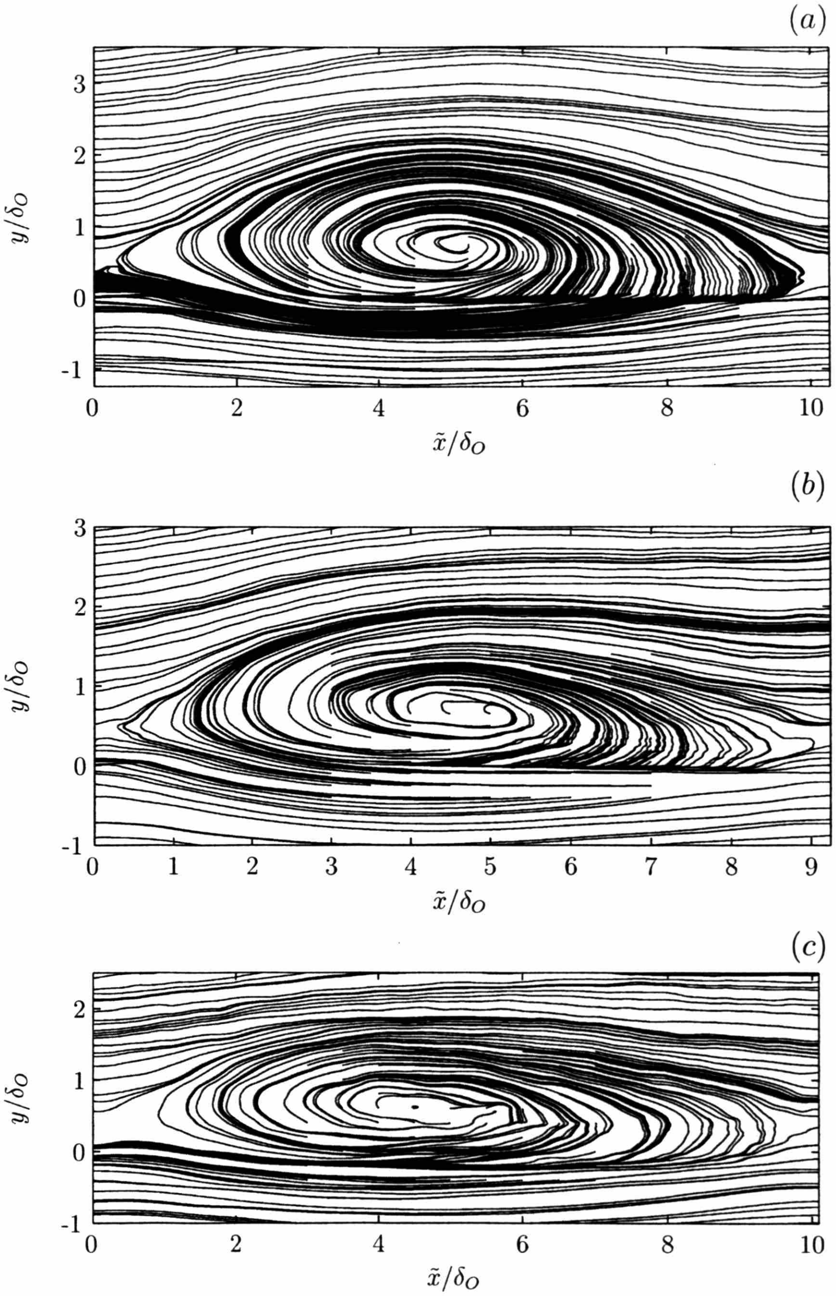

Figure 4-12: Sectional streamlines of the conditionally-averaged flow for three different cases: case I ($Re = 5.1 \times 10^4$, $\phi = 0.02$) (*a*), case VII ($Re = 5.1 \times 10^4$, $\phi = 0.10$) (*b*), case V ($Re = 1.2 \times 10^4$, $\phi = 0.045$) (*c*). Streamlines are shown over one vortex wavelength and the Taylor hypothesis is used to convert time to longitudinal distance. The $x-$ and $y-$ coordinates are both normalized by the outer layer width, δ_O, for each case and are plotted on the same scale.

structures, was diminished for the low *Re* experimental cases. This is likely due to a greater role in viscous stresses from the bed at low *Re*, which contributes to a less organized vortex core.

From the distribution of λ_i, the vortex aspect ratio, the ratio of width to wavelength, can be compared across experimental cases. The width, b, for each case was determined by plotting the transect of λ_i on the line intersecting the vortex center, demonstrated in figure 4-14(a), and plotted for each case in 4-14(b). The distribution of λ_i shows considerable variability across cases within the array ($y > 0$). This due predominantly to the spatial heterogeneity on the cylinder scale. However, each case shows a peak in λ_i at the interface, $y = 0$, and a broad distribution in the open region, where the vortex predominantly resides. The width of the vortex core for each case was measured as the distance between the interface and the position in the open region at which λ_i decays to zero (the first zero-crossing). The width is generally consistent across experimental cases, and the mean result is $b/\delta_O = 2.2 \pm 0.2$. The wavelength, also consistent across cases is $L_v/\delta_O = 9.1 \pm 1.1$. Taken together, these give an aspect ratio of $b/L_v = 0.24 \pm 0.05$.

It is interesting to compare this result with vortices typically observed in free (unbounded) shear flows. Several authors (Browand & Weidman, 1976; Pierrehumbert & Widnall, 1982) have found that the organized vortices that form in a mixing layer downstream of a splitter plate are well-described by Stuart vortices, a family of solutions to the steady-state Euler equations, which have a streamfunction,

$$\psi = \frac{1}{2}\ln(\cosh 2y - \rho\cos 2x). \tag{4.17}$$

The best comparison with observations of shear layer vortices in terms of the vorticity distribution is obtained for $\rho = 0.25$ (Pierrehumbert & Widnall, 1982). It is straightforward to compute the deformation matrix and thus find the distribution of λ_i for the Stuart vortex. Defining the width, b, as the point along the vortex center transect at which λ_i is reduced to 10% of its value at center, the aspect ratio for a Stuart vortex with $\rho = 0.25$ is $b/L_v = 0.54$ (if the width criterion is changed from

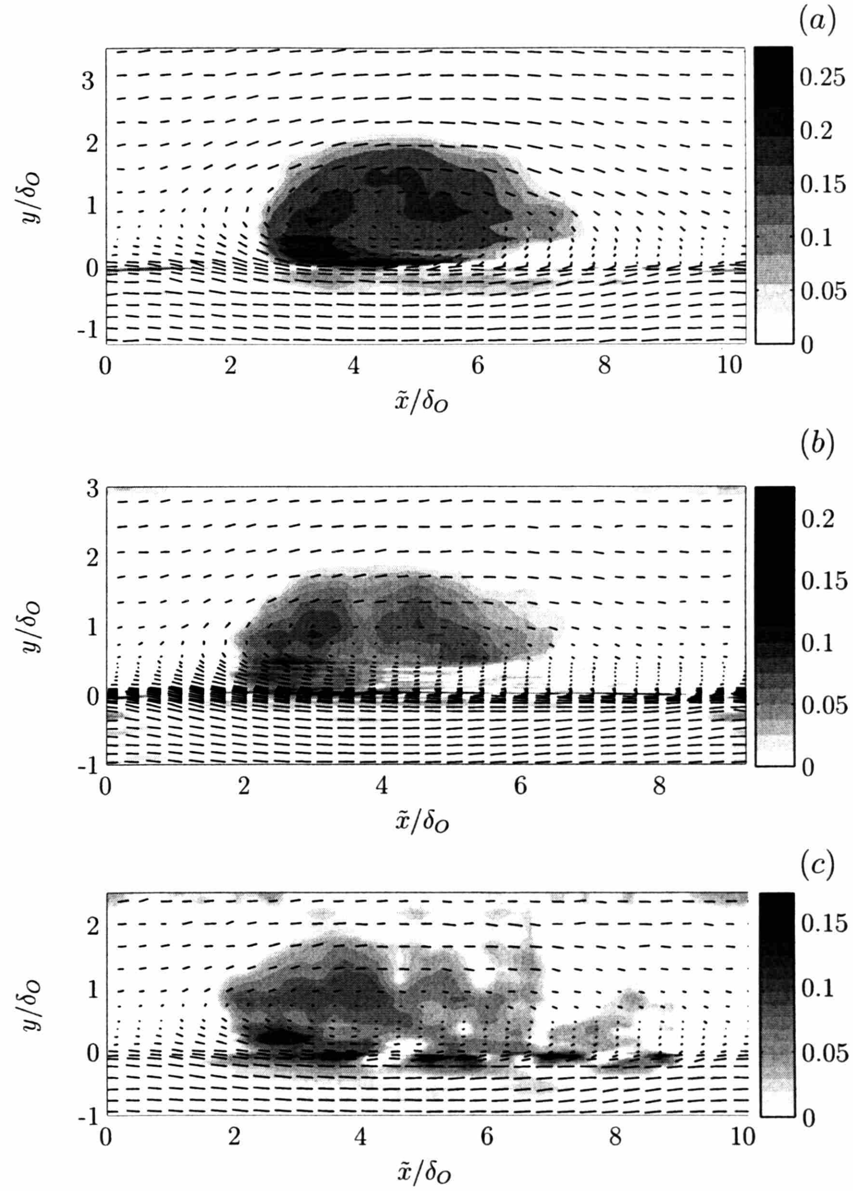

Figure 4-13: Distribution of the local swirl, λ_i, for experimental cases I: $\phi = 0.02$, $Re = 5.13 \times 10^4$ (a), VII: $\phi = 0.1$, $Re = 5.1 \times 10^4$ (b) and and V: $\phi = 0.045$, $Re = 1.2 \times 10^4$ (c). Grayscale shading shows the $\lambda_i > 0$ contours. Vector plots are shown for reference.

λ_i to vorticity decay, the aspect ratio is nearly identical, $b/L_v = 0.52$). The decay length scale is used instead of a zero-crossing, as with the experimental data, because the analytical solution for the Stuart vortex decays asymptotically to zero.

Returning to the present experiments, the vortices, with aspect ratio $b/L_v = 0.24$, are more elongated by at least a factor of two than those observed in free shear flows. It appears that this disparity is due to a difference in the natural frequency. In section 4.2.2 the frequency of oscillation from experiments, f_d, was shown to equal the natural frequency of a free shear layer from linear stability theory, $f_n = 0.032\overline{U}/\theta$. The frequency can be written in terms of the passage speed and wavelength,

$$f_d = 0.032\frac{\overline{U}}{\theta} = \frac{U_v}{L_v} \tag{4.18}$$

and it follows that the aspect ratio is constrained by

$$\frac{b}{L_v} = 0.032\frac{\overline{U}}{U_v}\frac{b}{\theta}. \tag{4.19}$$

The mean passage speed from experiments is $U_v/\overline{U} = 1.1 \pm 0.1$, while the ratio $b/\theta \approx 7.7$. A rough estimate from (4.19) yields $b/L \approx 0.22$ consistent within error with the directly measured value, $b/L_v \approx 0.24$.

The Stuart vortex, with aspect ratio $b/L_v = 0.54$, $b/\theta = 6.5$, and $U_v = \overline{U}$ by necessity has a dimensionless frequency

$$f_d\frac{\theta}{\overline{U}} = \frac{U_v}{\overline{U}}\frac{b}{L_v}\frac{\theta}{b} = 0.080, \tag{4.20}$$

which is approximately 2.5× the value, 0.032, from linear theory, and thus accounts for the larger aspect ratio, b/L_v. Similarly, Browand & Troutt (1985) in a high Reynolds number ($Re_\theta = O(10^4 - 10^5)$) mixing layer found a dimensionless frequency approximately twice the value from linear theory. However lower values of the dimensionless frequency were found experimentally by Winant & Browand (1974) in a low Reynolds number ($Re = 50 - 1000$) mixing layer ($f_d\theta/\overline{U} = 0.044$) and by Hussain & Zaman (1985) in a mixing layer originating from a fully turbulent boundary

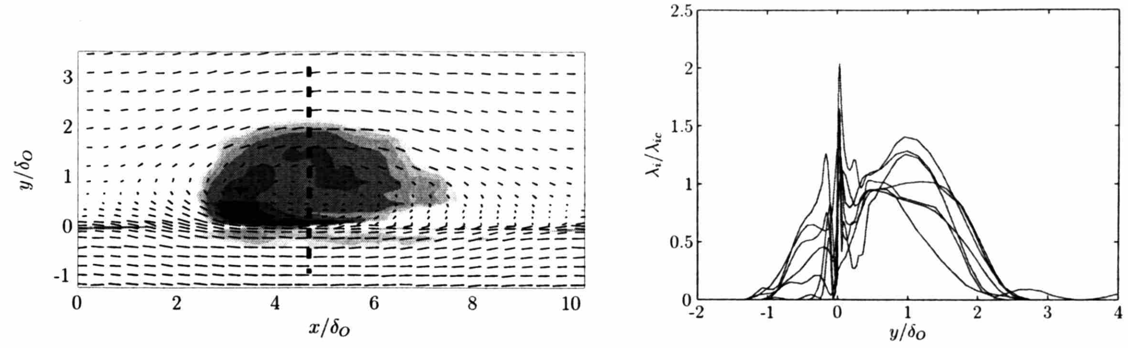

(*a*) (*b*)

Figure 4-14: Comparison of the vortex width across experimental cases. The width is measured by the transect of λ_i on the line intersecting the vortex center (demonstrated in (*a*)). Transects for each available experimental case (VII, X, I, II, III, IV, V) are plotted together in (*b*), normalized by the value at the vortex center, λ_{ic}. The vortex width is taken as the first zero-crossing of λ_i.

layer ($f_d\theta/\overline{U} = 0.024$). Thus it appears that unforced free shear layers exhibit significant variance in the fluctuation frequency. This variance for free shear layers lends even greater relevance to the excellent agreement with linear theory observed in the present experiments in the shallow vegetated shear layer and those of Ghisalberti & Nepf (2002) in a submerged canopy. While the results from free shear layers are too numerous and varied to suggest specific reasons for their disagreement with linear theory, they all have in common continuous downstream development and absence of an equilibrium frequency. It is suggested that the equilibrium in the present case is one possibility for the excellent agreement with linear theory, i.e., if conditions favor an equilibrium frequency, it is most natural for that frequency to be the most unstable mode from linear theory.

4.5 Influence of the Coherent Structures on Momentum Transport

Having established the presence and characteristics of the coherent structures, their influence on the dynamics of the shear layer can be examined. Results will show that the coherent vortices are the dominant contributors to the transport of momentum across the shear layer, shaping both its spatial development and its equilibrium structure.

4.5.1 Quadrant Contributions to the Reynolds Stress

As a first step, time series of both velocity components, $u(t)$ and $v(t)$ along with the instantaneous momentum flux, $u'v'(t)$ are shown in figure 4-15 at three different positions across a representative experimental shear layer transect. In each of the time series, the regularity of the velocity fluctuations make the presence of the coherent structures readily apparent. It is customary to divide the contributions to $u'v'$ into quadrants in the (u', v') plane (Raupach, 1981; Nakagawa & Nezu, 1977; Grass, 1971). Instantaneous contributions from quadrant II ($u' < 0, v' > 0$), outward fluxes of low momentum fluid originating in the array, are termed ejections; contributions from quadrant IV ($u' > 0, v' < 0$), inward fluxes of high momentum fluid originating in the outer region, are termed sweeps. Together, contributions from quadrants I and III represent counter-gradient transport, or fluxes in the direction of the mean velocity gradient. In each plot sweep events are labeled "Sw", ejections "Ej", and counter-gradient fluxes "CG".

Shown in 4-15(b) are time series for the position $y = 3\ cm$, lying just outside the array edge, within the central vortex region. The fluctuations $u'(t)$ and $v'(t)$ are antiphase, with sweep and ejection events leading to strong correlations (negative $u'v'(t)$) and strong fluxes of momentum. At the interface, $y = 0$, shown in 4-15(d), ejections and sweeps are still the predominant dynamic events ($u'v' < 0$), but small counter-gradient fluxes ($u'v' > 0$) regularly appear in the latter half of the ejection phase. The fluctuations deep within the array, shown in 4-15(c), are of a fundamentally different nature. Here the $u-$ and $v-$ components are close to $\pi/2$ out of phase. As a result the $u'v' < 0$ events approximately cancel the $u'v' > 0$ events, and the net momentum transport is exceedingly small. The difference between the momentum transport inside and outside the array can be understood in terms of the vortex/wave properties of the coherent structures discussed in section 4.2.3. In the vortex central region the velocity fluctuations are phase correlated, while in the far

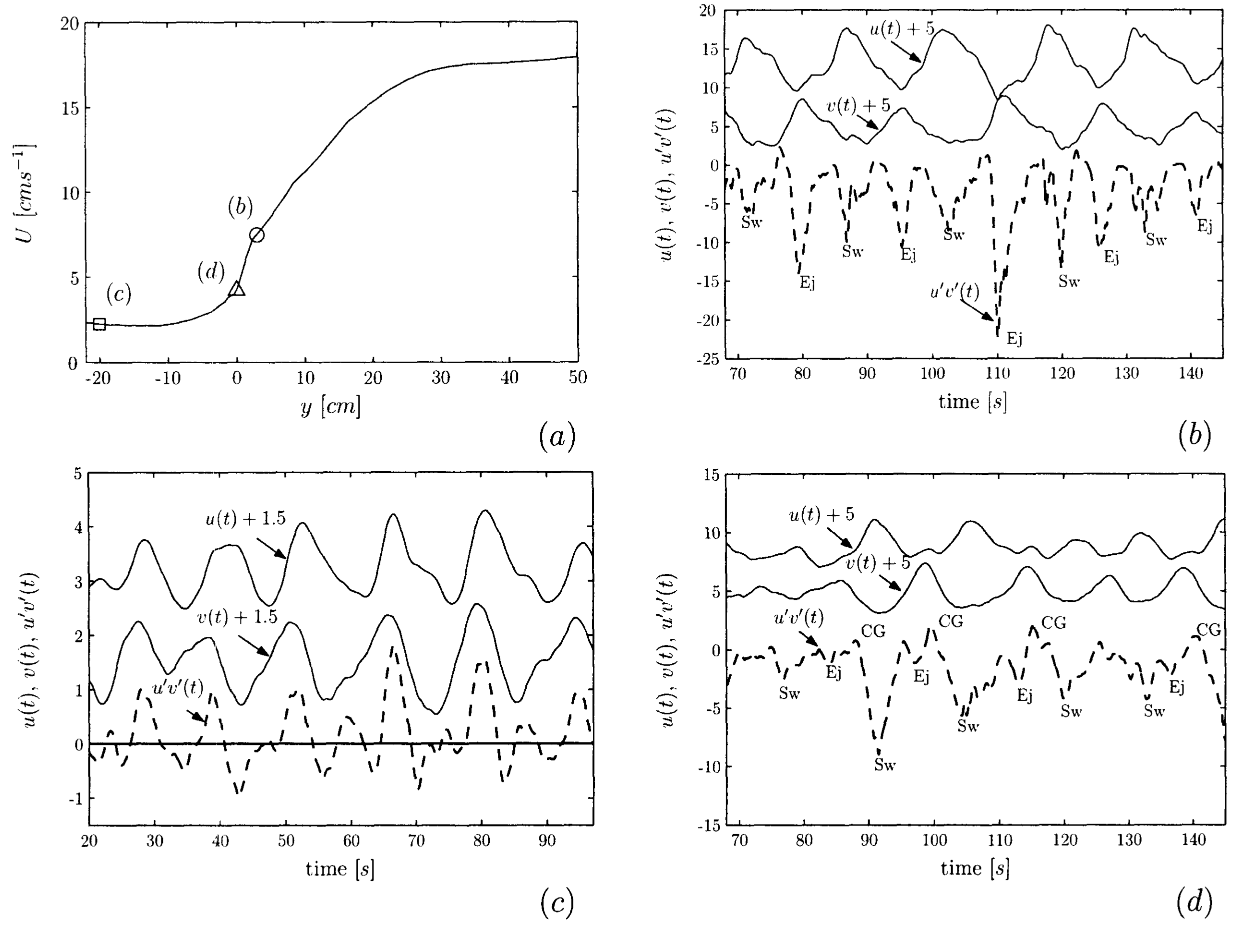

Figure 4-15: Time series of velocity components, $u(t)$ and $v(t)$, and instantaneous Reynolds stress, $u'v'(t)$ for three different positions in the shear layer (case I). (a) shows the mean velocity profile, $U(y)$, with the positions marked for reference. (b) is taken from a position just outside the array, $y = 3$ cm; (c) is from deep in the array, $y = -20$ cm, and (d) is from the array edge, $y = 0$. Velocity fluctuation events and corresponding correlations, $u'v'(t)$ are labeled according to quadrant; "Ej" denoting quadrant II, "Sw" quadrant IV and "CG" quadrant I and III events.

field pressure-wave region outside the core, the fluctuations are uncorrelated.

4.5.2 Spatial Structure of the Reynolds Stress

Insight into the contribution of the coherent structures to the overall momentum transport can be gained by examining the conditionally-averaged Reynolds stress. The conditional average, $\widetilde{u'v'}(\tilde{x}, y)$, is defined as in (4.11), in contrast to the temporal mean, $\langle u'v'(y)\rangle$. Figure 4-16 shows the spatial dependence of the conditionally-averaged Reynolds stress, normalized with u_*^2. The three plots, representing a range of packing densities and Reynolds numbers, exhibit qualitatively identical structure. As a representative, consider the $\phi = 0.02$ case shown in 4-16(a). The Reynolds stress maxima are located in regions of strong crossflow, the inflow region near the vortex front and the outflow region near the tail, and are located just outside the array interface. These regions correspond to the sweep and ejection phases of the conditionally-averaged structure and are responsible for the instantaneous momentum fluxes observed in figure 4-15. The ejection region makes a greater contribution to the net momentum transport (higher $u'v'$ maximum) than the sweep region. The fraction of stress carried by the ejections relative to the sweeps is quantified by the quadrant analysis of section 4.6.2.

The maxima of $\langle u'v'\rangle$, just outside the array interface, coincide with regions of high velocity shear, $\partial U/\partial y$. This is indicative of gradient driven momentum flux. More importantly, it implies a high rate of turbulent energy production at the interface, $\langle P\rangle = -\langle u'v'\rangle \partial U/\partial y$. As discussed in section 4.4, the vortex sweep enhances the velocity gradient at the interface by bringing high momentum fluid into contact with low momentum fluid. This results in large local value of $\langle u'v'\rangle$, leading to enhanced energy production. It is proposed that through this mechanism the vortex is able to feed its own energy production.

Both within the array, and beyond the vortex core in the open region, there exist alternating regions of co-gradient and counter-gradient momentum flux. These regions alternate along the streamwise axis, but are antisymmetric about the array interface. Within the array, the countergradient fluxes correspond to the "CG" events identified in figure 4-15(d). However, the magnitude of $\langle u'v' \rangle$ in these regions is small relative to the co-gradient sweeps and ejections.

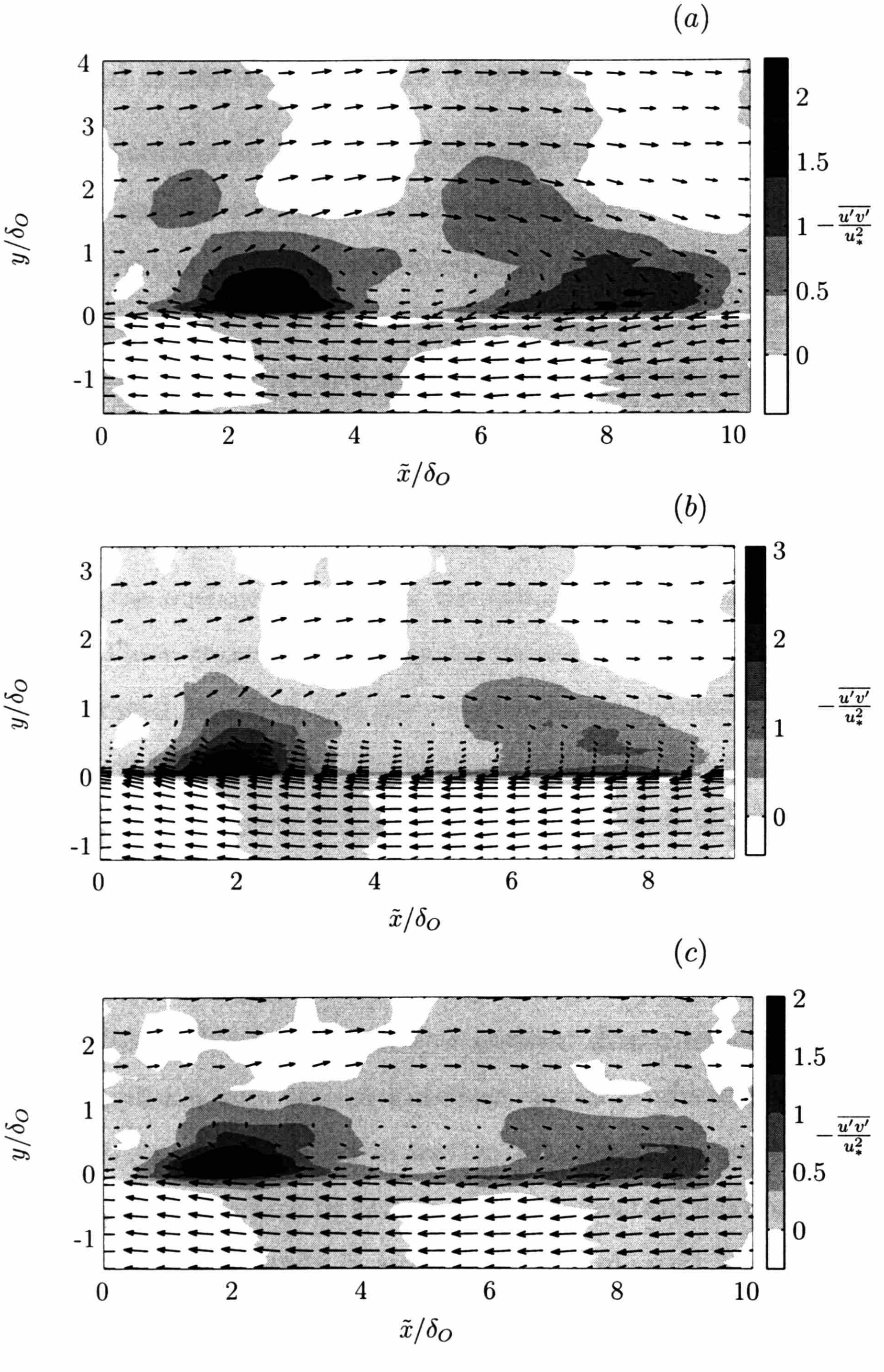

Figure 4-16: Spatial contours of the conditionally-averaged Reynolds stress over one coherent structure cycle for cases I (*a*), VII (*b*), and V (*c*). The magnitude of $-\overline{u'v'}/u_*^2$ corresponding to the grayscale levels is shown in the legend. Areas of white represent $-\overline{u'v'} < 0$, or regions of counter-gradient momentum transport. Velocity vectors are shown for reference

4.6 Influence of Coherent Structures on Turbulence Characteristics

Prior sections have established the spatial structure of the coherent vortices and related the sweep and ejection cycles of the Reynolds stress to that structure. In this section, experimental results for several common turbulence parameters are presented and interpreted in light of the coherent structures. Measurement of these parameters facilitates comparison with results from other shear flows, particularly rough boundary layers and free mixing layers.

4.6.1 Momentum Transport Efficiency

For reference, distributions of the time-averaged Reynolds stress, $\langle u'v' \rangle$ and the turbulent kinetic energy (TKE), $k = \frac{1}{2}(\sigma_u^2 + \sigma_v^2)$ are shown in figure 4-17(*a*) and (*b*) for cases spanning the range of packing density studied. Each distribution collapses reasonably well within the outer region, in accordance with the outer layer similarity discussed in section 2.5.6. Moreover, both $\langle u'v' \rangle$ and k peak near the interface, $y = 0$, near the shear and TKE production maximum. The Reynolds stress decays to zero at the outer shear layer edge ($\eta_O \approx 2$) and within a very short distance into the array. However, k persists, due to the wave-like oscillatory flow induced outside the vortex core (see section 4.2.3).

A common measure of the efficiency of turbulent momentum transport is the ratio of Reynolds stress to the TKE,

$$a_1 = \frac{-\langle u'v' \rangle}{\frac{1}{2}(\sigma_u^2 + \sigma_v^2)}. \tag{4.21}$$

Boundary layers exhibit a nearly universal distribution (Bradshaw, 1967; Bandyopadhyay & Watson, 1988), with a constant $a_1 \approx 0.3$ throughout the boundary layer. In mixing layers, Townsend (1976) gives a value that is slightly higher, approximately 0.34, but does not specify anything about the distribution. From figure 4-17(*c*), a_1 peaks immediately outside the interface with a value very close to 0.3, consistent with the boundary layer and mixing layer results. Bandyopadhyay & Watson (1988) reported that a_1 was slightly lower for rough walls compared with smooth walls, and suggested that small-scale turbulence generated by roughness elements contributes proportionally less to to the total shear stress than the large structures which scale with the boundary layer width. Similarly, the present results are slightly lower for the highest density ($\phi = 0.10$) cases, reduced from about 0.32 to 0.24, very similar to Bandyopadhyay & Watson, figure 3 ($a_1 \approx 0.30$, smooth; $a_1 \approx 0.25$, rough). The higher cylinder density produces more wake-scale turbulence, but the reduction in a_1 suggests that the wake turbulence increases the TKE, without appreciably increasing momentum transport, i.e., k increases, but $\langle u'v' \rangle$ does not increase proportionally. This is reasonable because the turbulent length scale associated with the element wakes is much less than that of the coherent structures. Also note that the large scatter in a_1 within the array, $y < 0$, is due to the cylinder-scale heterogeneity in turbulence structure. When a spatial average is taken over cylinder spacing scale, the mean of a_1 becomes zero within the array. This is consistent with the pressure-wave nature of the oscillations in the array, which produce fluctuations, and thus contribute to the measured value of k, but produce very little Reynolds stress.

Another measure of the momentum transport efficiency of the coherent structures is the correlation coefficient, defined as

$$R = -\langle u'v' \rangle / \sigma_u \sigma_v. \tag{4.22}$$

The distribution of R, shown in figure 4-17(d), is qualitatively similar in structure to that of a_1, not surprising since they both measure momentum flux relative to fluctuation strength. These results can be compared with the rough boundary layer data of Raupach (1981); Nakagawa & Nezu (1977), in which $R \approx 0.4$ over much of the boundary layer width. In contrast, in 4-17(d) R peaks just outside the array interface, and declines almost linearly to its value of zero outside the boundary layer. The decay is due, as the decay of a_1, to the persistence of the vortex-induced oscillations well beyond the region in which they generate Reynolds stress.

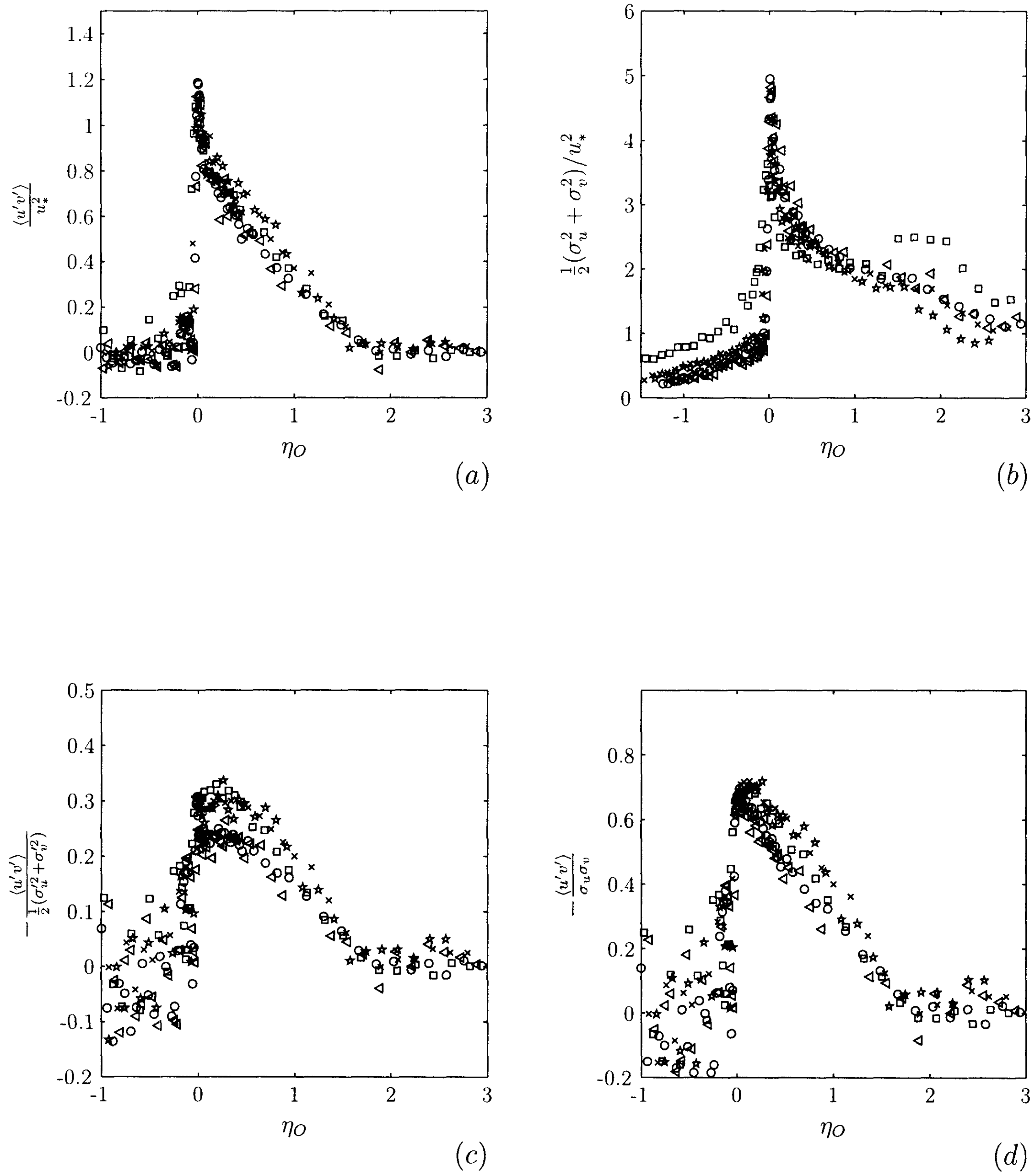

Figure 4-17: Efficiency of momentum transport. Reynolds stress (a), turbulent kinetic energy (b), the ratio of Reynolds stress to turbulent kinetic energy, $a_1 = -\langle u'v' \rangle/(\sigma_u^2/2 + \sigma_v^2/2)$ (c), and the correlation coefficient, $R = -\langle u'v' \rangle/\sigma_u \sigma_v$ (d) for experimental cases ranging from sparse to dense packing densities–symbols are the same as in Table 2.1.

The peak value of the correlation is $R \approx 0.7$, significantly higher than the peak of $R \approx 0.4$ observed in boundary layers, and the value of $R \approx 0.5$ from mixing layers (Townsend, 1976, Table 4.1). This suggests the Reynolds stress generation near the interface is more efficient than the production either near a solid boundary or in a free shear layer. However, this result is in apparent conflict with the good agreement of the a_1 peak with boundary layer and mixing layer results. While a_1 and R both measure efficiency, their dependence on σ_u and σ_v is different. Comparing (4.22) with (4.21) it can be seen that differences between R and a_1 are related to the degree of isotropy between σ_u and σ_v. For isotropic turbulence, i.e., $\sigma_u = \sigma_v$, it follows that $a_1 = R$, but for anisotropy, $R > a_1$. The higher value of R in the present experiments thus suggests a greater degree of anisotropy than in either boundary layers or mixing layers. This can be confirmed by inspection of figure 4-7*c* and *d*, which shows that $\sigma_u = \langle u'^2 \rangle^{1/2}$ is larger than $\sigma_v = \langle v'^2 \rangle^{1/2}$ throughout the shear layer. Specifically, the ratio R/a_1 is

$$\frac{R}{a_1} = \frac{\frac{1}{2}(\sigma_u^2 + \sigma_v^2)}{\sigma_u \sigma_v}. \tag{4.23}$$

From figure 4-7*c* and *d* the peak of σ_u/u^* is approximately 2 and the peak of σ_v/u^* is approximately 1.2, while from figure 4-17*b*, the peak of $(\sigma_u^2+\sigma_v^2)/2$ is approximately 5. Thus from (4.23), R/a_1 is approximately 2, and this is what is observed ($R_{max} \approx 0.7$ and $a_{1,max} \approx 0.3$).

4.6.2 Stress Fractions Through Quadrant Analysis

The fractional contributions of sweeps and ejections to the net momentum transport can be measured by quadrant analysis. As previously defined, the sweep contribution is $\langle u'v' \rangle|_{IV}$ and the ejection contribution is $\langle u'v' \rangle|_{II}$, where angle brackets represent the long-time averaging procedure and the subscripts represent the quadrant-dependent conditional sampling,

$$\langle u'v' \rangle_i = \lim_{T \to \infty} \frac{1}{T} \int_0^T u'(t) v'(t) I_i dt \tag{4.24a}$$

$$I_i = \begin{cases} 1, & \text{if } (u', v') \text{ is in quadrant } i \\ 0, & \text{otherwise.} \end{cases} \tag{4.24b}$$

One measure of the relative importance of sweeps and ejections is the stress differential, the difference between the net contributions from quadrants II (ejections) and IV (sweeps),

$$\Delta S = \frac{\langle u'v' \rangle_{II} - \langle u'v' \rangle_{IV}}{\langle u'v' \rangle_{y_o}}, \tag{4.25}$$

where the normalization is by the peak Reynolds stress, $\langle u'v' \rangle_{y_o} = -u_*^2$. Figure 4-18($a$) shows the relative contributions of $\langle u'v' \rangle_{II}/u_*^2$ and $\langle u'v' \rangle_{IV}/u_*^2$ for several experimental cases. The distribution of sweeps and ejections are similar, both peaking near the interface, but, importantly, sweeps are more prevalent. This is more clearly demonstrated by the stress differential, ΔS, shown in 4-18(b). In general, there is a thin region within the array near the interface in which sweeps are the dominant stress producing events, while a broader region exists outside the array in which stress from ejections is more prominent.

The relative contributions of these two modes of momentum transport are consistent with the picture of the coherent structures. The vortices create strong bi-directional flows normal to the interface. Because the velocity inflection point is near the interface, the maximum gradient, $\partial u/\partial y$, is to the channel side of points within the array, but to the array side of points outside the array. As a result, sweeps from the channel side constitute the largest momentum flux for the array, and ejections from the array constitute the largest flux in the open region. However, there is an asymmetry, because the penetration of sweeps is limited by array drag. By comparison, ejections, opposed only by the small effect of bed friction, extend further into the main channel, leading to a broader distribution of ΔS outside the array.

A second metric of interest is the ratio of sweeps to ejections, defined

$$S_r = \frac{\langle u'v' \rangle_{IV}}{\langle u'v' \rangle_{II}}. \tag{4.26}$$

The distribution of S_r is shown in figure 4-18(c). The dominance of sweeps, $S_r >$

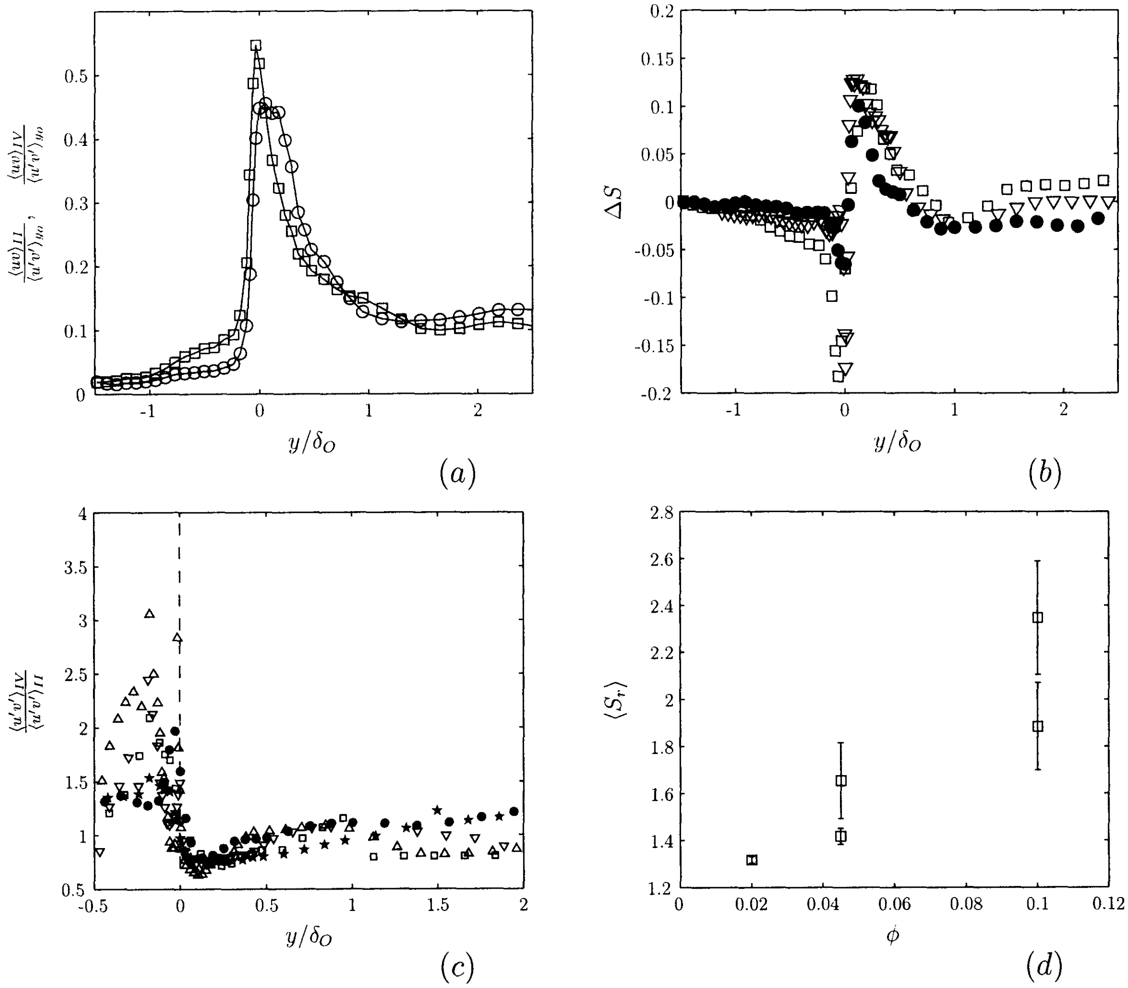

Figure 4-18: Quadrant distribution of the Reynolds stress. Shown in (*a*) are $\langle u'v'\rangle_{II}/\langle u'v'\rangle_{y_o}$ (circles) and $\langle u'v'\rangle_{IV}/\langle u'v'\rangle_{y_o}$ (squares), the quadrant II (ejection) and quadrant IV (sweep) contributions to the net Reynolds stress for a representative experimental case (V). Shown in (*b*) is ΔS, the stress differential for cases X ($\triangledown$), I ($\bullet$), and V ($\Box$). Shown in (*c*) is the distribution of the stress ratio, $\langle u'v'\rangle_{IV}/\langle u'v'\rangle_{II}$ for cases X ($\triangledown$), XI ($\triangle$), I ($\bullet$), IV ($\star$), and V ($\Box$). In (*d*) is the array-averaged stress ratio, $\langle S_r\rangle_a$ plotted vs. the array volume fraction, ϕ. The array edge is demarcated by a dotted line for reference.

1, is apparent within the array, and ejections dominate, $S_r < 1$, just outside the interface. Within the array, there appears to be some dependence on array density, with the maximum of S_r varying between about 1.5 for $\phi = 0.02$ and nearly 3 or $\phi = 0.10$. The array-averaged value of S_r, denoted $\langle S_r \rangle_a$ is plotted against ϕ in 4-18(d), demonstrating an increasing relationship (96% confidence). However, outside the array, where ejections dominate, the distributions of S_r collapse reasonably well, with all profiles reaching a minimum of about 0.7. This gives further support for the theory that the inner layer at the interface is highly dependent on the array density, but the outer layer is relatively independent of array density.

It is instructive to compare the quadrant results to those from rough-wall boundary layers and canopy flows. It is well-established that in a wall-bounded flow, there exists a quasi-cyclic, self-sustaining turbulent production sequence resulting in ejections of low momentum fluid from near the wall (Grass, 1971; Robinson, 1991). These motions, often termed bursts, are associated with coherent structures, which lift up near wall vorticity and eject it into the outer flow. Raupach (1981), Grass (1971), and Nakagawa & Nezu (1977), among others, have found that ejections contribute the majority of Reynolds stress in the outer flow, but sweeps become dominant in the roughness sublayer, a thin $O(k_s)$ region near the wall, where k_s is the roughness height. Moreover, the quadrant-based measurements of Nakagawa & Nezu near a rough wall suggested that sweeps are more important than ejections in maintaining the near-wall Reynolds stress and hence the burst cycle.

The stress contributions of the present case, shown in figure 4-18(b) and (c), particularly the sweep dominance in the array, can be compared with figure 14 of Nakagawa & Nezu and figure 9 of Raupach. Values of S_r in figure 14 of Nakagawa & Nezu are very similar to those in 4-18(c), with $S_r \approx 0.7 - 1.0$ (ejection dominance) in the outer region and $S_r = 1 - 2$ (sweep dominance) in the roughness sublayer. In addition, figure 9 of Raupach shows that the predominance of sweeps within the roughness sublayer increases with roughness concentration, just as S_r increases with ϕ in the present case.

The array interface, separating regions of sweep and ejection dominance, appears to be analogous to the roughness sublayer in a rough boundary layer. A parameter can be defined that places the partially vegetated channel, canopy flows, and rough boundary layers on a continuous spectrum. Define the dimensionless obstructed layer width,

$$\xi = C_D a B \tag{4.27}$$

where a is the projected frontal area of the roughness per unit volume, B is the width of the obstructed layer, and C_D is mean drag coefficient of the individual elements. In boundary layer terminology $B = k_s$, the roughness height, and in canopy terminology $B = h$, the canopy height. The density a is commonly used in both canopy and rough wall literature. The dimensionless parameter ξ measures the ability of sweeps to penetrate the obstructed layer. In section 2.5.5 it was shown that the inner layer width is $\delta_I \sim (C_D a)^{-1}$ for the vegetated channel, and similar results are observed for canopy flows (White *et al.*, 2004), implying that ξ is a proxy for the ratio B/δ_I. Thus when $\xi \ll 1$, i.e., a sparse array of obstructions, or a thin obstructed layer, as for rough walls, sweeps will penetrate the entire obstructed layer. However, for $\xi \gg 1$, characteristic of most canopies and vegetated channels, and the present experiments (ranging from $4 < \xi < 100$), sweeps will be confined to a thin region near the edge of the obstructed layer.

The analogy between the array and the roughness sublayer suggests that the cycle by which the Reynolds stress is maintained may also be similar, and the parameter ξ can illustrate the similarities and differences. The discussion in sections 4.4 and 4.5.2 suggested that the coherent vortices feed their own production by the sweeps which steepen the velocity gradient, $\partial U/\partial y$, near the interface. From an energy framework, the combination of high shear and Reynolds stress creates a turbulent energy production maximum. This is similar to the conclusion of Nakagawa & Nezu (1977) that the sweeps are more important for driving the Reynolds stress production in a rough boundary layer. In addition, for denser arrays, with larger ξ, the penetration length of the sweeps into the array is reduced, leading to a steeper velocity gradient at the interface (smaller δ_I). Because the velocity gradient is higher, the net Reynolds stress contributed by the sweeps, though confined to a thinner region, is also higher, explaining the increase in S_r with ϕ in figure 4-18(*d*) (where S_r is averaged only over the penetration width δ_I), and the same trend seen in the experiments of Raupach (1981). Ghisalberti & Nepf (2005*b*) have also compiled data which show S_r increases consistently with array density in canopy flows. Moreover, higher values of ξ will lead to the inflectional velocity profile necessary for the regular Kelvin-Helmholtz vortices. Some boundary layers, e.g., the grooved wall of (Ghaddar *et al.*, 1986) exhibit an inflection point with regular oscillations, but most do not and their cycle of coherent structures is irregular. Data from Poggi *et al.* (2003) shows that the inflection point at the top of the canopy is erased for $C_Dah < 0.01$. Thus, obstructed arrays with larger values of ξ, can be expected to be more efficient at feeding the production of coherent structures through a combination of increased shear and Reynolds stress, and the formation of an inflection point necessary to sustain regular oscillations.

4.6.3 Velocity Triple Correlations

Further insight into the momentum transport can be gained from the triple correlations of the velocity distribution, $\langle u'^3 \rangle$, $\langle v'^3 \rangle$, $\langle u'^2 v' \rangle$, and $\langle u' v'^2 \rangle$. As noted by Antonia & Krogstad (2001), in boundary layers the triple correlations are particularly sensitive to the surface roughness and reveal information about the direction of turbulent fluxes of shear stress and kinetic energy at the wall. Moreover, they are closely related to the sweep and ejection cycles of the coherent structures. To demonstrate, consider $\langle v'^3 \rangle$, the transverse flux of the Reynolds normal stress, v'^2. Because $v'(t)^2$ is positive definite, the sign of $\langle v'^3 \rangle$ is determined by whether ejections ($v' > 0$, $\langle v'^3 \rangle > 0$) or sweeps ($v' < 0$, $\langle v'^3 \rangle < 0$) are the predominant dynamic events. The significance of the signs of $\langle u'^2 v' \rangle$ and $\langle u' v'^2 \rangle$ can be inferred by similar reasoning.

The experimental results for the triple correlations are shown in figure 4-19 for the high Reynolds number cases from each cylinder volume fraction. Triple correlations are normalized by u_*^3 and plotted with outer layer coordinates. It is instructive to compare each of the triple correlations to results for rough-wall boundary layers which have been presented by, among others, Bandyopadhyay & Watson (1988); Raupach

(1981), and Antonia & Krogstad (2001). These results will be discussed along with the present ones. Beginning with the distribution of $\langle u'^3 \rangle$, 4-19(a), there is reasonable collapse of the curves from different volume fractions. The most striking feature is the very sharp peak directly at the interface, $\eta_O = 0$. This peak can be attributed to the positive u' component from sweeps, which carry high momentum fluid with high u'^2 toward the interface. The sweeps, and thus the fluctuations, u', and their energy, u'^2, decay quickly into the array, leading to the precipitous drop in u'^3 seen in 4-19(a). Outside the array, there is first a region in which $\langle u'^3 \rangle$ is positive and then a crossover after which it is briefly negative, before becoming zero outside the boundary layer. The rough boundary layer results of Bandyopadhyay & Watson (1988) and Raupach (1981) also show a change in sign in the outer region, but it occurs closer to the wall, so that $\langle u'^3 \rangle$ is negative throughout a greater portion of the boundary layer than in the present cases. Moreover, the boundary layer results, for which $\xi \ll 1$, do not exhibit a sharp peak at the wall like the one observed here at the interface, evidence that sweeps play a greater role in the vegetated channel for which $\xi >> 1$.

The distribution of $\langle v'^3 \rangle$ also exhibits the sharp peak just inside the array edge, but here it is negative, signifying a strong flux of v'^2, the energy associated with the transverse fluctuations, into the array. This flux is due to the negative v' component from coherent sweeps. Interestingly, immediately outside the array, η_O^+, there is a sharp positive peak in $\langle v'^3 \rangle$, corresponding to the dominance of ejections, and the transport of v'^2 away from the array. This sharp discontinuity and the change from ejection to sweep dominance over such an exceedingly thin width demonstrates just how steep the gradients are in the inner layer. The distribution of $\langle v'^3 \rangle$ bears a strong resemblance, both qualitatively and quantitatively, to the results presented in Bandyopadhyay & Watson (1988) near rough walls. The dip and subsequent rise from their figure 6 as the wall is approached is apparent in the present results as the interface is approached from the open region. The distributions of $\langle u'v'^2 \rangle$ and $\langle u'^2 v' \rangle$ (4-19(c) and (d)) are similar to that of v'^3, with a peak and change of sign near the interface due to the crossover from ejection to sweep dominance.

Bandyopadhyay & Watson's results indicate a difference between smooth, sand-

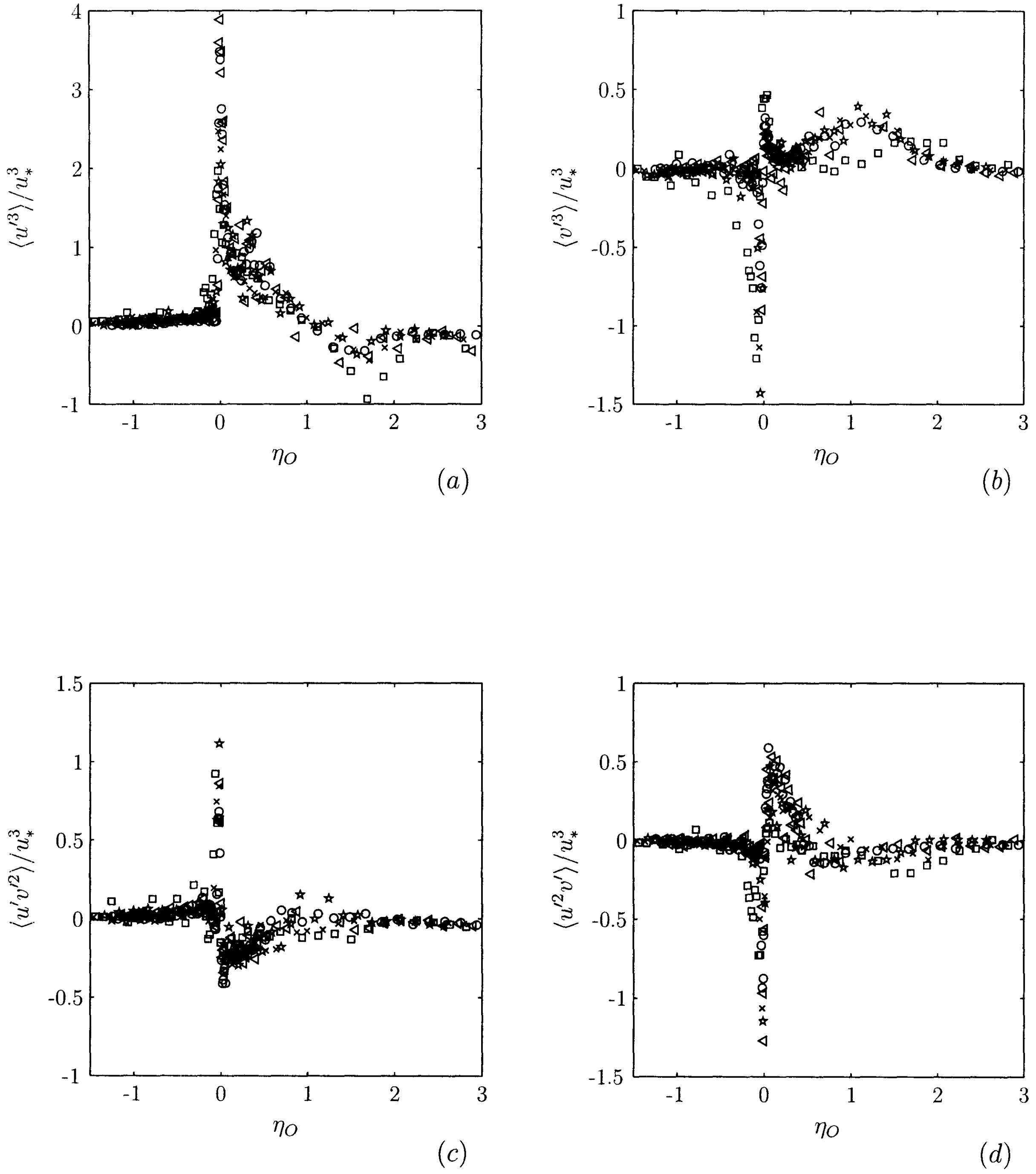

Figure 4-19: Transverse distributions of the velocity triple correlations. $\langle u'^3\rangle$ (a), $\langle v'^3\rangle$ (b), $\langle u'v'^2\rangle$ (c), and $\langle u'^2v'\rangle$ (d). Experimental cases range from sparse to dense cylinder volume fractions –symbols are the same as in Table 2.1.

grain-roughened, and grooved walls, for which $\langle v'^3 \rangle > 0$ near the wall as compared with plant canopies of Raupach *et al.* (1986); Seginer *et al.* (1976), for which $\langle v'^3 \rangle < 0$ near the top of the canopy. However, negative values of $\langle v'^3 \rangle$ were observed both in canopy-like rod-roughened walls by Raupach and Nakagawa & Nezu near a grain-roughened wall, so it appears both types may support strong sweeps. A possible explanation is that because the sweep-dominated region near a rough solid wall lies in the exceedingly thin roughness layer, the crossover from positive to negative $\langle v'^3 \rangle$ is difficult to resolve experimentally for walls with small roughness height. Based on the results of Raupach; Nakagawa & Nezu; Grass and others, as well as the present results, it appears that sweep-dominated regions are intrinsic to rough walls, and should result in a change in sign of the triple products within the roughness sublayer. However, for canopies, and the present experiments, the presence of sweeps is unmistakable due to the coherent shear layer vortices. The result is a much more distinct peak in $\langle v'^3 \rangle$, $\langle u'v'^2 \rangle$, and $\langle u'^2 v' \rangle$ in figure 4-19$(b)-(d)$ than in the boundary layer results.

4.7 Kinetic Energy Dynamics

In this section, the terms contributing to the balance of kinetic energy across the shear layer are described. From the velocity measurements, it is possible to estimate the kinetic energy budget and show the dominant contributions. It will be demonstrated that the sweep and ejection nature of the shear layer plays a prominent role in the balance, and in maintaining the coherent structures.

The turbulent kinetic energy (TKE) for the purposes of this section is defined as the energy associated with the two-dimensional fluctuating velocity field, $u'(x, y, t)$ and $v'(x, y, t)$, including the total contributions from the coherent structures and incoherent turbulence,

$$k = \frac{1}{2}(\langle u'^2 \rangle + \langle v'^2 \rangle). \tag{4.28}$$

The TKE is assumed to be depth-averaged, but experimental LDA results presented in this section have all been taken at mid-depth and the flow assumed two-dimensional. The ratio of depth to channel width is $h/B = 0.06$, making a two-dimensional assumption a good one. Moreover, most of the energy is contained in the horizontal coherent structures, and the vertical component of the total TKE, $\langle w'^2 \rangle$, is associated predominantly with the incoherent depth-scale turbulence. From experiments, the incoherent turbulence intensity is $\approx (0.2 - 0.3)$ of the coherent turbulence intensity. This is calculated by high-pass filtering the turbulent velocity time series for frequencies above the coherent structure frequency and finding u_{rms} and v_{rms} of the filtered signal. On the basis of the strength of the small scale turbulence (assuming $w_{rms} \approx u_{rms} \approx v_{rms}$) it is expected that

$$\frac{\langle w'^2 \rangle}{\langle u'^2 \rangle} = \frac{\langle w'^2 \rangle}{\langle v'^2 \rangle} = O(0.1) \tag{4.29}$$

or smaller and thus the two-dimensional budget is acceptable.

Assuming the mean flow, $U(y)$, is fully-developed and there is no net transverse current, $V = 0$, the depth-averaged TKE budget is given by

$$\frac{Dk}{Dt} = \underbrace{-\frac{\partial}{\partial y}\left[\frac{1}{\rho}\langle v'p' \rangle\right]}_{T_{py}} - \underbrace{\frac{\partial}{\partial y}\left[\langle v'\frac{1}{2}v'^2 \rangle + \langle v'\frac{1}{2}u'^2 \rangle\right]}_{T_{ty}} - \underbrace{\langle u'v' \rangle \frac{\partial U}{\partial y}}_{P_{ty}} + D_d + D_c - \Phi_v. \tag{4.30}$$

The term P_{ty} is the production of TKE from the mean transverse and shear by the Reynolds stress. The term T_{ty} describes the transport of TKE by the fluctuating velocity. Inspection shows that the triple correlations play a prominent role. The sum of $\frac{1}{2}\langle v'v'^2 \rangle$ and $\frac{1}{2}\langle v'u'^2 \rangle$ is the transverse flux of k. The gradients of the flux terms give rise to net transport.

The term T_{py} is the correlation between the fluctuating velocity and pressure. Using continuity, it can be rewritten as $-\langle v' \partial p' / \partial y \rangle$, from which it can be seen that it comprises the mean rate of work done by the fluctuating pressure gradient, and constitutes either a source or a sink for k depending on the sign.

The term D_d is of particular importance. It represents the work done by mean flow against the array drag. As is well-documented in the canopy literature (see, e.g., Katul & Albertson, 1998), when the momentum equation for the mean flow is averaged over the cylinder spacing scale, the drag from the cylinders appears as a constant body force within the vegetation,

$$\vec{F_D} = \frac{C_D a}{2}(U\vec{i} + V\vec{j})\sqrt{U^2 + V^2}, \qquad y < 0. \tag{4.31}$$

The work done against this drag force extracts energy from the largest scales of the flow and redistributes it to the smaller scales through the interaction with the individual cylinder elements. Specifically, this occurs through vortex shedding and wake turbulence. As a result, the work done against drag, D_d, is a source of TKE. However, in the canopy literature, the kinetic energy budget is often divided into coherent and incoherent scales, or in LES simulations, resolved and unresolved scales (see Dwyer *et al.*, 1987). In this formulation, D_d constitutes a sink for large-scale TKE and a source for small-scale TKE. In the present experiments, the turbulence is not partitioned into scales, so D_d is a source of (wake-scale) TKE within the vegetation, and is given by

$$D_d = UF_{Dx} + VF_{Dy} = \frac{C_D a}{2}(U^2 + V^2)\sqrt{U^2 + V^2}\rangle, \qquad y < 0 \tag{4.32}$$

Similar to the wake production within the vegetation, the term D_c is the production of TKE by depth-scale turbulence in the open channel. In analogy to (4.32), the depth scale production, acting in the open region, is given by

$$D_c = \frac{c_f/h}{2}(U^2 + V^2)\sqrt{U^2 + V^2}\rangle, \qquad y > 0 \tag{4.33}$$

The final term in (4.30), Φ_v, is the viscous dissipation of TKE. Due to its dependence on the instantaneous velocity gradient tensor, it is the most difficult term to measure experimentally, and its magnitude could not be estimated in this experimental study. Nonetheless viscous dissipation is essential as the final sink for all turbulent kinetic energy.

The total kinetic energy budget was computed from experimental results for case X ($Re = 9.59 \times 10^4$, $\phi = 0.10$). It is straightforward to estimate the production and transport terms from measurements of the mean velocity, Reynolds stress, and triple correlations, available throughout the shear layer. The pressure correlation term was obtained from simultaneous measurements of the free surface variation, using displacement gauges, and the fluctuating velocity, using the LDV, at approximately 43 positions across the shear layer. These measurements were time consuming and were only carried out for a single experimental configuration (case X). The instantaneous pressure was then calculated from the surface displacement by the hydrostatic approximation, $p(t) = \rho g(h_o + h'(t))$.

The accurate measurement of the wake scale production term, D_d, requires the spatially- and temporally-fluctuating drag force, which is prohibitively complex. However, an estimate may be made from the array-averaged drag, computed from the total force balance over the array,

$$\overline{F_D} = g\overline{S} = \frac{1}{2} C_D a \overline{U}^2 \tag{4.34}$$

where the overbar represents an average over the entire vegetated layer and $S = -dh/dx$ is the water surface slope. The measurements of C_D using surface displacement gauges were detailed in section 2.5.4. The wake production term, D_d was then estimated from 4.32 using the array-averaged value of C_D.

Finally, the depth-scale turbulent production term, D_d, was measured in the channel by finding the bed friction velocity, u^*_{bed} from the best logarithmic fit to the vertical velocity profile,

$$U(z) = \frac{u^*_{bed}}{\kappa} \log\left(\frac{z u^*_{bed}}{\nu}\right) + B. \tag{4.35}$$

Shown in figure 4-20 is the experimental TKE budget measured for case X. Each of the terms is normalized by u_*^3/δ_I. That δ_I is the appropriate length scale is apparent from the plot, which shows that the dominant contributions to the budget come from within a few inner layer thicknesses of the array interface. The dominant production mechanism is the mean shear, P_{ty}, which peaks very close to the interface and decays quickly into the array, while decaying more slowly in the open region. In the open region, the shear, while still appreciable, is smaller than the interfacial shear, and

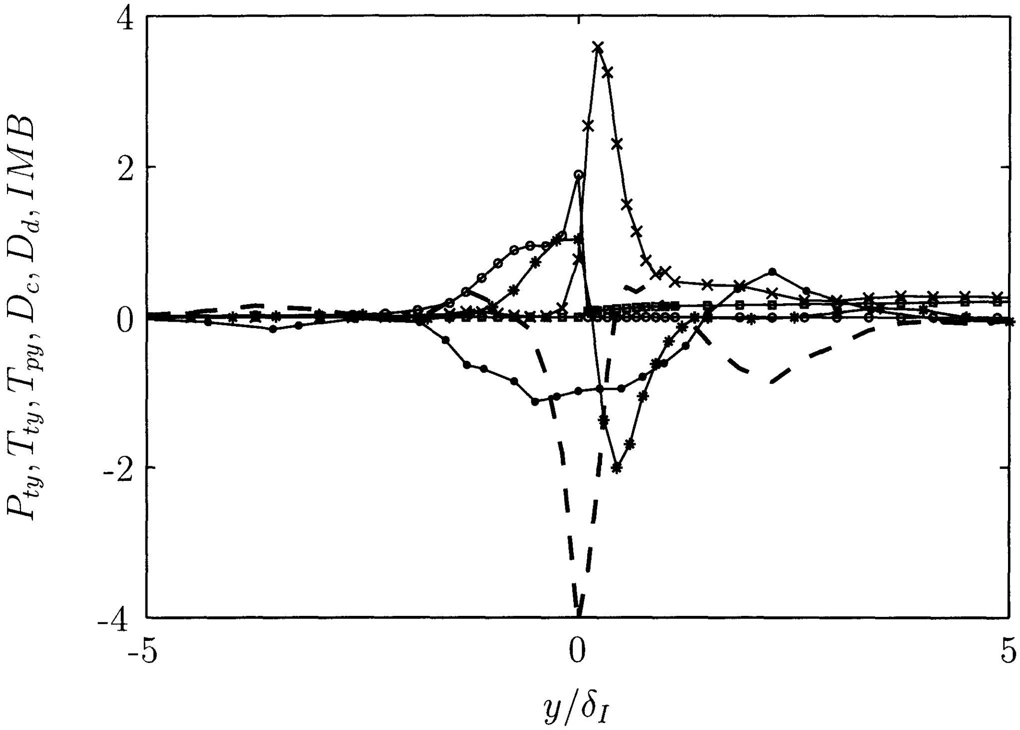

Figure 4-20: Turbulent kinetic energy budget across the shear layer, measured for case X. Shear production terms, P_{ty} (—×), turbulent transport, T_{ty} (—$*$), Pressure transport, T_{py} (—•), production by array drag (indirect measurement), D_d (—○), production by bed turbulence, D_c (—□), and net imbalance (- -), each normalized by u_*^3/δ_I.

$\langle u'v' \rangle$ is much smaller, so the production is small compared with the peak at the interface. This is consistent with the picture of the coherent structures originating in the inner layer where the shear and Reynolds stress is most intense. It is instructive to compare the results for the TKE budget with those from measurements in canopy flows. Results from the LES simulations Dwyer *et al.* (1987) and the data from natural forest canopies presented in Finnigan (2000) also show that the peak in production occurs near the top of the canopy, with rapidly decreasing production within the canopy.

The transport term, T_{ty}, is zero except within a few δ_I of the interface. It is a source of TKE within the array and a sink outside the array. This demonstrates a transfer of energy to the array from the open region, which occurs within only a very short penetration distance into the array. The transport can be explained in light of the sweep/ejection structure discussed in the previous section. The sweeps transport high energy fluid into the array, while ejections transport lower energy fluid out of the array. The result is a net gain of k within the array and a net loss of k in the open region. These results are in good agreement with the canopy layer results of Dwyer *et al.* and Finnigan and agree qualitatively with the near-wall rough boundary layer results of Nakagawa & Nezu (1977) and Raupach (1981). As the transport term is tied to the sweep and ejection cycles near a roughness layer, it appears that a net energy gain within the roughness and a loss outside may be intrinsic to solid- and porous- wall-bounded flows.

The pressure correlation term, T_{py}, is a net loss throughout the inner region. The coherent structures create a free surface fluctuation, a depression near their center necessary to balance rotation. The structures must do work against the resulting pressure gradient in order to maintain the rotation, hence $T_{py} = -\langle v'\partial p'/\partial y\rangle$ is a net loss. Similarly, Dwyer *et al.*'s LES results show the pressure correlation to be a net sink for TKE near the top of the canopy. However, because they partition the TKE into large and small scales, they find that deep within the canopy the pressure correlation is the primary source of TKE, balancing the dissipation of large scale TKE by canopy drag. Essentially, the pressure fluctuations do work against the canopy drag. In our experiments, the TKE is not partitioned, so drag within the array does not extract energy, but simply transfers it from the large scale fluctuations to the wake scale. Moreover, while the vortices create regular fluctuations within the array (see section 4.2.3), the oscillations are radiated away, resulting in zero net transport of energy, so from figure 4-20, $T_{py} \approx 0$ within the array. Note that figure 4-20 shows only the region near the interface; the flume extends as much as 20 to 80 inner layer units to either side of $y = 0$.

The indirect measurement of the wake production term, D_d, is also shown in figure

4-20. The production is greatest near the array interface, where the mean velocity is elevated, and decays over a short distance into the array as the velocity decays to its array-averaged value, U_1. By necessity, $D_d = 0$ outside the array. However, small scale turbulence is produced in the open region as well, due to the interactions with the bed. This is shown in the plot by the contribution from D_d. Near the interface, the contribution of the bed generated turbulence is much smaller than that associated with the lateral shear production, P_{ty}. However, by approximately $y/\delta_I = 3$ the bed generation has become comparable to the lateral production, demonstrating an increasing contribution of the bottom drag to the turbulence structure in the main channel.

The net imbalance, also shown in figure 4-20, is composed of the sum of the errors from all measured terms and viscous dissipation, Φ_v. This term peaks near the interface, presumably due to a viscous dissipation maximum. This is to be expected due to the high shear stress in this region. In general the imbalance is negative, consistent with viscous dissipation, which has not been measured and is thus included in the imbalance.

While the net TKE budget is useful for illustrating the mean turbulent quantities, more insight into the dynamics of the coherent structures can be gained from the conditionally-averaged energy production and fluxes in the vortex frame of reference. These are defined from the coherent structure conditional average (see 4.11),

$$\overline{P_{ty}} = \overline{u'v'}\frac{\partial \overline{U}}{\partial y} \tag{4.36a}$$

is the energy production,

$$\frac{1}{2}\left(\overline{v'^3} + \overline{v'u'^2}\right) \tag{4.36b}$$

the transverse flux of kinetic energy, and

$$\frac{1}{2}\left(\overline{u'v'^2} + \overline{u'^3}\right) \tag{4.36c}$$

the longitudinal flux of kinetic energy. Note that the flux terms contribute to the transport terms T_{ty} and T_{tx} of kinetic energy in the budget (4.30). Figures 4-21(a)–(c) show the spatial distribution of the energy and production. Also shown for reference are the temporal averages for each, which are a proxy for the average over the vortex wavelength, L_v. From figure 4-20(a) it is apparent that nearly all TKE production occurs near the interface. This is to be expected as both the velocity gradient and Reynolds stress peak in this region. In the sweep region of the vortex (the front), the production occurs along an exceedingly thin line near the interface, $y = 0$, ranging from $\tilde{x}/\delta_O \approx 3.5$ to $\tilde{x}/\delta_O \approx 6.5$. The ejection-phase production extends slightly into the main channel, but exists over a shorter streamwise extent, from $\tilde{x}/\delta_O \approx 0.75$ to $\tilde{x}/\delta_O \approx 2$. The accompanying plot of the temporally-averaged production, $\langle P_{ty} \rangle$, also demonstrates the sharp interfacial peak. It can be inferred, both from the spatial plot and from the peak in the temporal average, that the sweep region of the vortex contributes more to this high production than the ejection region, attaining a maximum of $\overline{P_{ty}} \approx 8$ vs. a maximum of $\overline{P_{ty}} \approx 4$ for ejections, and extending over a longer streamwise extent. This is particularly interesting because figure 4-16 in section 4.5.2 showed that the maximum Reynolds stress derives from ejections. Thus, from the definition of production (4.36), the steep gradient, $\partial \overline{U}/\partial y$, in the sweep region overcomes the slight Reynolds stress deficiency to create the production maximum. This is consistent with the notion that the sweeps play the biggest role in maintaining the coherent structures.

The conditionally-averaged fluxes of kinetic energy in 4-21(b) also demonstrate the transport by sweeps and ejections. From figure 4-21(b), there is an influx of kinetic energy toward the array during the sweep phase and a flux toward the open region on the ejection phase. The temporal average of the transverse flux, shown adjacent to the contour plot for reference, demonstrates the large negative peak of $\frac{1}{2}\left(\overline{v'^3} + \overline{v'u'^2}\right)$, which demonstrates that the instantaneous flux due to sweeps $(-v')$ is greater than that due to ejections. The time-averaged flux is composed of the triple products discussed in section 4.6.3 and the conclusions drawn there about the dominance of sweeps can be observed here in the spatial contour plots.

Figure 4-22 shows the spatial distribution of $\overline{P_{ty}}$ along with the directional vectors

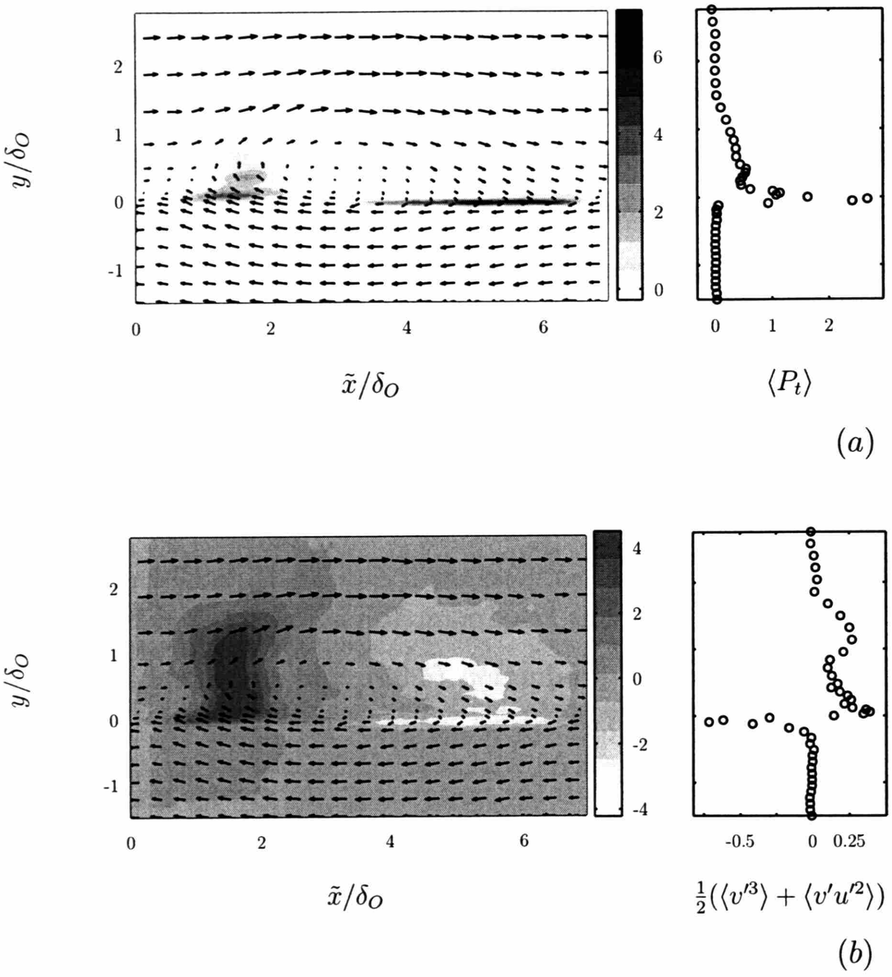

Figure 4-21: Spatial distribution of the conditionally-averaged production and fluxes of kinetic energy. In (a), shear production, $\overline{P_{ty}}$, in the vortex frame and transverse distribution of the time-average, $\langle P_{ty} \rangle$. In (b), transverse flux of kinetic energy, $\frac{1}{2}(\overline{v'^3} + \overline{v'u'^2})$, in the vortex frame and time-average, $\frac{1}{2}(\langle v'^3 \rangle + \langle v'u'^2 \rangle)$.

of the kinetic energy flux,

$$\frac{1}{2}(\overline{u'v'^2}+\overline{u'^3})\vec{i}+\frac{1}{2}(\overline{v'^3}+\overline{v'u'^2})\vec{j}. \tag{4.37}$$

It can be seen that the regions of maximum production coincide with regions of maximum transport. At the sweep, the flux of kinetic energy is toward the line of peak production and with a positive (downstream) longitudinal component. At the ejection, the outward flux is toward the tail (upstream). The fluxes decay to zero at the edge of the shear layer ($y/\delta_O \approx 2$). It is interesting to compare the results for the kinetic energy budget to those from free shear flows. The experimental results of Wygnanski & Fiedler (1970) for a developing mixing layer have several features in common with the partially-obstructed shear flow studied here. The energy production peaks near the inflection point of the velocity profile, but there is significant production throughout the mixing layer. In contrast, in the partially-vegetated channel, the intense shear at the interface confines the maximum production to the thin interfacial region. This disparity is strongly related to the fact that free shear layers possess only a single length scale, while the partially-obstructed shear layer possesses two distinct length scales: the inner layer, where production peaks, and the outer layer where the vortices predominantly reside. In addition, the results of Wygnanski & Fiedler show that the transport of kinetic energy in the mixing layer is significant at the edge of the layer, resulting in a net energy gain at the fringes. They suggest that the flux at the edge is significant in determining the layer growth. In the partially-obstructed channel, the transport of energy is confined to the interfacial region, with no net gain at the lateral fringes, consistent with the equilibrium of the shear layer.

4.8 Spatial Development

Experiments were undertaken to study the longitudinal development of the shear layer downstream of the splitter plate. Initially separated by the splitter plate, the slow flow in the array merges with the faster flow in the open region, and the width

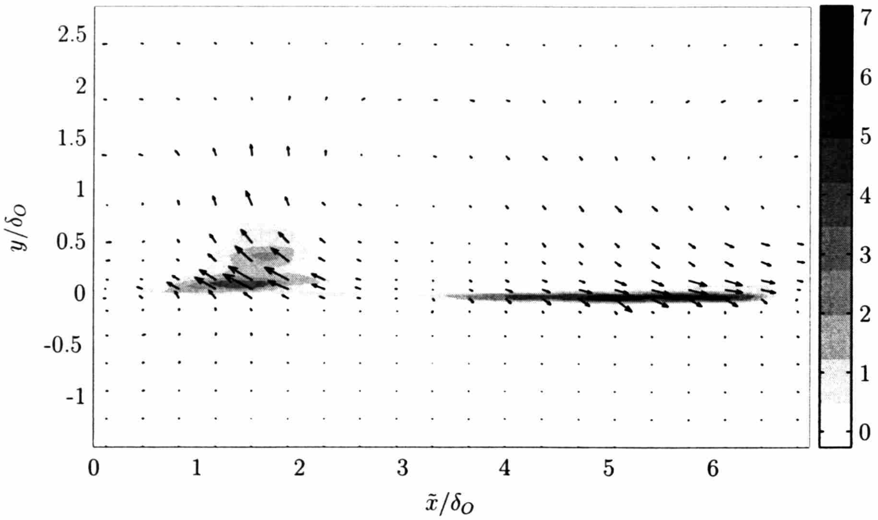

Figure 4-22: Spatial distribution of production and flux vectors of kinetic energy in the vortex frame. Kinetic energy production, $\overline{P_{ty}}$ is shown along with the vectors of the kinetic energy flux, $\frac{1}{2}(\overline{u'v'^2} + \overline{u'^3})\vec{i} + \frac{1}{2}(\overline{v'^3} + \overline{v'u'^2})\vec{j}$.

of the layer between them grows as momentum is mixed between the streams. This scenario is like a free mixing layer but for the presence of the solid obstructions. As in a mixing layer, as the flow develops a portion of the momentum from the free stream is transferred to the flow in the array, raising its velocity. However, similar to a wall-bounded flow, the array is a sink for momentum, thus acting as a partially-absorbing porous wall. This sink is not present in a free shear flow. Essential to the initial shear layer growth is the development of the coherent structures. As the structures grow they are responsible for the transport of energy and momentum across the shear layer from the free stream to the array. As previously discussed (see figure 4-2) the onset of the coherent structures is marked by a distinct frequency peak, which moves to lower frequencies before locking into the fundamental shear layer harmonic, f_n. This accompanies a dynamic equilibrium in which the momentum absorption by the array balances the transport of momentum by the coherent structures.

Detailed transects of velocity and Reynolds stress at increasing longitudinal positions demonstrate the growth of the shear layer and the approach to an equilibrium velocity distribution and turbulence structure. Before discussing the spatial development it is important to be clear about the initial conditions. At $x = 0$, immediately following the splitter plate, the spectral distribution is relatively broad-banded, but a few peaks are discernible (see figure 4-2(a) and (b) in particular). This initial turbulence is due to (i) the remnants of the turbulence created by the upstream adjustment of the flow upon first encountering the array and (ii) turbulence associated with the twin boundary layers created on either side of the splitter plate. Ideally, for purposes of generalization, the qualitative details of the spatial development and certainly the final equilibrium state should be independent of the initial turbulence intensity and structure. Fortunately, the development of the spectral distributions in figure 4-2 strongly support this independence. Not only is the final spectral peak, f_n, uncorrelated with the initial peaks, but there is significantly greater turbulent energy contained in the flow at the final stage than the initial level. This suggests energy inputs from the mean flow during the development stage are responsible for the equilibrium mode, rather than energy transfers from the initial spectral components. However, it is important to note that the initial turbulence structure is dependent upon upstream conditions before eventually being shaped by the developing coherent structures. From figure 4-2, this transition seems to occur within the first three to four stations following the splitter plate (by around x = 99 cm), when the fundamental instability frequency, $f_d = 0.032\overline{U}/\theta$ first can be observed and begins to grow.

The development of case IV, with $Re = 5.3 \times 10^4$ and $\phi = 0.045$, was studied in detail. The velocity distributions, shown in figure 4-23(a), undergo initial spreading downstream of the splitter plate, but eventually reach an equilibrium. From figure 4-24(a), the shear layer width, measured by the momentum thickness, θ, increases from an initial value of 2 cm before asymptotically reaching a constant value of approximately 5 cm. Moreover, the velocity distributions from the final three locations ($x = 386$, $x = 513$, and $x = 577$ cm) all collapse well.

In the outer region (beyond $y \approx 5$ cm) the profiles resemble a developing mixing layer. In fact, if the profiles were anti-symmetric about $y \approx 5$ cm, the flow would be unmistakably a mixing layer. However, because of the asymmetry of the channel, and the momentum absorption by the array, there is a sharp change in slope between the inner and outer layers. The transport of main-channel momentum toward the array

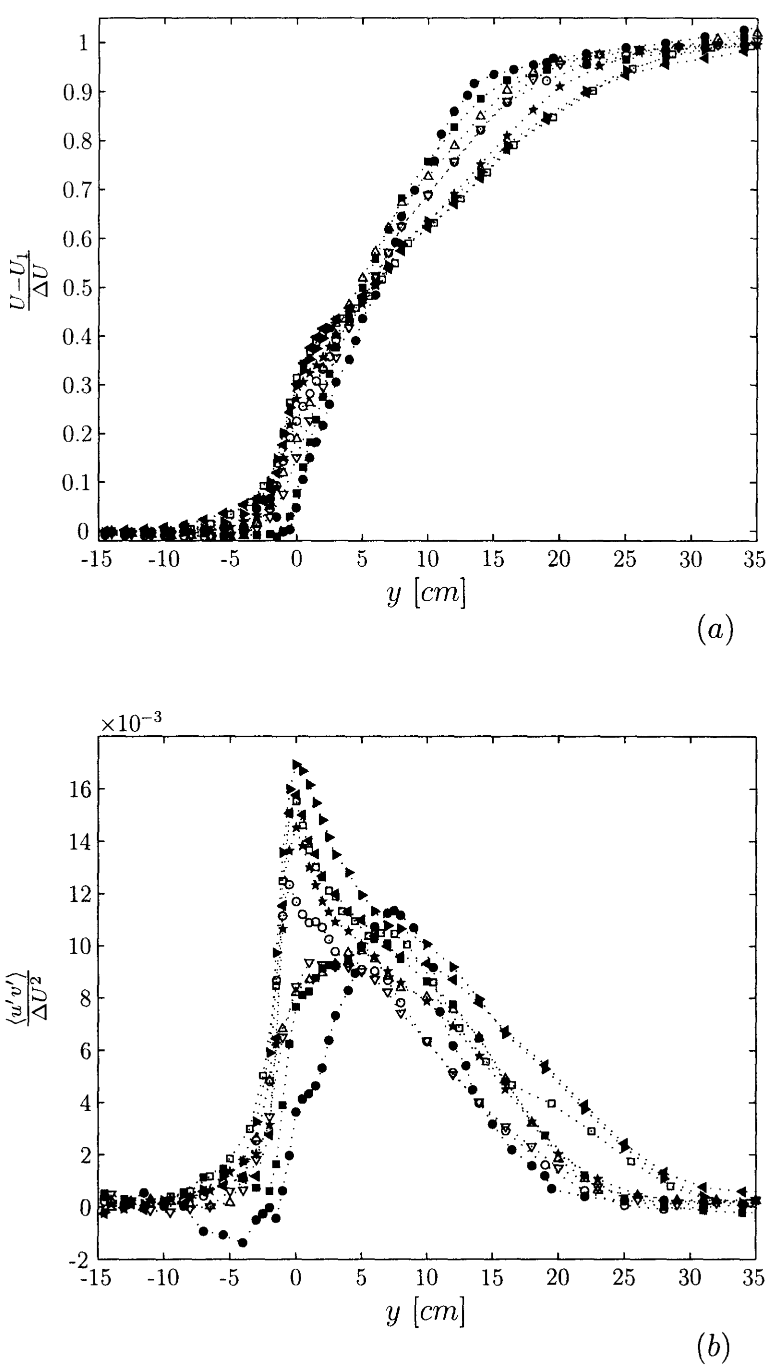

Figure 4-23: Streamwise development of the velocity (a) and Reynolds stress (b) distributions. Results of transects at various longitudinal positions for case IV ($Re = 5.27 \times 10^4$, $\phi = 0.045$): $x = 0$ (●), $x = 33$ cm (■), $x = 66$ cm (△), $x = 99$ cm (▽), $x = 132$ cm (○), $x = 195$ cm (★), $x = 386$ cm (□), $x = 513$ cm (▶), $x = 577$ cm (◀).

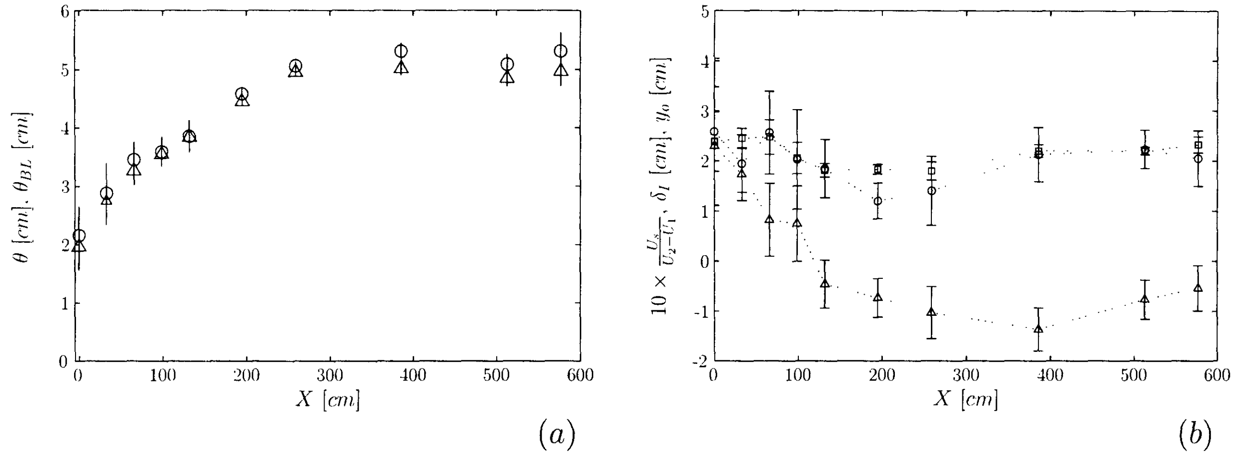

Figure 4-24: Longitudinal development of the shear layer width (*a*) and inner layer properties (*b*) for a typical experimental case (IV). In (*a*), shear layer momentum thickness, θ (○) and outer layer momentum thickness, θ_{BL} (△). In (*b*), inner layer width, δ_I (○), dimensionless slip velocity, $U_s/(U_2 - U_1)$ (□), and virtual origin, y_o (△).

increases the velocity near the interface, but the drag from the array elements absorbs a portion of that momentum, limiting its penetration. Nonetheless, as the inner layer develops with the influx of channel momentum, the velocity distribution, and its inflection point, penetrates further into the array. The migration with downstream distance, of the virtual origin, y_o, the location of the inflection point, is shown in figure 4-24(*b*). Note the gradient at the inflection point remains approximately constant, even as the inflection point shifts toward the array. From section 2.5.3, the gradient is given by

$$\left.\frac{\partial U}{\partial y}\right|_{y_o} = \frac{U_s}{\delta_I}. \tag{4.38}$$

From figure 4-24(*b*) it can be seen that the ratio between U_s and δ_I remains relatively unchanged with downstream distance. In fact, from figure 4-24(*b*), neither U_s nor δ_I grow significantly as the mixing layer develops, both fluctuating slightly, but remaining relatively unchanged between the initial and equilibrium values. These observations are consistent with the theory for the inner layer (2.5.5), which states that δ_I is set by the array conditions, particularly near the interface. Thus an equilibrium in the inner region of the shear layer appears to be established rather quickly by the array. The equilibrium shear is maintained as the outer layer develops and the momentum flux from the channel raises the velocity in the inner layer and shifts the inner layer profile toward the array. Note that because U_s is defined at y_o, the velocity at $y = 0$ may increase even while U_s does not. This demonstrates that it is more useful to define the slip velocity at y_o, the inflection point, than at the geometric edge of the array.

The development of the Reynolds stress profiles, figure 4-23(*b*), sheds greater light on the development process. Immediately following the splitter plate, the distribution of $\langle u'v' \rangle$ is rather broad, with the peak lying well into the open region. Initially, both the Reynolds stress peak and the velocity inflection point lie in the open region, suggesting this is the initial origin of the instability leading to coherent structures. Indeed, from the profiles of the developing TKE production, figure 4-25, production maximum initially occurs in the open region. Moreover, per previous discussion, the velocity profiles resemble a spreading mixing layer in the open region beyond $y \approx 5$ *cm*. Interestingly, this approximate origin of the right half-plane mixing layer roughly corresponds to the initial production maximum. But while the coherent structures appear to originate well into the open region, the Reynolds stress peak, the point of maximum stress moves increasingly toward the array interface with increasing downstream distance. By $x = 132$ *cm* the peak has shifted approximately to the interface, and the distribution has become much more peaked, with a sharp decay into the array from the maximum at the interface. From this point until equilibrium is reached, the distribution changes very little except for a rise in the interfacial stress, u_*^2.

The downstream drift of the Reynolds stress peak towards the array interface coincides with the drift of the velocity inflection point, y_o, shown in figure 4-24(*b*), which shifts the production maximum toward the array. As the shear layer develops, the sweeps associated with the coherent structures drive the Reynolds stress maximum toward the array until the obstructions prevent further migration (by about $x = 132$ *cm* from figure 4-23(*b*)). After that point, the sweeps continue to increase the interfacial stress which in turn increases the production of kinetic energy and shifts the velocity inflection point further into the array. When the vortices can penetrate no further, an equilibrium is attained, in which a constant rate of energy production

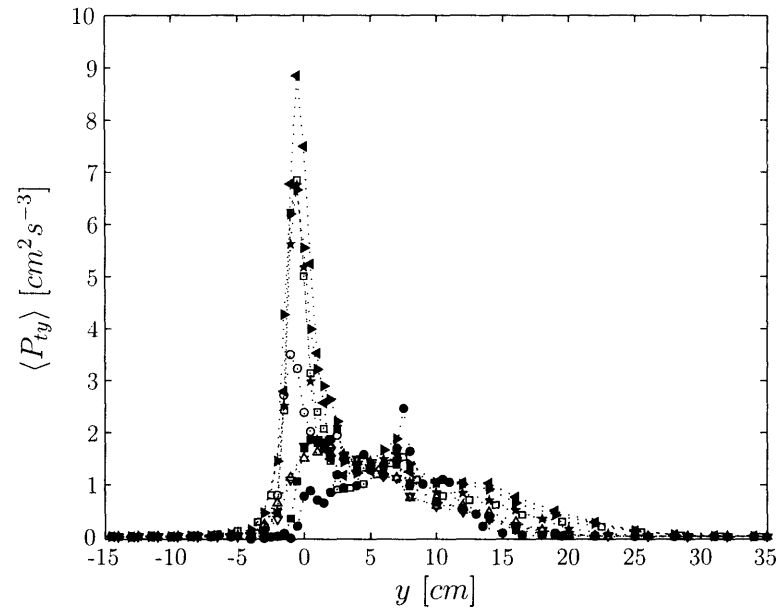

Figure 4-25: Streamwise development of the kinetic energy production. Results of transects at various longitudinal positions for case IV ($Re = 5.27 \times 10^4$, $\phi = 0.045$): $x = 0$ (●), $x = 33$ cm (■), $x = 66$ cm (△), $x = 99$ cm (▽), $x = 132$ cm (○), $x = 195$ cm (⋆), $x = 386$ cm (□), $x = 513$ cm (▶), $x = 577$ cm (◀).

and Reynolds stress is maintained by the coherent structures, resulting in a constant velocity distribution.

Chapter 5

The Impact of Coherent Structures on Exchange between the Vegetation and Main Channel

It has been established that coherent vortex structures form at the interface between an open channel and a vegetated region. Such scenarios are often found in shallow coastal environments, where networks of tidal creeks intersect fringing mangroves or salt marshes, and in overbank flow between rivers and their associated vegetated floodplains. The coherent structures create strong crossflows across the interface, transporting both momentum and mass between the main channel and the vegetation. In section 5.1, a unified framework is presented for relating both momentum and scalar fluxes between the main channel and the vegetation to the characteristics of the coherent structures. The flux is related to a mass transfer coefficient, k, and a parameter, α, which characterizes the volume of fluid exchanged by each vortex. The model successfully describes the shear stress at the vegetation interface across a range of vegetation conditions. It also shows good agreement with the results of experiments by Ghisalberti & Nepf (2005*a*) measuring the scalar flux across the interface of a submerged aquatic canopy.

In section 5.2 the structure of the coherent vortices, demonstrated in chapter 4, is used as a basis for numerical particle transport experiments which illustrate the modes of material transport and demonstrate the validity of the proposed model. It is shown that the particle tracking experiments very nearly reproduce the vortex exchange parameter α from the laboratory experiments. It appears that the results for mass and momentum exchange can be generalized to a range of flow and vegetation conditions, from emergent vegetation in shallow channels to submerged vegetation, such as eelgrass meadows.

In section 5.7 the model for material transport is applied to the problem of overbank transport of suspended sediment in a channel-floodplain system. A form of the advection-diffusion equation with a term to account for settling is used in conjunction with the mass flux condition at the vegetation interface. The solution yields suspended sediment concentrations and rates of deposition on the floodplain for typical systems.

In section 5.8, experimental results are presented which demonstrate the existence of secondary circulations induced by the coherent structures. These currents, outward flows from the canopy near the bottom and return flows near the surface may enhance material transport near the vegetation interface.

5.1 Material Flux at the Vegetation-Main Channel Interface

The impact of coherent structures on momentum fluxes at the vegetation interface was discussed in detail in section 4.5. The shear instability both creates and is reinforced by strong lateral motions that transport high momentum fluid from the main channel into the vegetation via sweeps, and low momentum fluid out of the vegetation by ejections. The result is a strong momentum flux at the interface, observable in a high shear stress between the two regions. Like momentum, dissolved and suspended materials will also be transported by the sweeps and ejections across the interface. The interface separates two very distinct regions of flow, quiescent with low turbulent diffusivity within the vegetation and high flow with large diffusivity in the main channel. It also separates two regions with significantly distinct chemical and biological characteristics, and many of the complex biogeochemical and ecological processes within the vegetation rely on the exchange of fluid with the main channel. A fairly good understanding of flow within vegetated stands has been achieved, in terms of the turbulence structure (Nepf, 1999) and turbulent diffusion (Nepf *et al.*, 1997; Ackerman & Okubo, 1993). In the main channel, classic open channel hydraulics prevail, so the flow and transport are easily described. It is the exchange of material between these two regions, the rate of transport across the interface, that is needed in order to obtain a system-level understanding.

5.1.1 A Model for the Interfacial Flux

The structure of the coherent vortices suggests a model for the interfacial flux. The vortices exist as a traveling wave train with frequency f_d and wavelength L. In chapter 4 it was established that the structures primarily occupy the main channel region, with a width of the order of the channel boundary layer scale, δ_O, and penetrate into the vegetation a distance on the order of the inner layer width, δ_I. To quantify the exchange between the main channel and the vegetation, the entire vegetated channel is divided into three zones: the main channel, with a characteristic width, B_2, and velocity, U_2; the vegetated layer, with width B_1 and velocity, U_1; and the region at the vegetation interface that undergoes active exchange with the main channel, having a characteristic width, δ_I. A schematic is shown in figure 5-1.

The vortices can be viewed as a turnstile that allows material to pass between the vegetation and the main channel. Because the coherent structures are periodic, the interfacial flux can be expressed in terms of the volume of fluid, V_e, exchanged between the vegetation and the main channel in one wavelength, L, over one period, $T_d = 1/f_d$, of the vortex. As discussed in chapter 4, the vortex structure is a traveling wave that induces strong crossflows: ejections out of the vegetation and sweeps into the vegetation. Thus it is argued that the following scenario describes the exchange mechanism. As a vortex passes, the pressure perturbation it induces drives an ejection, which results in the entrainment into the vortex of fluid originating in the vegetation. The total volume of fluid entrained in time T_d, the duration of the vortex passage, is V_e. To satisfy conservation of mass, an equal volume of fluid must be transported from the free stream into the vegetation by a sweep. Further, because the fluid entrained from the vegetation, along with fluid entrained from the free stream, make up the total volume of the vortex at any instant, it is reasonable to argue that V_e scales with the total fluid volume contained in a single vortex,

$$V_e = \alpha \delta_O L h \tag{5.1}$$

where h is the fluid depth and α is the factor of proportionality that describes the efficiency of exchange. Normalizing 5.1 by the interfacial area per wavelength, hL, and the period of each vortex cycle, T_d yields the rate of volumetric flux of fluid per unit interfacial area,

$$k = \frac{V_e}{hLT_d} = \frac{\alpha \delta_O}{T_d}. \tag{5.2}$$

The units of k are of velocity, representing a mass transfer, or exchange, coefficient. Using the expression for the natural period of the vortices (4.1),

$$T_d = \frac{\theta}{0.032\overline{U}}, \tag{5.3}$$

the mass transfer coefficient can be written

$$k = \alpha \delta_O \frac{0.032\overline{U}}{\theta}. \tag{5.4}$$

If α is a constant, the mass transfer coefficient, then the normalized mass transfer coefficient, $k/\overline{U}$ depends only on the dimensionless vortex passage frequency,

$$\frac{k}{\overline{U}} = f\left(\frac{\delta_O f_d}{\overline{U}}\right). \tag{5.5}$$

There is no *a priori* reason to expect this is the case, as $k/\overline{U}$, and thereby α, may additionally depend on the velocity difference, $\Delta U/\overline{U}$ which is often used as a scale for vortex rotation rate in free shear flows (see, e.g., Schlichting, 1979), or the array

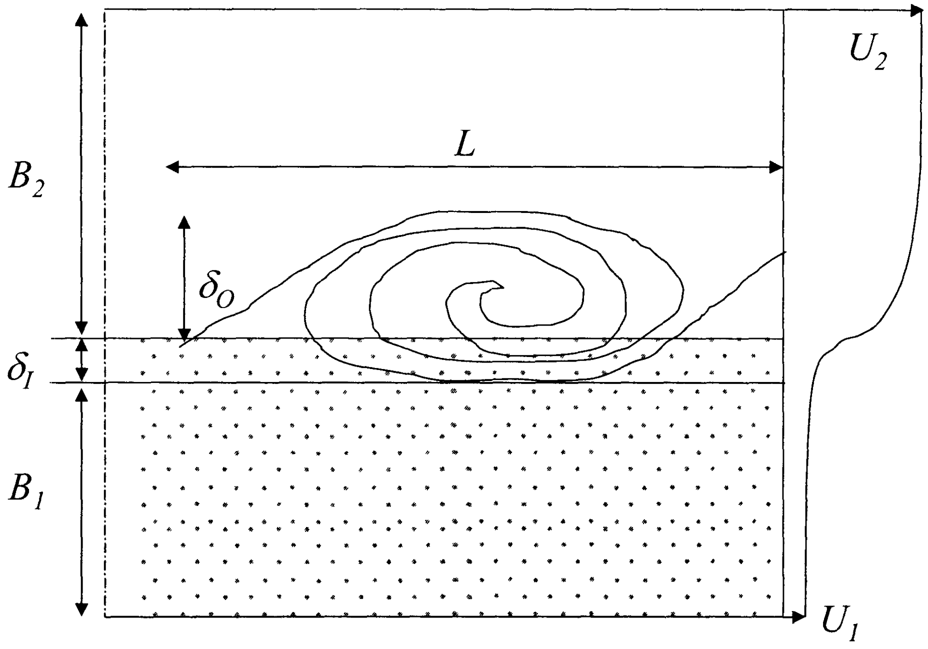

Figure 5-1: A schematic of the exchange zone. The vortices extend a width, δ_O into the open channel and penetrate δ_I into the vegetation. There are three zones: layer, with characteristic width B_2 and velocity U_2, the vegetated layer, with width B_1 and velocity U_1, and zone of active exchange with characteristic width δ_I.

drag acting on the vortex, which can be described by $C_D a \delta_O$, which also characterizes the degree of penetration of the vortex. However the experimental results presented will demonstrate that α is approximately constant, and nearly independent of $\Delta U/\overline{U}$ and $C_D a \delta_O$. In the next section, α is determined from experimental values and this will shed light on the contributions of both vortex passage frequency and rotation rate to the total mass exchange.

5.1.2 Dependence of α on Vegetation and Flow Conditions

In this section, α, the proportion of vortex volume exchanging over each cycle, is obtained both from the momentum exchange results in the experimental shallow vegetated channel, and from the scalar transport results of Ghisalberti & Nepf (2005*a*) in a submerged aquatic canopy. It is found that α is approximately the same for both the submerged and emergent vegetated channels, across a range of flow and canopy conditions.

The tracer experiments by Ghisalberti & Nepf were conducted in a submerged layer of model vegetation, an array of circular cylinders with volume fractions between $0.008 < \phi < 0.026$. Dye was injected continuously at the top of the canopy and the flux of dye between the canopy and the overlying fluid was measured. In the experiments, the width of the exchange zone normalized by the canopy depth ranged from, $0.48 < \delta_I/B_1 < 0.63$. This suggests that a the majority of canopy width is involved in active exchange with the overlying flow. Consistent with this, Ghisalberti & Nepf proposed a two-layer model, consisting of the canopy, with velocity U_1, and concentration C_1 (in our nomenclature), and the overlying fluid with velocity U_2, and concentration, C_2 (see figure 5-1). The concentration in each layer downstream of the dye injection is described by the following equations,

$$\frac{\partial C_1}{\partial x} = \frac{k}{B_1 U_1}(C_2 - C_1) \tag{5.6a}$$

within the canopy, and

$$\frac{\partial C_2}{\partial x} = \frac{k}{B_2 U_2}(C_1 - C_2) \tag{5.6b}$$

within the main channel, where k is the mass transfer coefficient, as defined in (5.2). The results obtained by Ghisalberti & Nepf demonstrated that the dependence,

$$k = \frac{\Delta U}{40}, \tag{5.7}$$

held over the entire range of cylinder volume fraction and Reynolds number studied. From these results, we can determine the exchange ratio α according to (5.2),

$$\alpha = \frac{k T_d}{\delta_O}, \tag{5.8}$$

where δ_O is found for Ghisalberti & Nepf's velocity distributions by the method described in section 2.5.6. The results for α derived from the data of Ghisalberti & Nepf are shown in figure 5-2 (open circles) as a function of the depth Reynolds number. The exchange ratio is approximately constant across these experimental cases, $\alpha = 0.31 \pm 0.03$.

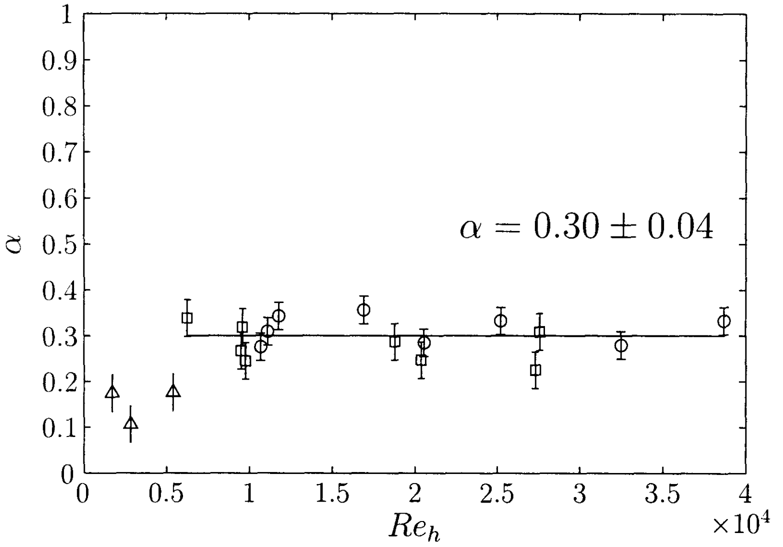

Figure 5-2: Values of the the vortex exchange ratio, α plotted with $Re_{ha} = \Delta U h/\nu$. Values are obtained from the tracer experiments of Ghisalberti & Nepf (2005*a*) (○), calculated from the u_*^2 in the shallow vegetated layer experiments (□) and at low Re_h (△).

The exchange ratio, α can also be calculated from the present experiments in the shallow vegetated channel from the measurements of momentum exchange. In Ghisalberti & Nepf's two-layer model (5.6), the mass (or scalar) flux across the interface is

$$J_s = -k\Delta C = -\alpha \frac{\delta_O}{T_d} \Delta C \tag{5.9}$$

where $\Delta C = C_2 - C_1$ is the concentration difference between the layers. The momentum flux is analogous to the mass flux. In each vortex cycle, the volume of fluid, V_e, exchanged between the vegetated layer and the main channel carries with it a momentum flux proportional to the velocity difference between the layers, ΔU. The momentum flux across the vegetation interface can be thus be written

$$J_s = -\gamma k \Delta U = -\gamma \alpha \frac{\delta_O}{T_d} \Delta U \tag{5.10}$$

where $\Delta U = U_2 - U_1$ is the velocity difference between the layers, and γ is an unknown parameter that describes the difference in the rates of mass and momentum transport. The turbulent momentum flux is typically less by some factor than the mass flux as a result of pressure fluctuations (see Hinze, 1975). By comparing the mass fluxes to the momentum fluxes in the submerged canopy results of Ghisalberti & Nepf, the parameter γ was determined. Specifically, the momentum flux (5.10) can be rewritten in terms of the Reynolds shear stress at the top of the canopy,

$$J_s = \langle u'v' \rangle|_{y=0} = -u_*^2. \tag{5.11}$$

which yields

$$u_*^2 = \gamma \alpha \frac{\delta_O}{T_d} \Delta U. \tag{5.12}$$

Since u_* is available from the velocity measurements of Ghisalberti & Nepf and α from the scalar flux measurements, γ can be determined from (5.12). The results give a value of $\gamma = 0.8 \pm 0.1$.

The value of γ obtained from the data of Ghisalberti & Nepf can be used to determine the mass transfer coefficient, k, and the exchange ratio, α for the present experiments in the shallow vegetated channel. From (5.12),

$$\alpha = \frac{u_*^2 T_d}{\delta_O \Delta U \gamma}. \tag{5.13}$$

The experimental LDV data yield the interfacial shear stress, u_*^2, the velocity difference between the vegetation and the free stream, ΔU, and the vortex oscillation period, T_d. Thus α can be determined from 5.13. The results for α obtained are shown in figure 5-2 along with those from the scalar transport experiments of Ghisalberti & Nepf (2005*a*). The data are plotted as a function of the Reynolds number based on spanwise width, which is h, the water depth, for the present cases, and the flume width, 38 *cm*, for the submerged canopy data of Ghisalberti & Nepf). The exchange ratio is approximately constant at high Reynolds number for the present study, and nearly equal to the values obtained from the scalar transport experiments. However, the three low *Re* data are lower by at least a factor of two than the high *Re* data and the low *Re* data from the scalar transport experiments. It is likely that in the shallow channel, bottom friction and bed confinement affects the characteristics of the vortices, weakening their transport efficiency. This is most pronounced at low Reynolds number, when viscous effects are most significant. These effects are less pronounced in the submerged canopy experiments because in the wide flume the shear layer is relatively unaffected by the side walls. Because the high Reynolds cases are more representative of field conditions, the high Re data for both the shallow and submerged experiments have been averaged to obtain a mean exchange ratio of $\alpha = 0.30 \pm 0.04$.

That α is nearly constant across a wide range of experimental conditions suggests that the mass transport by the vortices is described quite well by the vortex size and passage frequency, according to (5.2). In the following section this result is explored in greater detail by simulating transport by numerical particle tracking.

5.2 Numerical Particle Transport Experiments

The semi-empirical theory that describes the material flux at the vegetation interface (5.18) relies upon the fluid exchange by the coherent structures, expressed through the exchange parameter α. The constant value of $\alpha \approx 0.3$ obtained from experimental data suggests that a constant proportion of the coherent vortex volume exchanges in each period of its oscillation. To demonstrate the exchange mechanism more clearly, numerical particle tracking experiments were performed using the velocity field of the coherent structures found from experiments. This allowed the flux of tracer particles across the vegetation interface to be measured and compared with the experimental results.

Shown in figure 5-3 is the conditionally-averaged velocity field in the vortex frame of reference, obtained from the eduction scheme described in chapter 4. The vortices are periodic with wavelength L and move with a wave speed, $U_v = L/T_d$. Here the velocity field is repeated over three structures to demonstrate how successive vortices are joined in a wavetrain. In a moving frame of reference of speed U_v the conditionally-averaged velocity field is steady and the flow within the vegetation, $y < 0$, appears to move in reverse because it is slower than U_v, while the faster flow in the free stream appears to move forward. The vortex centers, which are displaced into the free stream, are fixed points in the moving frame of reference, or points with zero velocity; the saddles connecting vortices are also fixed points.

Also shown are the limiting streamlines, known as manifolds. The manifolds emanate from each of the fixed points, the vortex centers at $x^* = -\pi, \pi, 3\pi$, and the saddles between vortices at $x^* = -2\pi, 0, 2\pi, 4\pi$, where $x^* = kx = 2\pi x/L$. By tracing flow paths, one can observe that these lines separate particle trajectories. Particles that begin between the same two lines, in the same "alleyway", will travel similar paths, while particles that begin in different alleyways can undergo significantly different trajectories, separating quickly in time. Treating tracer trajectories as steady in the vortex frame of reference is only an approximation. Turbulence at scales smaller than the coherent structures, as well as the inevitable unsteady motion of the vortices as they travel, act to perturb these steady streamlines and allow tracer transport across them. However, the vortex velocity field, which appears steady in the moving frame, but oscillates at a point fixed in the laboratory frame, is the dominant temporal frequency present in the flow. In chapter 4, it was demonstrated that this structure is the dominant contributor to the transport of momentum through sweeps and ejections, and in the previous section it was shown that the momentum and scalar flux can be expressed in terms of its large-scale properties. For this reason, we study the transport of passive tracer particles in the conditionally-averaged flowfield in an attempt to understand the transport induced by the coherent structures.

In the simulations the numerical velocity field is seeded with particles at a grid of initial conditions, x_o, y_o at an initial time, $t = 0$. The particles are passively advected by the velocity field. Thus the trajectories $x(x_o, y_o, t)$ and $y(x_o, y_o, t)$ are described by the initial value problem

$$\frac{dx}{dt} = u(x, y, t) \tag{5.14a}$$

$$\frac{dy}{dt} = v(x, y, t). \tag{5.14b}$$

Here u and v are the velocity components in the frame of reference of the moving vortex. The initial value problem can easily be solved using the fourth order Runge-Kutte "ode45" algorithm in MATLAB.

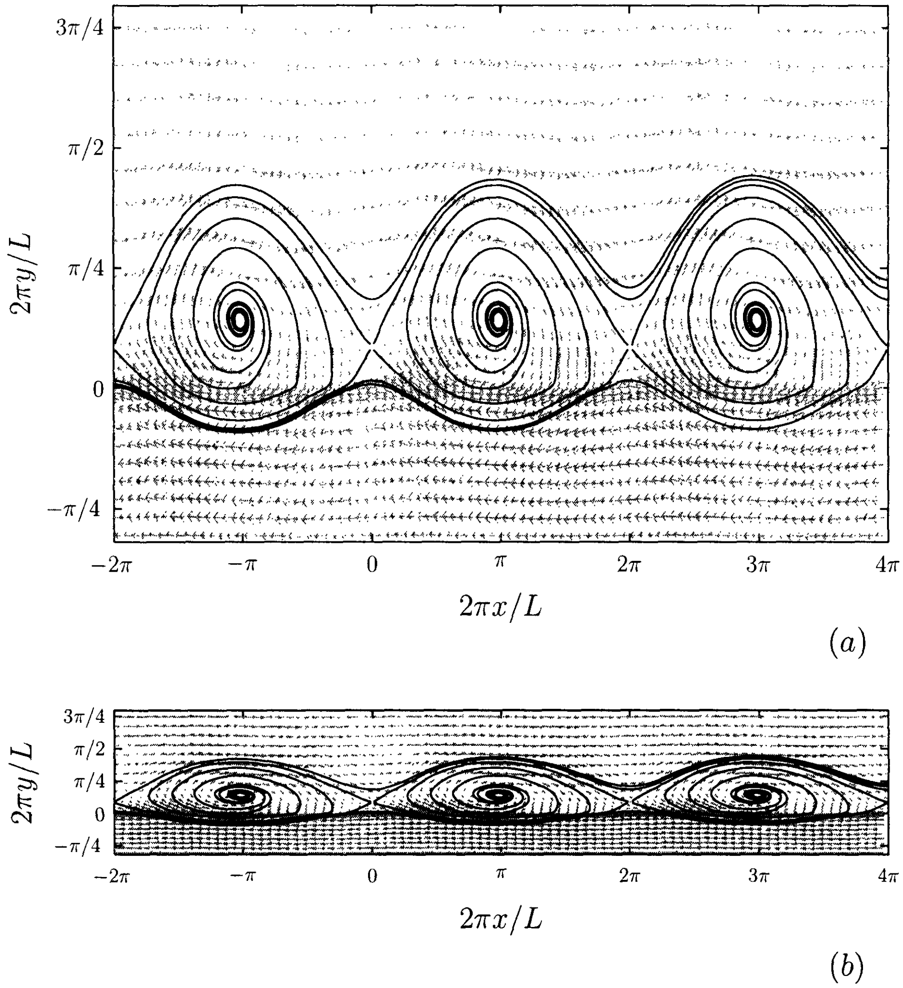

Figure 5-3: Velocity vectors and streamlines of the conditionally-averaged coherent structures. The velocity field is shown in a frame of reference traveling with the vortex center, at speed U_v. The streamwise and transverse axes are normalized by the vortex wavenumber, $x^* = 2\pi x/L$, $y^* = 2\pi y/L$. The the x^* and y^* axes are distorted in (a) for the purpose of visual clarity; in reality the vortices are highly elongated in the streamwise direction, as shown in (b) with undistorted axes.

The model for exchange outlined in section 5.1 relates the material flux across the interface to the temporal period, T_d, and the the area of vortices in the horizontal plane, $\delta_O L$ through the exchange ratio α. To measure the interfacial flux, and obtain a measure of α for comparison with the experimental result, numerical particle trajectories were integrated in time over one vortex period, and the total particle flux across the line $y = 0$ was noted. Figure 5-4$(a) - (e)$ shows the results of one such simulation (case I). The results for cases IV and VII are shown in figures 5-6 and 5-7. A region within the vegetation, $y^* < 0$, is initially dyed over a steamwise distance of two vortex wavelengths, $0 \leq x_o^* \leq 4\pi$. Over the duration of a single period, a portion of the particles are drawn across the interface, $y = 0$,and entrained into the passing vortex, while a portion travel backwards in the moving frame. It is easy to translate this reverse motion in the moving frame to the stationary laboratory frame: a stationary point moves to the left with a velocity L/T, so the initial dyed region at $t = 0$ is the same physical space as the region $-2\pi \leq x_o^* \leq 2\pi$ at $t = T$. Thus it can be seen from figure 5-4 that over one period, between (a) and (e), the particles have moved slightly downstream in the laboratory frame, albeit more slowly than those particles drawn into the vortex, which have effectively moved downstream one wavelength relative to their starting positions. This is made more clear in figure 5-5, which shows the same simulation, but in the fixed reference frame. The passing vortices are numbered for reference, demonstrating that they move to the right at a speed, U_v, that is much faster than the speed of the particles within the vegetation. Moreover, the simulation is run for a duration of $\Delta t = 3T_d$, demonstrating the separation in space between the particles entrained into the vortices and those that remain in the vegetation.

The particle trajectories also demonstrate the effect of the periodic flow within the vegetation induced by the pressure wave behavior of the passing vortices. The particles trajectories are oscillatory in both space and time, making the tracer distribution appear sinusoidal in figures 5-4–5-7. In figure 5-5 particle trajectories originating at five different transverse positions are shown in markers to demonstrate the oscillatory particle paths. Note that the excursion amplitude appears greater for case IV (figure

5-6) because the vortex wavelength, L, and thus the normalization length scale, is slightly lower for this case (and the aspect ratio, $L/2\delta_O$, larger). In table 5.1, the vortex wavelength is given for each case.

The pressure wave characteristics of the vortex directly influence the exchange rate, as the pressure perturbation induced by the vortex drives the cross flows that lead to exchange. An important parameter characterizing the potential for exchange is the communication length, l_c, which is defined as the length into the vegetation over which particles can be entrained into the vortex in one passage cycle. Particles residing beyond l_c from the vegetation edge will remain within the vegetation for the current cycle. This length scale is determined from the transport simulations and shown in table 5.1. Also shown for reference is the inner layer width, δ_I. Notice that l_c declines much less with increasing density than the inner layer width. This is because even for dense arrays, the crossflows, or ejections, driven by the vortex pressure fluctuation are able to carry out some particles beyond the inner layer width. It is suggested that this is one reason the the vortex exchange ratio, α does not appear to strongly depend on the cylinder density.

The particles trajectories in each simulation adhere very closely to the separating streamlines. Those particles that are drawn into a vortex follow the outer streamline of the central core and are ejected into the free stream by the rotation of the vortex, appearing as an arcing filament of dyed fluid. These filament structures closely resemble those observed in experimental particle visualization experiments in the flume, shown in figure 5-8. In these experiments, a fine powder consisting of reflective glass microspheres are sprinkled onto the water surface within the cylinder array and their transport into the free stream is imaged with a CCD camera. The good qualitative comparison of the particle distribution with those of the numerical simulations suggests that the gross characteristics of the particle flux is captured by the conditionally-averaged velocity field.

However, to see the importance of the unresolved small scale turbulence, consider the particles that are not drawn into a vortex. In the simulations, these particles, which begin outside the innermost separating streamline, are forever confined to the vegetated layer, unable to cross the steady streamline to enter the vortex. In reality, there exists a range of turbulence scales smaller than the coherent structures which perturb the streamlines and allow turbulent diffusion of mass across them. However, it is postulated that the rate of rotation and the length scale associated with the coherent structures, as the dominant scales of the flow, are also the dominant contributors to the rate of flux across the interface. The good qualitative comparison between the particle flux in the numerical simulations and in the experiments seems to bear this out. However, as a quantitative measure, the particle flux, and particularly the exchange ratio, α, in the simulations will now be compared with the experimental results discussed in section 5.1.

The exchange ratio, α for the transport process can be estimated by calculating the net particle flux across $y = 0$ over one period within one wavelength. First, the total volume of fluid crossing the interface into the vegetation over the duration of the simulation, $\Delta t = T_d$, is V_e. Initially the dyed region has a particle concentration of C_o, and thus, in terms of (5.1), the volume (per unit depth) exchanged is

$$\frac{V_e}{h} = \frac{N_{out} - N_{in}}{C_o}, \tag{5.15}$$

where N_{out} and N_{out} are the number of particles leaving and returning to the vegetated layer over the cycle and C_o is the initial particle concentration [*particles*/*area*] of the dyed region. The exchange ratio, α is then determined from (5.1) as the ratio of the volume exchanged to the vortex volume,

$$\alpha = \frac{V_e}{\delta_O L h}. \tag{5.16}$$

The values of α obtained for the steady streamline cases are shown in Table 5.1 under the heading ($\epsilon = 0$). The comparison is reasonable, but the values of α obtained numerically are $20\% - 50\%$ below the experimental value $\alpha \approx 0.3$. This is to be expected due to the neglect of small scale turbulent diffusion.

To evaluate the contribution of small-scale turbulence, separate simulations were performed with a time-perturbed velocity field. A periodic temporal perturbation with strength characterized by the small parameter, ϵ, was added to the conditionally-averaged velocity field. There is an exhaustive body of work on the enhancement of mixing caused by periodic perturbations of an otherwise steady two-dimensional velocity field. Work by Weiss & Knobloch (1989); Pierrehumbert (1991) studied the mixing induced by perturbations to traveling Rossby waves, which like the basic coherent structures studied here are steady in the traveling frame of reference. They found that the structure of the basic flow largely controls the rate of transport, but the perturbations enhance the diffusion of tracer across the basic streamlines. This effect is captured by the perturbation.

In our simulations, perturbations in the form of traveling waves were superimposed on the conditionally-averaged streamline structure to obtain the total time-varying velocity field

$$u^* = \frac{u}{U_v} + \epsilon \sin(y^*) \left[\cos(x^* - \omega_1 t^*) + \cos(x^* - \omega_2 t^*) + \cos(x^* - \omega_3 t^*)\right] \tag{5.17a}$$

$$v^* = \frac{v}{U_v} + \epsilon \cos(y^*) \left[\sin(x^* - \omega_1 t^*) + \sin(x^* - \omega_2 t^*) + \sin(x^* - \omega_3 t^*)\right]. \tag{5.17b}$$

where the velocity components are normalized by the vortex wave speed, U_v. The choice of three traveling waves and their frequencies is somewhat arbitrary, but a superposition of multiple frequencies was expected to be, while still a gross approximation, a better representation of a turbulent field than a single frequency. Additionally, it can be verified that the two-dimensional perturbations are non-divergent and thus satisfy conservation of mass.

In the simulations the perturbation frequencies were taken as $\omega_1 = 1$, $\omega_2 = 2$, and $\omega_3 = 5$ in the frame of reference of the coherent structures, which correspond to oscillations of, respectively, 2×, 4×, and 10× the coherent structure frequency in the laboratory frame. The results for $\epsilon = 0.2$ are shown in figure 5-9. The results in the stationary frame of reference are shown in figure 5-10. It can be seen that the addition of the perturbations enables the transport of particles across the limiting streamlines, creating, in essence, leaky vortices. This enhances the flux of particles across the interface, and leads to higher values of α (table 5.1). In fact with the addition of the perturbation, particularly for $\epsilon = 0.2$, the values of α are very close to the experimental value, $\alpha = 0.3$. Also shown in table 5.1 are the magnitudes of the small-scale turbulent fluctuations, u^*_{rms} (normalized by U_v) from experimental data. These are obtained from the the experimental LDA data for each velocity record by high pass-filtering the velocity fluctuations above the frequency of the coherent structures. The value of u^*_{rms} shown in the table is the maximum value across the shear layer, which occurs at the array interface. The magnitudes of u^*_{rms}, between $0.1 - 0.2$, are comparable to the parameter range of ϵ used in the numerical experiments. While ϵ is not a direct proxy for u^*_{rms}, both measure the approximate strength of the small scale fluctuations compared with the velocity of the coherent structures.

Although α increases with increasing ϵ, it is apparent from figure 5-9 that large-scale transport is still controlled by the rotation of the coherent structures, and the filaments of ejected tracer appear qualitatively similar to the basic case (figure 5-6). This suggests that together the coherent structures and small scale turbulence can account for the mass and momentum fluxes observed in the shallow and submerged vegetated layers presented in section 5.1.

Table 5.1: Vortex exchange ratio, α, from numerical tracer simulations.

case	$\epsilon = 0$	$\epsilon = 0.1$	$\epsilon = 0.2$	u^*_{rms}	L (cm)	l_c (cm)	δ_I (cm)
I	0.21	0.31	0.41	0.14	164	7.7	3.7
IV	0.24	0.29	0.34	0.18	116	8.8	2.6
VII	0.14	0.20	0.28	0.17	152	5.7	1.2

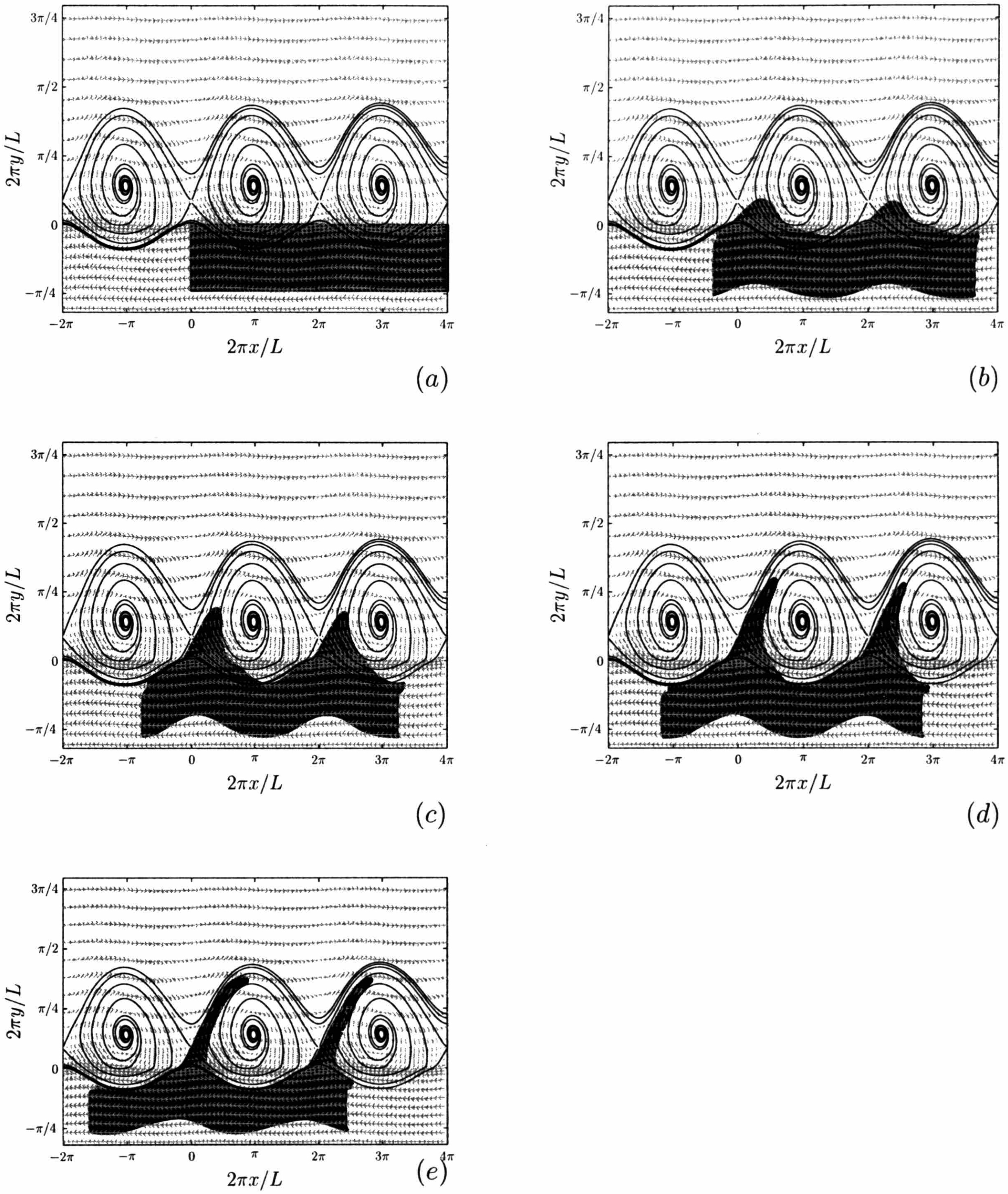

Figure 5-4: Results of numerical tracer experiments for case I. Particle positions are shown at various times: $t = 0$ (a), $t = T_d/4$ (b), $t = T_d/2$ (c), $t = 3T_d/4$ (d), $t = T_d$ (e). The flow is initially seeded with the rectangle of particles shown in (a). Because of the moving reference frame, the initial seeded area, $0 < x^* < 4\pi$ at $t = 0$, corresponds to final area $-2\pi < x^* < 2\pi$ at $t = T_d$. Streamlines and velocity vectors are shown for reference.

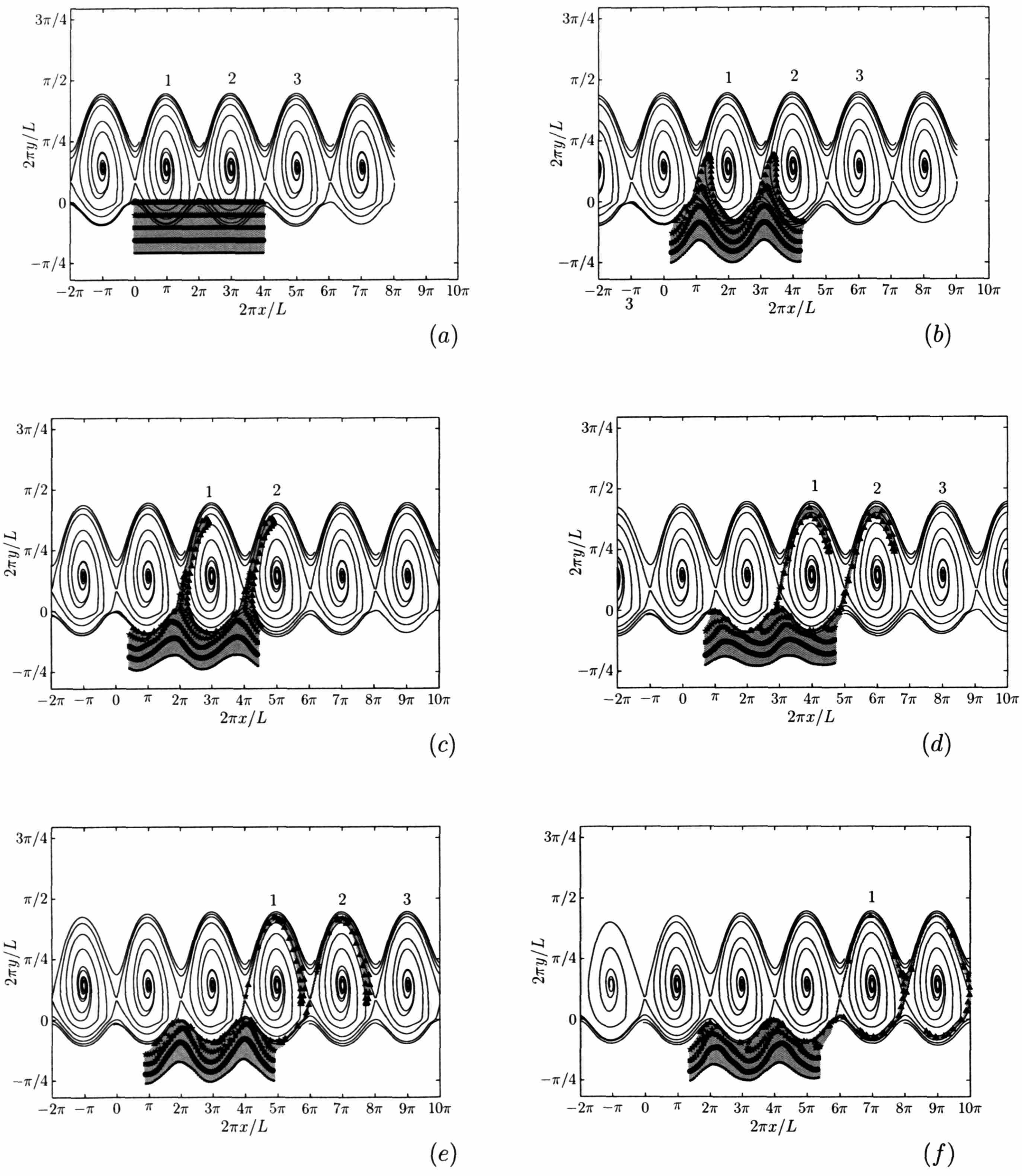

Figure 5-5: Results of numerical tracer experiments for case I in the stationary reference frame over a longer duration of $3T_d$. The entire ensemble is shown in gray and individual particles beginning at five different initial transverse positions (see (*a*)) are shown with markers. Snapshots of the trajectories are shown at $t = 0$ (*a*), $t = T_d/2$ (*b*), $t = T_d$ (*c*), $t = 3T_d/2$ (*d*), $t = 2T_d$ (*e*), and $t = 3T_d$ (*f*). The vortex streamlines, shown for reference, move to the right with speed U_v, and individual vortices are numbered to aid the reader in following the time evolution.

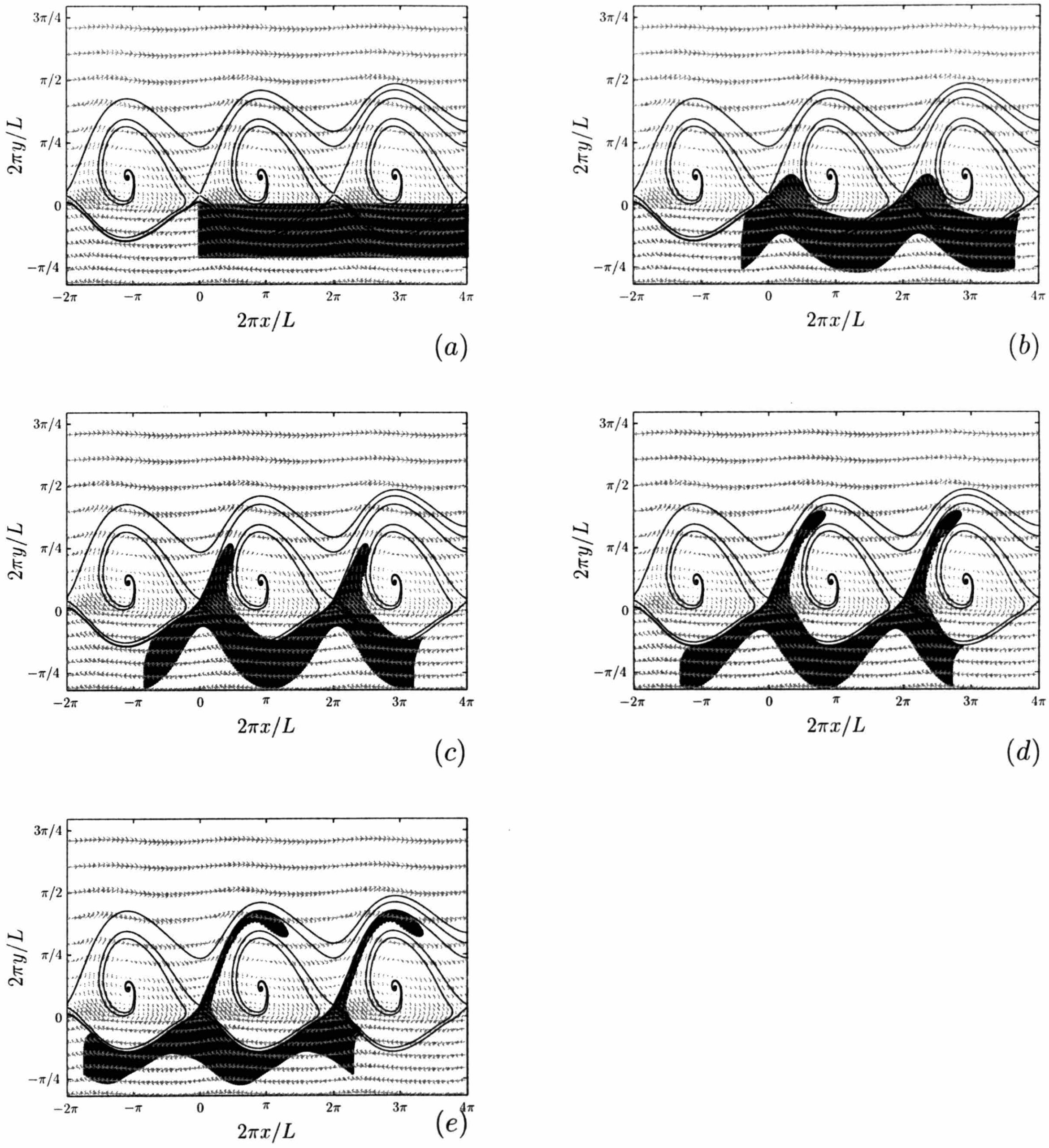

Figure 5-6: Results of numerical tracer experiments for case IV. Particle positions are shown at various times: $t = 0$ (a), $t = T_d/4$ (b), $t = T_d/2$ (c), $t = 3T_d/4$ (d), $t = T_d$ (e). The excursion amplitude within the array appears larger for this case because the wavelength, $L = 116$ is less, and the aspect ratio, $L/2\delta_O$ smaller than the other two cases shown (see table 5.1 for details).

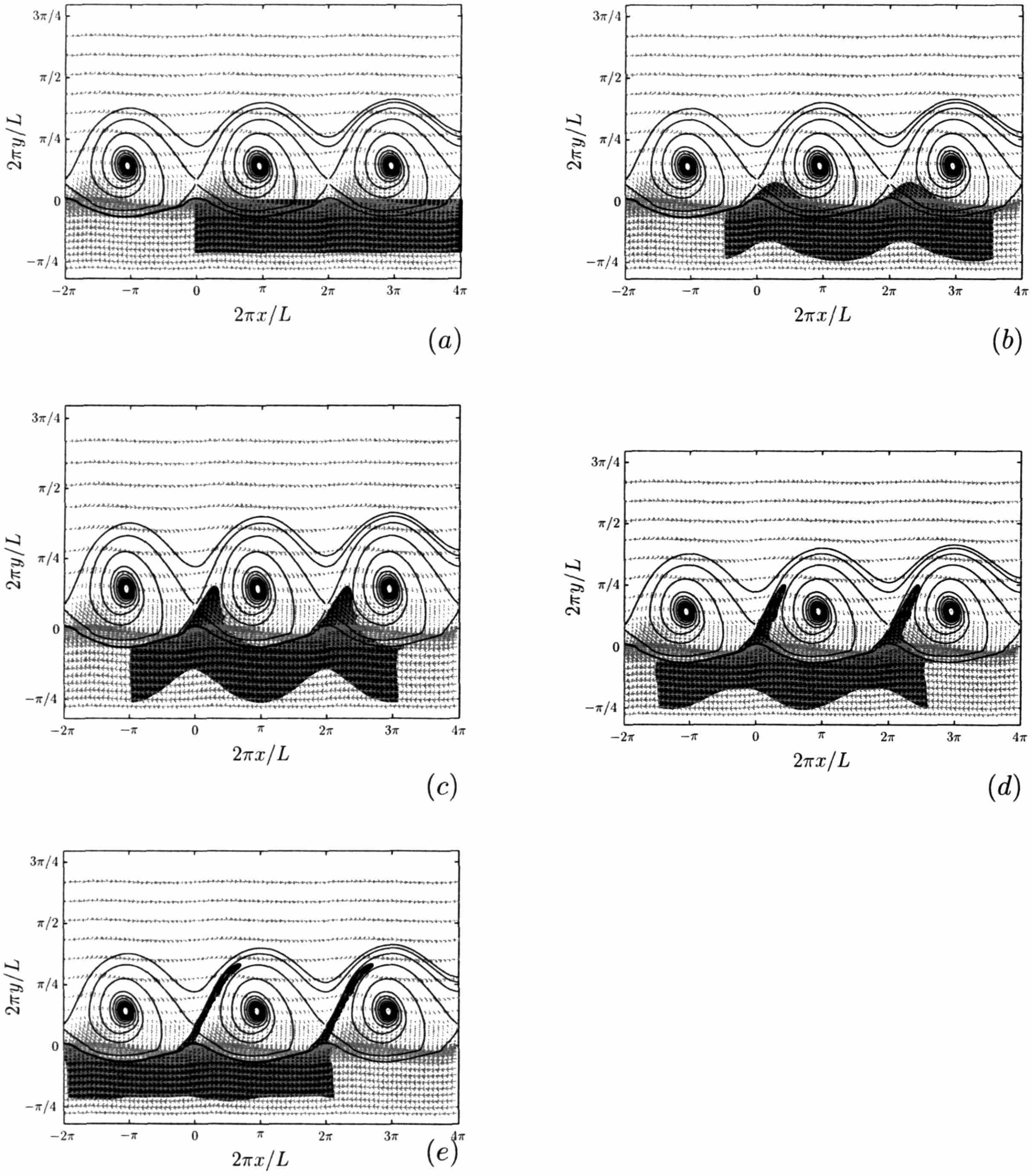

Figure 5-7: Results of numerical tracer experiments for case VII. Particle positions are shown at various times: $t = 0$ (a), $t = T_d/4$ (b), $t = T_d/2$ (c), $t = 3T_d/4$ (d), $t = T_d$ (e).

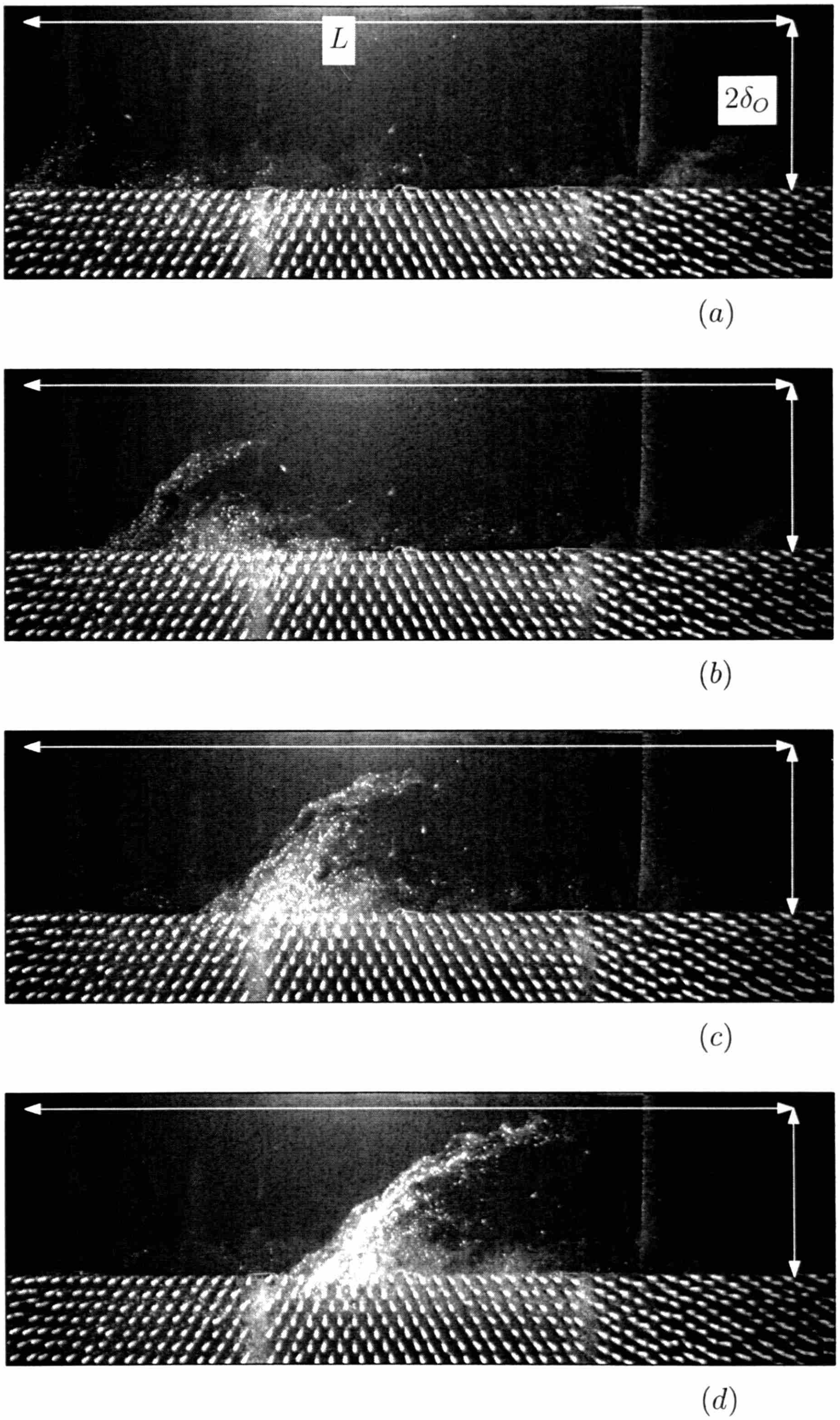

Figure 5-8: Time sequence of images from flow visualization of reflective tracer particles on the free surface. Particles are initially sprinkled over the cylinder array and are transported into the free stream by ejection motions associated with the coherent vortices. The vortex wavelength, L, and width scale, $2\delta_O$ are shown for reference and snapshots are taken at $t = 0$ (a), $t = 0.2T_d$ (b), $t = 0.4T_d$ (c), and $t = 0.6T_d$ (c).

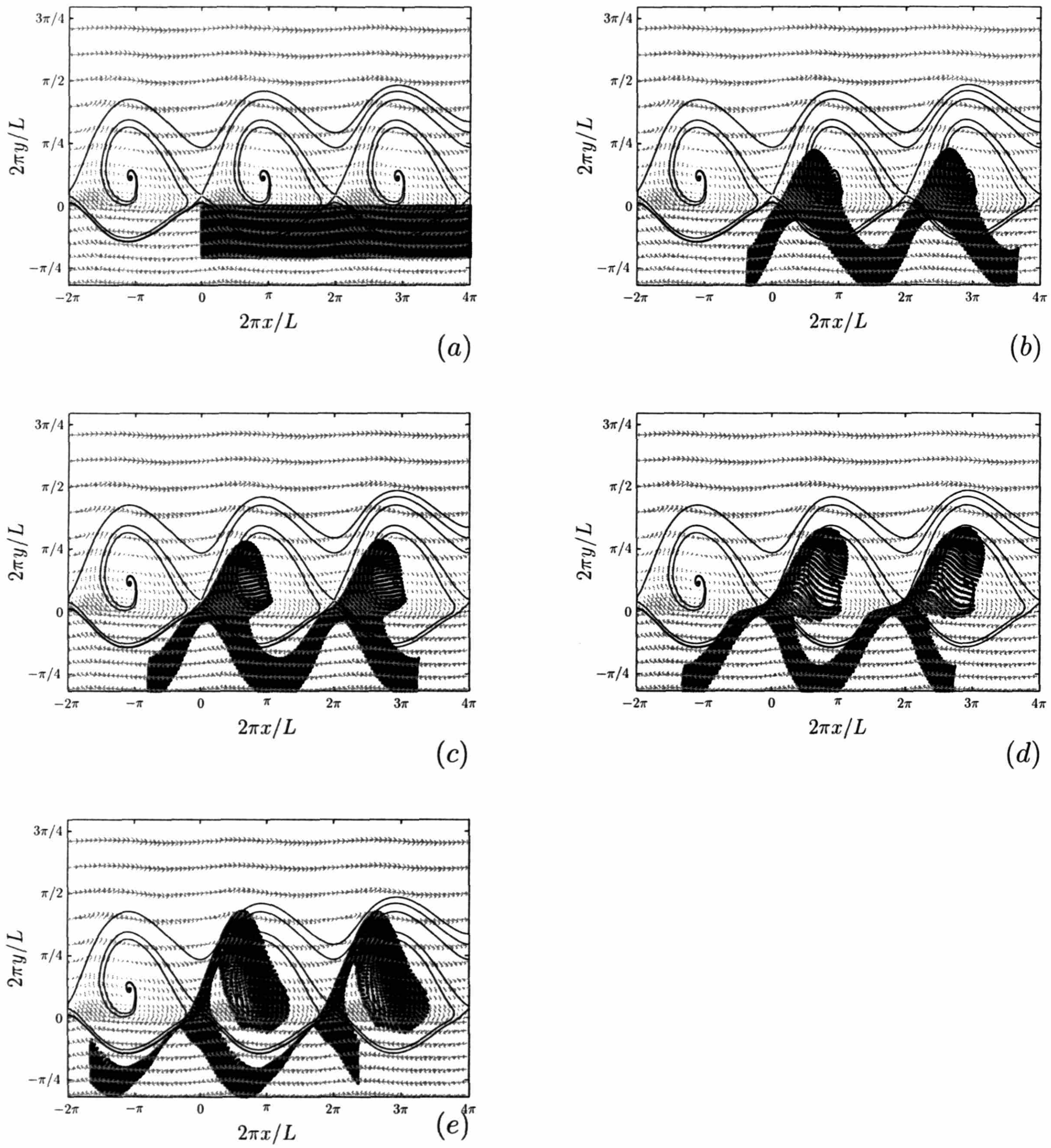

Figure 5-9: Results of numerical tracer experiments for case IV with imposed temporal perturbation of strength $\epsilon = 0.2$. Particle positions are shown at various times: $t = 0$ (*a*), $t = T_d/4$ (*b*), $t = T_d/2$ (*c*), $t = 3T_d/4$ (*d*), $t = T_d$ (*e*).

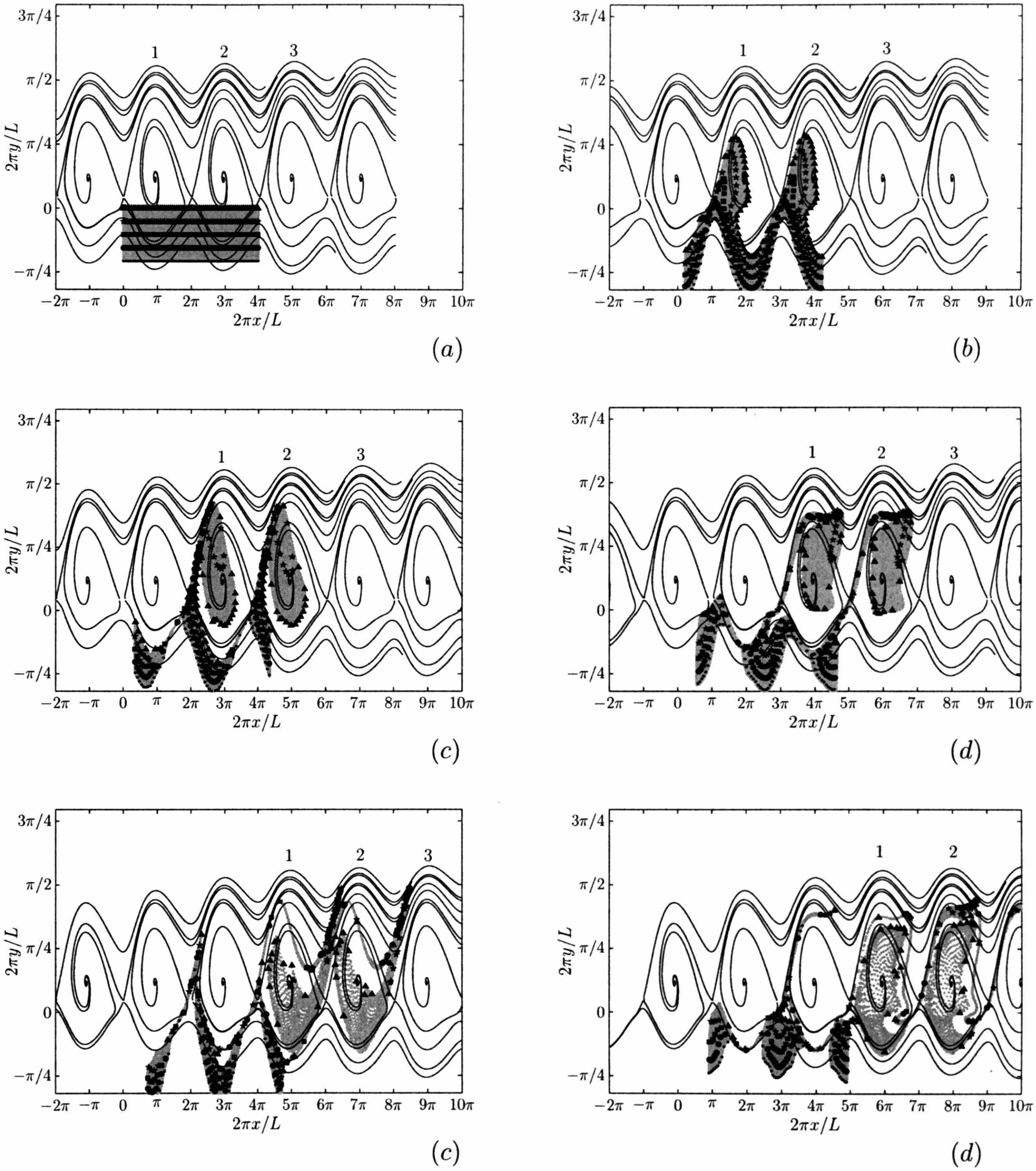

Figure 5-10: Results of numerical tracer experiments for case IV with imposed temporal perturbation of strength $\epsilon = 0.2$ over a longer duration of $3T_d$. The entire ensemble is shown in gray and individual particles beginning at five different initial transverse positions (see (a)) are shown with markers. Snapshots of the trajectories are shown at $t = 0$ (a), $t = T_d/2$ (b), $t = T_d$ (c), $t = 3T_d/2$ (d), $t = 2T_d$ (e), and $t = 5T_d/2$ (f). The vortex streamlines, shown for reference, move to the right with speed U_v, and individual vortices are numbered to aid the reader in following the time evolution.

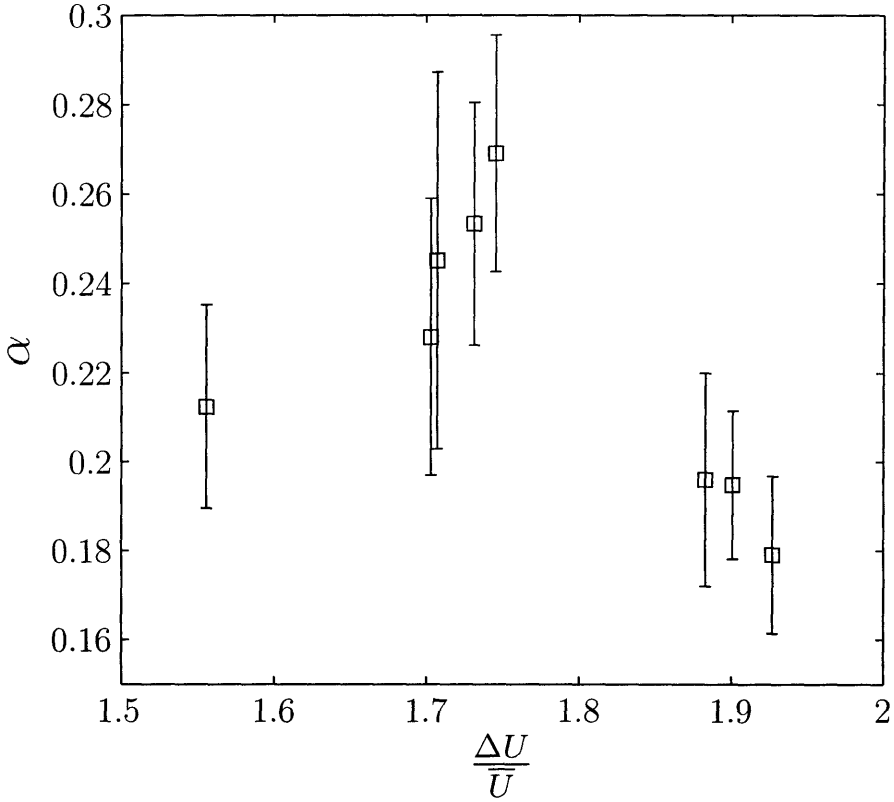

Figure 5-11: Vortex exchange ratio, α plotted against the normalized velocity difference, $\Delta U/\overline{U}$. There does not exist a statistically significant correlation (p-value = 0.16).

5.3 Higher Order Dependence of α on Vortex Rotation and Array Drag

The fact that α is approximately constant across experimental conditions suggests that the vortex volume turnover is approximately self-similar when normalized by the vortex size and passage frequency. However, as discussed in section 5.1.1, α, may also depend on the vortex rotation rate and the vortex penetration width. However, α appears to be nearly constant, and indeed there does not exist a significant correlation between α and $\Delta U/\overline{U}$, as shown in figure 5-11.

It was also suggested that the exchange ratio may depend on the array drag, expressed through $C_D a \delta_O$. In figure 5-12 this relationship is plotted, from which it can be seen that α does depend weakly on the array drag, with a highly significant correlation (p-value = 0.013). This dependence is further illuminated by the relationship between the strength of the vortex crossflows and the array drag. It has been found that increasing array drag leads to a decrease in the strength of the crossflows, measured by V_{rms}, the root mean square transverse velocity averaged over the vortex period. Figure 5-12 shows the decline of $V_{rms}/\Delta U$ with $C_D a \delta_O$. The normalization by the velocity difference, ΔU, is significant because it demonstrates that for a given ΔU, the strength of the crossflows, which may also be considered a measure of the vortex rotation strength, declines with increasing density. This clarifies a result of Ghisalberti & Nepf (2005a) which concluded that the mass transfer coefficient was proportional to the velocity difference, $k \propto \Delta U$. In fact, over a wider range of array drag than that used in the experiments of Ghisalberti & Nepf, the strength of the vortex crossflows, and thus the potential for exchange, decreases with increasing density. In contrast to the $k \propto \Delta U$ conclusion of Ghisalberti & Nepf, the model presented for vortex exchange in this chapter (5.4), with a constant value of α, predicts that $k \propto \overline{U}$. In the next section the behavior of the interfacial friction coefficient, f_i, a measure of momentum exchange, over a wide range of canopy densities, suggests that the present model better captures this decline in exchange efficiency with increasing density.

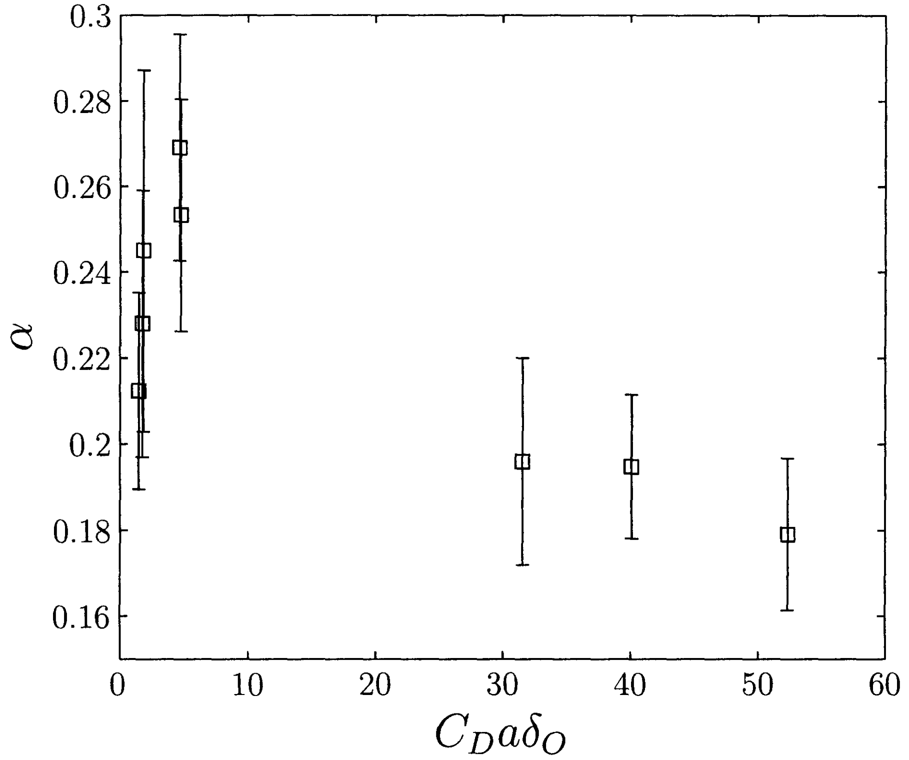

Figure 5-12: Values of the the vortex exchange ratio, α plotted with the array drag parameter, $C_D a d \delta_O$. There is a statistically significant (p-value = 0.013) trend, demonstrating a weak inverse relationship.

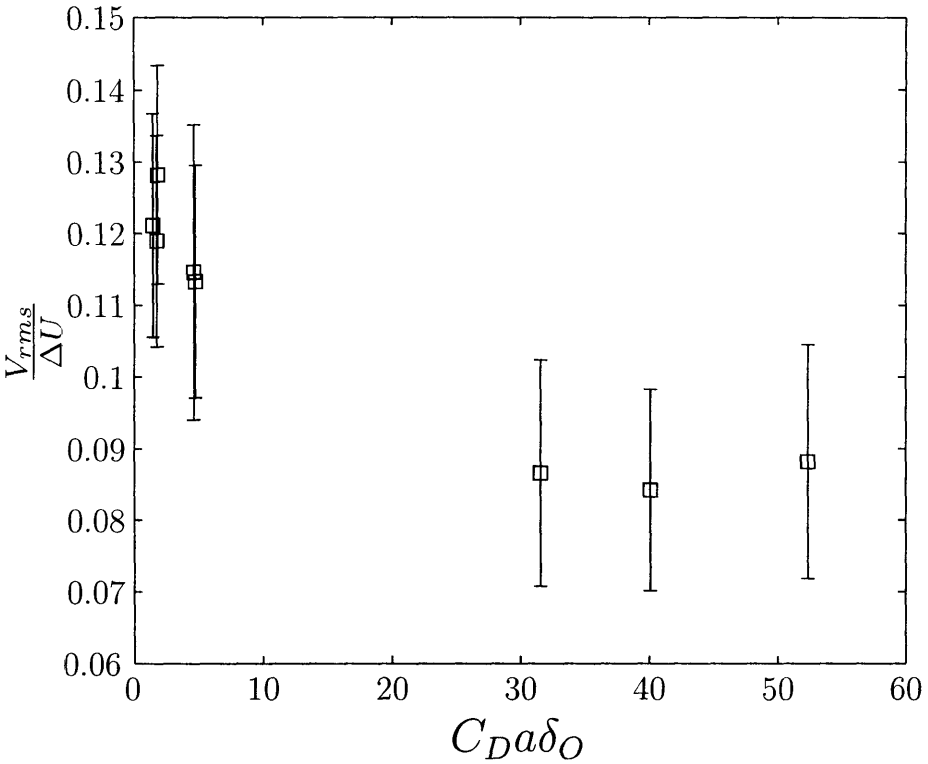

Figure 5-13: Strength of the vortex crossflows, $V_rms/\Delta U$, plotted with the array drag parameter, $C_D a d \delta_O$. There is a statistically significant (p-value = 0.001) inverse relationship.

5.4 A Predictive Framework for the Interfacial Mass and Momentum Fluxes

It appears that the vortex volume turnover is self-similar across a wide range of vegetation and flow conditions, leading to a nearly constant value of α. This provides a fairly simple means of predicting the mass transfer coefficient, k, for a wide range of flows near the interface of aquatic vegetation. From the relationship between k and α (5.2),

$$k = 0.032\alpha \frac{\delta_O}{\theta} \overline{U}, \tag{5.18}$$

where the fundamental shear layer frequency,

$$f_d = \frac{1}{T_d} = 0.032 \frac{\overline{U}}{\theta} \tag{5.19}$$

has been used. Thus the mass transfer coefficient can be related simply to the mean velocity, $\overline{U}$, across the channel, and a measure of the shear layer width, δ_O/θ. This latter ratio is determined by the shape of the velocity profile and has been found from both the present data and from that of Ghisalberti & Nepf (2005*a*) to be approximately constant and equal to $\delta_O/\theta \approx 3$.

While the mass transfer coefficient, k, may be of the ultimate interest, often only the momentum flux, or the interfacial shear stress, will be available for a particular system, and the mass flux can be obtained by analogy. Relationships relating the mass flux to the momentum flux are desirable for natural systems, in which the momentum flux typically easier to measure, requiring only velocity measurements of the Reynolds shear stress, $\langle u'v' \rangle$ at carefully-chosen points in the flow. In some instances, for instance for bank stability, the interfacial shear stress may be of interest in its own right. From (5.10) and (5.12) the interfacial shear stress, or momentum flux, is given in terms of α as

$$u_*^2 = k\gamma\Delta U = \gamma\alpha\frac{\delta_O}{T_d}\Delta U. \tag{5.20}$$

It can be seen from (5.20) that given a measurement of u_* in a natural channel, k can be determined and applied to mass transfer calculations. It is useful to defined a friction coefficient to describe the interfacial shear, which is given by

$$f_i = \frac{u_*^2}{\frac{1}{2}\Delta U^2} = 0.032\alpha\gamma\frac{\delta_O}{\theta}\frac{2\overline{U}}{\Delta U}. \tag{5.21}$$

The factor $R = \Delta U/2\overline{U}$ is commonly referred to as the dimensionless velocity ratio in free shear layer literature (Ho & Huerre, 1984). The friction coefficient is thus inversely proportional to R. Figure 5-14 shows the interfacial shear stress, $u_*^2/\Delta U^2 = f_i/2$, as a function of the dimensionless velocity ratio, R, for data taken from submerged aquatic canopies, terrestrial canopies, and the present experiments. The curve represents the semi-empirical prediction from (5.21) using $\alpha = 0.3$, $\gamma = 0.8$, and δ_O/θ taken as the average value across all of the velocity distributions from the

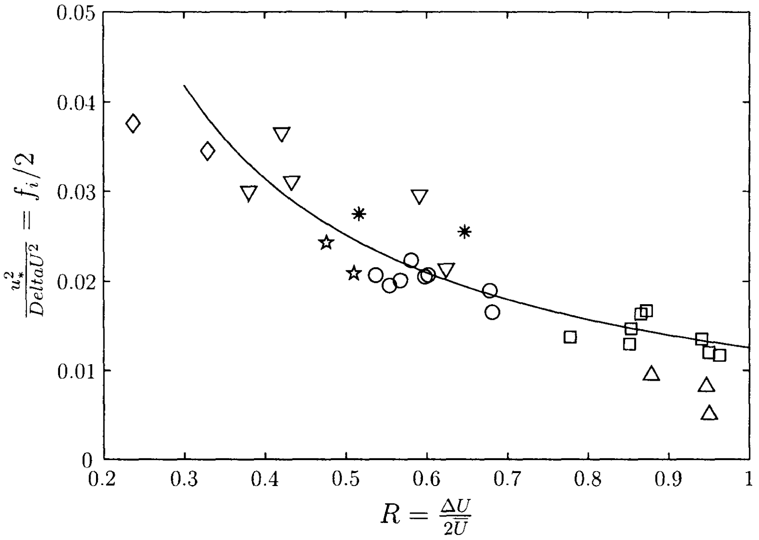

Figure 5-14: Interfacial shear stress, $u_*^2/\Delta U^2 = f_i/2$ plotted vs. the dimensionless velocity ratio, $R = \Delta U/2\overline{U}$. Experimental data collected from the present shallow channel experiments ($\square$, $\triangle$-low Re_θ) and submerged canopies; Ghisalberti & Nepf (2005*a*) ($\circ$), ?: rigid cylinders ($\triangledown$), flexible strips ($\star$), Nepf & Vivoni (2000) ($*$). The solid line is the semi-empirical prediction from (5.21).

present experiments and those from Ghisalberti & Nepf (2005*a*), ($\delta_O/\theta \approx 3.29 \pm 0.38$). The semi-empirical fit from (5.21) describes the data quite well, capturing the decline in friction coefficient with increasing velocity ratio. In general, denser canopies result in higher R, and thus a lower friction coefficient.

The relationship (5.21) appears to be applicable to a wide range of vegetated flows. However, to provide true predictive capability for field conditions, the velocity ratio, R must be determined for the system of interest. For shallow channels with vegetated floodplains, this is relatively straightforward. From Ikeda *et al.* (1991); Pasche & Rouvé (1985), among others, the flow far outside the interfacial shear region can be partitioned into two zones: the vegetated zone, with resistance by the vegetative drag, and the main channel zone, with resistance by the channel bed drag. For an applied forcing, given in terms of a free surface slope, $S = -dh/dx$, the velocity in each zone follows

$$gS = \frac{1}{2} C_D a U_1^2 \tag{5.22a}$$

in the vegetation, and

$$gS = \frac{c_f}{2h} U_2^2 \tag{5.22b}$$

in the main channel.

Rearranging yields the velocity difference in terms of the drag in each zone,

$$R = \frac{U_2 - U_1}{U_2 + U_1} = \frac{C_D a \sqrt{c_f/h} - c_f/h \sqrt{C_D a}}{C_D a \sqrt{c_f/h} + c_f/h \sqrt{C_D a}}. \tag{5.23}$$

For submerged vegetated flows, it is more difficult to determine the velocity difference because the flow in the overlying layer is restricted only by the vegetative drag, and thus U_2 depends on the interfacial shear stress, u_*. From, e.g., Nepf & Vivoni (2000), the velocity distribution above the canopy can be described by a logarithmic profile,

$$U(z) = \frac{u_*}{\kappa} \log\left(\frac{z - d}{z_o}\right) \tag{5.24}$$

where d is the zero-plain displacement and z_o the roughness height (for details, see Nepf & Vivoni, 2000). Thus, if U_2 is to be defined at some height, h, above the canopy, then

$$U_2 = \frac{u_*}{\kappa} \log\left(\frac{h - d}{z_o}\right) \tag{5.25}$$

and the velocity difference is

$$R = \frac{U_2 - U_1}{U_2 + U_1} = \frac{U_2 - \sqrt{\frac{gS}{\frac{1}{2}C_D a}}}{U_2 + \sqrt{\frac{gS}{\frac{1}{2}C_D a}}}. \tag{5.26}$$

Since R depends upon u_* through U_2, and from (5.21), u_* depends on R, an iterative method must be used to solve the interfacial shear stress for the system. This makes submerged canopies more complex than shallow vegetated channels.

5.5 Transport Equation Across the Interface

The majority of this chapter to this point has been devoted to determining the fluxes across the interface separating the vegetated and unvegetated regions. In addition to this exchange, the spatial variability of the material concentration field is often of interest. Using the turnstile model for exchange at the interface, the evolution of the full concentration field may be modeled by the advection-diffusion equation. Returning to the three zone model shown in figure 5-1, we wish to capture the spatial variation in concentration, particularly within the vegetation, where the bulk of the biological and chemical processes of interest occur, and where there is significant spatial heterogeneity due to the vegetation. Diffusion within aquatic vegetation is slow due to the reduced turbulent length scales (Nepf, 1999). Thus for wide layers, $B_1 \gg \delta_I$, the exchange with the main channel may be limited by the rate at which transverse diffusion can supply material to the exchange zone. Within the framework of the three zone model, the spatial variation in concentration can be captured by writing a separate advection-diffusion equation within each zone, and treating the interfacial flux (5.2) as a boundary condition between them. Specifically, within the vegetated zone,

$$\frac{\partial C_1}{\partial t} + U_1 \frac{\partial C_1}{\partial x} = D_{y1} \frac{\partial^2 C_1}{\partial y^2} + D_{x1} \frac{\partial^2 C_1}{\partial x^2} \tag{5.27a}$$

and within the main channel,

$$\frac{\partial C_2}{\partial t} + U_2 \frac{\partial C_2}{\partial x} = D_{y2} \frac{\partial^2 C_2}{\partial y^2} + D_{x2} \frac{\partial^2 C_2}{\partial x^2}, \tag{5.27b}$$

where D_{x1} and D_{y1} are the diffusivities (turbulent or molecular) within the vegetation, and D_{x2} and D_{y2} those within the main channel. The flux between the layers, J_s, is controlled by the rate of mass transfer by the vortices, which establishes a boundary condition along the interface,

$$J_s\big|_{y=0} = -D_{y1} \frac{\partial C_1(x,0,t)}{\partial y} = -k\Delta C. \tag{5.28}$$

where $\Delta C = C_2(x,0,t) - C_1(x,0,t)$, thus linking the concentration field in the vegetation to that in the main channel. This mass transfer boundary condition allows a discrete jump in the concentration in the main channel just outside the interface, $C_2(x,0,t)$, and the concentration within the vegetation just inside the interface,

$C_1(x, 0, t)$. This jump condition is physically justified by the fact that the exchange zone width, δ_I, is expected, from the results of section 2.5.5, to be small compared with either the main channel scale or the width of the vegetated layer (see figure 5-1). Thus, for sufficiently wide vegetated layers, $B_1 \gg \delta_I$, the interfacial flux can be viewed as confined to a vanishingly thin layer near $y = 0$.

5.6 Flushing Timescale for Vegetated Layer

The flushing timescale for the vegetated layer is of primary importance for biological processes in coastal marshes and riverine systems. It can affect, for example, the frequency at which hypersaline water in a mangrove stand is replenished by freshwater, or the residence time of nutrient spikes in a floodplain following a storm surge. The flushing time scale can be determined from the the transport equations (5.27) and (5.28) with some simplifying assumptions. First assume that the vegetated layer is long, such that streamwise gradients are negligible. Second, assume that mass mixes much faster over the main channel than the time required for flushing of the vegetated layer, as we are generally interested in systems for which exchange with the vegetation is the slowest step. Thus the concentration within the main channel can be taken as constant and equal to C_2. Since we are interested in the problem of the flushing of some material of interest from the vegetated layer, we can take $C_2 = 0$. Given these constraints, (5.27) and (5.28) reduce to

$$\frac{\partial C}{\partial t} = D_y \frac{\partial^2 C}{\partial y^2} \tag{5.29a}$$

$$D_y \frac{\partial C(x, 0, t)}{\partial y} = -kC(x, 0, t) \tag{5.29b}$$

and

$$\frac{\partial C(x, -B, t)}{\partial y} = 0, \tag{5.29c}$$

where the subscripts have been dropped since we are now interested only in the concentration within the vegetated layer. The second boundary condition (5.29c) is the no flux condition at the interior edge of the vegetated layer ($y = -B$). For the flushing problem, assume that at the initial time, $t = 0$, there is uniform concentration C_o within the vegetation. Before proceeding, it is useful to first define three dimensionless numbers that are important for the flushing problem. The ratio of the rate of mass transfer at the interface to the rate of diffusive mass transfer within the vegetation is the mass transfer Biot number,

$$Bi_m = \frac{kB}{D_y}, \tag{5.30}$$

and determines whether the rate of interfacial flux is limited by the rate of diffusion from within the vegetated layer. If $Bi_m \gg 1$, the exchange by the coherent structures at the interface is much faster than the rate of diffusion. The dimensionless exchange zone width,

$$\delta_{ex} = \delta_I / B \tag{5.31}$$

describes the proportion of the vegetated layer undergoing active exchange with the main channel (see figure 5-1). The mass transfer Fourier number,

$$Fo_m = \frac{D_y t}{B^2} \tag{5.32}$$

is a dimesionless time, scaled by the diffusive timescale. Using Bi_m and Fo_m (5.29) can be rescaled as

$$\frac{\partial C^*}{\partial Fo_m} = \frac{\partial^2 C^*}{\partial y^*} \tag{5.33a}$$

$$\frac{\partial C^*(x, 1, Fo_m)}{\partial y^*} = -Bi_m C^*(x, 1, Fo_m) \tag{5.33b}$$

and

$$\frac{\partial C^*(x, 0, Fo_m)}{\partial y^*} = 0 \tag{5.33c}$$

where

$$y^* = \frac{y + B}{B} \tag{5.34a}$$

and

$$C^* = \frac{C}{C_o}. \tag{5.34b}$$

Solutions to the system 5.33 are well-studied in the heat transfer literature (see, e.g., Incropera & DeWitt, 1981). There are two regimes based on the values of Bi_m. For $Bi_m \ll 1$, the flux of material at the interface is not limited by the rate of diffusion within the vegetated layer and the concentration is uniform across the vegetated layer. In this limiting regime, the solution is

$$\frac{C}{C_o} = \exp(-Bi_m Fo_m) = \exp(-\frac{k}{B}t). \tag{5.35}$$

The flushing timescale can be defined as the inverse of the exponential rate of decay, the e-folding time scale,

$$T_f = B/k = \frac{T_d}{\alpha}\frac{B}{\delta_O}. \tag{5.36}$$

The solution (5.35) prevails if either $Bi_m \ll 1$ or δ_{ex} is $O(1)$, regardless of Bi_m. In this case the active exchange zone occupies the entire vegetated layer and the interfacial flux is not limited by diffusion.

However, in the regime $\delta_{ex} \ll 1$ and $Bi_m \geq O(1)$, the interfacial flux is diffusion-limited, and concentration gradients develop within the vegetated layer. In this regime, (5.33) is an eigenvalue problem with a fairly complex series solution (see Incropera & DeWitt, 1981, section 5.4.1). However, the behavior is well-studied and results are tabulated for various values of Bi_m. For sufficiently large dimensionless time, $Fo_m \geq 0.2$, the solution is well-approximated by the first term in the series,

$$C^* = \beta_1 \exp(-\zeta_1^2 Fo_m) \cos(\zeta_1 y^*) \tag{5.37a}$$

where the eigenvalue, ζ_1 satisfies

$$\zeta_1 \tan(\zeta_1) = Bi_m. \tag{5.37b}$$

and

$$\beta_1 = \frac{4\sin(\zeta_1)}{2\zeta_1 + \sin(2\zeta_1)}. \tag{5.37c}$$

A highly accurate approximation for ζ_1 is given by Stevens & Luck (1999),

$$\zeta_1 = z_1 + \frac{-G + \sqrt{G^2 + 4H}}{2} \tag{5.38a}$$

where

$$G = (Bi_m + 1)\tan(z_1) + z_1, \tag{5.38b}$$

$$H = Bi_m - z_1 \tan(z_1), \tag{5.38c}$$

and

$$z_1 = \frac{\pi}{4}\left(1 + \frac{Bi_m - \pi/4}{Bi_m + \pi/4}\right) \tag{5.38d}$$

It is straightforward to evaluate the flushing timescale, by setting $Fo_m = 1/\zeta_1^2$ to yield

$$T_f = \frac{B_1^2}{\zeta_1^2 D_{1y}}. \tag{5.39}$$

It can be verified that in the regime where diffusion is not limiting, termed the exchange-dominated regime, $Bi_m \ll 1$ (or $\delta_{ex} = O(1)$), the solution (5.37) and the eigenvalue approximation (5.38) reduce to the uniform layer solution (5.35). In this case the flux across the exchange zone, driven by the coherent structures, controls the rate of flushing and the timescale is (5.36). In the diffusion-limited regime, $Bi_m \gg 1$, the rate of flushing is controlled almost exclusively by the rate of transverse diffusion within the vegetation, which limits the supply of mass to the exchange zone. In this limit, the solution (5.37) reduces to

$$\frac{C}{C_o} = \frac{\pi}{4}\exp(\frac{\pi^2}{4}\frac{D_{1y}t}{B_1^2})\cos(\frac{\pi}{2}y^*). \tag{5.40}$$

and the flushing timescale is

$$T_f = \frac{4}{\pi^2}\frac{B_1^2}{D_{1y}}. \tag{5.41}$$

To illustrate the diffusion-limited and exchange-dominated regimes, it is useful to normalize T_f by the rate of interfacial exchange,

$$T_f^* = \frac{T_f k}{B_1}. \tag{5.42}$$

In figure 5-15(a), T_f^* is plotted as a function of Bi_m along with the limiting $Bi_m \ll 1$ and $Bi_m \gg 1$ solutions. For $Bi_m \ll 1$, T_f^* is independent of diffusion, and hence independent of Bi_m. For $Bi_m \gg 1$, the flushing timescale is independent of the interfacial flux, hence, $T_f^* \approx (4/\pi^2)Bi_m$, the dimensional flushing time increasing in proportion to the diffusive time scale, B_1^2/D_y. With the small diffusivities observed deep within aquatic vegetation (Nepf, 1999), this time scale could be quite long.

In figure 5-15(b) is shown the transverse dependence of concentration within the vegetated layer for different values of Bi_m at time $t = T_f$. For $Bi_m = 0.01$, the exchange-dominated regime, the concentration is nearly constant, as the entire layer actively exchanges with the main channel. For $Bi_m = 3$ transverse diffusion is becoming important, creating a concentration gradient across the layer and limiting the concentration near the vegetation interface at $y^* = 1$. Finally, for $Bi_m = 100$, transverse diffusion is entirely limiting, and the concentration at the interface approaches zero, the mass flux carried by the coherent structures being limited completely by the supply of mass by transverse diffusion.

5.7 Application to a Natural System: Overbank Transport of Suspended Sediment in a River-Floodplain System

In section 5.1 a framework was outlined for predicting material flux across the main channel-vegetation interface. The flux was related to the properties of the flow in the main channel through (5.18) and a solution to the advection-diffusion equation with a prescribed first order interfacial flux was given in section 5.6. In this section, the framework is applied to problems of overbank transport of suspended sediment

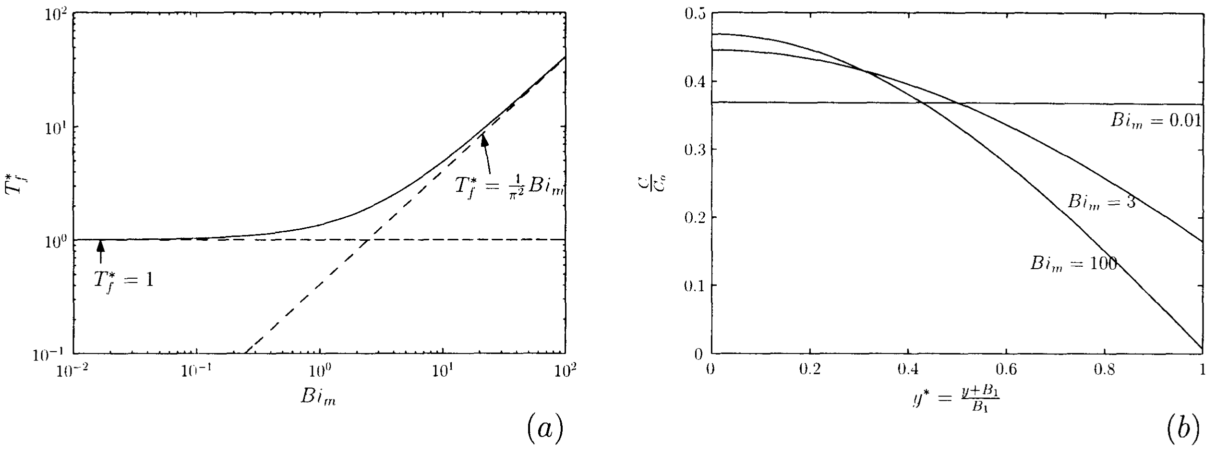

Figure 5-15: Graphical representations of the solutions to the flushing problem (5.37). In (*a*), the dimensionless flushing time, T_f^*, is plotted as a function of the Biot number, Bi_m. Also shown are the behavior in the exchange-dominated regime, $Bi_m \ll 1$, and the diffusion-limited regime, $Bi_m \gg 1$ (broken lines). In (*b*) is shown the transverse concentration distribution, $C^* = C(y^*)/C_o$ at $t = T_f$ for various values of Bi_m.

in river-floodplain or channel-marsh systems by including a term in the diffusion equation to account for particle settling and deposition on the floodplain. A dimensionless number is introduced which expresses the relative rates of floodplain flushing and particle settling, and which influences patterns of deposition.

The problem of overbank sediment transport has implications both for the geomorphology and contaminant fate in riverine and estuarine environments. In many low energy rivers the evolution of floodplains is primarily due to deposition of suspended sediments from the main channel during times of flood (Lecce & Pavlowsky, 2004). In coastal salt marshes or mangrove forests, sediment supply from tidal creeks is an important process in the sediment balance that dictates, for example, whether marsh accretion can keep pace with sea level rise (Stumpf, 1983). Further, Allen (1992) suggested the best framework for sediment fluxes in salt marshes is from the perspective of overbank transport, in analogy to floodplains.

Suspended sediments also can carry significant concentrations of adsorbed contaminants, such as heavy metals (Macklin, 1996), and when deposited in the floodplain or marsh, can affect the health of ecosystems and the quality of water intended for human use. Several workers have noted the importance of the channel vegetation interface for fluxes of suspended sediments, and many have noted the existence of coherent vortices between the floodplain and the main channel (Allen, 1992; Pizzuto, 1987) (though most are laboratory studies, with very few, if any, field observations). In general, observations of sediment deposits over floodplains reveal a decrease in total deposition and a progressive fining on the floodplain with increasing lateral distance away from the main channel (Allen, 1992; Lecce & Pavlowsky, 2004). Pizzuto (1987) proposed a model to account for this which relied on turbulent diffusion from the main channel to carry sediment to the floodplain. He solved a form of the advection-diffusion equation with a first order settling term to yield sediment deposition patterns away from the channel.

Here, an alternative formulation of the diffusion equation is presented that explicitly accounts for the interfacial flux of material driven by the coherent structures. This can be done by making the boundary condition at the channel-vegetation interface a flux-driven boundary condition, with the mass transport rate equal to that associated with the coherent structures. Then a first-order decay term is simply added to the diffusion equation presented in section 5.6 to account for sediment deposition. Equation (5.29*a*) then becomes

$$\frac{\partial \widetilde{C}}{\partial t} = D_y \frac{\partial^2 \widetilde{C}}{\partial y^2} - r\widetilde{C} \tag{5.43}$$

where where $\widetilde{C}$ is the depth-integrated concentration,

$$\widetilde{C} = \int_0^h C(y, z, t)dz \tag{5.44}$$

and r is the settling rate (the tilde notation will be dropped from here forward). If there is not significant sediment resuspension, a simple characterization of the settling rate is

$$r = \frac{V_s}{h}, \tag{5.45}$$

where V_s is the grain-size dependent settling velocity.

Because the governing equation and the boundary conditions of (5.43) are identical to the original problem without settling (5.29) except for the first order decay term, the well-known method of Danckwerts (1951) can be applied to find the solution to the settling problem. According to the method, if $C'(y,t)$ is the solution to the original flushing problem, the solution to the problem with settling is

$$C(y,t) = k\int_0^t e^{-\frac{V_s^2}{D_z}t'} C'(y,t')dt' + C'(y,t)e^{-\frac{V_s^2}{D_z}t}. \tag{5.46}$$

In section 5.6 the flushing problem was solved with the interfacial flux boundary condition (5.5b) and an initial material concentration, C_o, in the vegetated layer at $t = 0$. In the deposition problem, it is desired to know the transient deposition from the main channel onto the floodplain with time from the onset of flood stage. Hence the initial conditions are a constant main channel concentration, C_c, and zero initial concentration on the floodplain. The boundary and initial conditions for (5.43) are thus

$$D_y \frac{\partial C(0,t)}{\partial y} = k(C_c - C(x,0,t)), \tag{5.47a}$$

$$\frac{\partial C(B,t)}{\partial y} = 0 \tag{5.47b}$$

and

$$C(y,0) = 0. \tag{5.47c}$$

The solution is obtained by the same method as in section 5.6 with the substitution (5.46). The full solution is in the form of a Fourier series,

$$C = C_c \left[1 - \sum_{n=1}^{\infty} \left(\frac{4\sin(\zeta_n)}{2\zeta_n + \sin(2\zeta_n)} \right) \cos(\zeta_n y^*) \frac{S}{S + \frac{\zeta_n^2}{\zeta_1^2}} \left(\frac{1}{S}\frac{\zeta_n^2}{\zeta_1^2} e^{-Fo_m(\zeta_n^2 + S\zeta_1^2)} + 1 \right) \right], \tag{5.48}$$

where the dimensionless time and lateral coordinate, Fo_m and y^*, and the eigenvalues, ζ_n, are identical to those of the flushing problem, presented in section 5.6. The dimensionless number S, termed the settling number, is the ratio of the flushing to settling time scales,

$$S = rT_f = \frac{V_s}{h}\frac{B^2}{\zeta_1^2 D_y}. \tag{5.49}$$

For wide vegetated plains for which flushing is limited by transverse diffusion, $Bi_m \gg 1$, the settling number reduces to

$$S = \frac{V_s}{h}\frac{B^2}{D_y}, \tag{5.50}$$

while for narrower floodplains controlled by vortex-induced mass transfer, $Bi_m \ll 1$, the settling number becomes

$$S = \frac{V_s}{h}\frac{B}{k}. \tag{5.51}$$

In section 5.6 only the first term in the series solution for concentration was necessary to approximate the solution without settling for $Fo_m \geq 0.2$. Thus, in the limit of slow settling, $S \to 0$, the first term in (5.48) will also be sufficient for the settling problem. However, for large values of S, i.e., larger grain sizes, it has been found that several terms in the series are necessary. For these cases, the simple method of Stevens & Luck (1999) yields the eigenvalues, ζ_n, the same method described for calculating ζ_1 in section 5.6. As in the flushing problem, the eignevalues, ζ_n are functions of the Biot number, $Bi_m = kB/D_y$, the ratio of the timescales for flushing by interfacial mass transfer and by turbulent diffusion.

When (5.48) is compared with the asymptotic ($Fo_m \geq 0.2$) solution in the absence of settling,

$$C(y^*, t) = C_c \left(1 - \beta_1 e^{-\zeta_1^2 Fo_m} \cos(\zeta_1 y^*)\right), \tag{5.52}$$

it can be seen that settling has two effects. For higher rates of settling (higher S), the system will reach a steady-state concentration distribution faster, as the product $Fo_m\,(\zeta_n^2 + S\zeta_1^2)$ in the exponential of (5.48) increases with S. In addition, the steady state suspended sediment concentration distribution,

$$C = C_c \left[1 - \sum_{n=1}^{\infty} \left(\frac{4\sin(\zeta_n)}{2\zeta_n + \sin(2\zeta_n)}\right) \cos(\zeta_n y^*) \frac{S}{S + \frac{\zeta_n^2}{\zeta_1^2}}\right], \tag{5.53}$$

is reduced by due to the factor

$$\frac{S}{S + \frac{\zeta_n^2}{\zeta_1^2}}. \tag{5.54}$$

To illustrate, without settling, i.e., $S = 0$, the factor in (5.54), and hence the total Fourier sum in (5.53), tends to zero. In this case so the steady state concentration on the floodplain is equal to that in the main channel concentration, C_c. However with increased settling, this factor becomes nonzero, and the Fourier sum in (5.53) takes on a value between 0 and 1. The floodplain concentration is thus reduced from that in the main channel. The reduced suspended sediment concentration for increasing S implies an increased rate of deposition. The dependence on S can be explained as follows. When the rate of flushing is much faster than the rate of settling, parcels of fluid tend to complete a circuit from main channel to floodplain and back again before the sediment they contain can deposit on the floodplain. However, when the settling rate is faster (high S) significant deposition is possible within the time a given fluid parcel spends on a floodplain excursion. This results in the reduced suspended sediment concentration, i.e., greater deposition.

The rate of deposition is simply the loss term from (5.43),

$$R(y,t) = \frac{V_s^2}{D_z} C(y,t), \tag{5.55}$$

from which a normalized rate of deposition can be defined

$$R^* = \frac{R(y,t)}{C_c} T_f = S \frac{C(y,t)}{C_c}. \tag{5.56}$$

It can be seen that the deposition rate is proportional to the settling number.

Also of interest is the total mass deposited per unit area, A, for example, over the duration of a flood. This is easily computed by the integral of the settling rate,

$$\begin{gathered} A^* = \frac{A}{SC_c} = \frac{1}{SC_c} \int_0^t \frac{V_s^2}{D_z} C(y^*, t') dt' = \\ \zeta_1^2 Fo_m - \sum_{n=1}^{\infty} \left(\frac{4 \sin(\zeta_n)}{2\zeta_n + \sin(2\zeta_n)} \right) \cos(\zeta_n y^*) \frac{1}{S + \frac{\zeta_n^2}{\zeta_1^2}} \left[\frac{1 - \exp\left(-Fo_m \left(\zeta_n^2 + S\zeta_1^2\right)\right)}{1 + S\frac{\zeta_1^2}{\zeta_n^2}} + \zeta_1^2 S Fo_m \right]. \end{gathered} \tag{5.57}$$

where A is normalized by the main channel concentration and the settling number.

The normalization demonstrates that the total deposition is also proportional to the settling number, S.

Note that several assumptions are inherent in the model for sediment transport used in this section. First, a constant transverse eddy diffusivity, D_y is assumed over the floodplain. In fact, spatial variations are likely to exist due to variations in water depth, topography, and density of floodplain vegetation. A second assumption is that suspended sediments are deposited only by gravitational settling. In fact Allen (1992) found that sediment capture by salt marsh vegetation can account for as much as 50% of the sediment loss from the water column. This capture is likely to be reasonably captured by a first order loss term like that in (5.43), but with a different form than (5.45).

To characterize sediment deposition in natural systems, typical length and velocity scales in channel-floodplain systems will now be given. The width of a characteristic floodplain valley, B, like that studied by Lecce & Pavlowsky (2004) is of the order of $10-100$ m, and the water depth on the floodplain, h, is of order $10-100$ cm (Nicholas & Walling, 1998). Typical values of the vegetation density, in terms of a the frontal plant area per unit fluid volume, are $0.01-0.1$ cm^{-1} both for salt marsh grass (Nepf, 1999) and also, for example, for agricultural crops such as corn (Aylor, 2005), which may occupy a river floodplain. From the vegetation density, the characteristic width of the exchange zone, the penetration of the coherent structures onto the vegetated plain, is

$$\delta_I = c(C_D a)^{-1}, \tag{5.58}$$

where c is a constant found empirically, as in section 2.5.5 figure 2-10. Taking the drag coefficient to be $C_D = O(1)$, and with the range of a given above, the exchange zone width is $O(10-100)$ cm. Clearly, the typical exchange zone width is small compared with the valley width, such that $\delta_{ex} = \delta_I/B \ll 1$. Thus, the interfacial material flux driven by the coherent structures is well-approximated by the interfacial boundary condition at $y=0$, (5.47a).

Typical velocities in the main channel are of order $0.5-1.0$ ms^{-1}. Thus the interfacial exchange coefficient, $k \approx 0.03\overline{U}$, from (5.18) is of the order 1 cms^{-1}. From k, the mass transfer Biot number, may be computed, $Bi_m = kB/D_y$, which determines the predominance of either turbulent diffusion or interfacial mass transfer and thus requires an estimate of D_y within the vegetated floodplain. Nepf (1999) gives an expression for turbulent diffusion within emergent vegetation,

$$D_y \approx 0.8\left(C_D a d\right)^{1/3} U_v d, \tag{5.59}$$

where d is the characteristic stem diameter and U_v the mean velocity in the vegetation. Rough values for d and U_v are 1 cm and $1 - 10$ cms^{-1}, yielding a diffusivity of the order, $D_y \approx 1$ cm^2s^{-1}. The Biot number is then estimated to be of order $10^3 - 10^4$. Thus floodplain flushing is limited by turbulent diffusion from within the vegetation.

The importance of settling relative to flushing is determined by the settling number S, defined in (5.51). The settling rate is determined by the sediment grain size, d, which can be divided into three ranges from largest to smallest: course silt ($16\mu m < d < 62.5\mu m$), fine silt, ($4\mu m < d < 16\mu m$), and clay ($d < 4\mu m$) (Stumpf, 1983). For each size class, the settling velocity, V_s can be calculated from the well-known Dietrich curve (Dietrich, 1982). For course silt ($d = 62.5\mu m$) $V_s = 3 \times 10^{-1}$ cms^{-1}; for fine silt ($d = 16\mu m$) $V_s = 2 \times 10^{-2}$ cms^{-1}; for clay ($d = 4\mu m$) $V_s = 1 \times 10^{-3}$ cms^{-1}. Further, the settling rate depends on the water depth, h, which can be taken, as above, to be $h \approx 50$ cm. The settling number is then calculated as

$$S = \frac{V_s}{h}\frac{B^2}{D_y} = O\left(\frac{[V_s]}{[50\ cm]}\frac{[1000\ cm]^2}{[1\ cm^2s^{-1}]}\right) \tag{5.60}$$

and yields a range of settling numbers from $S = O(1)$ for clay, $S = O(10^2)$ for fine silt and $S = O(10^5)$ for course silt. Thus, it can be concluded that, for the typical floodplains characterized here, all particle fractions of silt, which have a settling rate much greater than the rate of flushing ($S \gg 1$), will deposit substantially on the floodplain. Only a portion of the largest clay fractions, with settling timescales comparable to the flushing time scale ($S = O(1)$), will be deposited. However, smaller clay fractions, with $S < O(1)$, will settle too slowly in comparison to the flushing time scale, and will not be appreciably deposited on the floodplain.

Solutions for suspended sediment concentration and deposition rate are shown in figure 5-16 for various values of S and Bi_m. In (a) and (b) are shown profiles for $Bi_m = 1000$, corresponding to the parameter regime calculated above for natural floodplains, and indicative of the diffusion-limited regime. Consistent with this, significant concentration gradients develop across the floodplain (a). The normalized concentration, C/C_c for each value of S attains a maximum value equal to 1 at the vegetation interface ($y^* = 1$). However strong particle size fractionation can be observed, as the concentrations of silt particles ($S = 100$ and $S = 1000$ based on the calculations above) decay rapidly with distance onto the floodplain, due to strong settling. Finer particles, particularly clays ($S \leq 1$ based on the above calculations) tend to remain in suspension and still have appreciable concentration at the inner floodplain extent ($y^* = 0$). Consistent with these results, the deposition rate (b) for larger size fractions (higher S) is very high near the vegetation interface, but decays quickly with distance onto the floodplain. Fines have a much lower relative deposition rate near the interface, but, as their concentration is still appreciable, constitute the only sediment deposition further onto the floodplain. Thus the commonly-observed fining with increasing distance onto the floodplain (Allen, 1992; Lecce & Pavlowsky, 2004) is described by the present model.

The results for the interfacial mass transfer-limited regime, $Bi = 0.01$, are shown in figure 5-16(c) and (d). In this regime, the entire floodplain is in the zone of active exchange with the main channel, and thus the suspended sediment concentration (c) is approximately constant across the floodplain for each value of S. As expected, the floodplain concentration declines steadily with an increase in the settling number. The rate of deposition (d) is dominated by course material near the interface, and finer material further onto the floodplain. However, the progressive fining is not as marked as in the diffusion-limited regime. The concentration of course material does not decay as rapidly onto the floodplain as in the diffusion-limited case, and thus an appreciable amount of course material is still deposited at the inner floodplain extent, $y^* = 0$.

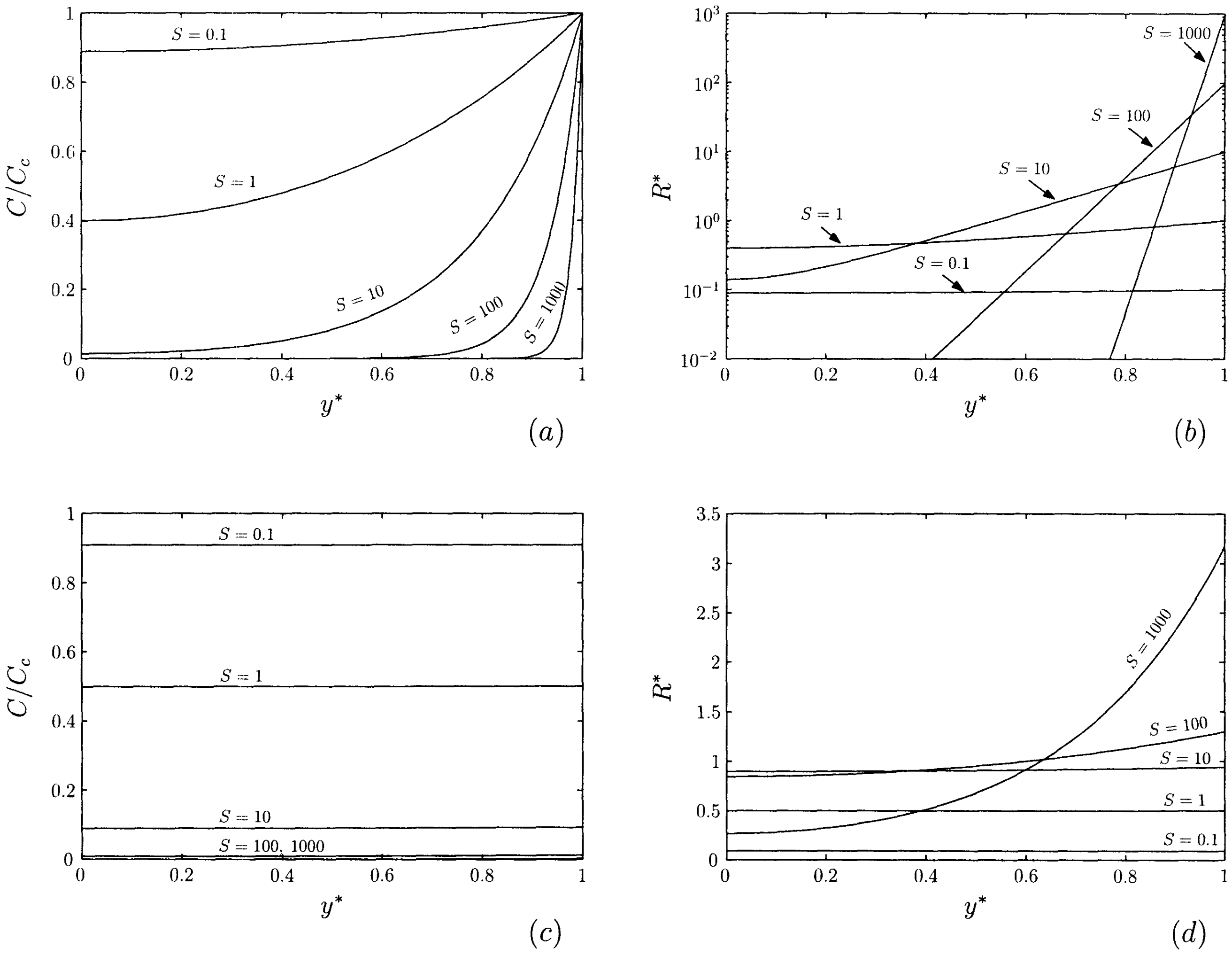

Figure 5-16: Suspended sediment concentrations and rates of deposition for various values of the settling number, S and the Biot number, Bi_m at steady state. $Bi_m = 1000$ (diffusion-limited regime): (*a*), normalized concentration and (*b*), normalized deposition rate. Deposition is plotted on a semilog scale. $Bi_m = 0.01$ (mass-transfer-limited regime): (*c*), concentration and (*d*), deposition rate. $Bi_m = 1000$ typifies most natural floodplains, with $S \geq 100$ for silt and $S \leq 1$ for clay sediments.

5.8 Secondary Circulations

It is well known that the shear layer vortices that form between the main channel and the floodplain in compound channels create secondary circulations that contribute to the overall shear stress (Shiono & Knight, 1991). The same effect may be expected of shallow partially vegetated channels. For fully-developed flow, the depth-averaged momentum equation for a composite channel with a free surface is

$$0 = g\frac{\partial \zeta}{\partial x} + \frac{\partial}{\partial y}\left(-\widetilde{\langle u'v'\rangle} + \widetilde{UV}\right) - (\tau_b + \tau_v) \tag{5.61}$$

where the tilde represents a depth-average, and $\langle u'v'\rangle$ is the turbulent Reynolds stress.

$$\tilde{f} = \frac{1}{h}\int_0^h f dz. \tag{5.62}$$

In addition, the height of the free surface above a datum is introduced, $\zeta = h + z_d$, where z_d is the height of the bed above the datum. The quantities τ_b and τ_v denote the stress due to bottom friction and vegetative drag, which, when allowed to vary with transverse position, make the form (5.61) applicable both inside and outside the vegetated layer. It can be seen that the time-averaged Reynolds stress, $-\langle u'v'\rangle$ is augmented by an additional shear stress due to secondary currents, $\widetilde{UV}$. Experiments by Shiono & Knight (1991) in a compound channel demonstrated that the shear stress due to secondary circulations can be of comparable magnitude with the Reynolds stress. The secondary currents are enhanced by the transverse depth variation characteristic of compound channels.

In addition to directly affecting momentum and material transport across the interface by the sweep and ejection cycle, the coherent structures in the present experiments contribute to secondary currents, by inducing a near-bed flow. This is is illustrated by the conditionally-averaged velocity vectors and streamlines in the horizontal plane, shown in figure 5-17 at two different depths, $z = 0.5$ *cm* (*a*) and $z = 4.0$ *cm* (*b*). At $z = 4.0$ *cm* the velocity structure is the same as the mid-depth measurements presented throughout chapter 4. The streamlines spiral outward from

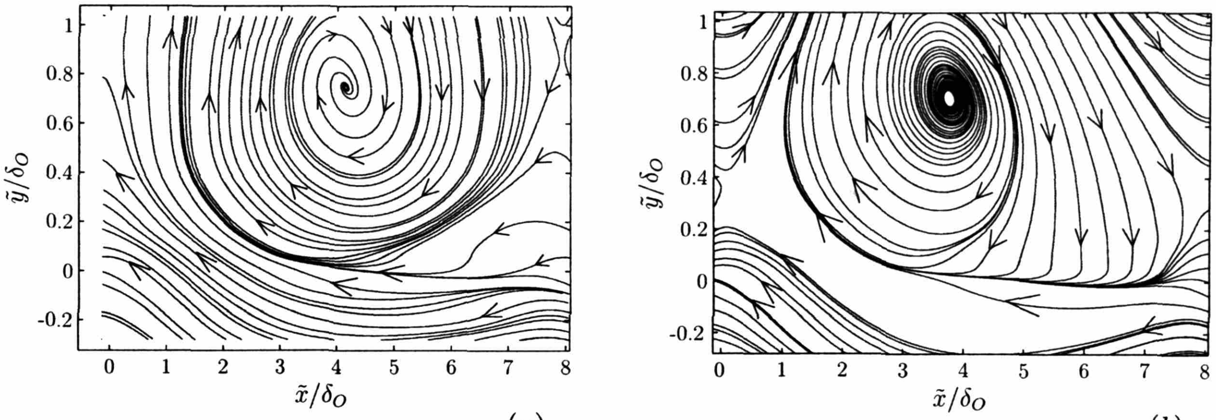

(*a*) (*b*)

Figure 5-17: Sectional streamline plots in the horizontal plane at two different vertical depths (case X). In (*a*) $z = 0.50\ cm$; in (*b*) $z = 4.0\ cm$. In (*a*), the circulation spirals toward the center (stable focus); in (*b*) it spirals away from the center (unstable focus).

the vortex center, in the pattern of an unstable focus (Visbal & Gordnier, 1994), suggesting fluid is drawn away from the center. However, near the bed, the streamlines spiral toward the center, a stable focus pattern, suggesting fluid is drawn toward the center. It would appear that fluid is drawn toward the center of the coherent vortex structure near the bed and directed outward through the bulk of the water column, thus creating the secondary circulation. To assess the effect of these currents, transverse velocity distributions were measured at several depths. These are shown in figure 5-18 for case X. First consider the dependence outside the vegetation, $y > 0$. In the transects measured closest to the bed ($z = 1.25\ cm$ and below) $V > 0$, suggesting net flow directed away from the vegetation, consistent with flow toward the vortex center in the boundary layer. In those measured further above the bed ($z = 2.33\ cm$ and above) $V < 0$, suggesting a net current toward the vegetation, consistent with the outward spiral of the vortex near the surface. The current associated with the secondary circulation is weak (at its strongest $V = 0.02\Delta U$ near the bed), but it may be important for some near-bed processes.

Note from figure 5-18 that inside the vegetation, the profiles nearly collapse, revealing a uniform current directed out of the vegetation. Because the cylinder array exerts drag uniformly over depth, the velocity also tends to be uniform over depth. However, note that the flow leaving the vegetation, by conservation of mass, implies that there is a compensating flow downstream, and hence, $\partial/\partial y \neq 0$. This is explained by the spatial nonuniformity on the scale of the cylinder spacing, which creates streamwise velocity gradients. When a spatial average is taken over the cylinder spacing scale, and the flow is fully-developed, the gradient vanishes $\partial/\partial y = 0$.

The net shear stress due to the secondary circulation, $\widetilde{UV}$ has also been computed, and its transverse dependence is shown in figure 5-19. The shear stress, normalized by the velocity difference ΔU, can be compared with the interfacial friction due to the Reynolds stress, which was shown in figure 5-14. The stress contribution from secondary circulations is small compared with the Reynolds stress. From figure 5-14, typical values of the normalized Reynolds stress are of the order 10^{-2}, while the stress due to secondary circulations is at most of order 10^{-4}. This is a much more modest contribution to the overall stress balance than that made by secondary circulations in compound channels, which is comparable to the Reynolds stress (Shiono & Knight, 1991). This is due to the depth variability in compound channels which accentuates three-dimensional motions, as compared with the constant, shallow, depth in these experiments which makes the flow nearly two-dimensional.

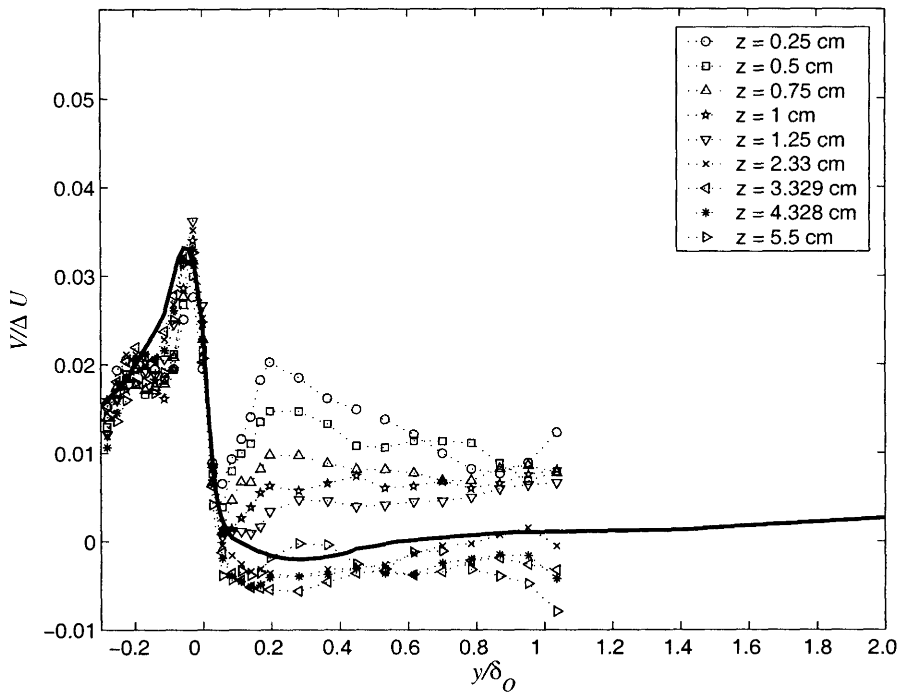

Figure 5-18: Distributions of the time-averaged transverse velocity, V at various depths (shown in legend) for case X. Depth-resolved transects extend to approximately the vortex center, $y/\delta_O \approx 1$. The solid black line is the transect at mid-depth, demonstrating the behavior beyond the vortex center. The transverse velocity is normalized by the velocity difference, ΔU and the transverse coordinate is rescaled by the outer layer width, δ_O.

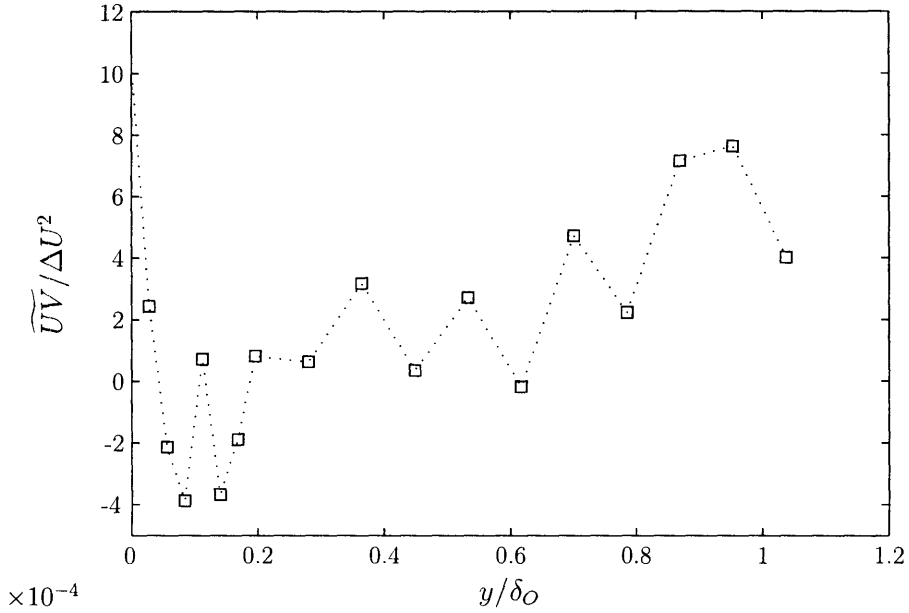

Figure 5-19: Transverse dependence of the net shear stress due to the secondary circulation. Net stress, $\widetilde{UV}$, is normalized by the velocity difference ΔU, rendering it in the form of a friction coefficient, comparable to figure 5-14.

Chapter 6

Conclusions and Remaining Questions

The structure of the shear layer in a partially vegetated channel is dominated by the signature of coherent vortices. These structures derive from the instability associated with the velocity inflection point and their frequency is well-predicted by linear stability theory. Through strong lateral sweeps and ejections, they dominate the turbulent Reynolds stress and increase the friction coefficient at the vegetation interface. Moreover, they contribute to the maintenance of a two layer velocity structure, with a thin rapidly changing region near the interface, and a wider outer boundary layer region in the main channel. The vortices are maintained by the high shear at the interface which is accentuated by the sweeps, and feeds further turbulent energy production. Further, the structures facilitate material exchange between the main channel and the vegetated region in proportion to their size and frequency. This exchange rate has been quantified and applied to the flushing from a vegetated stand and transport of suspended sediments from a river channel to its floodplain.

The results of this study give the first quantitative linkage between the shear layer vortices in a partially vegetated channel and the momentum and mass exchange between the main channel and the vegetation. In previous studies of channel-floodplain flow, the shear region has been modeled with either an eddy viscosity model, or a one-dimensional Darcy-Weisbach friction factor. While some studies have previously observed the coherent vortices at the vegetation interface, this study is the first to relate the shear stress at the vegetation interface and the mass exchange to the physical characteristics of these vortices, namely their size, vorticity, and contribution to the turbulent stresses.

The study also establishes for the first time the mechanism by which the vortices are created and maintained. The inflection point created by the intense shear across the vegetation interface gives rise to the instability that forms the vortices. In this regard the vegetated channel resembles a free shear layer. However, this study demonstrates that the partially vegetated channel has a unique mechanism of reinforcing and maintaining this instability. The sweeps generated by the vortices in conjunction with the strong hydrodynamic drag by the vegetation maintains a high velocity gradient at the interface. As a result, the vortices are able to feed their own energy production, and an equilibrium cycle is achieved, marked by a self-sustaining oscillation. In this regard, the vegetated flow is very different from free shear layers, which have been exhaustively studied for decades in the fluid mechanics literature. Free shear layers do not exhibit an equilibrium oscillation, but rather grow continuously in amplitude, becoming increasingly turbulent, while exhibiting a wide spread range of frequencies. The laboratory results presented here suggest that, in fact, shallow vegetated shear flows result in an oscillation that is more regular, and in better accord with the natural frequency predicted by linear hydrodynamic instability theory than free shear layers. Thus these results should be of fundamental interest to the study of turbulence, shear flows, and particularly, wall-bounded flows. That presence of self-sustained oscillation in the channel with an array of obstructions brings up a suite of questions about the continuum between solid-wall-bounded flows, which do not exhibit regular periodic oscillations, and free shear flows, which exhibit transient oscillations. The laboratory results presented here suggest that porous walls in general may be conducive to self-sustained oscillations because they permit crossflows into and out of the porous region.

Another important result is the self-similarity of the inner layer and outer layer velocity profiles. The results demonstrate that there is an inner layer that is only dependent on the vegetation characteristics, and an outer layer that is independent of the vegetation. To date, shear layers in vegetated flows and on floodplains have been treated with a single length scale. This study is the first to recognize that there are in fact two independent regions. This fact is essential for understanding the velocity structure and shear layer size. However, a better understanding of what controls the outer layer width is needed, as discussed below.

This work has also demonstrated that mass and momentum transfer in a range of vegetated flows can be understood in terms of the physical characteristics of the vortices. This is important, e.g., for the prediction of turbulent fluxes of momentum, aerosols, and water vapor above forest canopies, or for predicting the total conveyance of a connected channel-floodplain flow at flood stage. Moreover, the results can be viewed at a paradigmatic level. In the past, aquatic vegetation has often been treated as simply a drag force, or a dissipator of energy, with the literature full of Manning "n"s and Darcy-Weisbach "f"s to describe channel head loss. The vortex formation mechanism is a strong example that vegetation, in fact, redistributes energy, transporting mass and momentum and opening lines of communication between different regions of an aquatic system, like the main channel and a floodplain, which have very different ecological, and geomorphological characteristics.

From the perspective of application to natural systems, some questions are still outstanding. While the laboratory experiments suggested the outer layer scale is unaffected by vegetation, its upper limit in a natural channel, and thus the constraint on the horizontal scale of the vortices, is uncertain. It appears that the vortices are free to grow up to the scale of the lateral boundary layer, but results from shallow mixing layers, e.g., at river confluences, suggest they may be dissipated by bottom friction when they reach a critical size. Studies over a greater range of open channel conditions, with varying channel width and flow depth, must be undertaken in order to establish precisely what factors affect the outer boundary layer width.

The results suggest that the vortex exchange is an important mechanism for mass transport across the vegetation interface in natural channels. This mechanism may be of particular interest for overbank suspended sediment transport. Field studies of these vortices are, it appears, wholly lacking, as all (published) accounts of floodplain vortices appears to be laboratory studies. Thus observation of these vortices in a natural channel is a worthy goal, though such an effort would be complicated by the need to make such an observation when the channel is at flood stage. In addition, it may be possible to conduct tracer studies in field scale floodplain-channel flows to determine the rate of transport onto the floodplain and compare it to the prediction based on the vortex characteristics. Finally, measurements of the sediment grain size distribution on floodplain banks would be of use in evaluating the vortex exchange model. Even additional laboratory studies of sediment transport in the partially vegetated channel configuration would be useful, as the sediment deposition pattern could be measured and interpreted in light of the vortices. For slightly greater realism, a depth-varying compound channel could be used, with a slightly elevated floodplain.

While it is hoped that this experimental study sheds light on the hydrodynamics of natural vegetated flows, the results should also afford a more fundamental understanding of partially-obstructed shear flows. Shear flows adjacent to porous layers have been studied extensively at low Reynolds numbers, but few, if any, under turbulent conditions. Considerable effort has been poured into determining the appropriate boundary condition for laminar flow adjacent to a porous medium, but none to date have studied the transition to shear instability. This transition should be studied and the critical Reynolds number for instability found in terms of the porous medium characteristics.

In addition, the turbulence structure in the experimental channel studied here resembles elements of both free shear layers and wall-bounded flows, and might offer a connection between the turbulence structure and instability mechanisms in each. At low Reynolds number, the turbulent transition in a wall-bounded flow occurs through the development of Tollmien-Schlichting waves. In a free shear layer the transition occurs through the Kelvin-Helmholtz instability. As the flow adjacent to the cylinder array has elements of both, there may be a transition between the two types of instabilities depending on the array characteristics, particularly the packing density. Thus a stability analysis, and laboratory experiments, could be carried out at low Reynolds number to study the continuum between the boundary layer and shear layer instabilities for flow near a cylinder array with varying porosity.

Finally, an understanding of the transition to nonlinear instability in shallow, partially vegetated flows is of interest, particularly as they appear capable of converging to a wave-like oscillatory flow. A nonlinear analysis would demonstrate the competing physical affects, presumably drag and Reynolds stress, that lead to the equilibrium and frequency lock-in. One approach would be to derive and study a Stuart-Landau equation for the system, where the coefficients would represent the balancing physical processes that lead to the equilibrium.

Appendix A

Velocity Transects with the Laser Doppler Velocimeter (LDV) System

In chapter 2, section 2.4, the experimental measurements of velocity and turbulent quantities using Laser Doppler Velocimetry (LDV) was described. Here, more detail is given on the use and operation of the experimental flume and the LDV and positioning system.

A.1 Details of the Flume and Pump Operation

All experiments were conducted in the 1.2 m wide, 13 m long flume with recirculating pump, which provides flows between approximately $2 - 50\ Ls^{-1}$. A schematic of the flume is shown in figure A-1. The pump draws from a stilling basin on the downstream end and delivers it via a PVC pipe to an upstream stilling basin. As the water enters the upstream basin from the pipe, a multiport diffuser ensures equal distribution of the discharge and a baffling system in the basin further redistributes the flow. These two effects help to achieve smooth entrance conditions at the upstream end of the flume. At the downstream end, a slotted frame at the entrance to the stilling basin accepts weirs of different heights. The presence of a weir causes supercritical flow at the entrance to the stilling basin, resulting in a spillover of water from the channel into the basin. This is advantageous for removing surface scum that can produce unwanted surface tension effects in the experiment. Ideally, the height of the still water depth, in the absence of a current, should rise 1-3 cm above the weir height in order to achieve the supercritical flow. At the onset of an experiment, the water level can be optimized with the pump running to establish the water level at which the ideal supercritical flow over the weir is observed.

The pump speed is varied using an AC controller, which controls the current delivered to the pump. By adjusting current setting on the controller, given in Hz (the frequency of the AC current), the flowrate of the pump can be varied. In general, there is a nonlinear relationship between the current setting, C, the water depth, h, and the ultimate flowrate delivered, Q, which can be written mathematically as $F(C, h, Q) = 0$. This function must be calibrated uniquely for different experimental conditions, as it depends on the frictional resistance within the channel, and thus depends on the density of the cylinder array or any other solid obstructions, as well as the roughness of the channel bed substrate, and the height of the weir.

For maintenance of the flume, the water should be drained regularly, at least twice weekly, to avoid the growth of algae and other biofilms. If biofilms develop, the addition of 2 L of regular Clorox bleach (Sodium hypochlorite) to the flume when completely filled with water is sufficient for disinfection. In addition, the flume is equipped with a filtration system, with replaceable fiber filters, and run by a secondary pump.

A.2 Laser Doppler Velocimetry

A.2.1 Principles of Operation

The Laser Doppler Velocimeter (LDV) system uses optical scattering to determine the velocity of small particles moving through the water. The system consists of four laser beams focused at a point in the flow, which create an optical pattern,

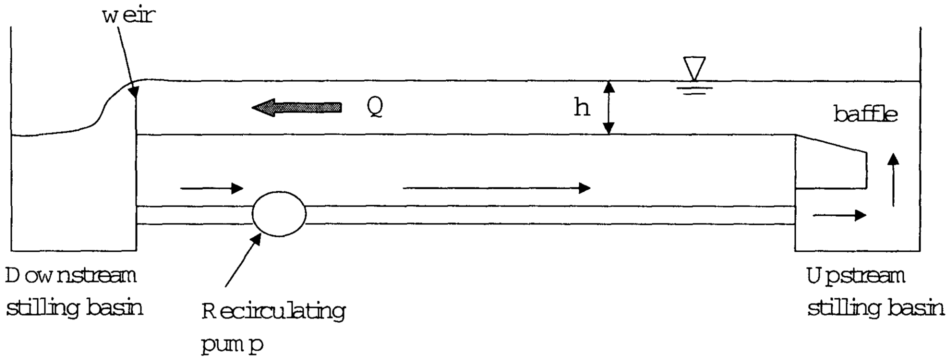

Figure A-1: A schematic of the laboratory flume.

known as a fringe pattern, at their intersection. When a particle passes, the fringe pattern is optically reflected, with a doppler shift dependent on the velocity of the particle. When the reflected pattern is processed, the velocity of the particle can be determined. LDV is an ideal measurement technique because it is both non-invasive and results in high temporal data rates. It's shortcoming is that it can measure the instantaneous flow only at one point. For details on the well-established method, (see, e.g., Buchhave *et al.*, 1979).

The LDV system used in the experiments was manufactured by Dantec Dynamics, and includes a 300 mW Argon-ion laser, a beamsplitter, a Bragg cell, an optical probe, and a processer. The 514 nm beam generated by the laser is first split into two by the beam splitter and the two beams are then shifted relative to one another by the Bragg cell, producing one 514 nm beam and one 488 nm beam. These two beams are then split again, producing four beams, one pair for each wavelength. The four beams are then directed through a fiber optic cable to the optical probe.

The optics focus the four beams into a cylindrical measurement volume approximately 0.8 mm in diameter and approximately 1 cm in length (long axis is in the direction of the beam projection). The dimensions of the measurement volume depend on the focal length of the probe optics, which can be varied from 16 to 40 cm by changing lenses. The fringe pattern at the beam intersection is backscattered when a particle passes, and the reflection is returned to the optical probe. Thus the optics are both transmitting and receiving. The scattered light is carried back through the fiber optic cable to a photomultiplier, which converts the light pattern to a voltage signal and amplifies it. The processor then performs a spectral analysis on the voltage signal to determine the frequency of the waveform, from which the velocity of the particle which originally reflected the light can be determined by doppler shift theory. The reflected signal from one passing particle is termed a "burst". Each of the two beam pairs is responsible for measuring one velocity component, and together, the four-beam system can measure the simultaneous two-dimensional velocity vector in the plane normal to the beam projection axis.

A.2.2 Optimization of Sampling Rate

The LDV sampling rate is predominantly determined by three factors: the rate at which particles pass through the measurement volume, the transmissivity of the optical path between the probe and the sampling volume, and the high voltage setting, or signal amplification, of the returned signal by the photomultiplier. These are briefly detailed below.

Particle Seeding

The first factor, the particle flux through the measurement volume, is determined by the concentration of particles in the flow and the flow velocity. To achieve an optimum sampling rate, the flow is seeded with small, highly reflective particles. Borosilicate glass particles, 10 μm in diameter, manufactured under the trade name Sphericel by Potters Industries, are both inexpensive and effective at scattering light. The particles come in a fine powder and should be mixed in a liquid slurry before adding to the flume. A carboy can be set up on a continuous drip to supply the seeding particle slurry and produce a well-mixed distribution throughout the flume. However, as both the particle concentration and the flow velocity influence the sampling rate, it should be noted that the sampling rate will drop substantially for low flow, regardless of particle concentration. As a rough guideline, the optimum sampling rate for a mean velocity of 1 $cm\ s^{-1}$ is about 10 Hz, while the optimum sampling rate for a mean velocity of 10 $cm\ s^{-1}$ is about 100 Hz.

A.2.3 Optical Path

The clarity of the optical path also substantially influences the sampling rate. For instance, if the concentration of particles is too high, the light attenuation in the water will be too great, and the sampling rate compromised. The same effect is caused by too much background turbidity in the water. In addition, the transparent surface through which the beams pass to enter the flow must be free of debris, and should be cleaned frequently. Also note that both glass and cast acrylic allow the beams to pass effectively, but extruded acrylic contains imperfections which destroy the optical signal and are thus incompatible with LDV.

A.2.4 Signal Amplification

The third factor influencing the sampling rate is the high voltage setting of the photomultiplier. This can be tuned between a range of 1000 and 1800 V within the Dantec BSA Flow software. Higher settings amplify the optical signal, but also amplify the noise, so it is recommended to use the lowest voltage that gives an acceptable sampling rate.

A.2.5 Sampling Duration

The LDV processor accepts only bursts with sufficiently high cross-correlation between $u(t)$ and $v(t)$, ensuring sound statistics for the cross moments, such as the Reynolds stress, $\langle u'v' \rangle$. Nonetheless, for convergence of the higher turbulent moments, a sampling duration at any single position was of at least four minutes is needed. However, this duration depends on the velocity and relevant time scales in the flow and should be optimized accordingly. In the present experiments, the criterion was that samples at any one position should be sufficiently long to capture at least 10 coherent vortex structures.

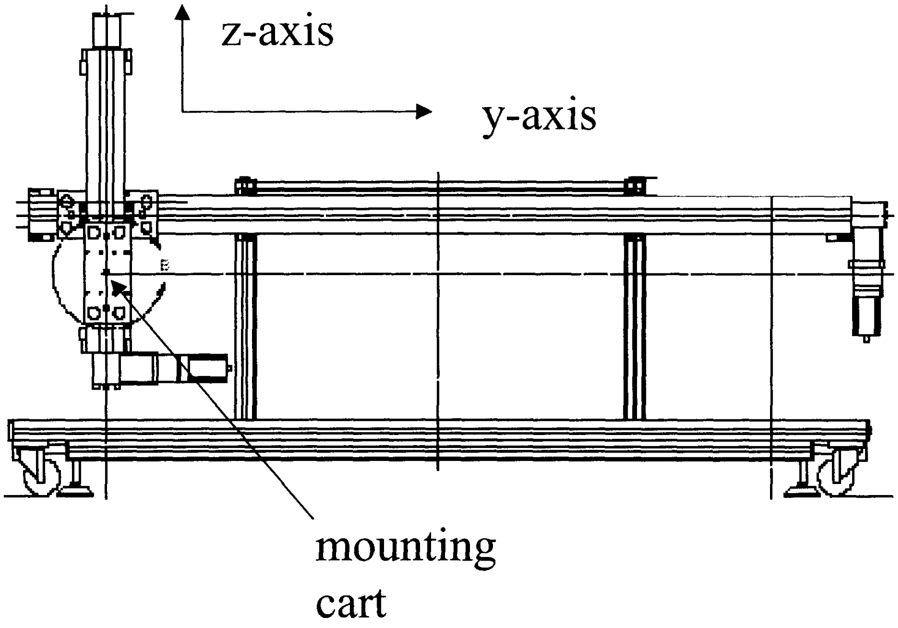

Figure A-2: A schematic of the mechanical two-axis traverse.

A.3 Positioning

A.3.1 Mechanical Traverse

In the present experiments, lateral velocity transects were made at mid-depth, and at various longitudinal positions along the flume. The LDV was positioned under the flume and directed upward through the bottom glass. Because opaque PVC baseboards were used to hold the cylinder array, cast acrylic spacers (1/2" wide) were placed between adjacent baseboards to allow a clear optical path for the LDV beams. For positioning, the LDV optical probe was mounted on a positioning system driven by a stepper motor and controller (OEM750X), manufactured by Parker-Hannifin, and connected to a PC over an RS-232 cable. The positioning system consists of two perpendicular axes mounted together, with a belt-driven linear actuator on each axis. Thus motion is allowed in both the vertical ($z-$) and horizontal ($y-$) directions, with a resolution of approximately 0.1 mm. A schematic of the traverse is shown in figure A-2 and a schematic of the LDV and positioning setup is shown in figure A-3.

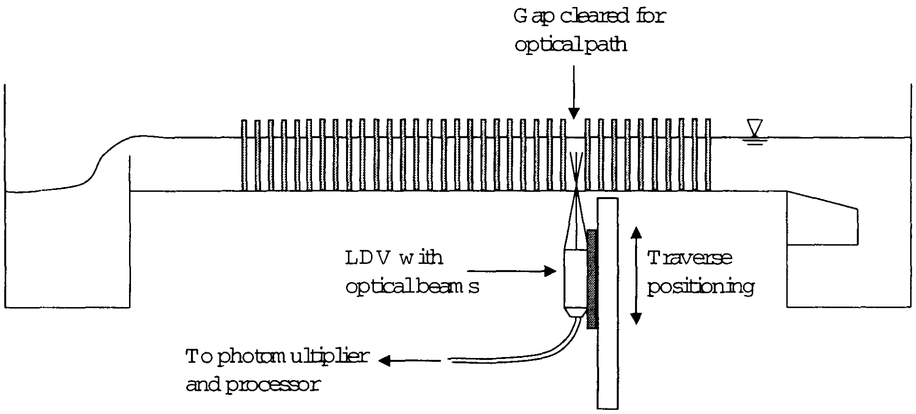

Figure A-3: A schematic of the LDV with positioning system in relation to the flume.

A.3.2 Initial Positioning

To position the LDV, the optical probe is mounted on the mounting cart and controlled by the Parker-Hannifin X-Ware terminal emlulator software on the PC, which allows a variety of simple motion commands, such as distance settings, stop and go commands, and position zeroing. The X-Ware manual has a detailed description of all commands. Before collecting data, the LDV measurement volume must be aligned with the bottom of the flume to establish the position of the bed, $z = 0$. This is done simply by placing a flat, solid sheet, e.g., a small plate of opaque plexiglass, in the bottom of the flume and focusing the beam on the surface until all four beams converge. This defines the zero. The X-Ware software can be used to zero the vertical traverse axis at this position by entering a "2PZ" command (commands referring to the y-axis are prefaced with a "1" and those referring to the z-axis with a "2"). Similar zeroing can be done with the horizontal axis. For instance, in the present experiments, the lateral zero was taken as the center-line of the first row of cylinders. Thus the y-axis was moved laterally until the LDV beams converged at the center of the first cylinder. Entering the command "1PZ" then zeroes the y-axis of the traverse.

After setting the zeroes of the traverse, limits switches must be set to restrict the motion of the traverse in order to avoid collisions with the bottom glass or with the frame of the flume. Magnetic limit switches on each of the two axes can be moved manually using the adjustable Allen screws and should be manually placed at the desired limits of the probe motion. Both the zeroing and the limit switch positioning is done manually, typically under the flume with the laser on. As such, safety precautions are taken to minimize the stray laser reflections and eye protection should be worn.

A.4 LDV Traverse Programming

A.4.1 Writing a Script for the Traverse

Once the initial positioning of LDV optics is complete, a traverse can be made while collecting data with Dantec BSA flow software. For a traverse, the X-Ware software can be programmed to execute a series of motions contained in a script file. An sample script is shown below with comments. The script first positions the traverse at the global zero position, then executes 30 successive movements at 1 cm increments. After each move, the traverse pauses for 240 seconds. During this time, the LDV can acquire 240 seconds of data at that particular position.

```
XD1      % initiates script
MPA      % sets positioning to absolute mode
1D0      % sets the distance to be the absolute zero
1G       % go command: initiates the move to x = 0
MPI      % sets position to incremental mode
1D7500   % sets distance to an increment of 7500 revolutions = 1 cm
L30      % loop: the following commands will be repeated 16 times
1PR      % position report: queries traverse position and returns the value
T240     % traverse pauses for 240 seconds
1G       % go command: moves the increment assigned above (1 cm)
N        % the "end" statement for the loop
XT       % the "end" statement for the script
```

A.4.2 Synchronizing the Traverse and the LDV Sampling

Because the LDV data collection is not synchronized with the traverse, a simple method is needed to correlate the data sampling with the traverse position. The following method was employed in the experiments. The LDV data collection was set for a duration long enough to cover the entire traverse time. For the above example, that time would be at least $T = 30 \times 240\ s = 2$ hours. The traverse simply was allowed to execute its positions as the data collection ran continuously. In the post-processing it was possible to determine the time at which the traverse moved between positions by velocity spikes in the time series. The individual position-records can then be parsed from the single long time series for the whole traverse by cutting around the spikes. This can be done in a very straightforward way in Matlab.

A.5 Processing

The Dantec processor calculates the velocities returned from each burst and the data is logged continuously on a computer using the Dantec BSA Flow software. The data can be output in the form of an ASCII text file containing the sample number, the time it was logged, the transit time, which is the time the particle responsible for the burst spends in the measurement volume, and each component of velocity, $u(t)$ and $v(t)$.

Once the data are exported and after they are parsed into individual position records using the method detailed above, they can be processed by Matlab for the mean velocities and turbulent second and third moments. Of interest are the Reynolds stress, $\langle u'v' \rangle$, the second moments, $\langle u'^2 \rangle$, $\langle v'^2 \rangle$, and the triple correlations, $\langle u'^3 \rangle$, $\langle v'^3 \rangle$, $\langle u'^2 v' \rangle$, and $\langle v'^2 u' \rangle$. Because the data are unevenly-spaced in time, there is a natural bias toward higher velocities (more samples at higher velocity move through the measurement volume). The LDV processor employs transit-time-weighting to calculate the moments (see Buchhave *et al.*, 1979). However, if the raw data are exported and moments are to be calculated in Matlab, as they were in the present experiments, the weighting scheme must be used in the processing. The moments are calculated as follows, using the mean streamwise velocity, $\langle u \rangle$ as an example.

$$\langle u \rangle = \sum_{i=1}^{N} w_i u_i \tag{A.1a}$$

where

$$w_i = \frac{tt_i}{\sum_{i=1}^{N} tt_i} \tag{A.1b}$$

and i represents the $i^t h$ sample in the time series, tt_i is the transit time, N is the total number of samples in the time series, and w_i is the weighting function. The same procedure should be carried out for $\langle v \rangle$ and all higher moments.

Because of the uneven time sampling, the time series must also be resampled onto a evenly spaced grid before any Fourier analysis can be carried out. In the present experiments, the data were resampled onto a grid with temporal spacing, Δt, equal to the shortest time duration between samples in the given velocity record. Then the standard MATLAB power spectral density function, "PWELCH.m" can be used to obtain the power spectral densities, P_{uu} and P_{vv}. This function is preferable to the more antiquated MATLAB function "PSD.m" because it produces spectra that are properly normalized, i.e.,

$$\int_0^\infty P_{uu} df = \langle u'^2 \rangle \tag{A.2}$$

where f is the frequency. Note that, as detailed by Tummers & Passchier (2001), resampling the time series onto a regularly-spaced grid reduces the maximum frequency at which the PSD is accurate to $f_{max} = S/(2\pi)$ where S is the mean data rate of the raw, irregularly-spaced LDA data.

Appendix B

Measuring Surface Slope with Wave Gauges

The method for measuring the free surface slope was discussed in chapter 2, section 2.5.4. The mean force balance over the entire array is between the pressure gradient and the hydrodynamic resistance by the array, given by (2.16) as

$$\frac{1}{2}C_D a U_1^2 = (1-\phi)gS. \tag{B.1}$$

where $S = -dh/dx$ is the surface slope. The mean slope over a length of array, L, is $S = -\Delta h/L$. Surface displacement gauges were used to measure Δh between the beginning and the end of the array, and thus calculate C_D given U_1 and a. Here the method for measuring the displacement is described.

The surface displacement gauges are analog capacitance-based probes that can measure a time series at 25 Hz of surface displacement relative to a reference. The gauges consist of two closely-spaced parallel rods, which, when submerged in water develop a potential between the rods which is in proportion to the depth of submergence. The voltage signal is sent to an amplifier and then to a analog-to-digital converter board from which it can be logged to a computer. Up to eight wave gauges may be connected to the amplifier and the voltage time series are logged using SonTek ADV data collection software. A schematic of a representative

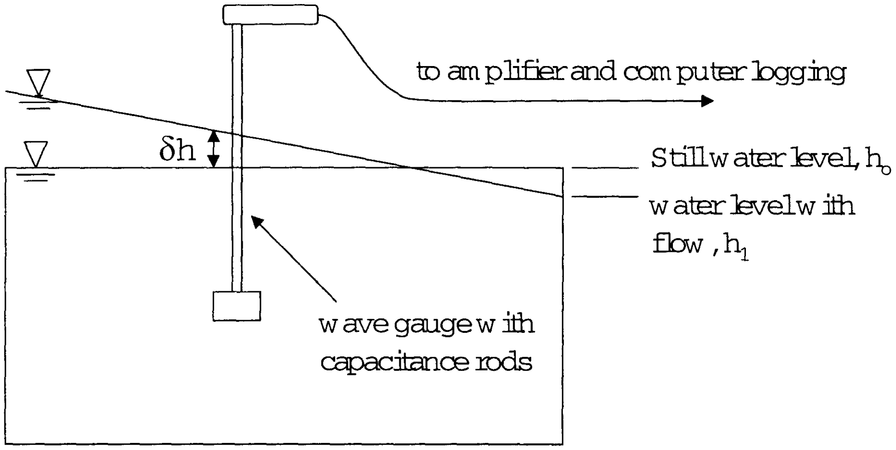

Figure B-1: A schematic of a representative surface displacement gauge with demonstrating the free surface displacement between the still water level and the level with flow, δh.

surface displacement gauge and the measurement of surface slope is shown in figure B-1.

Before collecting surface displacement data, each probe must be calibrated to determine the relationship between voltage, V, and displacement, δh,

$$\delta h = B\delta V \tag{B.2}$$

where B is a constant. The calibration was performed by moving each wave gauge over a range of depths, $z = z_0,\ z_1, ...z_n$ and measuring the corresponding voltage, $V = V_0,\ V_1, ...V_n$. In general, the total range of depths spanned approximately 1 cm, and approximately five different depths were used for each calibration. In addition, six gauges were used in all. To simplify the calibration, three gauges each at the upstream and downstream ends of the array were placed on a vertical traverse, which could be vertically positioned very accurately, such that all three gauges moved simultaneously for each vertical displacement. The displacements were measured using Vernier calipers with a resolution of 0.001 *cm*. By plotting V vs. z for each calibration, the slope, B, between displacement and voltage was calculated for each gauge. This was done at least once per week during the times at which the surface slope measurements were being made. Based on the results of the calibrations, the resolution of the wave gauges is in the range between approximately 0.1 to 0.5 mm, and varies slightly between individual gauges. A note on data processing. The voltage records logged by the ADV data collection application, "ADVA.exe", were processed in MATLAB. The voltage, V, for one position record was simply taken as the long-time average of the time series. However, some of the wave gauges had a tendency to occasionally produce occasional isolated values of very low voltage in the time series. These "drop outs" were rejected in the data processing, by rejecting outliers lower than 2 standard deviations of V. The "drop outs" are likely an artifact of the analog nature of the signal and amplification.

After calibrating the probes, the surface slope could then be measured for each experimental condition of interest. Three gauges were placed at the upstream end of the array and three gauges were placed at the downstream end, and the length of array between them, L, was measured. The flume was then filled with water to the still water depth desired for the experimental run to be measured. A time record of voltage over approximately 4 minutes duration was then logged. For each of the six wave gauges, this still water case provides the voltage, V_o, corresponding to the reference depth of submergence, h_o. Following the reference measurement, the flume pump is then set to the flow rate of interest. With flow, the depth rises everywhere in the flume, but a surface slope develops in response to the frictional resistance of the array. After waiting for transients to cease, a second set of voltage measurements was logged. The time duration for logging depends on the flow, but should be much longer, by a factor of at least 10, than the longest turbulent or oscillation time scale present in the flow. In these experiments, data were logged for a time of at least 10 vortex periods. The measurements with flow provided the voltages, V_1, corresponding the surface elevation after displacement, h_1. The surface displacement for each probe between the still water case and the flow case was then calculated from the calibration curve for that probe as

$$\delta h_i = (h_1 - h_o)_i = B_i(V_1 - V_o)_i \tag{B.3}$$

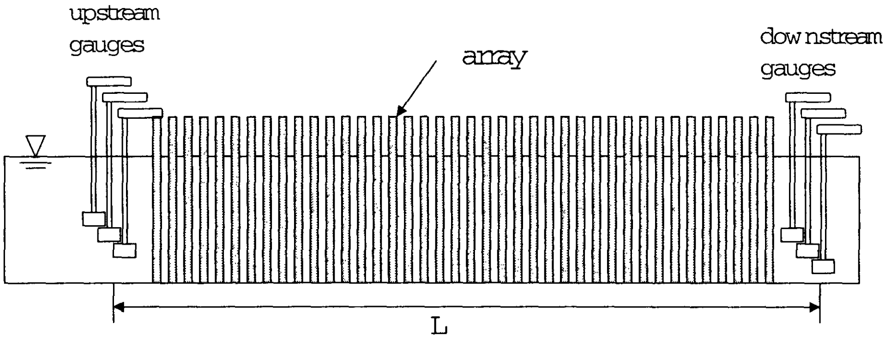

Figure B-2: A schematic of a representative surface slope measurement with three wave gauges on the upstream and three on the downstream end.

where i represents the i^{th} wave gauge.

To calculate the free surface elevation drop over the array, the mean displacement at the upstream end is first calculated,

$$\overline{\delta h_u} = \sum_{i=1}^{N} \delta h_{i,u} \tag{B.4}$$

where the u represents wave gauges at the upstream end. Similarly, for gauges at the downstream end,

$$\overline{\delta h_d} = \sum_{i=1}^{N} \delta h_{i,d}. \tag{B.5}$$

The surface elevation change between the upstream and downstream end is then simply

$$\Delta h = \overline{\delta h_d} - \overline{\delta h_u}. \tag{B.6}$$

A schematic of the surface slope measurement across the array is shown in figure B-2.

In the present experiments, three gauges were used on both the upstream and downstream ends of the array. This yields $6 - 4 = 2$ statistical degrees of freedom for Δh (since it is necessary to have at least 2 wave gauges, one upstream and one downstream, to have 1 independent measurement). To have a greater statistical sample size, in the present experiments, more measurements were made by moving the traverse with the three gauges to a different set of locations within the array.

This was done both with the upstream and downstream gauges. The experiments were then run again by turning off the pump, letting transients subside, making still water reference measurements, and then turning on the pump and taking measurements with flow. This yielded an additional 3 measures of Δh. Within the array, there is considerable heterogeneity of the free surface due to the wakes behind cylinders. Thus it is advantageous to have several independent measurements of Δh. Finally, the surface slope is

$$S = \frac{\Delta h}{L} \tag{B.7}$$

and the drag coefficient, C_D can be calculated from (B.1) as

$$C_D = 2\frac{-(1-\phi)gS}{aU_1^2} \tag{B.8}$$

Bibliography

ACKERMAN, J. & OKUBO, A. 1993 Reduced mixing in a marine macrophyte canopy. *Functional Ecology* **7**, 305–309.

ADRIAN, R., CHRISTENSEN, K. & LIU, Z.-C. 2000 Analysis and interpretation of instantaneous turbulent velocity fields. *Experiments in Fluids* **29**, 275–290.

AKINLADE, O. G., BERGSTROM, D. J., TACHIE, M. F. & CASTILLO, L. 2004 Outer flow scaling of smooth and rough wall turbulent boundary layers. *Experiments In Fluids* **37** (4), 604–612.

ALLEN, J. 1992 Large-scale textural patterns and sedimentary processes on tidal salt marshes in the severn estuary, southwest britain. *Sedimentary Geology* **81**, 299–318.

ANTONIA, R. & KROGSTAD, P.-Å. 2001 Turbulence in boundary layers over different types of surface roughness. *Fluid Dynamics Research* **28**, 139–157.

AYLOR, D. 2005 Quantifying maize pollen movement in a maize canopy. *Agricultural and Forest Meteorology* **131**, 247–256.

BANDYOPADHYAY, P. 1987 Rough-wall turbulent boundary layers in the transition regime. *Journal of Fluid Mechanics* **180**, 231–266.

BANDYOPADHYAY, P. & WATSON, R. 1988 Structure of rough-wall turbulent boundary layers. *Physics of Fluids* **31** (7), 1877–1883.

BEAVERS, G. & JOSEPH, D. 1967 Boundary conditions at a naturally permeable wall. *Journal of Fluid Mechanics* **30**, 197–207.

Betchov, R. & Criminale, W. J. 1967 *Stability of Parallel Flows*. New York: Academic Press.

Bisset, D., Antonia, R. & Browne, L. 1990 Spatial organization of large structures in the turbulent far wake of a cylinder. *Journal of Fluid Mechanics* **218**, 439–461.

Bonnet, J., Delville, J., Glauser, M., Antnonia, R., Bisset, D., Cole, D., Fiedler, H., Garem, J., Hillberg, D., Jeong, J., Kevlahan, N., Ukeiley, L. & Vincendeau, E. 1998 Collaborative testing of eddy structure identification methods in free turbulent shear flows. *Experiments in Fluids* **25**, 197–225.

Bousmar, D., Riviere, N., Proust, S., Paquier, A., Morel, R. & Zech, Y. 2005 Upstream discharge distribution in compound-channel flumes. *Journal of Hydraulic Engineering, ASCE* **131** (5), 408–412.

Bradshaw, P. 1967 The turbulence structure of equilibrium boundary layers. *Journal of Fluid Mechanics* **29**, 625.

Broadwell, J. & Breidenthal, R. 1982 A simple model of mixing and chemical reaction in a turbulent shear layer. *Journal of Fluid Mechanics* **125**, 397–410.

Browand, F. & Troutt, T. 1985 The turbulent mixing layer: geometry of large vortices. *Journal of Fluid Mechanics* **158**, 489–509.

Browand, F. & Weidman, P. 1976 Large scales in the developing mixing layer. *Journal of Fluid Mechanics* **76**, 127.

Brown, G. & Roshko, A. 1974 On density effects and large structure in turbulent mixing layers. *Journal of Fluid Mechanics* **64**, 775–816.

Buchhave, P., George, W. & Lumley, J. 1979 The measurement of turbulence with the laser doppler anemometer. *Annual Review of Fluid Mechanics* **11**, 443–503.

Buzzelli, C., Wetzel, R. & Meyers, M. 1999 A linked physical and biological framework to assess beogeochemical dynamics in a shallow estuarine system. *Estuarine, Coastal and Shelf Science* **49**, 829–851.

Chen, D. & Jirka, G. 1997 Absolute and convective instabilities of plane turbulent wakes in a shallow water layer. *Journal of Fluid Mechanics* **338**, 157–172.

Chen, D. & Jirka, G. 1998 Linear stability analysis of turbulent mixing layers and jets in shallow water layers. *Journal of Hydraulic Research* **36**, 815–830.

Chu, V. & Babarutsi, S. 1988 Confinement and bed-friction effects in shallow turbulent mixing layers. *Journal of Hydraulic Engineering* **114** (10), 1257–1274.

Chu, V., Wu, J.-H. & Khayat, R. 1991 Stability of transverse shear flows in shallow open channels. *Journal of Hydraulic Engineering* **117** (10), 1370–1388.

Danckwerts, P. 1951 Absorption by simultaneous diffusion and chemical reaction into particles of various shapes and into falling drops. *Transactions of the Faraday Society* **47**, 1014–1023.

Dietrich, W. 1982 Settling velocity of natural particles. *Water Resources Research* **18** (6), 1615–1626.

Djenidi, L., Elavarasan, R. & Antonia, R. 1999 The turbulent boundary layer over transverse square cavities. *Journal of Fluid Mechanics* **395**, 271–294.

Drazin, P. & Reid, W. 1981 *Hydrodynamic Stability*. Cambridge University Press.

Dwyer, M., Patton, E. & Shaw, R. 1987 Turbulent kinetic energy budgets from a large-eddy simulation of airflow above and within a forest canopy. *Boundary-Layer Meteorology* **84**, 23–43.

Finnigan, J. 2000 Turbulence in plant canopies. *Annual Review of Fluid Mechanics* **32**, 519–571.

FU, H. & ROCKWELL, D. 2005 Shallow flow past a cylinder: control of the near wake. *Journal of Fluid Mechanics* **539**, 1–24.

GHADDAR, N., KORCZAK, K., MIKIC, B. & PATERA, A. 1986 Numerical investigation of incompressible flow in grooved channels. part i. stability and self-sustained oscillations. *Journal of Fluid Mechanics* **163**, 99–127.

GHISALBERTI, M. & NEPF, H. 2004 The limited growth of vegetated shear layers. *Water Resources Research* **40** (7), W07502, doi:10.1029/2003WR002776.

GHISALBERTI, M. & NEPF, H. 2005*a* Mass transfer in vegetated shear flows. *Environmental Fluid Mechanics, In Press* .

GHISALBERTI, M. & NEPF, H. 2005*b* The structure of the shear layer in flows over rigid and flexible canopies. *Environmental Fluid Mechanics, In Press* .

GHISALBERTI, M. & NEPF, H. M. 2002 Mixing layers and coherent structures in vegetated aquatic flows. *Journal of Geophysical Research-Oceans* **107** (C2), 3011.

GHISALBERTI, M. A. 2005 Momentum and scalar transport in vegetated shear flows. PhD thesis, Massachusetts Institute of Technology.

GOYEAU, B., LHUILLIER, D., GOBIN, D. & VELARDE, M. 2003 Momentum transport at a fluid-porous interface. *International Journal of Heat and Mass Transfer* **46**, 4071–4081.

GRASS, A. 1971 Structural features of turbulent flow over smooth and rough boundaries. *Journal of Fluid Mechanics* **50**, 233–255.

HELMIÖ, T. 2004 Flow resistance due to lateral momentum transfer in partially vegetated rivers. *Water Resources Research* **40**, W05206.

HINZE, J. O. 1975 *Turbulence*, 2nd edn. McGraw-Hill.

HO, C.-M. & HUERRE, P. 1984 Perturbed free shear layers. *Annual Review of Fluid Mechanics* **16**, 365–424.

HUSSAIN, A. 1983 Coherent structures—reality and myth. *Physics of Fluids* **26** (10), 2816–2850.

HUSSAIN, A. & ZAMAN, K. 1985 An experimental study of organized motions in the turbulent plane mixing layer. *Journal of Fluid Mechanics* **159**, 85–104.

HUSSAIN, A. F. & HAYAKAWA, M. 1987 Eduction of large-scale organized structures in a turbulent plane wake. *Journal of Fluid Mechanics* **180**, 193–229.

IKEDA, S., IZUMI, N. & ITO, R. 1991 Effects of pile dikes on flow retardation and sediment transport. *Journal of Hydraulic Engineering* **117** (11), 1459–1478.

INCROPERA, F. & DEWITT, D. 1981 *Fundamentals of Heat and Mass Transfer*, 2nd edn. Wiley.

JAMES, D. & DAVIS, A. 2001 Flow at the interface of a model fibrous porous medium. *Journal of Fluid Mechanics* **426**, 47–72.

JIMENEZ, J. 2004 Turbulent flows over rough walls. *Annual Review of Fluid Mechanics* **36**, 173–196.

JIMENEZ, J., UHLMANN, M., PINELLI, A. & KAWAHARA, G. 2001 Turbulent shear flow over active and passive porous surfaces. *Journal of Fluid Mechanics* **442**, 89–117.

KATUL, G. & ALBERTSON, J. 1998 An investigation of higher-order closure models for a forested canopy. *Boundary Layer Meteorology* **89**, 47–74.

KLINE, S. & ROBINSON, S. 1989 Quasi-coherent structures in the turbulent boundary layer. Part I: status report on a community-wide summary of the data. In *Near Wall Turbulence. Proceedings of Zaric Memorial Conference* (ed. S. Kline & N. Afgan), pp. 200–217. New York: Hemisphere.

KOCH, D. & LADD, A. 1997 Moderate Reynolds number flows through periodic and random arrays of aligned cylinders. *Journal of Fluid Mechanics* **349**, 31–66.

KROGSTAD, P.-Å., ANTONIA, R. A. & BROWNE, L. W. B. 1992 Comparison between rough-wall and smooth-wall turbulent boundary-layers. *Journal of Fluid Mechanics* **245**, 599–617.

KUNDU, P. K. & COHEN, I. M. 2004 *Fluid Mechanics*, 3rd edn. Elsevier.

LARSON, R. & HIGDON, J. 1986 Microscopic flow near the surface of two-dimensional porous media. part 1. axial flow. *Journal of Fluid Mechanics* **166**, 449–472.

LECCE, S. & PAVLOWSKY, R. 2004 Spatial and temporal variations in the grains-size characteristics of historical flood plain deposits, blue river, wisconsin, usa. *Geomorphology* **61**, 361–371.

LEONARD, L. & LUTHER, M. 1995 Flow hydrodynamics in tidal marsh canopies. *Limnology and Oceanography* **40**, 1474–1484.

MACKLIN, M. 1996 Fluxes and storage of sediment-associated heavy metals in floodplain systems: assessment and river basin management issues at a time of rapid environmental change. In *Floodplain Processes* (ed. M. Anderson, D. Walling & P. Bates), chap. 13, pp. 441–460. Wiley.

MASSEL, S., FURUKAWA, K. & BRINKMAN, R. 1999 Surface wave propagation in mangrove forests. *Fluid Dynamics Research* **24**, 219–249.

MONKEWITZ, P. & HUERRE, P. 1982 Influence of the velocity ratio on the spatial instability of mixing layers. *Physics of Fluids* **25** (7), 1137–1143.

NADAOKA, K. & YAGI, H. 1998 Shallow-water turbulence modeling and horizontal large-eddy computation of river flow. *Journal of Hydraulic Engineering* **124** (5), 493–500.

NAKAGAWA, H. & NEZU, I. 1977 Prediction of the contributions to the Reynolds stress from bursting events in open-channel flows. *Journal of Fluid Mechanics* **80**, 99–128.

NEPF, H. 1999 Drag, turbulence, and diffusion in flow through emergent vegetation. *Water Resources Research* **35** (2), 479–489.

NEPF, H., SULLIVAN, J. & ZAVISTOSKI, R. 1997 A model for diffusion within emergent vegetation. *Limnology and Oceanography* **42** (8), 1735–1745.

NEPF, H. M. & VIVONI, E. R. 2000 Flow structure in depth-limited, vegetated flow. *Journal of Geophysical Research* **105** (C12), 28527–28546.

NEZU, I. & ONITSUKA, K. 2000 Turbulent structures in partly vegetated open-channel flows with lda and piv measurements. *Journal of Hydraulic Research* **39** (6), 629–642.

NICHOLAS, A. & WALLING, D. 1998 Numerical modelling of floodplain hydraulics and suspended sediment transport and deposition. *Hydrological Processes* **12**, 1339–1355.

PASCHE, E. & ROUVÉ, G. 1985 Overbank flow with vegetatively roughened floodplains. *Journal of Hydraulic Engineering* **111** (9), 1262–1278.

PERRY, A. & CHONG, M. 1987 A description of eddying motions and flow patterns using critical-point concepts. *Annual Review of Fluid Mechanics* **19**, 125–155.

PIERREHUMBERT, R. 1991 Chaotic mixing of tracer and vorticity by modulated traveling Rossby waves. *Geophysical and Astrophysical Fluid Dynamics* **58**, 285–320.

PIERREHUMBERT, R. & WIDNALL, S. 1982 The two- and three-dimensional instabilities of a spatially periodic shear layer. *Journal of Fluid Mechanics* **114**, 59–82.

PIZZUTO, J. 1987 Sediment diffusion during overbank flows. *Sedimentology* **34**, 301–317.

POGGI, D., PORPORATO, A. & RIDOLFI, L. 2003 The effect of vegetation density on canopy sub-layer turbulence. *Boundary-Layer Meteorology* **111**, 565–587.

POPE, S. B. 2000 *Turbulent Flows*. Cambridge University Press.

PRESS, W. H., FLANNERY, B. P., TEUKOLSKY, S. A. & VETTERLING, W. T. 1992 *Numerical Recipes in C : The Art of Scientific Computing*, 2nd edn. Cambridge University Press.

PRINOS, P., SOFIALIDIS, D. & KERAMARIS, E. 2003 Turbulent flow over and within a porous bed. *Journal of Hydraulic Engineering* **129** (9), 720–733.

VAN PROOIJEN, B. & UIJTTEWAAL, W. 2002 A linear approach for the evolution of coherent structures in shallow mixing layers. *Physics of Fluids* **14** (12), 4105–4114.

RAUPACH, M. 1981 Conditional statistics of Reynolds stress in rough-wall and smooth-wall turbulent boundary layers. *Journal of Fluid Mechanics* **108**, 363–382.

RAUPACH, M., COPPIN, P. & LEGG, B. 1986 Experiments on scalar dispersion within a plant canopy, part i: the turbulence structure. *Boundary Layer Meteorology* **35**, 21–52.

RAUPACH, M., FINNIGAN, J. & BRUNET, Y. 1996 Coherent eddies and turbulence in vegetation canopies: The mixing layer analogy. *Boundary Layer Meteorology* **78**, 351–382.

ROBINSON, S. 1991 Coherent motions in the turbulent boundary layer. *Annual Review of Fluid Mechanics* **23**, 601–639.

SAHRAOUI, M. & KAVIANY, M. 1992 Slip and no-slip velocity boundary conditions at interface of porous, plain media. *International Journal of Heat and Mass Transfer* **35**, 927–943.

SCHATZ, M., BARKLEY, D. & SWINNEY, H. 1995 Instability in a spatially periodic open flow. *Physics of Fluids* **7** (2), 344–358.

SCHLICHTING, H. 1979 *Boundary-Layer Theory*, seventh edn. McGraw-Hill.

SEGINER, I., MULHEARN, P., BRADLEY, E. & FINNIGAN, J. 1976 Turbulent flow in a model plant canopy. *Boundary Layer Meteorology* **10**, 423453.

SHIONO, K. & KNIGHT, D. 1991 Turbulent open-channel flows with variable depth across the channel. *Journal of Fluid Mechanics* **222**, 617–646.

SOCOLOFSKY, S. & JIRKA, G. 2004 Large scale flow structures and stability in shallow flows. *Journal of Environmental Engineering Science* **3**, 451–462.

STEVENS, J. & LUCK, R. 1999 Explicit approximations for all eigenvalues of the 1-d transient heat conduction equations. *Heat Transfer Engineering* **20** (2), 35–41.

STUART, J. 1958 On the nonlinear mechanics of hydrodynamic stability. *Journal of Fluid Mechanics* **4**, 1–21.

STUMPF, R. 1983 The process of sedimentation on the surface of a salt marsh. *Estuarine, Coastal and Shelf Science* **17**, 495–508.

TACHIE, M., JAMES, D. & CURRIE, I. 2003 Velocity measurements of a shear flow penetrating a porous medium. *Journal of Fluid Mechanics* **493**, 319–343.

TAMAI, N., ASAEDA, T. & IKEDA, H. 1986 Study on generation of periodical large surface eddies in a composite channel flow. *Water Resources Research* **22** (7), 1129–1138.

TENNEKES, H. & LUMLEY, J. 1972 *A First Course in Turbulence*. MIT Press.

TOWNSEND, A. 1976 *The Structure of Turbulent Shear Flow*. Cambridge University Press.

TUMMERS, M. & PASSCHIER, D. 2001 Spectral analysis of biased lda data. *Measurement Science and Technology* **12**, 1641–1650.

UIJTTEWAAL, W. & BOOIJ, R. 2000 Effects of shallowness on the development of free-surface mixing layers. *Physics of Fluids* **12** (2), 392–402.

UIJTTEWAAL, W. & TUKKER, J. 1998 Development of quai two-dimensional structures in a shallow free-surface mixing layer. *Experiments in Fluids* **24**, 192–200.

VIONNET, C., TASSI, P. & VIDE, J. M. 2004 Estimates of flow resistance and eddy viscosity coefficients for 2d modelling on vegetated floodplains. *Hydrological Processes* **18**, 2907–2926.

VISBAL, M. & GORDNIER, R. 1994 Crossflow topology of vortical flows. *AIAA Journal* **32** (5), 1085–1087.

WEISS, J. & KNOBLOCH, E. 1989 Mass transport and mixing by modulated traveling waves. *Physical Review A* **40** (5), 2579–2589.

WHITE, B., GHISALBERTI, M. & NEPF, H. 2004 Shear layers in partially vegetated channels: analogy to shallow water shear layers. In *Shallow Flows: Research Presented at the International Symposium on Shallow Flows, Delft, Netherlands* (ed. G. Jirka & W. Uijttewaal). Balkema.

WHITE, B. & NEPF, H. 2003 Scalar transport in random cylinder arrays at moderate reynolds number. *Journal of Fluid Mechanics* **487**, 43–79.

WINANT, C. & BROWAND, F. 1974 Vortex pairing, the mechanism of turbulent mixing-layer growth at moderate reynolds number. *Journal of Fluid Mechanics* **63**, 237–255.

WOLANSKI, E., MAZDA, Y., FURUKAWA, K., RIDD, P., KITHEKA, J., SPAGNOL, S. & STIEGLITZ, T. 2001 Water circulation in mangroves, and its implications for biodiversity. In *Oceanographic Processes of Coral Reefs*, chap. 5. CRC.

WYGNANSKI, I. & FIEDLER, H. 1970 The two-dimensional mixing region. *Journal of Fluid Mechanics* **41**, 327–361.

XIAOHUI, S. & LI, C. 2002 Large eddy simulation of free surface turbulent flow in partly vegetated open channels. *International Journal for Numerical Methods in Fluids* **39**, 919–937.

ZAMAN, K. & HUSSAIN, A. 1981 Taylor hypothesis and large-scale coherent structures. *Journal of Fluid Mechanics* **112**, 379–396.